# COMPUTATIONAL STUDIES OF THERMOELECTRICITY IN STRONGLY CORRELATED ELECTRON SYSTEMS

BY GUNNAR PÁLSSON

A dissertation submitted to the

Graduate School—New Brunswick

Rutgers, The State University of New Jersey

in partial fulfillment of the requirements

for the degree of

Doctor of Philosophy

Graduate Program in Physics and Astronomy

Written under the direction of

Professor Gabriel B. Kotliar

and approved by

New Brunswick, New Jersey

May, 2001

© 2001

Gunnar Pálsson

ALL RIGHTS RESERVED

## ABSTRACT OF THE DISSERTATION

# Computational Studies of Thermoelectricity in Strongly Correlated Electron Systems

**by Gunnar Pálsson**

**Dissertation Director: Professor Gabriel B. Kotliar**

We compute transport properties of strongly correlated electron systems with special attention to thermoelectric transport properties. The transport parameters are computed within the dynamical mean field theory using the non-crossing approximation and iterated perturbation theory to solve the dynamical mean field equations. The results of our calculations compare favorably with experiments on $La_{1-x}Sr_xTiO_3$.

In the second half of the thesis we develop a method for computing the transport properties of strongly correlated materials using real bandstructure data and self energy provided by extensions of the dynamical mean field theory to real systems. The method is tested on data for alkali and noble metals using a simple functional form for self energies. The method is also applied to compute the transport parameters for a simple $t_{2g}$ model of the $La_{1-x}Sr_xTiO_3$ system.

## Acknowledgements

I am grateful to my adviser, Gabriel Kotliar for providing guidance and direction for my research over the last few years. Special thanks go also to Sergej Y. Savrasov whose help was crucial in bringing this work to conclusion.

I would moreover like to thank Aram Mekjian, Joel Lebowitz, Mark Croft and Sergej Savrasov for acting as members of my Ph.D. committee.

Thanks to my many friends here at Rutgers, Markus Raschke, Andrew Ho, Kevin Chase, Venkateswara (Venky) Sarma Kancharla, Ken Ahn, Balakrishna Subramanian, George Patani, Clifford Smyth, Thomas Walker, Ekkehard Lange, Victor Oudovenko and Alexander Poteryaev for enjoyable, interesting, and at times fruitful discussions.

Special thanks go to my good friends and compatriots, Rúnar Helgi Andrason, Heiðdís Karlsdóttir and their son Kristinn for making me feel at home on Thursday nights.

To my parents in law, Harish and Kumud Chandra, and the rest of the family my heartfelt gratitude for the warmth with which they have accepted me into their hearts.

Many thanks to my uncle Bjarni Magnússon for numerous philosophical discussions, stories, travelogues, poetry and general considerations for my well being.

To my parents, Áslaug Magnúsdóttir and Ragnar Haraldsson, my love for helping me stay grounded and miraculously extending the feeling of home across the seven seas.

Finally my deepest love goes to my wonderful wife, Giti, whose loving care, wit and wisdom has been an endless source of inspiration and confidence, (and whose talent for nonsensical blathering has never failed to pick up my spirits).

# Dedication

I dedicate this thesis to my grandparents, the shipbuilder Magnús Bjarnason and his wife Ingibjörg Halldórsdóttir; the farmer Kristján Sigurðson and his wife Aðalbjörg Vilhjálmsdóttir.

# Table of Contents

# Chapter 1

# Introduction

In the last decade or so our understanding and ability to tackle problems of strongly correlated electron systems has dramatically increased. This is in no small part due to the development of dynamical mean field theory [1] (DMFT) which allows us to map models of strongly correlated lattice electrons onto an Anderson impurity model subject to a self consistency condition much like we solve the Ising model within mean field theory by mapping it onto a single spin interacting with the self consistent field of its neighbors. Since its introduction the DMFT has been successfully applied to describe many aspects of the physics of three dimensional strongly correlated materials such as the Mott metal insulator transition in transition metal oxides.

The work in this thesis is a direct application of the DMFT to the problem of computing and understanding transport properties in strongly correlated electron systems. The experimental motivation for the work is in large part provided by the work of Y. Tokura's group which has demonstrated that within the class of ternary perovskites one can control various parameters such as the orbital degeneracy, bandwidth and carrier concentration to provide an experimental realization of the density driven Mott transition.

With this goal in mind we will in the first part of the thesis look at the grandfather of all strongly correlated models, the Hubbard model, in the limit of infinite interactions. This allows us to introduce the tools of the DMFT and the mapping to the impurity model. We then employ one of the various methods for solving for the dynamical properties of the impurity model, the so called non-crossing approximation (NCA) and outline how this method is implemented numerically. We then proceed to compute the transport properties of this model with special attention to the thermoelectric properties.

This brings us into the realm of thermoelectric devices and their performance and we introduce here the thermoelectric coefficient of performance.

The thermoelectric properties of materials are interesting to consider for a variety of reasons. One is the practical application of thermoelectric phenomena for heating or cooling purposes – already there are small commercial heater/coolers available but we have yet to see such appliances in the kitchen, for that the efficiency of the thermoelectric devices still has to improve to catch up with the compressor based alternatives. Another use is in power generation and one could imagine that such devices could make use of the waste heat generated by fossil fuel engines. One of the main applications though, would be in space travel and satellites where such generators are used with nuclear heat sources to provide electricity. For this reason much of the attention that thermoelectricity receives is focused on ways to improve the so called thermoelectric performance.

From a theoretical standpoint the thermoelectricity is also quite interesting since it provides insight into the nature of the carriers in the material – we will see that there is an intimate connection between the entropy of carriers and their thermoelectric power and thus the thermopower can tell us whether the carriers in the system are coherent, i.e. in a delocalized state with small entropy, or localized and incoherent. Compared to the electrical resistivity the thermoelectric power is also a much more sensitive probe of the topology of the Fermi-surface and the scattering experienced by carriers around the Fermi-surface.

As a practical example of some of these issues we will consider the transport properties of $La_{1-x}Sr_xTiO_3$ close to the Mott transition, i.e. at small $x$. Here we will also employ another method for solution of the DMFT equations, namely the so called iterated perturbation theory (IPT). This method complements the NCA quite well since the NCA is known to work well at high temperatures and not so well in the low temperature regime whereas the opposite holds for the IPT.

The second half of the thesis is somewhat motivated by the success of the numerical computations in the first half and anticipates the further application of the DMFT for real materials. Here the main goal is to develop a computational tool that allows for the computation of transport properties in real strongly correlated materials. The DMFT starts out with the non-interacting or bare Hamiltonian of the system in question, then an interaction term is introduced, such as the on-site density-density interaction which is well known from the Hubbard model, and from there the DMFT furnishes a self energy for the system. Thus the ingredients that we have for our computation of the transport properties are the bare Hamiltonian which we obtain from first-principles band structure calculations and the self energy which is furnished by the DMFT. The bulk of the second half is devoted to the details of this computation and it's numerical implementation.

Towards the end we will look at two simple applications of this procedure. The first example we will consider are the simple metals, i.e. alkali and noble metals with some simple assumtions about the scattering around the Fermi-level. In the second example we revisit the $La_{1-x}Sr_xTiO_3$ system with a more realistic model than before and consider the behavior of the system as a function of doping and interaction strength.

# Chapter 2

# The Hubbard model

## 2.1 Introduction

The Hubbard model was first proposed in 1963 independently by Hubbard [2] and Gutzwiller [3] in an attempt to describe the effects of correlations for d electrons in metals. Transition metals where the d-band is partially full display characteristics which in some circumstances can be best understood in terms of localized atomic-like electrons but in other cases the experimental features are better described in terms of band theory. The Hubbard model is essentially the simplest model that captures this duality and it can be derived from the full electronic Hamiltonian for the metal by keeping only interaction terms between electrons that are situated on the same site, or more specifically between electrons of different spins which are in the same Wannier state. For an s-band the Hubbard Hamiltonian is given by:

$$H = -\sum_{\langle ij\rangle\sigma} t_{ij} c^{+}_{i\sigma} c_{j\sigma} + U \sum_{j} n_{j\uparrow} n_{j\downarrow}. \tag{2.1}$$

Here $c^{+}_{i\sigma}$ creates an electron in a Wannier state localized at site $i$ with spin $\sigma$, $U$ is the local on site interaction between different spins and $t_{ij}$ is the hopping integral between sites $i$ and $j$. For our purposes we will want to generalize this Hamiltonian by increasing the spin degeneracy from 2 to $N$ and since we will be working in the grand canonical ensemble we introduce a chemical potential that we add to the Hamiltonian. Thus we have:

$$H = -\sum_{\langle ij\rangle\sigma} t_{ij} c^{+}_{i\sigma} c_{j\sigma} + \frac{U}{2} \sum_{j\sigma\neq\sigma'} n_{j\sigma} n_{j\sigma'} - \mu \sum_{j\sigma} n_{j\sigma}. \tag{2.2}$$

Here $\sigma$ runs from $-j$ to $j$ where $2j+1=N$. This model has a higher spin degeneracy than the original Hamiltonian of Hubbard and can thus be expected to be a better representation of the physics in the materials of interest, i.e. compounds of transition and rare earth metals which have partly filled d and f bands. In spite of being one of the simplest model of correlated electrons on a lattice the Hubbard model has proven to be quite difficult to tackle theoretically. It is only during the last few years that some real progress has been made, especially with the development of the dynamical mean field theory [1].

## 2.2 An overview of dynamical mean field theory

The dynamical mean field theory can be regarded as the quantum analog of the classical Curie-Weiss mean field theory for magnets. As its classical counterpart it can be shown to be the exact formulation of the model in question in the limit when the number of dimensions or the coordination number of the lattice goes to infinity, with an appropriate scaling of parameters. When the number of neighbors of a given lattice site increases it is reasonable to assume that its interactions with the neighbors can be replaced by an effective interaction with some average field that represents the dynamic state of the neighbors. These ideas can be concretely realized in the following way: A given lattice site is selected, $o$ say, and an effective action is derived for the degrees of freedom living on this site by integrating out the degrees of freedom of the other sites in the lattice. The effective action can be represented in terms of the Green's functions, $G^0_{ij}$, of the so called cavity Hamiltonian, i.e. the lattice Hamiltonian obtained by deleting the site $o$ and all the bonds associated with it. By scaling the hopping integral such that $z^{|i-j|}t^2_{ij}$ is a constant, where $z$ is the coordination number of the lattice and $|i-j|$ is the Taxi-cab distance between the sites $i$ and $j$, and then taking the limit when $z \to \infty$ the action simplifies tremendously and we obtain:

$$S_{eff} = -\int_0^\beta d\tau \int_0^\beta d\tau' \sum_\sigma c^+_{o\sigma}\mathcal{G}^{-1}(\tau-\tau')c_{o\sigma} + \frac{U}{2}\int_0^\beta d\tau \sum_{\sigma\neq\sigma'} n_{o\sigma}n_{o\sigma'} \tag{2.3}$$

where the function $\mathcal{G}$ is the so called Weiss function and plays the role of the Weiss field of the Curie-Weiss theory and is given by,

$$\mathcal{G}^{-1}(i\omega_n) = i\omega_n + \mu - \sum_{\langle ij\rangle} t_{io}t_{jo}G^0_{ij}(i\omega_n). \tag{2.4}$$

Given an explicit form for the action, the on-site interacting Green's function $G$ can in principle be calculated (in practice this is a nontrivial problem) by evaluating the following expectation value:

$$G(\tau - \tau') = -\langle T c_o(\tau) c_o^+(\tau') \rangle_{S_{eff}}. \tag{2.5}$$

The self consistency condition that is now imposed is that this Green's function be the same as the diagonal, on site lattice Green's function, $G_{oo} \equiv G_{loc}$. To compute the full, lattice Green's function it is useful to switch over to momentum representation and introduce a self energy $\Sigma$ which is momentum independent in the infinite dimensional limit and given by,

$$\Sigma(i\omega_n) = \mathcal{G}^{-1}(i\omega_n) - G^{-1}(i\omega_n). \tag{2.6}$$

Then the momentum dependent Green's functions are given by,

$$G(k, i\omega_n) = \frac{1}{i\omega_n + \mu - \varepsilon_k - \Sigma(i\omega_n)} \tag{2.7}$$

where $\varepsilon_k$ is the dispersion relation of the lattice. The general inter-site lattice Green's function can be computed from this expression by Fourier transform and the diagonal term is of course simply the momentum integral of the expression above. At this point it is useful to stop and look over the equations that we have so far. Let us for a moment assume that we have a guess for the self energy, $\Sigma$. From there we can compute the local Green's function by momentum integration over $G(k, i\omega)$ and then the Weiss field can be computed from equation (2.6). We now have all the ingredients to compute the local Green's function from the action, and then we can use equation (2.6) again to get a new solution for the self energy. This process can now be started over and iterated until self consistency is attained. Thus it seems that we have all that is necessary to solve our problem but we still haven't used the cavity Green's function, $G^0$. In the limit $z \to \infty$ the cavity Green's function, $G^0_{ij}$, is very simply related to the full lattice Green's function , $G_{ij}$. This relation is,

$$G^0_{ij} = G_{ij} - \frac{G_{io} G_{jo}}{G_{oo}} \tag{2.8}$$

and it is quite simple to understand: using the interpretation of the Green's function as the likelihood of finding an electron at site $j$ if it is created at $i$ we see that this likelihood is the same in the full lattice as in the lattice with a cavity at $o$, except that in the cavity lattice we cannot go through the site $o$ and thus we must subtract those contributions off after normalization for processes that start at $o$ and come back to $o$. Putting this relation into the equation (2.4) and using the form for the momentum dependent Green's functions we end again up with equation (2.6). So, somehow this relation between the cavity Green's function and the full Green's function seems to be equivalent to the momentum independence of the self energy. Here it is useful to use the representation of the local Green's function in terms of the density of states:

$$G(i\omega_n) = \int \frac{D(\epsilon)d\epsilon}{\zeta - \epsilon} \tag{2.9}$$

where $D(\epsilon)$ is the bare density of states of the lattice and $\zeta = i\omega_n + \mu - \Sigma(i\omega_n)$. We see that $G$ is essentially given by a Hilbert transform over the density of states and if we can invert that we can express the self energy in term of the Green's function and then the Weiss function can be expressed solely in terms of the Green's function through equation (2.6).

In the calculations that follow we will use the Bethe lattice of infinite connectivity with only nearest neighbor hopping given by $t_o$, $zt_o^2 = t^2$. In that case the self consistency condition becomes especially simple and we get,

$$\mathcal{G}^{-1}(i\omega) = i\omega + \mu - t^2 G_{loc}(i\omega) - G_{loc}^{-1}(i\omega). \tag{2.10}$$

Given the physical picture embodied in the DMFT, i.e. of an electron on a single site interacting with a bath of electrons on the rest of the lattice it is not surprising that a connection can be made between the dynamical mean field theory described above and impurity models like the Anderson impurity model,

$$H^{AIM} = \sum_{k\sigma} \tilde{\varepsilon}_k c_{k\sigma}^+ c_{k\sigma} - \mu \sum_{\sigma} f_\sigma^+ f_\sigma + \sum_{k\sigma} (V_k c_{k\sigma}^+ f_\sigma + h.c.) + \frac{U}{2} \sum_{\sigma \neq \sigma'} n_\sigma n_{\sigma'} \tag{2.11}$$

by noting that if the conduction electrons $c_{k\sigma}$ are integrated out an action of the form

(2.3) is obtained with

$$\mathcal{G}^{-1}(i\omega) = i\omega + \mu - \int d\varepsilon \frac{\Delta(\varepsilon)}{i\omega - \varepsilon} \quad \text{where} \quad \Delta(\varepsilon) = \sum_k V_k^2 \delta(\varepsilon - \tilde{\varepsilon}_k) \tag{2.12}$$

is the hybridization function of the Anderson model. The full impurity Green's function will now be equal to $G_{loc}$ provided $\Delta$ is chosen such that the self-consistency condition is fulfilled. On the Bethe-lattice that requirement gives us

$$\Delta(\varepsilon) = t^2 \rho_{loc}(\varepsilon) = -\frac{t^2}{\pi} Im G_{loc}(\varepsilon + i0). \tag{2.13}$$

The impurity model connection is very fortunate since impurity models have been studied intensely in the past, their physics is well known and many tools and methods exist to deal with such models such as quantum Monte-Carlo methods, exact diagonalization methods, iterated perturbation methods and the so called non-crossing approximation (NCA) which we will mainly focus on here.

## 2.3 The non-crossing approximation

The NCA solution to the Anderson model applies specifically to the case where the interaction strength $U$ goes to infinity which prevents more than one electron from occupying each site in the lattice. Then the interaction term in the Anderson Hamiltonian goes away but is replaced by the auxiliary condition that the occupancy of the impurity be less than or equal to one. In this case the Hamiltonian can be rewritten in the form [4],

$$H_{AIM} = \sum_{k\sigma} \tilde{\varepsilon}_k c_{k\sigma}^+ c_{k\sigma} - \mu \sum_\sigma f_\sigma^+ f_\sigma + \sum_{k,\sigma} [V_k c_{k\sigma}^+ b^+ f_\sigma + h.c.] \tag{2.14}$$

where $b$ is a bosonic operator that represents the empty impurity and $f_\sigma$ is a pseudo-fermion with the original fermion now being represented by the combination $f_\sigma^+ b$. We can think of it in such a way that in order to create an electron at an empty impurity site we first need to destroy the empty impurity and then create the electron from some new unphysical vacuum state. The physical subspace is the one in which the number operator, $Q = b^+ b + \sum_\sigma f^+ f$ takes the value 1. This condition can be imposed by introducing a chemical potential associated with $Q$ and then let it tend to infinity in order to project out the physical subspace. The non-crossing approximation to the solution of the impurity problem consist, as the name implies, in calculating the self energies for the boson $b$ and the fermion $f$ by summing up all the Feynman diagrams that do not have any crossing lines. This procedure leads to the equations[1]:

$$G_b(\omega) = \frac{1}{\omega - \Sigma_b(\omega)}, \qquad \Sigma_b(\omega) = N\int_{-\infty}^{\infty} d\varepsilon \Delta(\varepsilon) f(\varepsilon) G_f(\omega+\varepsilon), \tag{2.15}$$

$$G_f(\omega) = \frac{1}{\omega + \mu - \Sigma_f(\omega)}, \quad \Sigma_f(\omega) = \int_{-\infty}^{\infty} d\varepsilon \Delta(\varepsilon)(1-f(\varepsilon)) G_b(\omega-\varepsilon). \tag{2.16}$$

where $f(\varepsilon)$ is the Fermi function. The impurity Green's functions is now given in terms of the auxiliary Green's functions by:

$$G_{imp}(\omega) = \int_{-\infty}^{\infty} d\varepsilon \left(\eta_b(\varepsilon) G_f(\varepsilon+\omega) - \eta_f(\varepsilon) G_b^{\star}(\varepsilon-\omega)\right) \tag{2.17}$$

Here the $\eta$'s are given by:

$$\eta_f(\omega) = \frac{1}{Z} e^{-\beta\omega} \rho_f(\omega), \qquad \eta_b(\omega) = \frac{1}{Z} e^{-\beta\omega} \rho_b(\omega). \tag{2.18}$$

with

$$\rho_f(\omega) = -\frac{1}{\pi} Im G_f(\omega), \qquad \rho_b(\omega) = -\frac{1}{\pi} Im G_b(\omega). \tag{2.19}$$

and $Z$ is the impurity partition function. To avoid numerical problems at negative energies when $\eta$ is calculated from $\rho$ it is beneficial to have explicit NCA equations for the $\eta$'s. These are easily found from the original NCA equations and turn out to be

$$\phi_b(\omega) \equiv \eta_b(\omega)|G_b(\omega)|^{-2} = N\int_{-\infty}^{\infty} d\varepsilon \Delta(\varepsilon)(1-f(\varepsilon))\eta_f(\omega+\varepsilon) \tag{2.20}$$

$$\phi_f(\omega) \equiv \eta_f(\omega)|G_f(\omega)|^{-2} = \int_{-\infty}^{\infty} d\varepsilon \Delta(\varepsilon) f(\varepsilon) \eta_b(\omega-\varepsilon) \tag{2.21}$$

Note that the equations for $\eta_b$ and $\eta_f$ determine these functions only up to a constant and thus we need some additional relation to determine them uniquely. This is furnished by the following equation for the partition function:

$$Z = \int_{-\infty}^{\infty} d\varepsilon \left(\rho_b(\varepsilon) + N\rho_f(\varepsilon)\right) e^{-\beta\varepsilon} \tag{2.22}$$

[1]All Green's functions and self energies are assumed to be retarded unless explicitly indicated otherwise.

from which we obtain

$$\int_{-\infty}^{\infty} d\varepsilon \left(\eta_b(\varepsilon) + N\eta_f(\varepsilon)\right) = 1. \tag{2.23}$$

For numerical calculations the following sum rules are quite useful as a check on the validity of the solution [5]:

$$\int_{-\infty}^{\infty} \rho_b(\varepsilon) d\varepsilon = 1, \qquad \int_{-\infty}^{\infty} \rho_f(\varepsilon) d\varepsilon = 1, \tag{2.24}$$

$$\int_{-\infty}^{\infty} \rho_{imp}(\varepsilon) f(\varepsilon) d\varepsilon = \frac{n}{N}, \qquad \int_{-\infty}^{\infty} \rho_{imp}(\varepsilon)(1 - f(\varepsilon)) d\varepsilon = 1 - n, \tag{2.25}$$

where $n$ is the occupancy of the impurity.

## 2.4 Numerical implementation of the NCA+DMFT

Before starting the numerical calculations it is useful to define new functions as follows:

$$\begin{aligned} \widetilde{G}_f(\omega) = G_f(\omega - \mu), &\qquad \widetilde{G}_b(\omega) = G_b(\omega), \\ \widetilde{\Delta}(\omega) = \Delta(\omega - \mu), &\qquad \widetilde{G}_{loc}(\omega) = G_{loc}(\omega - \mu), \end{aligned}$$

with the same convention for the other boson and pseudo-fermion functions $(\phi, \rho, \eta)$. In terms of these functions the set of equations becomes:

$$\widetilde{G}_b(\omega) = \frac{1}{\omega - \widetilde{\Sigma}_b(\omega)}, \quad \widetilde{\Sigma}_b(\omega) = N \int_{-\infty}^{\infty} d\varepsilon \widetilde{\Delta}_p(\varepsilon) \widetilde{G}_f(\omega + \varepsilon), \tag{2.26}$$

$$\widetilde{G}_f(\omega) = \frac{1}{\omega - \widetilde{\Sigma}_f(\omega)}, \quad \widetilde{\Sigma}_f(\omega) = \int_{-\infty}^{\infty} d\varepsilon \widetilde{\Delta}_h(\varepsilon) \widetilde{G}_b(\omega - \varepsilon), \tag{2.27}$$

$$\widetilde{\phi}_b(\omega) \equiv \widetilde{\eta}_b(\omega) |\widetilde{G}_b(\omega)|^{-2} = N \int_{-\infty}^{\infty} d\varepsilon \widetilde{\Delta}_h(\varepsilon) \widetilde{\eta}_f(\omega + \varepsilon) \tag{2.28}$$

$$\widetilde{\phi}_f(\omega) \equiv \widetilde{\eta}_f(\omega) |\widetilde{G}_f(\omega)|^{-2} = \int_{-\infty}^{\infty} d\varepsilon \widetilde{\Delta}_p(\varepsilon) \widetilde{\eta}_b(\omega - \varepsilon) \tag{2.29}$$

$$\widetilde{G}_{imp}(\omega) = \int_{-\infty}^{\infty} d\varepsilon \left( \widetilde{\eta}_b(\varepsilon) \widetilde{G}_f(\varepsilon + \omega) - \widetilde{\eta}_f(\varepsilon) \widetilde{G}_b^{\star}(\varepsilon - \omega) \right) \tag{2.30}$$

and

$$\widetilde{\Delta}(\omega) = t^2 \widetilde{\rho}_{imp}(\omega) \tag{2.31}$$

Here we have defined

$$\widetilde{\Delta}_p(\varepsilon) = \widetilde{\Delta}(\varepsilon) f(\varepsilon - \mu) \quad \text{and} \quad \widetilde{\Delta}_h(\varepsilon) = \widetilde{\Delta}(\varepsilon)[1 - f(\varepsilon - \mu)]. \tag{2.32}$$

The equations above constitute a closed set of self consistent equations for the impurity Green's function $G_{imp} = G_{loc}$. The energy scale of the model is set by the hopping integral, $t$, which we will in all our calculations set equal to $\frac{1}{2}$ which corresponds to a bare DOS of half-width $D = 1.0$ on the Bethe-lattice. We solve these equations numerically by cutting off the integrals and then introduce a uniform mesh of points between the cutoffs. Traditionally the NCA equations are solved on logarithmic meshes [6–8] due to singularities in the spectrum but here these singularities are less pronounced due to the smoothing effects of the mean field consistency condition. For this reason and also to be able to use fast Fourier transform techniques we use uniform meshes. Because of this we could not, however, go to very low temperatures in our calculations but as we will see later this is not the limiting factor in the usefulness of the method.

On a uniform mesh the convolution integrals can either be done by straightforward integration or by the Fast Fourier Transform. We actually implemented both methods. The FFT method is of course faster but it turned out that the direct method gave better results as determined by the convergence of the chemical potential (or thermopower) to the value given by Heikes formula (see §3.5). The upshot was that the FFT method is used first to find an approximate solution for a given temperature and density and then the direct method is used to improve upon this solution.

For the FFT solution we define our Fourier transforms as follows.

$$g(\omega) = \int_{-\infty}^{\infty} dt e^{i\omega t} g(t), \qquad g(t) = \int_{-\infty}^{\infty} \frac{d\omega}{2\pi} e^{-i\omega t} g(\omega). \tag{2.33}$$

After having imposed an energy cutoff, $\omega_{max}$, the Fourier transforms are approximated by

$$g(t) \simeq \int_{-\omega_{max}}^{\omega_{max}} \frac{d\omega}{2\pi} e^{-i\omega t} g(\omega). \tag{2.34}$$

and the cutoff Fourier integral is then calculated by using cubic B-splines and the Fast

Fourier Transform [9]. After the Fourier transformation the equations for the self energies are

$$\widetilde{\Sigma}_b(t) = 2N\pi\widetilde{\Delta}_p^*(t)\widetilde{G}_f(t), \qquad \widetilde{\Sigma}_f(t) = 2\pi\widetilde{\Delta}_h(t)\widetilde{G}_b(t). \tag{2.35}$$

To take care of the long $\frac{1}{\omega}$ tails of the Green's functions we also subtract off the real part of an almost free Green's functions[2]

$$G^0_{free}(\omega) = \frac{1}{\omega + i\Gamma} \tag{2.36}$$

before doing the transform and then add by hand its Fourier transforms which is equal to half of the Fourier transforms of the Green's function above,

$$G^0_{free}(t) = -i\theta(t)e^{-\Gamma t}. \tag{2.37}$$

Here $\Gamma > 0$ is a quantity of the order of the mesh spacing. Note that all the functions we are dealing with are retarded so they are zero at negative times. For the auxiliary Green's functions we have the condition that $G_b(t = 0^+) = G_f(t = 0^+) = -i$, and in the numerical calculation these values are put in by hand.

The direct integration is much simpler to implement. We approximate the functions by linear interpolation between mesh points and assume that they are identically zero outside of the cut-off which is chosen the same as for the FFT solution. The convolutions of the interpolating functions are then done analytically.

## 2.5 Results: Green's functions and self energies

In figures 2.1 and 2.2 we have displayed the results from the numerical calculations of the local Green's functions as described in the previous section. The calculations were done for several densities between zero and one, for degeneracies $N = 2, 4, 6$ and temperatures in the range of 0.025-5.0 in most cases[3]. The two main features of the spectra are the broad band corresponding to the incoherent lower Hubbard band and a

[2] We only subtract off the real part since the imaginary part of the Green's function already falls off faster than $\frac{1}{\omega^2}$.

[3] Remember that all energies are measured in terms of the half-bandwidth $D$ unless otherwise specified.

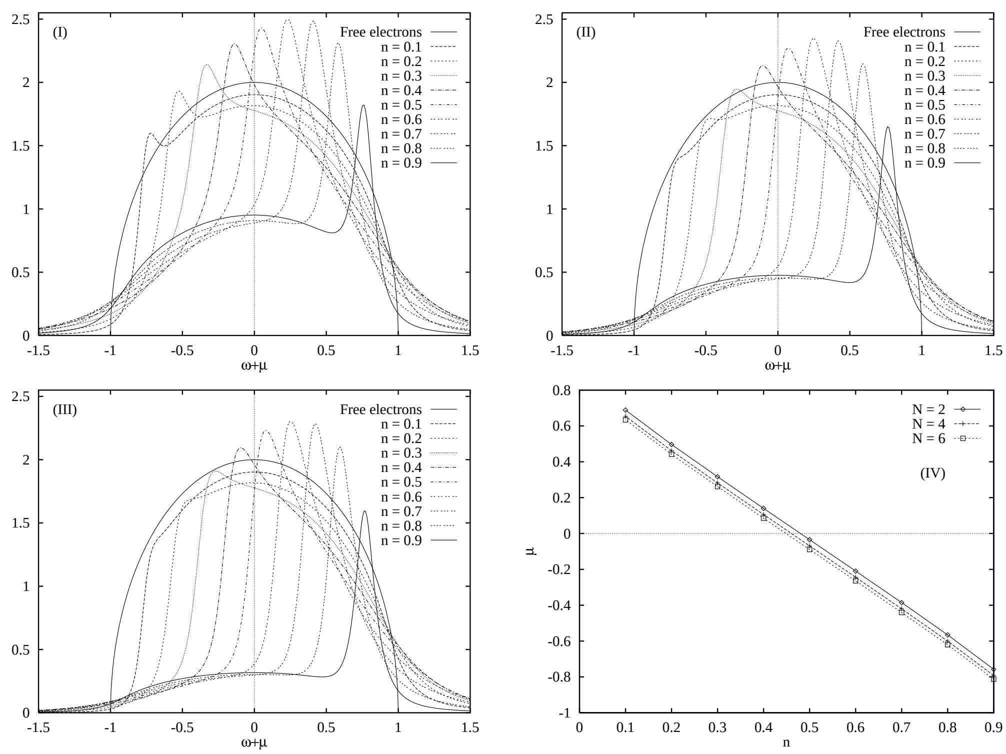


Figure 2.1: Results from NCA+DMFT calculations. I: imaginary part of the Green's functions for different densities, $n$, for degeneracy $N = 2$ and temperature $T = 0.05$. II: Same as I for $N = 4$. III: Same as I for $N = 6$. IV: The chemical potential corresponding to the Green's functions in I-III.

quasiparticle peak or Kondo peak just above the Fermi-surface. There is no sign of an upper Hubbard band since the interaction strength, $U$, is infinite and thus no charge excitations exist in the system – the upper Hubbard band has essentially moved off to infinity. But it takes a lot of spectral weight with it as we can see by computing the total integrated spectral weight of the system from the sum rules in equation (2.25):

$$\int_{-\infty}^{\infty} \rho_{loc}(\varepsilon) d\varepsilon = 1 - n + \frac{n}{N}. \tag{2.38}$$

As the density increases more and more spectral weight is lost and at half filling, i.e. $n = 1$ it is down to $1/N$. We note also that as the degeneracy of the system, $N$, increases the total spectral weight decreases. From the data we see however that this spectral weight is mostly taken from the incoherent band – both the width and the height of the quasiparticle peak show much weaker dependence on the degeneracy.

If we look at figure 2.1 we note that for the lowest values of density the spectral density is quite close to being equal to the free electron spectral density on the Bethe

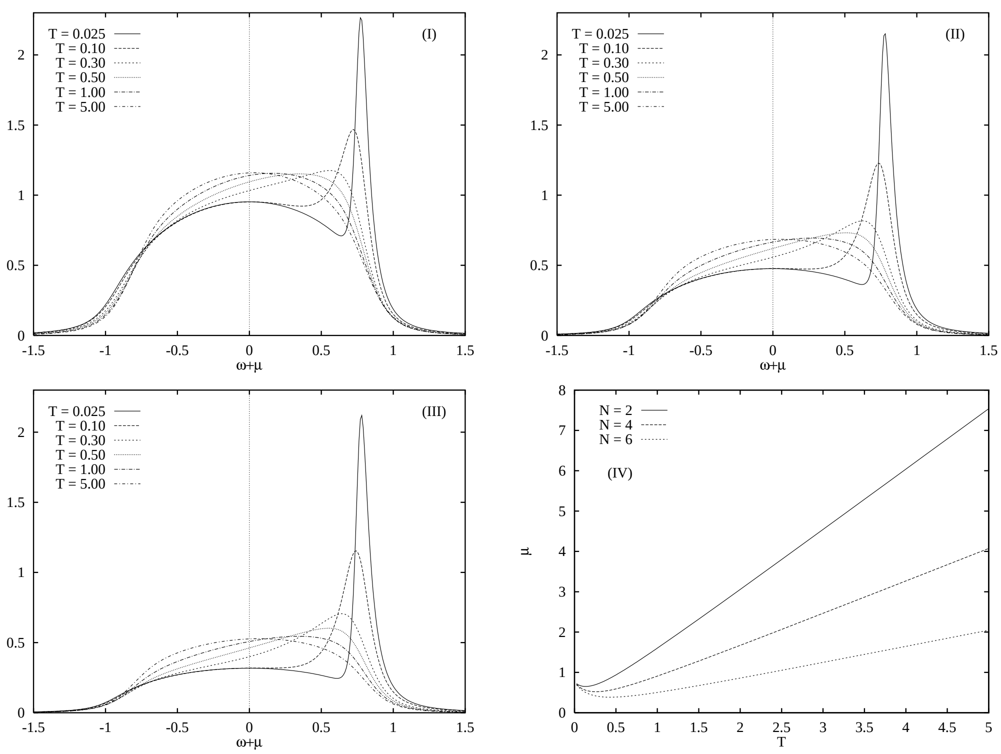


Figure 2.2: Results from NCA+DMFT calculations. I: imaginary part of the Green's functions for different temperatures, $T$, for degeneracy $N = 2$ and density $n = 0.90$. II: Same as I for $N = 4$. III: Same as I for $N = 6$. IV: The chemical potential corresponding to the Green's functions in I-III.

lattice. As the density increases we start seeing the formation of the quasiparticle peak. The quasiparticle peak corresponds to carriers that have a well defined momentum and are thus in a delocalized low entropy state. In order to form this state the carriers must get rid of their entropy and thus we can expect this state to appear earlier in the lower degeneracy systems that have a smaller entropy per carrier. This is exactly what can be observed in the data (see figure 2.1) – the quasiparticle peak is already evident in the lowest density curve for $N = 2$ whereas only a slight shoulder can be seen for the corresponding density in the $N = 6$ system.

From figure 2.2 we see that as the temperature increases the Kondo peak melts away, the weight is transferred into the Hubbard band which becomes increasingly more symmetric around $\omega = -\mu$ as the temperature increases.

From the NCA equations it is easy to see that if we start the DMFT iterations with a hybridization function $\widetilde{\Delta}$, and initial guesses for $\widetilde{G}_f$ and $\widetilde{G}_b$ which are symmetric around zero then the self consistent solutions for $\widetilde{G}_f$ and $\widetilde{G}_b$ are also symmetric around zero to lowest order in $\beta$ and therefore the self consistent solution, $\widetilde{G}_{loc}$, to the mean field equations will be symmetric to lowest order in $\beta$. To find how the chemical potential depends on temperature we use the sum rules (2.25) and write:

$$\begin{aligned} \frac{n}{N} &= \int_{-\infty}^{\infty} \rho_{imp}(\varepsilon) f(\varepsilon) d\varepsilon \simeq A f(-\mu) \\ 1-n &= \int_{-\infty}^{\infty} \rho_{imp}(\varepsilon) f(-\varepsilon) d\varepsilon \simeq A f(\mu) \end{aligned}$$

from which we get,

$$\frac{\mu}{T} = \ln(\frac{n}{N(1-n)}). \tag{2.39}$$

Thus the chemical potential is a linear function of $T$ at large $T$. This formula can clearly be regarded as the result of the competition between the empty site with density $1-n$ and the occupied site with density per spin $n/N$. If the empty site density is higher than the density per spin the chemical potential is forced to become negative and vice versa. This equation can also derived very simply by considering the high temperature entropy of a system of $N_e$ electrons with degeneracy $N$ on a lattice with $N_s$ sites, only one electron per site [10]. The partition function is obviously

$$Z = \frac{N^{N_e} N_s!}{N_e!(N_s - N_e)!} \tag{2.40}$$

and using the Stirling approximation we find that the entropy density is

$$S = \frac{\ln(Z)}{N_s} = -n\ln(n/N) - (1-n)\ln(1-n) \tag{2.41}$$

where $n = \frac{N_e}{N_s}$ is the density. Now using the fact that $\frac{\mu}{T} = \frac{\partial S}{\partial n}$ we obtain the formula for $\mu$ which is given above. If we look at the self energy for the same parameters as in figure 2.2 we obtain the graphs in figure 2.3. The main feature to observe is the sharp dip at low temperatures around the Fermi-level. This correspond to the quasiparticle peak in the local spectral density and as we can see the self energy spectral density actually becomes negative at that point if the temperature is low enough. This pathology is of course quite serious since it prevents the calculation of certain quantities like the transport parameters at temperatures below certain breakdown temperature at which

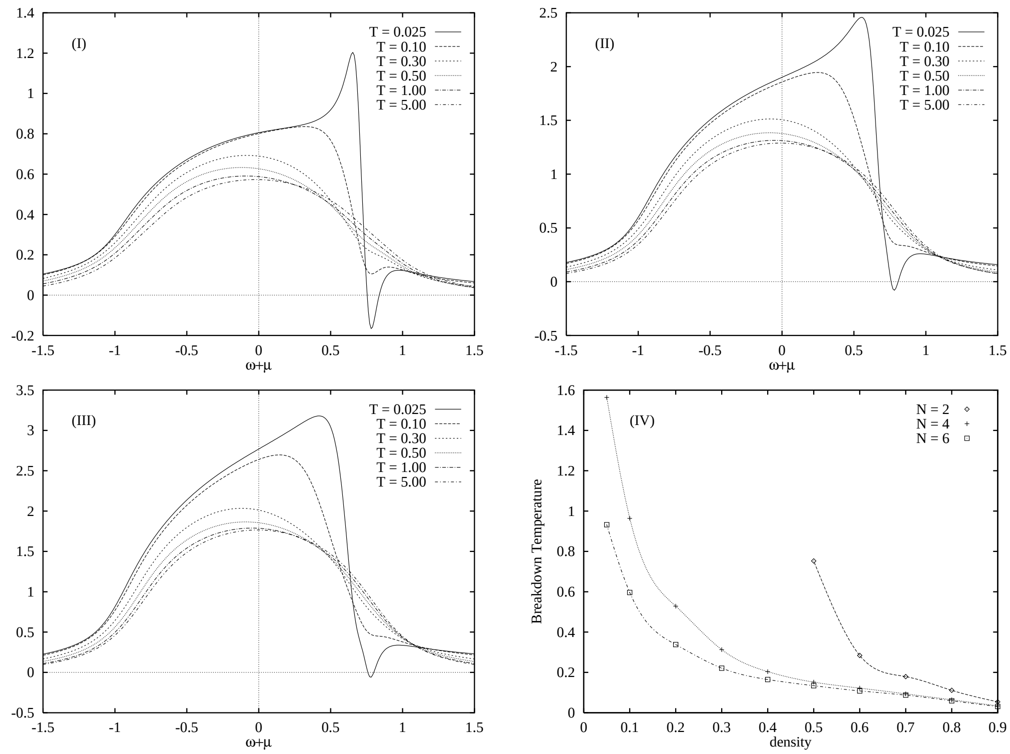


Figure 2.3: Results from NCA+DMFT calculations. I: imaginary part of the self energy for different temperatures, $T$, for degeneracy $N = 2$ and density $n = 0.90$. II: Same as I for $N = 4$. III: Same as I for $N = 6$. IV: The breakdown temperature for different densities (see main text).

the imaginary part of the self energy becomes zero. The breakdown temperature depends both on the density and degeneracy as we can see in figure 2.3(IV). The question that comes naturally up is; how does this pathology occur, and how is it that one can solve the model and obtain the spectral density if the self energy, through which the lattice self consistency proceeds, is so pathological. To see this we need to look at how the self consistency and the calculation of the self energy is carried out on the Bethe lattice:

$$\Delta(\omega) = t^2 \rho_{loc}(\omega), \qquad Im\Sigma(\omega) = ImG_{loc}(\omega)\left(\frac{1}{|G_{loc}(\omega)|^2} - t^2\right). \tag{2.42}$$

First of all we note that, since the solution of the associated impurity model furnishes the spectral density, $\rho_{loc}$ from which the new hybridization function is calculated, we never have to use the self energy in the solution to the model. It is not until one wants to calculate lattice dependent response functions that the self energy has to be used. We also see from the equations above why the self energy becomes pathological. Namely as long as $|G_{loc}|$ is less than $1/t$ everything is fine but if this doesn't hold, which happens at the quasiparticle peak at low temperatures, things go awry. It is also easy to understand why the breakdown temperature decreases with density and degeneracy. As we mentioned earlier the total weight of the spectral density is $1 - n + n/N$ so as $n$ and $N$ increase this weight becomes less and therefore the likelihood of crossing the bound on $|G_{loc}|$ is diminished.

We should note that faulty numerics can be ruled out as a possible source for this breakdown – it is known from analytic results [11, 12] that the solution of the NCA equations does indeed exceed this bound for low temperatures.

We should note that other lattice place similar condition on the local Green's function. To see this let us compute the local Green's function as prescribed by the DMFT:

$$\begin{aligned} -\operatorname{Im} G_{loc}(\omega) &= \operatorname{Im} \sum_k \frac{-1}{\omega + \mu - \epsilon_k - \Sigma(\omega)} \\ &= \int_{-\infty}^{\infty} d\epsilon D(\epsilon) \operatorname{Im} \left( \frac{-1}{\omega + \mu - \epsilon - \Sigma(\omega)} \right) \\ &\leq D(\epsilon)_{max} \int_{-\infty}^{\infty} d\epsilon \operatorname{Im} \left( \frac{-1}{\omega + \mu - \epsilon - \Sigma(\omega)} \right) \\ &= \pi D(\epsilon)_{max}. \end{aligned} \tag{2.43}$$

Here we have assumed that the self energy is properly retarded. We see now that the local spectral density $\rho(\omega) = -\operatorname{Im} G_{loc}(\omega)/\pi$ can never be greater than maximum value of the noninteracting density of states, $D(\omega)$. On the Bethe lattice this gives us the condition, $\rho_{loc}(\omega) \leq 1/t$. It would seem strange that the DMFT should place such restrictions on the spectral density; we are after all trying to capture the effects of strong correlations and thus one of the features that we can expect to see narrow resonances of large magnitude in the density of states.

We will not dwell on this pathology here, it is quite sufficient for our purposes to restrict the use of the NCA to higher temperatures and we will employ other methods in the low temperature regime in the computation of transport properties in the following chapters.

# Chapter 3

# Transport and Thermodynamic Properties

In this chapter we will use the results from chapter 2 to compute the transport properties of the Hubbard model with special attention to thermoelectric properties. As discussed in that chapter the NCA results are not valid at very low temperatures so we will use the IPT method in the second half of this chapter to extend the results to lower temperatures. However before we start computing the transport properties of the model let us start with a brief look at thermoelectricity and some basic transport theory.

## 3.1 A brief overview of thermoelectricity

Thermoelectric effects which are responsible for the direct conversion of heat energy into electrical energy and vice versa have in recent years received renewed attention [13]. This is in large part due to progress in material science and discoveries of new materials with promising thermoelectric potential but theoretical methods have also come to the fore and are now playing a key role in identifying likely candidates for thermoelectric applications.

It is now almost 200 years since thermoelectric phenomena were discovered and studied by Seebeck and although in hindsight he could in principle have generated electricity with quite favorable efficiency compared to steam engines there was little interest or progress in thermoelectricity during most of the nineteenth century. It was not until around 1910 that theory of thermoelectric power generation and refrigeration was developed and it was realized that the thermoelectric performance of materials could be quantified with the so called dimensionless figure of merit given by

$$Z_T T = \frac{S^2 \sigma T}{\kappa} = \frac{S\pi}{\kappa\rho} \tag{3.1}$$

where $S$ is the thermopower or Seebeck coefficient, $\sigma = 1/\rho$ is the electrical conductivity, $T$ is the temperature, $\kappa$ is the thermal conductivity and $\pi = TS$ is the Peltier coefficient [14]. In later chapters we will derive this equation more thoroughly but here we can already understand the figure of merit in the following simple manner,

- $Z_T T \propto S$ so as to get a large voltage drop for a given temperature difference.
- $Z_T T \propto \pi = \frac{J_Q}{J_C}$ so as to get a large heat current, $J_Q$ for a given electric current, $J_C$.
- $Z_T T \propto \frac{1}{\rho}$ so as not to incur Joule heating in the circuit.
- $Z_T T \propto \frac{1}{\kappa}$ in order not to lose heat through irreversible heat flow between the reservoirs.

Early on the study of thermoelectricity focused mostly on metals and metallic alloys but in the 1930 the attention shifted to semiconductors when it was realized that they could possess large thermopower and give better efficiency than metallic thermoelements. The theory of thermopower in semiconductors was developed around 1950 by Abraham Ioffe and subsequently the field enjoyed a tremendous revival motivated by industrial and military applications. The launch of the space program and the need for reliable autonomous sources of electricity was also an important factor in pushing forward the search for good thermoelectric materials.

The best thermoelectric elements found during this period [15] were doped bismuth telluride alloys ($Bi_2Te_3$) and antimony telluride alloys ($Sb_2Te_3$) for use in refrigeration with maximum operating temperatures of around 450 K. For higher temperature applications (1300K) such as power generation, the best materials have proven to be lead telluride alloys (PbTe) and to a greater extent, silicon germanium (SiGe) alloys. All of these materials have dimensionless figure of merit around 1.0 which is still today among the highest that can be found.

The search for new thermoelectric materials has in recent years been shifting towards more structurally complex materials such as skutterudites like $CeFe_4Sb_{12}$ or $La(Fe,Co)_4Sb_{12}$. This shift can on one hand be attributed to the fact that most simple semiconducting materials have already be studied for this purpose but behind this is also the guiding principle that a good thermoelectric material should conduct electricity like a crystal but the thermal conductivity should be more characteristic of a glass [16]. So one of the reason for the favorable thermoelectric properties of the materials above is the low value of thermal conductivity which can be attributed to the thermal motion or rattling of the rare earth ions in the crystal structure.

Another avenue that has recently been explored is to construct thermoelements out of quantum well superlattices and both experimental [17] and theoretical work [18–20] indicates that a significant increase in the figure of merit is possible. These effort are mostly academic as yet and it is doubtful whether practical applications are feasible.

Through the years some guidelines have been developed to aid in the search for good thermoelectric semiconductors. It is found that a good candidate for thermoelectric use should have the following properties [15, chapter 23]:

- A large value of the parameter, $A = \mu T (m^*)^{3/2}/\kappa_L$, where $\mu$ is the mobility, $m^*$ is the effective mass, T is the absolute temperature and $\kappa_L$ is the lattice thermal conductivity.
- The band gap should be greater that $4k_BT$.
- The material should be dopable to the extrinsic regime.[1]

It is intuitively clear that $\kappa_L$ should be small and the mobility should of course be large to minimize resistance. The effective mass enters here through the density of states at the Fermi level which also affects the electric conductivity. The restrictions on the band gap are made so as to minimize the excitations of minority carriers across the gap which would adversely affect the thermopower. In addition the requirement on the doping is so as to be able to have reasonable number of carriers while trying to balance the deleterious effects that overdoping has on the thermopower.

In a recent reevaluation of the analysis leading to the principles above Mahan [22] comes to essentially the same conclusion except that he requires the band gap to be

[1]This means that the conduction behavior is dominated by the dopants and not by the intrinsic properties of the medium [21].

around $10k_BT$ but not larger to avoid the increase of the lattice thermal conductivity that accompanies the increase of the bandgap. His conclusions seem to be consistent with the bismuth telluride semiconductors which have band gaps in this range.

In a recent paper by Mahan and Sofo [23] they consider the general mathematical problem of finding the optimal conditions for achieving good thermoelectric properties. Their approach is to separate the material characteristics from the expressions for the transport parameters (see equations (3.76),(3.71) and (6.2)) and define a function, $\Sigma_{MS}$, that embodies these characteristics. The function $\Sigma_{MS}$, which corresponds to our transport function in equation (6.2), is now taken as a free parameter essentially and the figure of merit is optimized by varying this function. The resulting optimal $\Sigma_{MS}$ turns out to be a delta function positioned slightly above the Fermi-surface. In real materials it is impossible for this function to be a real delta function but in strongly correlated materials with narrow bands near the Fermi-surface this function could be delta function like. On the other hand, in addition to the narrow correlated levels, there are usually also some very broad, featureless bands that cross the Fermi-surface and according to the analysis of Mahan and Sofo, those band have quite a deleterious effect on the figure of merit.

The theoretical analysis and the computation of transport properties in the semiconducting materials discussed above is all based on kinetic theory and the Boltzmann equation. However Boltzmann theory is not expected to be valid for strongly correlated materials where correlation effects significantly alter the electronic structure and the carriers in the system are in many particle cooperative state rather than being simply described by single electron physics.

## 3.2 Basic Transport Theory

In this section we will briefly review the basic notions of transport theory as described in references [24–27]. Consider a thermodynamic system which is acted upon by external forces $X_i$ which is turn induce currents, $J_i$ in the system. Within the linear response formalism we assume that the currents depend linearly on the external forces according to the phenomenological equation:

$$J_i = \sum_j Z^{ji} X_j. \tag{3.2}$$

The kinetic coefficients, $Z^{ji}$ describe the response of the system and our goal is to compute these coefficients and relate them to the transport parameters of the system. The choice of forces is to a certain extent arbitrary, but they are to be chosen such that the Onsager relationships, $Z^{ij} = Z^{ji}$ hold. The criterion for this is that the internal entropy generation be given by:

$$\left.\frac{\partial s}{\partial t}\right|_{gen} = \sum_i J_i \cdot X_i. \tag{3.3}$$

We shall now deduce what these forces are in the case where there are only two external driving forces: a temperature gradient and an electric potential gradient. Then we have the following equation for the total change in entropy density:

$$Tds = du - (\mu + qV)dn \tag{3.4}$$

where $u$ is the internal energy[2], $V$ is the external potential and $q$ is the charge of the constituent particles. It is convenient to define here $\tilde{\mu} \equiv \mu + qV$. From the equation above we find that

$$\left.\frac{\partial s}{\partial t}\right|_{total} = \frac{1}{T}\left(\frac{\partial u}{\partial t} - \tilde{\mu}\frac{\partial n}{\partial t}\right). \tag{3.5}$$

and using the continuity equation for the energy and particle currents:

$$\frac{\partial u}{\partial t} + \nabla \cdot J_e \qquad \text{and} \qquad \frac{\partial n}{\partial t} + \nabla \cdot J_p \tag{3.6}$$

we get

$$\begin{aligned} \left.\frac{\partial s}{\partial t}\right|_{total} &= \frac{-1}{T}\left(\nabla \cdot J_e - \tilde{\mu}\nabla \cdot J_p\right) \\ &= -\nabla \cdot \left(\frac{1}{T}J_e - \frac{\tilde{\mu}}{T}J_p\right) + \left\{J_e \cdot \nabla\left(\frac{1}{T}\right) - J_p \cdot \nabla\left(\frac{\tilde{\mu}}{T}\right)\right\} \end{aligned} \tag{3.7}$$

[2]From our microscopic viewpoint this corresponds to the expectation value of the canonical Hamiltonian.

The term $\frac{1}{T}(J_e - \tilde{\mu} J_p)$ is now recognized as the entropy current and the heat current is $J_Q = TJ_s = J_e - \tilde{\mu} J_p$. From this we get

$$\begin{aligned} \left.\frac{\partial s}{\partial t}\right|_{total} + \nabla \cdot J_s &= \left.\frac{\partial s}{\partial t}\right|_{gen} \\ &= J_e \cdot \nabla \left(\frac{1}{T}\right) - J_p \cdot \nabla \left(\frac{\tilde{\mu}}{T}\right) \\ &= J_Q \cdot \nabla \left(\frac{1}{T}\right) - \frac{1}{T} J_p \cdot \nabla \tilde{\mu} \end{aligned} \tag{3.8}$$

Note that we have switched over from the energy current to the heat current because it is really the heat current that is being measured in transport measurements. It is worth remarking here that our definition of the heat current does not agree with Mahan's definition [27, Sec. 3.9B], which is just $J_Q = J_e - \mu J_p$. On the other hand our definition does agree with both [24, Sec. 17.1] and [25, Sec. 2.2]. We should note however that since we are only considering linear response we will only need the currents in the equilibrium state and there the external potential is constant and the shift in the potential energy would simply be absorbed by the chemical potential making our result agree with Mahan's.

We have now found the currents of interest and the corresponding forces which are:

$$J_1 = J_p, \qquad \text{and} \qquad X_1 = \frac{-1}{T} \nabla \tilde{\mu} \tag{3.9}$$

$$J_2 = J_Q, \qquad \text{and} \qquad X_2 = \nabla \left(\frac{1}{T}\right) \tag{3.10}$$

and the linear response equations are:

$$J_1 = -L^{11} \frac{1}{T} \nabla \tilde{\mu} + L^{21} \nabla \left(\frac{1}{T}\right) \tag{3.11}$$

$$J_2 = -L^{12} \frac{1}{T} \nabla \tilde{\mu} + L^{22} \nabla \left(\frac{1}{T}\right) \tag{3.12}$$

where we now denote the kinetic coefficients corresponding to this choice of currents by $L^{ij}$. To see how these coefficients relate to the transport parameters we need to consider how the measurements are made. Remember here that the emf in the system is given by $\frac{-1}{q} \nabla \tilde{\mu}$ which in a homogeneous system reduces to $-\nabla V$.

1. Electrical conductivity: Here we do not allow any temperature gradients. The

electrical current can then be computed from equation (3.11),

$$J_C = qJ_p = -L^{11}\frac{q}{T}\nabla\tilde{\mu} = L^{11}\frac{q^2}{T}E = \sigma E \tag{3.13}$$

and hence the electrical conductivity is

$$\sigma = \frac{q^2}{T}L^{11} \tag{3.14}$$

2. Thermal conductivity: Here we do not allow any particle current. From equation (3.11) we get,

$$\frac{1}{T}\nabla\tilde{\mu} = \frac{L^{21}}{L^{11}}\nabla\left(\frac{1}{T}\right) \tag{3.15}$$

and putting this into equation (3.12) we get,

$$J_Q = \frac{-1}{T^2}\left(L^{22} - \frac{[L^{12}]^2}{L^{11}}\right)\nabla T = -\kappa\nabla T \tag{3.16}$$

and thus the thermal conductivity is

$$\kappa = \frac{1}{T^2}\left(L^{22} - \frac{[L^{12}]^2}{L^{11}}\right). \tag{3.17}$$

3. Thermopower: Here no particle current is allowed so we obtain from equation (3.11)

$$E = \frac{-1}{q}\nabla\tilde{\mu} = \frac{1}{qT}\frac{L^{12}}{L^{11}}\nabla T = S\nabla T \tag{3.18}$$

and hence the thermopower is given by:

$$S = \frac{1}{qT}\frac{L^{12}}{L^{11}}. \tag{3.19}$$

It is instructive to rewrite the phenomenological equations in terms of the transport parameters. It is easy to solve for the kinetic coefficients in terms of the transport parameters and plugging the solutions into the equations we get:

$$J_p = -\frac{\sigma}{q^2}\nabla\tilde{\mu} + \frac{ST^2\sigma}{q}\nabla\left(\frac{1}{T}\right) \tag{3.20}$$

$$J_Q = -\frac{ST\sigma}{q}\nabla\tilde{\mu} + \left(\kappa T^2 - S^2T^3\sigma\right)\nabla\left(\frac{1}{T}\right). \tag{3.21}$$

If we now solve for $\nabla\tilde{\mu}$ from the first equation and plug the result into the second one we get:

$$J_Q = STqJ_p + \kappa T^2 \nabla \left(\frac{1}{T}\right) \tag{3.22}$$

and since the entropy current is now given by $TJ_S = J_Q$ we see that

$$J_S = SJ_C + \kappa T \nabla \left(\frac{1}{T}\right) \tag{3.23}$$

where $J_C$ is the electric current. From this equation we see that the electric current carries entropy along with it which is directly proportional to the thermopower. Hence the thermopower can be regarded as the entropy transported per charge carrier.

Finally let us see how the thermopower relates to the so called Peltier heat and for that we imagine passing a current through a junction of two different materials, A and B that are kept at the same temperature. Due to the isothermal conditions the heat current in these materials is given by

$$J_{Q,A} = S_A T J_{C,A} \qquad \text{and} \qquad J_{Q,B} = S_B T J_{C,B}. \tag{3.24}$$

The electric currents are now the same in both conductors so we see that if the thermopowers in the two conductors are different, the heat carried in them will be different. Hence if the current passes from conductor A to B the heat extracted or deposited at the junction will be:

$$J_{Q,Junction} = J_{Q,B} - J_{Q,A} = (S_B - S_A)\, T J_C. \tag{3.25}$$

The Peltier coefficient for the junction is now defined as:

$$\pi_{AB} = \frac{J_{Q,Junction}}{J_C} = (S_B - S_A)\, T. \tag{3.26}$$

The kinetic coefficients are now evaluated for each model using the Kubo formalism [27] and here we simple quote the results. The simplest expressions are obtained using Matsubara representation where one must compute the time ordered current-current correlation function[3]:

$$Z^{mn}(i\omega) = \frac{1}{\beta k_B} \int_0^\beta d\tau e^{i\omega\tau} \langle T_\tau J_m(\tau) J_n(0) \rangle \tag{3.27}$$

[3]Note that our formula here includes a Boltzmann constant that seems to have been missing in reference [27].

and then we obtain our kinetic coefficients by analytically continuing to the real axis and taking the limit $\omega \to 0$, i.e.

$$L^{mn} = \lim_{\omega \to 0} \frac{1}{\omega} \operatorname{Im} Z^{mn}(i\omega \to \omega + i0). \tag{3.28}$$

## 3.3 Thermoelectric Performance and the Figure of Merit

The thermoelectric power is of course what makes it possible to convert heat energy directly into electrical energy and it is therefore natural to ask what is the maximum conversion efficiency that can be achieved. To see how this can be related to material parameters consider the simple thermoelectric refrigerator shown schematically in figure 3.1. We imagine that the device is made of up both n-type and p-type conductors but

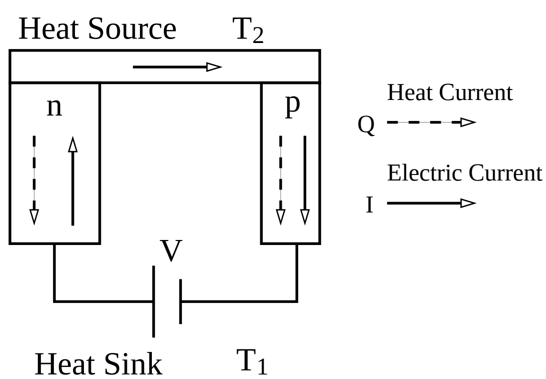


Figure 3.1: A schematic diagram of thermoelectric refrigerator.

in general any two materials with different thermopowers will do. The two arms are connected to a metallic cooling element at the heat source. The heat currents that enter the two arms at the cooling element are given by integrating the heat current densities in equation (3.22) and subtracting the contribution from Joule heating in the arms:

$$Q_n = -S_n I T_1 - K_n(T_1 - T_2) - \frac{1}{2} I^2 R_n \tag{3.29}$$

$$Q_p = S_p I T_1 - K_p(T_1 - T_2) - \frac{1}{2} I^2 R_p. \tag{3.30}$$

Here $K_{n,p}$ and $R_{n,p}$ denote respectively the thermal conductance and the electrical resistance of the two arms. We should note that $S_n$ is negative and thus the heat current induced by the particle current is transferred from the source in both arms. Some heat is also transferred from the source due to thermal conduction and then we have used the fact that half of the Joule heat generated in the arms will be returned to the source and half goes the sink [15]. The total heat current drawn from the source is then

$$Q_{total} = (S_p - S_n)IT_1 - K(T_1 - T_2) - \frac{1}{2}I^2R \tag{3.31}$$

and here we have denoted the total, parallel, thermal conductance by $K$ and the total, series, resistance by $R$. The current in the circuit can now be tuned to obtain maximum cooling power, which is given by

$$Q_{max} = \frac{1}{2}\frac{S_{pn}^2}{R}T_1^2 - K(T_1 - T_2). \tag{3.32}$$

We could now imagine running the refrigerator and thereby decreasing the temperature in the heat source but we see from the equation above that at some point the thermal conduction through the arms is going to balance the Peltier heat transferred from the source. Therefore the maximum temperature difference between source and sink that can be attained is

$$(T_1 - T_2)_{max} = \frac{1}{2}\frac{S_{pn}^2}{KR}T_1^2 = \frac{1}{2}Z^{pn}T_1^2. \tag{3.33}$$

Here we have defined the figure of merit, $Z^{pn}$ for the thermocouple and we note that the efficiency of the refrigerator is controlled by this parameter. In order to maximize the efficiency we have to maximize the difference between the thermopowers of the arms and minimize the product $KR$. The product depends on the dimensions (length $L$ and cross sectional area $A$) of the arms and if we write it in terms of the thermal conductivities and electrical resistivities as

$$KR = \left(\kappa_p\frac{A_p}{L_p} + \kappa_n\frac{A_n}{L_n}\right)\left(\rho_p\frac{L_p}{A_p} + \rho_n\frac{L_n}{A_n}\right) = \kappa_p\rho_p + \kappa_n\rho_n + \frac{A_pL_n}{A_nL_p}\kappa_p\rho_n + \frac{A_nL_p}{A_pL_n}\kappa_n\rho_p \tag{3.34}$$

and minimize with respect to one of the ratio, $\frac{A_pL_n}{A_nL_p}$ we find that the minimum is given by:

$$(KR)_{min} = \left(\sqrt{\kappa_p\rho_p} + \sqrt{\kappa_n\rho_n}\right)^2. \tag{3.35}$$

The maximal figure of merit that depends only on the material parameters is therefore:

$$Z^{pn} = \frac{S_{pn}^2}{\left(\sqrt{\kappa_p \rho_p} + \sqrt{\kappa_n \rho_n}\right)^2}. \tag{3.36}$$

It is evident that the figure of merit depends on both the materials that make up the thermocouple and it would be useful to have some independent measure of how good each material is for use in thermocouples. For this purpose one introduces the quantity

$$Z_T = \frac{S^2}{\kappa \rho} \tag{3.37}$$

and tries to maximize this figure of merit. We see however that there is no simple way of relating $Z_T$ for each of the materials to the figure of merit for the thermocouple except maybe in some simple cases. In practice however this is a useful quantity to consider and we will compute it for our model and consider how one would go about maximizing it with respect to material parameters.

## 3.4 Transport Parameters of the Hubbard Model

We turn now to the derivation of the operators for the particle and energy currents of the Hubbard model. Although we are mainly considering the case when the interaction strength $U$ is infinite we will derive the equation for the transport parameters assuming that $U$ is finite, but we will see that $U$ drops out of the equations and therefore they can be applied directly to the infinite $U$ case. The derivations will be done for the case of nearest neighbor hopping on the hyper-cubic lattice. The end results however will only depend on the dispersion relation of the lattice and its derivatives and is thus easily generalizable to other types of lattices or hoppings.

The current operators can be obtained from the corresponding density operators,

$$n_i = \sum_{\sigma} c_{i\sigma}^{+} c_{i\sigma} \quad \text{and} \quad h_i = -t_o \sum_{r\sigma} c_{i+r\sigma}^{+} c_{i\sigma} + \frac{U}{2} \sum_{\sigma \neq \sigma'} n_{i\sigma} n_{i\sigma'} - \mu \sum_{\sigma} n_{i\sigma} \tag{3.38}$$

by using the Heisenberg equations of motion and the continuity equations (here in complex time since we want to work in the Matsubara formalism),

$$i \frac{\partial n_i}{\partial \tau} + \nabla \cdot j_i = 0 \quad \textit{and} \quad i \frac{\partial h_i}{\partial \tau} + \nabla \cdot Q_i = 0 \tag{3.39}$$

From the anti-commutation relations

$$\{c^+_{i\sigma}, c_{j\sigma'}\} = \delta_{\sigma\sigma'}\delta_{ij}, \quad \{c^+_{i\sigma}, c^+_{j\sigma'}\} = 0, \quad \{c_{i,\sigma}, c_{j,\sigma'}\} = 0, \tag{3.40}$$

we find that

$$[n_{j\sigma'}, c_{i\sigma}] = -\delta_{ij}\delta_{\sigma\sigma'}c_{i\sigma} \qquad [n_{j\sigma'}, c^+_{i\sigma}] = \delta_{ij}\delta_{\sigma\sigma'}c^+_{i\sigma} \tag{3.41}$$

and then we get

$$\begin{aligned}
\frac{\partial c_{i\sigma}}{\partial \tau} &= [H, c_{i\sigma}] = -t_o \sum_{jr\sigma'} [c^+_{j+r\sigma'}c_{j\sigma'}, c_{i\sigma}] + \frac{U}{2} \sum_{j\sigma' \neq \sigma''} [n_{j\sigma'}n_{j\sigma''}, c_{i\sigma}] - \mu \sum_{j\sigma'} [n_{j\sigma'}, c_{i\sigma}] \\
&= -t_o \sum_{jr\sigma} [c^+_{j+r\sigma}, c_{i\sigma}]c_{j\sigma} + U \sum_{\sigma\neq\sigma'} [n_{i\sigma}, c_{i\sigma}]n_{\sigma'} + \mu c_{i\sigma} \\
&= t_o \sum_r c_{i+r\sigma} + c_{i\sigma}(\mu - U \sum_{\sigma'\neq\sigma} n_{i\sigma'}).
\end{aligned} \tag{3.42}$$

Similarly we get

$$\frac{\partial c^+_{i\sigma}}{\partial \tau} = -t_o \sum_r c^+_{i+r\sigma} - c^+_{i\sigma}(\mu - U \sum_{\sigma'\neq\sigma} n_{i\sigma'}). \tag{3.43}$$

Now we get for the number density

$$\frac{\partial n_i}{\partial \tau} = \sum_\sigma \left(\dot{c}^+_{i\sigma}c_{i\sigma} + c^+_{i\sigma}\dot{c}_{i\sigma}\right) = -t \sum_{r\sigma} \left(c^+_{i+r\sigma}c_{i\sigma} - c^+_{i\sigma}c_{i-r\sigma}\right). \tag{3.44}$$

And similarly for the energy density

$$\begin{aligned}
\frac{\partial h_i}{\partial \tau} &= -t_o \sum_{r\sigma} (\dot{c}^+_{i+r\sigma}c_{i\sigma} + c^+_{i+r\sigma}\dot{c}_{i\sigma}) - \sum_\sigma \dot{n}_{i\sigma}(\mu - U \sum_{\sigma'\neq\sigma} n_{i\sigma'}) \\
&= -t_o \sum_{r\sigma} \left\{ \dot{c}^+_{i+r\sigma}c_{i\sigma} + c^+_{i+r\sigma}\dot{c}_{i\sigma} - (c^+_{i+r\sigma}c_{i\sigma} - c^+_{i\sigma}c_{i-r\sigma})(\mu - U \sum_{\sigma'\neq\sigma} n_{i\sigma'}) \right\} \\
&= -t_o \sum_{r\sigma} \left(\dot{c}^+_{i+r\sigma}c_{i\sigma} - \dot{c}^+_{i\sigma}c_{i-r\sigma}\right)
\end{aligned} \tag{3.45}$$

To differentiate on the lattice we use the formulas

$$f(x+a) = f(x) + af'(x) \quad \text{and} \quad f(x-a) = f(x) - af'(x) \tag{3.46}$$

where $a$ is the lattice constant. Using these formulas we can easily identify the currents and if we consider specifically the $x$-component we have

$$j^x_i = it_o a \sum_\sigma \left(c^+_{i+x\sigma} - c^+_{i-x\sigma}\right) c_{i\sigma} \tag{3.47}$$

$$Q^x_i = it_o a \sum_\sigma \left(\dot{c}^+_{i+x\sigma} - \dot{c}^+_{i-x\sigma}\right) c_{i\sigma} \tag{3.48}$$

Now we Fourier transform this by writing

$$c_{i\sigma} = \frac{1}{V}\sum_k e^{iR_jk} c_{k\sigma} \quad \text{and} \quad c^+_{i\sigma} = \frac{1}{V}\sum_k e^{-iR_jk} c^+_{k\sigma} \tag{3.49}$$

and thus

$$j^x_j \;=\; \frac{iat_o}{V^2}\sum_{kq\sigma} c^+_{k\sigma} c_{q\sigma} e^{iR_j(q-k)}\left(e^{-iak_x} - e^{iak_x}\right) = \frac{2at_o}{V^2}\sum_{kq\sigma} sin(ak_x) c^+_{k\sigma} c_{k+q\sigma} e^{iR_jq}$$

so

$$j_x(q) \;=\; \frac{2at_o}{V}\sum_{k\sigma} sin(ak_x) c^+_{k\sigma} c_{k+q\sigma} \tag{3.50}$$

$$Q_x(q) \;=\; \frac{2at_o}{V}\sum_{k\sigma} sin(ak_x) \dot{c}^+_{k\sigma} c_{k+q\sigma} \tag{3.51}$$

Remember now that the dispersion relation for the cubic lattice is

$$\varepsilon_k = -2t_o \sum_i cos(ak_i) \tag{3.52}$$

and thus the equations above can be written on the form

$$j_x(q) \;=\; \frac{1}{V}\sum_{k\sigma}\left(\frac{\partial \varepsilon_k}{\partial k_x}\right) c^+_{k\sigma} c_{k+q\sigma} \tag{3.53}$$

$$Q_x(q) \;=\; \frac{1}{V}\sum_{k\sigma}\left(\frac{\partial \varepsilon_k}{\partial k_x}\right) \dot{c}^+_{k\sigma} c_{k+q\sigma} \tag{3.54}$$

Now that we have obtained expressions for the currents we can turn to the task of deriving the transport coefficient of the model. As noted before transport coefficients are most easily expressed in the Matsubara formalism as follows:

$$L^{mn} = \lim_{\omega \to 0} \frac{1}{\omega} Im Z^{mn}(\omega + i0) \tag{3.55}$$

where

$$Z^{mn}(i\omega) = \frac{1}{\beta k_B}\int_0^\beta d\tau e^{i\omega\tau}\langle T_\tau j_m(\tau) j_n(0)\rangle, \tag{3.56}$$

with $j_1 = j_x$ and $j_2 = Q_x$ and the currents are evaluated at $q = 0$. Putting in the expressions above and summing over spin we get,

$$\begin{aligned}\langle T_\tau j_x(\tau)j_x(0)\rangle &= \frac{1}{V^2}\sum_{k\sigma,k'\sigma'}\left(\frac{\partial\varepsilon_k}{\partial k_x}\right)\left(\frac{\partial\varepsilon_{k'}}{\partial k'_x}\right)\langle T_\tau c^+_{k\sigma}(\tau)c_{k\sigma}(\tau)c^+_{k'\sigma'}c_{k'\sigma'}\rangle \\ &= -\frac{N}{V}\sum_k\left(\frac{\partial\varepsilon_k}{\partial k_x}\right)^2 G_k(\tau)G_k(-\tau) \qquad (3.57)\\ \langle T_\tau j_x(\tau)Q_x(0)\rangle &= \frac{1}{V^2}\sum_{k\sigma,k'\sigma'}\left(\frac{\partial\varepsilon_k}{\partial k_x}\right)\left(\frac{\partial\varepsilon_{k'}}{\partial k'_x}\right)\langle T_\tau c^+_{k\sigma}(\tau)c_{k\sigma}(\tau)\dot{c}^+_{k'\sigma'}c_{k'\sigma'}\rangle \\ &= \frac{N}{V}\sum_k\left(\frac{\partial\varepsilon_k}{\partial k_x}\right)^2 \dot{G}_k(\tau)G_k(-\tau) \qquad (3.58)\\ \langle T_\tau Q_x(\tau)Q_x(0)\rangle &= \frac{1}{V^2}\sum_{k\sigma,k'\sigma'}\left(\frac{\partial\varepsilon_k}{\partial k_x}\right)\left(\frac{\partial\varepsilon_{k'}}{\partial k'_x}\right)\langle T_\tau \dot{c}^+_{k\sigma}(\tau)c_{k\sigma}(\tau)\dot{c}^+_{k'\sigma'}c_{k'\sigma'}\rangle \\ &= \frac{N}{V}\sum_k\left(\frac{\partial\varepsilon_k}{\partial k_x}\right)^2 \dot{G}_k(\tau)\dot{G}_k(-\tau) \qquad (3.59)\end{aligned}$$

In calculating the correlation functions here above we have used the fact that in the mean field limit $z \to \infty$ all vertex corrections to the current-current correlator drop out and we are left with a single bubble diagram [1]. We have also used equations from Appendix C to relate the expectation value of the time derivative of the creation and annihilation operators to the time derivative of the Green's function. To proceed further we make use of the spectral representation for the Green's function.

$$\begin{aligned} G_k(\tau) &= -\langle T_\tau c_{k\sigma}(\tau)c^+_{k\sigma}(0)\rangle = T\sum_{i\omega_n} e^{-i\omega\tau}G_k(i\omega). \qquad (3.60)\\ G_k(i\omega) &= \int_{-\infty}^{\infty} d\omega'\,\frac{\rho_k(\omega')}{i\omega-\omega'} \qquad (3.61)\end{aligned}$$

where

$$\rho_k(\omega) = \frac{-1}{\pi}ImG_k(\omega+i0) \qquad (3.62)$$

is the spectral function. Defining

$$\begin{aligned} Z_0(i\omega,k) &= \frac{1}{\beta k_B}\int_0^\beta d\tau e^{i\omega\tau}G_k(\tau)G_k(-\tau) \qquad (3.63)\\ Z_1(i\omega,k) &= \frac{1}{\beta k_B}\int_0^\beta d\tau e^{i\omega\tau}\dot{G}_k(\tau)G_k(-\tau) \qquad (3.64)\\ Z_2(i\omega,k) &= \frac{1}{\beta k_B}\int_0^\beta d\tau e^{i\omega\tau}\dot{G}_k(\tau)\dot{G}_k(-\tau) \qquad (3.65)\end{aligned}$$

and using the representation above for the Green's function we find that

$$\lim_{\omega\to 0}\frac{1}{\omega}ImZ_0(\omega+i0,k) = -\frac{\pi}{k_B}\int_{-\infty}^{\infty} d\omega\rho_k^2(\omega)\left(-k_BT\frac{df(\omega)}{d\omega}\right) \tag{3.66}$$

$$\lim_{\omega\to 0}\frac{1}{\omega}ImZ_1(\omega+i0,k) = \frac{\pi}{k_B}\int_{-\infty}^{\infty} d\omega\rho_k^2(\omega)\omega\left(-k_BT\frac{df(\omega)}{d\omega}\right) \tag{3.67}$$

$$\lim_{\omega\to 0}\frac{1}{\omega}ImZ_2(\omega+i0,k) = \frac{\pi}{k_B}\int_{-\infty}^{\infty} d\omega\rho_k^2(\omega)\omega^2\left(-k_BT\frac{df(\omega)}{d\omega}\right) \tag{3.68}$$

From this we get

$$L^{11} = \frac{A_0}{k_B}, \quad L^{12} = \frac{1}{\beta k_B}A_1 \quad \text{and} \quad L^{22} = \frac{1}{\beta^2 k_B}A_2 \tag{3.69}$$

where

$$A_n = N\pi\frac{1}{V}\sum_k\left(\frac{\partial\varepsilon_k}{\partial k_x}\right)^2\int_{-\infty}^{\infty} d\omega\frac{\rho_k^2(\omega)(\omega\beta)^n}{4\cosh^2(\frac{\beta\omega}{2})} \tag{3.70}$$

The spectral density depends on momentum only through the lattice dispersion relation $\varepsilon_k$ and hence we can write

$$A_n = \frac{N\pi}{z}\int_{-\infty}^{\infty} d\omega d\varepsilon\frac{\rho^2(\varepsilon,\omega)(\omega\beta)^n}{4\cosh^2(\frac{\beta\omega}{2})}\Phi(\varepsilon) \tag{3.71}$$

where

$$\Phi(\varepsilon) = \frac{z}{V}\sum_k\left(\frac{\partial\varepsilon_k}{k_x}\right)^2\delta(\varepsilon-\varepsilon(k)) = (2at)^2\int_{-\frac{\pi}{a}}^{\frac{\pi}{a}}\frac{d^dk}{(2\pi)^d}\sin^2(ak_x)\delta(\varepsilon-\varepsilon(k)) \tag{3.72}$$

Notice that this function is zero for $|\varepsilon| \geq zt_o = \sqrt{z}t$. The Fourier transform of this quantity can easily be calculated analytically as follows

$$\begin{aligned}\widetilde{\Phi}(s) &= \int_{-\infty}^{\infty} d\varepsilon e^{-is\varepsilon}\Phi(\varepsilon) \quad = \quad (2at)^2\int_{-\frac{\pi}{a}}^{\frac{\pi}{a}}\frac{d^dk}{(2\pi)^d}e^{-is\varepsilon_k}\sin^2(ak_x) \\ &= \frac{(2at)^2}{a^d}\left(\int_{-\pi}^{\pi}\frac{dk}{2\pi}e^{i2t_os\cos(k)}\right)^{d-1}\left(\int_{-\pi}^{\pi}\frac{dk}{2\pi}e^{i2t_os\cos(k)}\sin^2(k)\right) \\ &= \frac{(2at)^2}{a^d}J_0^{d-1}(2t_os)\frac{J_1(2t_os)}{2t_os}. \end{aligned}\tag{3.73}$$

Here $J_0$ and $J_1$ are Bessel functions and we have used the formula [28]

$$J_\nu(\zeta) = \frac{\left(\frac{\zeta}{2}\right)^\nu}{\Gamma(\nu+\frac{1}{2})\Gamma(\frac{1}{2})}\int_0^{\pi} d\phi e^{\pm i\zeta\cos(\phi)}\sin^{2\nu}(\phi). \tag{3.74}$$

The Fourier transform can now be used to calculate $\Phi(\varepsilon)$ numerically and in figure (3.2) we have plotted the result for $d = 3$ and $d = \infty$. In $z = 2d = \infty$, $\Phi$ can be calculated exactly and is given by

$$\Phi(\varepsilon) = \frac{(2at)^2}{2a^d\sqrt{2\pi t^2}} \exp\left(-\frac{\varepsilon^2}{2t^2}\right) = \frac{(2at)^2}{2} D_\infty(\varepsilon). \tag{3.75}$$

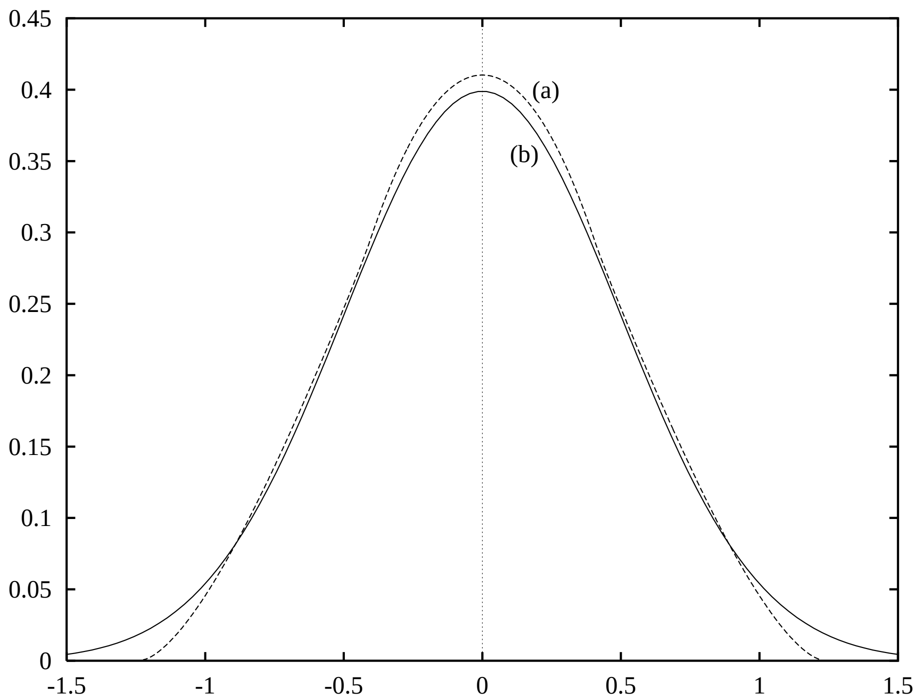


Figure 3.2: The function $\Phi(\epsilon)$ for (a) $d = 3$ and (b) $d = \infty$.

The thermal conductivity, the electrical conductivity and the thermopower are now given in terms of the correlation functions $L^{ij}$ and the $A_n$'s as follows,

$$\sigma = \frac{e^2}{T} L^{11} = e^2 \beta A_0 \tag{3.76}$$

$$\kappa = \frac{1}{T^2}\left(L^{22} - \frac{(L^{12})^2}{L^{11}}\right) = k_B \left(A_2 - \frac{A_1^2}{A_0}\right) \tag{3.77}$$

$$S = -\frac{1}{eT}\frac{L^{12}}{L^{11}} = -\frac{k_B}{e}\frac{A_1}{A_0}. \tag{3.78}$$

Note that as $z = 2d$ goes to infinity the functions $A_n$ defined in (3.71) tend to zero and thus the conductivities also go to zero. This is not surprising if we look at the formulas for the currents in (3.47) and then apply the scaling to the hopping integral $t_o$; the currents simply go to zero in the limit $z \to \infty$. What is finite however is the sum of the conductivities in all directions, i.e. $z\sigma$ and $z\kappa$. At this point it is in order to clarify the philosophy behind the infinite $d$ calculations. In the calculations of the local Green's functions the infinite $d$ limit has already been taken and although we profess to be doing calculations for the cubic lattice we use the self consistency conditions for the infinite Bethe lattice. The reason for doing that is that apart from some Van Hove singularities the density of states for the 3D cubic lattice and the Bethe lattice are very similar. Now when calculating correlation functions we saw earlier that upon taking the infinite $d$ limit we got rid of all vertex corrections which was a good thing. However, in the remaining expressions we do not necessarily have to take this limit and in fact we will henceforth take $z = 1$ in our calculations and take the $\Phi$ corresponding to the infinite dimensional Bethe lattice. One might ask here, how we can calculate the $\Phi$ for the Bethe lattice since the expression (3.72) obviously cannot be used. Well, we simply assume that on the Bethe lattice we obtain the same expression as on the infinite hyper-cubic lattice, i.e.

$$\Phi_{Bethe}(\varepsilon) = \frac{(2at)^2}{2} D_{Bethe}(\varepsilon) = \frac{(2at)^2}{2} \frac{1}{\pi t} \sqrt{1 - \left(\frac{\varepsilon}{2t}\right)^2} \tag{3.79}$$

This enables us to do the $\varepsilon$ integral in the expression for the $A_n$'s analytically (see appendix A) but we will also later compare our result to the results obtained when the proper cubic 3D version of $\Phi$ is used.

## 3.5 Results: Transport parameters

In figure 3.3 the transport parameters for density $n = 0.90$ are displayed versus temperature. At very low temperature the thermopower is seen to diverge and actually the same goes for the thermal and electrical conductivities due to the pathology of the solution mentioned in §2.5. Our results here are quite consistent with the results of Oguri and Maekawa [29] who computed the transport parameters for the infinite $U$ Hubbard model close to half filling using the retraceable path approximation for the motion of holes in a paramagnetic spin background. We see that the electrical resistivity is linear

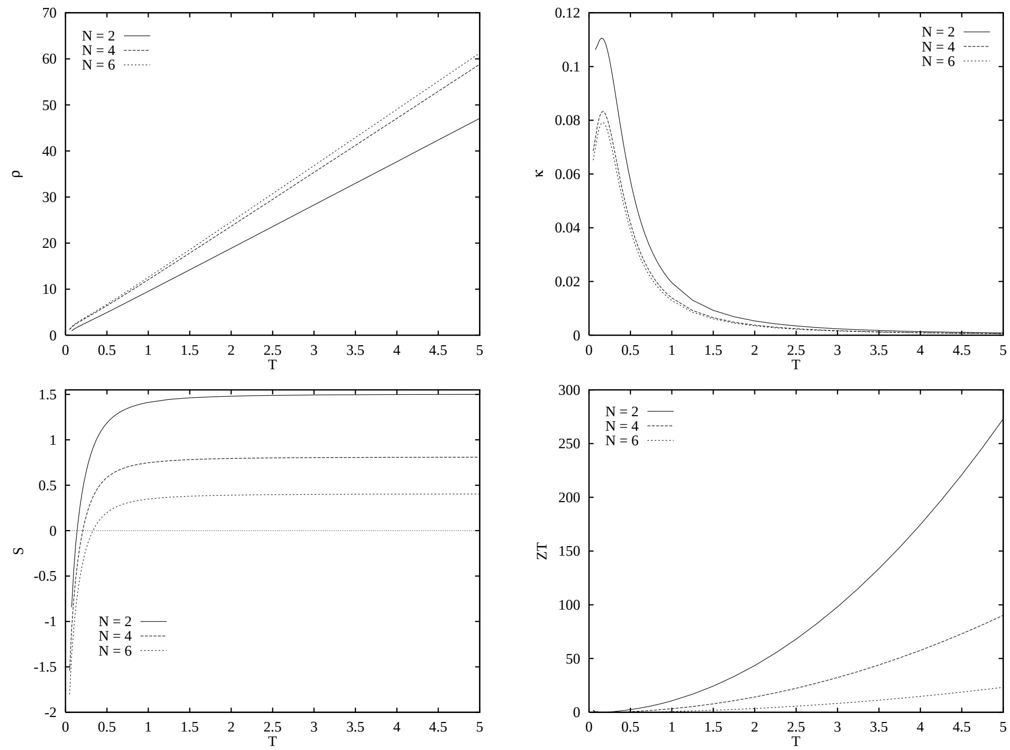


Figure 3.3: Results for transport parameters from NCA+DMFT calculations at density $n = 0.90$. $\rho$ denotes resistance and is measured in units of $\frac{z\hbar a}{e^2}$, $\kappa$ denotes thermal conductivity and is measured in units of $\frac{k_B D}{za\hbar}$, $S$ denotes thermopower and is measured in units of $\frac{k_B}{e}$ and $ZT$ denotes the dimensionless figure of merit. Here $a$ is the lattice constant, $D = 2t$ is the bare half-width of the band and $z$ is the coordination number of the lattice.

almost all the way down to the lowest temperatures displayed in the graph. The thermal conductivity displays a powerlaw behavior in the high temperature regime going as $1/T^2$ but at lower temperatures it reaches a maximum at temperatures around quarter of the bandwidth. Similar maxima were seen in the data by Oguri and Maekawa but at somewhat larger temperature. The thermopower on the other hand tends to a finite constant at large temperatures but starts decreasing at temperatures slightly below the bandwidth, becomes electron-like and seems to be diverging.

The behavior of the transport parameters in the high temperature region can be deduced from our results on spectral function in previous chapter. At high temperatures we have already seen that the spectral function behaves as a rigid band centered on

$\omega = -\mu$ and $\mu$ is a linear function of temperature, i.e. $\mu/T = \alpha = const$. Thus we write

$$\widetilde{\rho}(\omega, \epsilon) = \rho(\omega - \mu, \epsilon). \tag{3.80}$$

Hence the coefficients $A_n$ from §3.4 become[4]:

$$A_n = \frac{\pi N}{4} \int d\omega \frac{(\beta\omega - \alpha)^n}{\cosh^2(\frac{\beta\omega-\alpha}{2})} \int d\epsilon \widetilde{\rho}^2(\omega, \epsilon)\Phi(\epsilon). \tag{3.81}$$

We now expand the hyperbolic cosine in Taylor series around $\beta = 0$.

$$\frac{1}{\cosh^2(\frac{\beta\omega-\alpha}{2})} = \frac{1}{\cosh^2(\frac{\alpha}{2})}\left(1 + \beta\omega\tanh(\frac{\alpha}{2}) + \frac{\omega^2\beta^2}{4}\left[3\tanh(\frac{\alpha}{2}) - 1\right]\right). \tag{3.82}$$

Before we go any further we also define

$$\gamma_n = \int d\epsilon d\omega \omega^n \widetilde{\rho}^2(\omega, \epsilon)\Phi(\epsilon) \quad \text{and let} \quad \tau = \tanh(\frac{\alpha}{2}) \quad \text{and} \quad \zeta = \frac{1}{4\cosh^2(\frac{\alpha}{2})}. \tag{3.83}$$

Then calculating to second order in $\beta$ we get

$$A_0 = \pi N\zeta\left(\gamma_0 + \gamma_1\beta\tau + \frac{1}{4}\gamma_2\beta^2[3\tau - 1]\right) \tag{3.84}$$

$$A_1 = \pi N\zeta\left(-\alpha\gamma_0 + \gamma_1\beta\left[1 - \alpha\tau\right] + \gamma_2\beta^2\left[\tau - \frac{\alpha}{4}(3\tau - 1)\right]\right) \tag{3.85}$$

$$A_2 = \pi N\zeta\left(\alpha^2\gamma_0 + \gamma_1\beta\left[\alpha^2\tau - 2\alpha\right] + \gamma_2\beta^2\left[1 - 2\alpha\tau + \frac{\alpha^2}{4}(3\tau - 1)\right]\right) \tag{3.86}$$

Now we put these expressions into the formulas for the transport coefficient and calculate again to second order in $\beta$.

$$\sigma = e^2\pi N\zeta\beta\left(\gamma_0 + \gamma_1\beta\tau + \frac{1}{4}\gamma_2\beta^2[3\tau - 1]\right) \tag{3.87}$$

$$S = \frac{k_B}{e}\left(\alpha - \frac{\gamma_1}{\gamma_0}\beta - \frac{\tau(\gamma_2\gamma_0 - \gamma_1^2)}{\gamma_0^2}\beta^2\right) \tag{3.88}$$

$$\kappa = \frac{k_B\pi N\zeta(\gamma_2\gamma_0 - \gamma_1^2)}{\gamma_0}\beta^2. \tag{3.89}$$

The figure of merit is then to lowest order in $\beta$ given by

$$ZT = \frac{S^2\sigma T}{\kappa} = \alpha^2(kT)^2\frac{\gamma_0^2}{\gamma_2\gamma_0 - \gamma_1^2}. \tag{3.90}$$

It is interesting at this point to look at the spectral moments, $\gamma_n$, and see how they depend on temperature and density. As we can see from figure 3.4 both $\gamma_0$ and $\gamma_2$ tend

[4]Remember that we take $z = 1$.

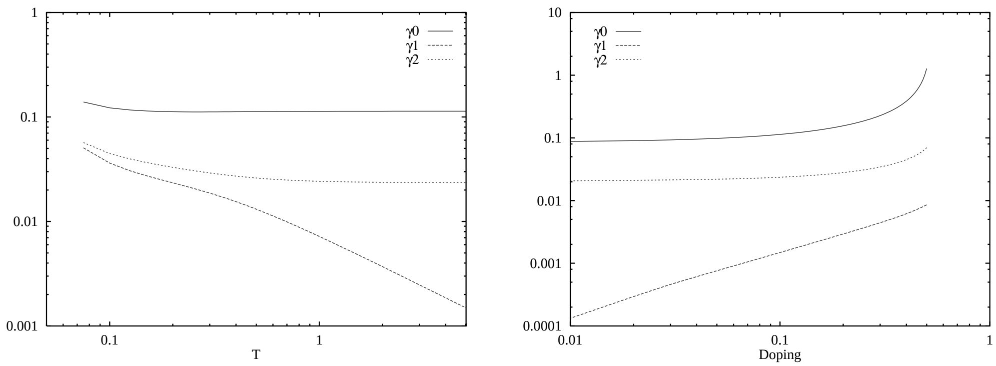


Figure 3.4: The spectral moments, $\gamma_n$, for $N = 2$. Versus doping, $\delta = 1 - n$, at $T = 5.0$ and versus temperature at density, $n = 0.90$.

to a constant at high temperature as could be expected from our previous discussion in section 2.5. We see also that the asymmetric part of the spectral density which is measured by $\gamma_1$ goes as $1/T$. If we look at the doping dependence we see essentially the same behavior as on the temperature graph, i.e. $\gamma_0$ and $\gamma_2$ seem to be tending to a constant while $\gamma_1$ goes as $\delta$. In some sense low doping corresponds to high temperature as we will see more clearly in section 3.6.2. We should also note the apparent increase of $\gamma_0$ and $\gamma_2$ around 30% doping or so. The reason is that the spectral moments scale approximately as $[n/N + (1-n)]^2$, i.e.

$$\gamma_0 \simeq \tilde{\gamma}_0[n/N + (1-n)]^2 \qquad \text{and} \qquad \gamma_2 \simeq \tilde{\gamma}_2[n/N + (1-n)]^2 \tag{3.91}$$

where $\tilde{\gamma}_0$ and $\tilde{\gamma}_2$ are constants, independent of doping. The factor $[n/N + (1-n)]^2$ is nothing but the square of the total integrated spectral weight of $\widetilde{\rho}$ and looking at the definition of the spectral moments this is indeed what we would have expected.

Now $\alpha$ is given by

$$\alpha = \ln\left(\frac{n}{N(1-n)}\right) \quad \text{so} \quad \zeta = \frac{nN(1-n)}{(n + N(1-n))^2}. \tag{3.92}$$

so finally we have to lowest order in $\beta$

$$\sigma = e^2\pi\frac{nN^2(1-n)}{(n+N(1-n))^2}\gamma_0\beta \simeq e^2\pi n(1-n)\tilde{\gamma}_0\beta \tag{3.93}$$

$$S = \frac{k_B}{e}\ln\left(\frac{n}{N(1-n)}\right) \tag{3.94}$$

$$\kappa = k_B\pi\frac{nN^2(1-n)}{(n+N(1-n))^2}\gamma_2\beta^2 \simeq k_B\pi n(1-n)\tilde{\gamma}_2\beta^2 \tag{3.95}$$

$$ZT = \ln^2\left(\frac{n}{N(1-n)}\right)(k_BT)^2\frac{\gamma_0}{\gamma_2} \tag{3.96}$$

Of the equations above the one for the thermopower is well known, at least for the case $N = 2$ and goes by the name of Heikes formula [10].

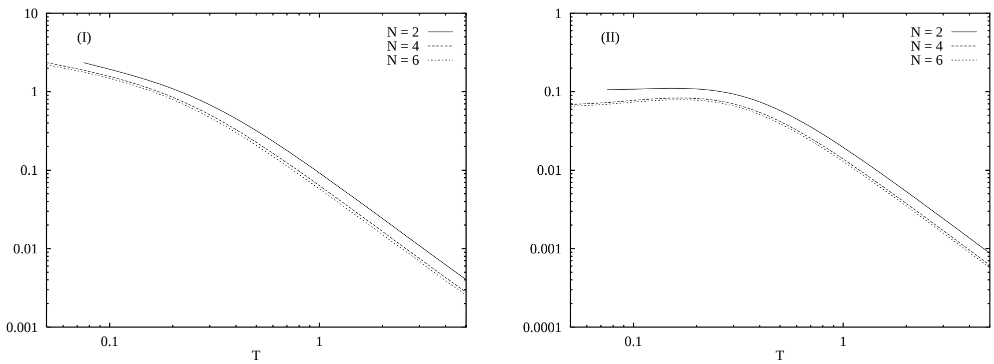


Figure 3.5: Results for transport parameters from NCA+DMFT calculations at density $n = 0.90$. I: The thermopower, $S_\infty - S(T)$ where $S_\infty$ is the infinite temperature limit given by Heikes formula. II: The thermal conductivity, $\kappa$.

From these formulas we see that indeed the resistivity should be linear in temperature at high temperatures and from figure 3.5 we see that the thermal conductivity and the next to leading order term in the thermopower go as $T^{-2}$ in agreement with the formulas above. We see also that the figure of merit increases quadratically with temperature and thus tends to infinity as $T$ goes to infinity and furthermore it goes to infinity at finite temperature if the density goes to one or zero. This behavior seems striking given that all known materials have figures of merit which are in the range of 0.0-2.0. The reason is of course that here we have neglected to take into account the lattice contribution to the thermal conductivity. If we assume a finite lattice contribution to the thermal conductivity then we can of course neglect the electronic contribution since it tends to zero at high temperatures and then we have:

$$ZT \simeq \frac{k_B \pi}{\kappa_L} \ln^2 \left( \frac{n}{N(1-n)} \right) \tilde{\gamma}_0 n(1-n). \tag{3.97}$$

Hence the figure of merit will actually go to zero at $n = 0$ and $n = 1$ and if lattice contribution is taken independent of temperature the FOM will tend to a constant at high temperatures.

We should also note that associated with the divergency of the figure of merit around density $n = 0, 1$ is the divergence of the chemical potential. Now of course this would never happen in a real physical system, eventually other bands would come into play and participate in the dynamics and thus the use of our model would no longer be justified. In this respect our model is somewhat unphysical and one needs to be aware of that when looking at results close to the two extremes in density.

## 3.6 Thermodynamics

As we saw in section 3.2 there is a close connection between the thermopower of the system and the entropy – the thermopower being essentially the entropy per carrier. It is therefore instructive to take a brief look at the energy and specific heat of the model.

### 3.6.1 Thermodynamic Equations

We now turn to the calculation of the total energy of the Hubbard model. The total energy corresponds to the expectation value of the canonical Hamiltonian:

$$H_c = -t_o \sum_{jr\sigma} c^+_{j+r\sigma} c_{j\sigma} + \frac{U}{2} \sum_{j\sigma \neq \sigma'} n_{j\sigma} n_{j\sigma'}. \tag{3.98}$$

Note however that all observables evolve according to the grand canonical Hamiltonian which we have been using so far. The total energy is thus:

$$\begin{aligned} E &= \langle H_c \rangle = \frac{1}{Z} Tr(e^{-\beta H} H_c) = \frac{1}{Z} \sum_n \langle \Psi_n | e^{-\beta H} H_c | \Psi_n \rangle \\ &= \sum_{k\sigma} \epsilon_k \langle c^+_{k\sigma} c_{k\sigma} \rangle + \frac{U}{2} \sum_{i\sigma \neq \sigma'} \langle n_{i\sigma} n_{i\sigma'} \rangle \end{aligned} \tag{3.99}$$

To calculate the expectation value involving the number operators we use the equation of motion for the creation operator which we have derived earlier and we find that

$$\frac{U}{2}\sum_{i\sigma\neq\sigma'} n_{i\sigma}n_{i\sigma'} = \frac{1}{2}\left(\sum_{k\sigma}\dot{c}^{+}_{k\sigma}c_{k\sigma} - \sum_{k\sigma}(\epsilon_k-\mu)c^{+}_{k\sigma}c_{k\sigma}\right) \tag{3.100}$$

and hence

$$\begin{aligned}
\langle H_c\rangle &= \frac{1}{2}\sum_{k\sigma}(\epsilon_k+\mu)\langle c^{+}_{k\sigma}c_{k\sigma}\rangle + \frac{1}{2}\sum_{k\sigma}\langle\dot{c}^{+}_{k\sigma}c_{k\sigma}\rangle \\
&= \frac{N}{2}\sum_{k}(\epsilon_k+\mu)\lim_{\tau\to0^+}G_k(-\tau) + \frac{N}{2}\sum_{k}\lim_{\tau\to0^+}\frac{d}{d\tau}G_k(-\tau) \\
&= \frac{N}{2}\sum_{k}T\sum_{i\omega_n}(\epsilon_k+\mu+i\omega_n)G_k(i\omega_n)e^{i\omega_n0^+}
\end{aligned} \tag{3.101}$$

Here we have used

$$G_k(\tau) = -\langle T_\tau c_k(\tau)c^{+}_{k}\rangle = T\sum_{i\omega_n}e^{-i\omega_n\tau}G_k(i\omega_n) \tag{3.102}$$

so

$$\langle c^{+}_{k}c_k\rangle = \lim_{\tau\to0^+}G_k(-\tau) \quad \text{and similarly} \quad \langle\dot{c}^{+}_{k}c_k\rangle = \lim_{\tau\to0^+}\frac{d}{d\tau}G_k(-\tau) \tag{3.103}$$

Using the spectral representation for the Green's function,

$$G_k(i\omega_n) = \int\frac{\rho_k(\varepsilon)d\varepsilon}{i\omega_n-\varepsilon} \tag{3.104}$$

we get

$$\langle H_c\rangle = \frac{N}{2}\sum_{k}\int d\varepsilon\rho_k(\varepsilon)T\sum_{i\omega_n}\frac{\epsilon_k+\mu+i\omega_n}{i\omega_n-\varepsilon}e^{i\omega_n0^+} \tag{3.105}$$

The sum over $i\omega_n$ can be done by contour integration if properly regulated. The convergence factor is $e^{i\omega_n0^+}$ which tends to zero in the half-plane $Im(i\omega)<0$ so the proper function to use to pick out the poles in the sum is the Fermi function which tends to zero in the other half-plane. Thus we get

$$\begin{aligned}
\langle H_c\rangle &= \frac{N}{2}\sum_{k}\int d\omega\rho_k(\omega)(\epsilon_k+\mu+\omega)f(\omega) \\
&= \frac{N}{2}\int d\omega d\varepsilon\rho(\varepsilon,\omega)(\varepsilon+\mu+\omega)f(\omega)D(\varepsilon) \\
&= \frac{N}{2}\int d\omega d\varepsilon\rho(\varepsilon,\omega)\varepsilon f(\omega)D(\varepsilon) + \frac{N}{2}\int d\omega\rho(\omega)_{loc}(\omega+\mu)f(\omega) \\
&= \frac{N}{2}\int d\omega d\varepsilon\rho(\varepsilon,\omega)\varepsilon f(\omega)D(\varepsilon) + \frac{N}{2}\int d\omega\rho_{loc}(\omega)\omega f(\omega) + \frac{1}{2}\mu n.
\end{aligned} \tag{3.106}$$

The first line in the expression above is the general formula. In the next three lines we have used the fact that in the mean field theory the sum over momenta can be replaced by an integral weighted with the lattice spectral density $D(\varepsilon)$, and then we use the fact that the local spectral density $\rho_{loc}(\omega)$ is given by the $\varepsilon$ integral over $\rho(\varepsilon, \omega)D(\varepsilon)$.

A further simplification arises in the infinite $U$ Hubbard model. In that case the potential energy is zero so the total energy equals the kinetic energy which corresponds to the first integral in the final expression above, i.e.

$$\langle H_c \rangle_{U=\infty} = N \int d\omega d\varepsilon \rho(\varepsilon, \omega) \varepsilon f(\omega) D(\varepsilon) \tag{3.107}$$

On the Bethe lattice the integral over the density of states can be done exactly (see appendix A) and combining that with the equations above we get the following two expressions for the energy.

$$\langle H_c \rangle_{U=\infty} = N \int d\omega \rho_{loc}(\omega) \omega f(\omega) + \mu n = 2Nt^2 \int d\omega f(\omega) \rho_{loc}(\omega) ReG_{loc}(\omega). \tag{3.108}$$

Note that this expression includes only the local spectral density so the breakdown of the self energy which was mentioned earlier would not be noticed in these computations.

### 3.6.2 Thermodynamic Results

The results for the energy and specific heat of the model are displayed in figure 3.6. Over the whole accessible temperature range the energy turned out to be independent of degeneracy, and goes as $n(1-n)$ with density, i.e. it is directly proportional to the product of the densities of electrons and holes. This seems reasonable since the energy is obviously zero in the limits $n = 0$ and $n = 1$. We note that at very low temperatures something interesting seems to be happening in the system at density $n = 0.90$ where a little more time was invested in solving the system at low temperatures. It is however unfortunate that with the method that we used to solve the NCA equations we are not able to go to very low temperatures and the lowest temperature that was obtained with $n = 0.9$ was around 0.007. Let us now use the density scaling of the energy and the data from $n = 0.90$ to calculate the entropy of the model using the formula:

$$S(T) = S_{\infty} + \int_{\infty}^{T} \frac{c_V(T')}{T'} \tag{3.109}$$

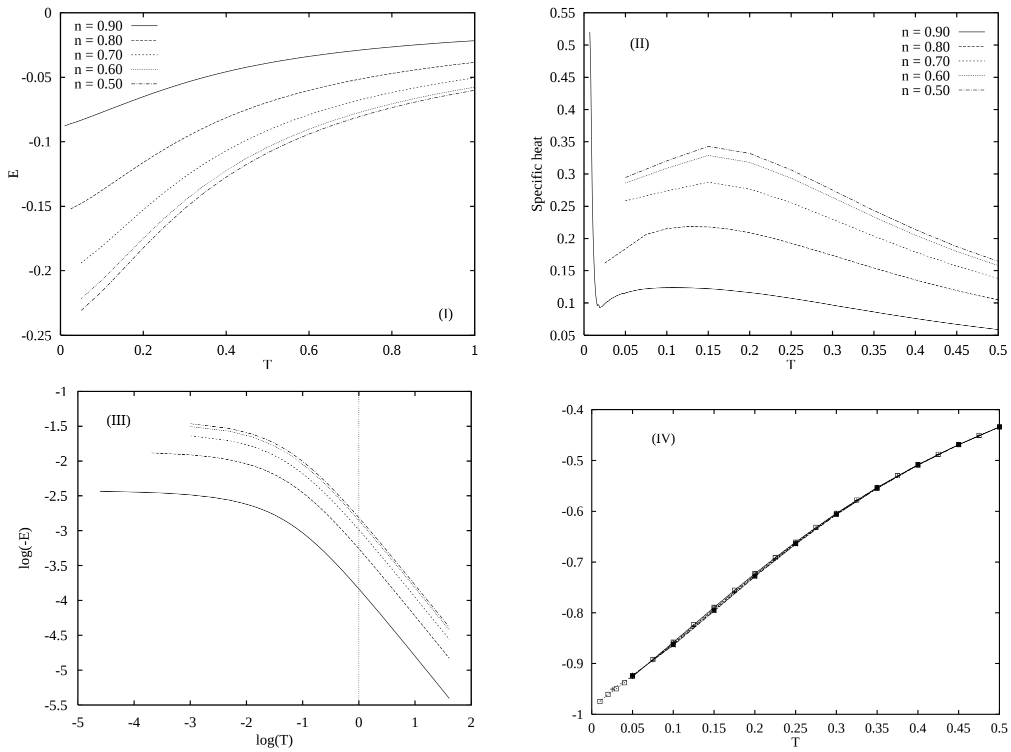


Figure 3.6: Thermodynamics for $N = 2$. I: Energy. II: Specific heat. III: Same data as in figure (I), graph shows clearly the $1/T$ behavior of energy in the high temperature regime. IV: The energy divided by $n(1-n)$ collapses onto a single curve for densities 0.1 - 0.9. The energy is measured in units of the bare band half-width, $D$, and the specific heat is measured in units of $k_B$.

where $S_\infty$ is the entropy at infinite temperature given by equation (2.41) and we take $T = 5$ to correspond to infinite temperature. The results from doing this are displayed in figure 3.7. Notice that the entropy becomes negative for all the densities except $n = 0.90$. This indicates that the density scaling cannot possibly persist down to zero temperature if we are to satisfy the requirement that the entropy be positive and go to zero when $T$ goes to zero. Therefore the temperature at which the entropy crosses zero can be regarded as some sort of breakdown temperature for the density scaling (it actually has to break down at a little higher temperature).

There is of course a more fundamental reason why the density scaling and the apparent independence of degeneracy cannot persist down to zero temperature. The fact is that the high temperature entropy density:

$$S = -n \ln(n/N) - (1 - n) \ln(1 - n) \tag{3.110}$$

does not scale with $n(1-n)$ and does depend on the degeneracy $N$. Hence if we want to get rid of all this entropy and no more as we turn the temperature down from infinity to zero the specific heat must have a more complicated density and degeneracy dependence at low temperatures. At high temperatures the electrons in the system can

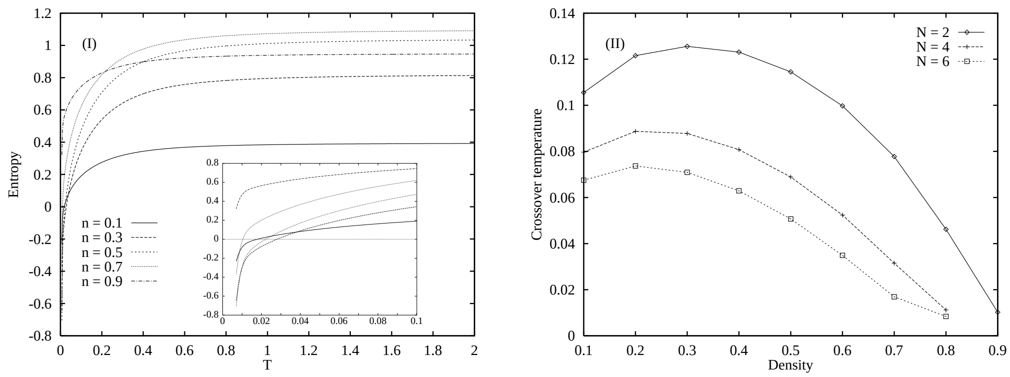


Figure 3.7: I: Entropy for N = 2 calculated from the $n = 0.9$ data using the density scaling $n(1-n)$. The inset shows that the scaling breaks down at temperatures below 0.05. II. Carrier crossover temperature. In the temperature-density plane above the curve the carriers are localized, below it they are extended (see text).

be regarded as essentially localized and this is reflected in the high value of entropy at $T = \infty$. As temperature decreases the electrons delocalize and at the same time the entropy decreases. This suggests that the entropy can be used as a measure of the localization of the carriers in the system and although we do not have any rigorous way of characterizing the crossover from localized to extended carriers we can define operationally a crossover temperature by the following criterion:

$$\frac{S(T_{xo})}{S_\infty} = \frac{1}{2}. \tag{3.111}$$

That is, we say that the carriers in the system are being localized when the entropy of the system has reached half its maximum value. This definition gives us the curves shown in figure 3.7. We see that the crossover temperature is very low for $n = 0.9$ and therefore we were required to spend more time on calculation for this particular density. It is not surprising that the crossover temperature is so low for $n = 0.9$, since we are then close to half filling and the carriers do not have much room to delocalize.

## 3.7 Iterated perturbation theory

To complement the result from the NCA which are mainly reliable in the high temperature regime, at least as far as the transport calculations are concerned, we did a few calculations using the iterated perturbation theory (IPT) modified for finite doping as described in [30]. This method is exact in various limits at zero temperature and has been extended to finite temperature in [31]. The IPT is a perturbation theory in the interaction strength, $U$, so it does not correspond exactly to the model we have considered so far. $U$ will nevertheless be the largest scale in the problem so one can expect that the results obtained will be somewhat indicative of what happens in models with large interaction. We will not delve further into the specifics of this method, it provides us with the local spectral density as the NCA and the calculation of response functions proceeds the same way as before. The results for the transport parameters

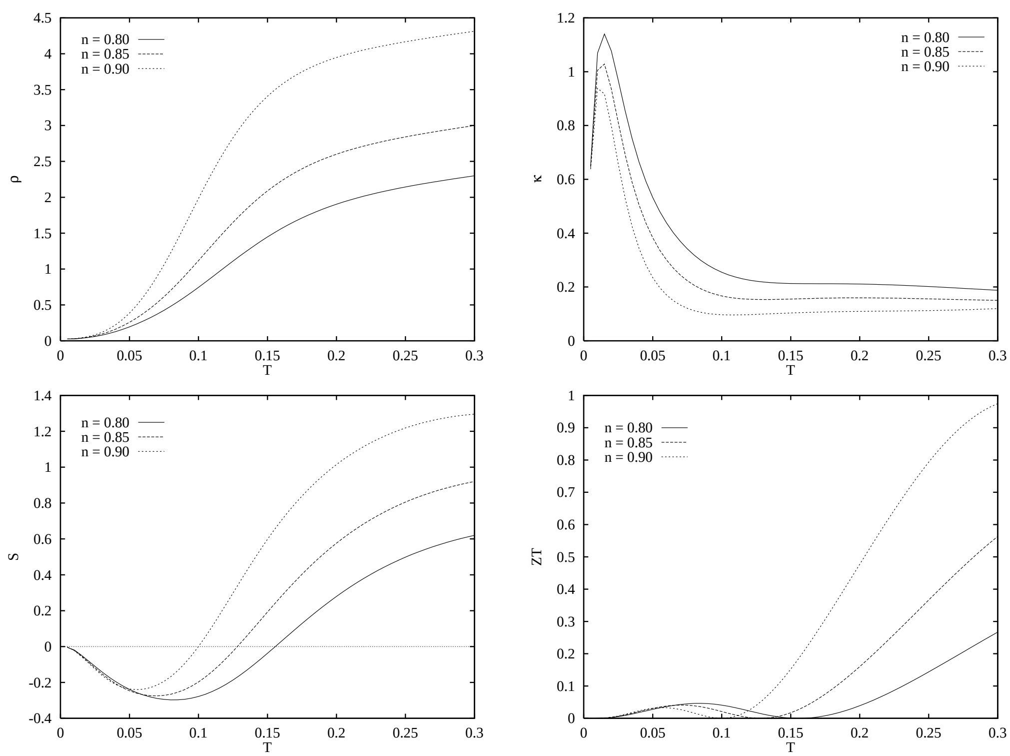


Figure 3.8: Results for transport parameters from IPT+DMFT calculations for $U = 2.82$. Here $\rho$ denotes resistance and is measured in units of $\frac{z\hbar a}{e^2}$, $\kappa$ denotes thermal conductivity and is measured in units of $\frac{k_B D}{za\hbar}$, $S$ denotes thermopower and is measured in units of $\frac{k_B}{e}$ and $ZT$ denotes the dimensionless figure of merit. Here $a$ is the lattice constant, $D = 2t$ is the bare half-width of the band and $z$ is the coordination number of the lattice.

are displayed in figure 3.8. These results should be discussed in the context of the low temperature Fermi liquid [32, 33] estimate for the transport parameters given by the following equations which are derived in appendix B:

$$\sigma = E_0 \frac{Ne^2}{2\gamma}\Phi(\tilde{\mu}) \qquad \kappa = E_2 \frac{k_B N(k_B T)}{2\gamma}\Phi(\tilde{\mu})$$
$$S = -\frac{k_B}{e}\frac{E_2}{E_0}\frac{k_B T}{Z}\frac{d\ln(\Phi(\tilde{\mu}))}{d\tilde{\mu}} \qquad ZT = \frac{E_2}{E_0}\left(\frac{k_B T}{Z}\frac{d\ln\Phi(\tilde{\mu})}{d\tilde{\mu}}\right)^2. \tag{3.112}$$

Here $\gamma = Im\Sigma(0)$ is the scattering rate at the Fermi-level, $Z = (1 - \frac{\partial Re\Sigma}{\partial\omega}|_{\omega=0})^{-1}$ is the quasiparticle residue at the Fermi-level, $\tilde{\mu} = \mu - Re\Sigma(0)$ is the effective chemical potential and the function $\Phi$ is defined in section 3.4. The quantities $E_n$ are constants with $E_0 = 0.82$ and $E_2 = 1.75$. These equations are derived assuming that the imaginary part of the self energy can be approximated by:

$$\operatorname{Im}\Sigma(\omega, T) = \gamma_0\left[(k_B T)^2 + \left(\frac{\omega}{\pi}\right)^2\right] \qquad \text{where} \qquad \gamma_0 = \text{constant} \tag{3.113}$$

to a good accuracy with several $k_B T$ of the Fermi surface while the other parameters are assumed to be nearly temperature independent. Notice that the Wiedeman-Franz law holds here just as it does for transport dominated by impurity scattering. However since the scattering is frequency dependent around the Fermi surface the ratio of $\sigma T$ and $\kappa$ is not equal to the classical Lorenz number.

The scattering at the Fermi surface is now $\gamma = \gamma_0(kT)^2$ and thus we see from the equations above that the temperature behavior of the transport parameters should be:

$$\rho \sim T^2 \qquad \kappa \sim T^{-1} \qquad S \sim T \qquad ZT \sim T^2 \tag{3.114}$$

and indeed it looks like the transport parameters are behaving this way, except for the thermal conductivity which reaches a maximum at a finite temperature and then seems to be going linearly to zero. This discrepancy can be attributed to an artificial numerical broadening of the spectral density, i.e. the scattering rate has a constant term which is put by hand into the computer code to ensure convergence.

In figures 3.9, 3.10 and 3.11 we have plotted the scattering rate, the effective chemical potential and the quasiparticle residue for $U = 2.82$ and $n = 0.80$ along with a comparison of the numerical and Fermi liquid calculation of the transport parameters

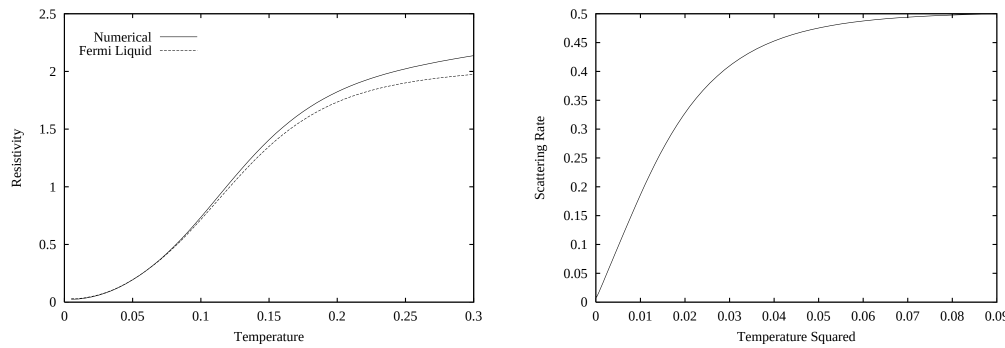


Figure 3.9: The electrical resistivity for $U = 2.82$ and $n = 0.80$ along with its Fermi liquid estimate. Also shown is the scattering rate at the Fermi surface as a function of $T^2$.

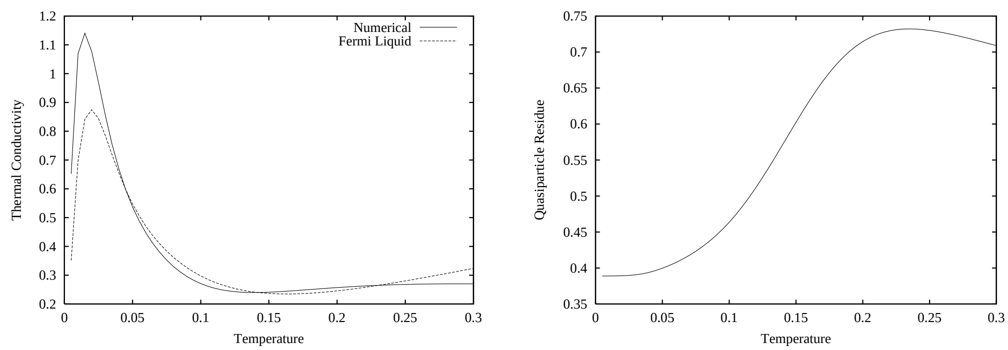


Figure 3.10: The electrical resistivity for $U = 2.82$ and $n = 0.80$ along with its Fermi liquid estimate. Also shown is the quasiparticle residue at the Fermi surface.

according to the equations above. We see indeed that the scattering rate goes as $T^2$ apart from a very small constant part and the other coefficients are nearly temperature independent at temperatures below $T = 0.05$ so as we indicated the main temperature dependence of the transport parameters should come from the scattering rate.

For the resistivity the two methods compare quite favorably with deviations occurring only for temperatures above 0.1. For the thermal conductivity and the thermopower however the Fermi liquid estimate is not as good although it does give the correct qualitative behavior. This indicates that the data does not obey the assumptions that we set out with although the resistivity seems to be less sensitive to this than the other quantities.

The reason for the discrepancy can be inferred from figure 3.12 where we have displayed the self energy close to the Fermi level along with the Fermi liquid approximations

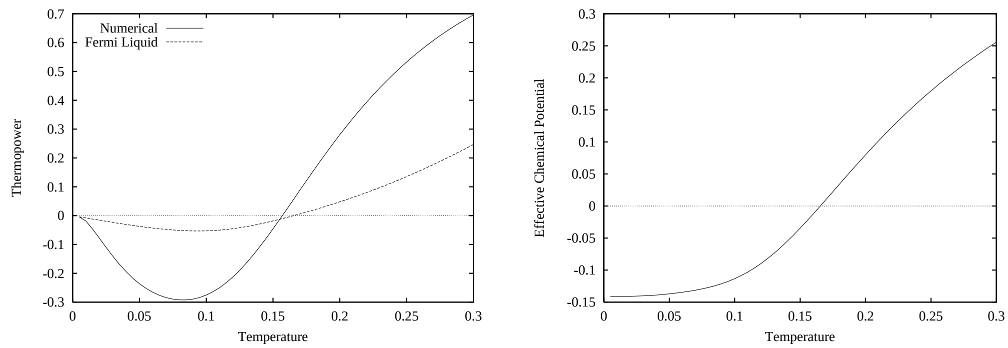


Figure 3.11: The thermopower for $U = 2.82$ and $n = 0.80$ along with its Fermi liquid estimate. Also shown is the effective chemical potential.

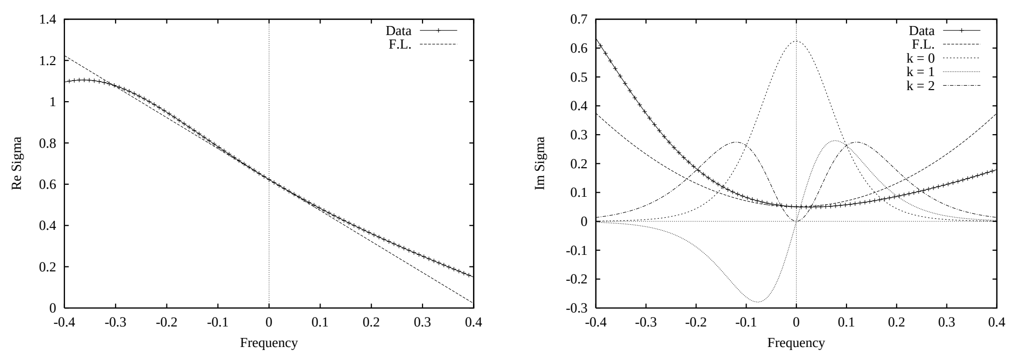


Figure 3.12: The real and the imaginary part of the self energy for $U = 2.82$ and $n = 0.80$ along with the Fermi liquid approximation of these quantities. The curves labeled with an integer value of $k$ correspond to the weight functions $f(\omega)f(-\omega)(\beta\omega)^k$ that are used to compute the transport functions.

to the to self energy and the weights that are used in the calculation of the transport parameters. In order for our simple Fermi liquid calculation to work the imaginary part of the self energy must obey equation (3.113) within an interval of width at least $8k_BT$ around the Fermi level. We also see that for the resistivity this bound can be relaxed somewhat since the weight function associated with the computation of the resistivity is narrower than the one for the other parameters.

The Fermi liquid assumption holds quite well for the real part of the self energy but the imaginary part does show significant asymmetry within this interval. The states below the Fermi surface are more strongly scattered than the ones above the Fermi surface with the result that the electron contribution to the thermopower is enhanced over the hole contribution and therefore the thermopower becomes more negative than the Fermi liquid estimate would indicate. According to the Fermi liquid estimate the thermopower should not depend on the scattering at all and be wholly dependent on the band structure through the transport function. This is a direct consequence of the assumption of symmetric scattering rate.

At higher temperature the transport parameters seem to be tending to some asymptotic high temperature values, and the thermopower is actually quite close to the high temperature value given by Heikes formula. This is consistent with the equation of Chaikin and Beni [10] for the thermopower at intermediate temperatures. In the high temperature regime which for this model is well above the interaction strength $U$ the asymptotic value for the thermopower is not given by Heikes formula but rather by:

$$S = \frac{k_B}{e} \ln\left(\frac{2-n}{n}\right). \tag{3.115}$$

This equation gives always lower thermopower than Heikes formula, although they do converge at low densities. Moreover the asymptotic value of the thermopower is always negative, tending to zero at zero doping. Thus if we could access higher temperatures within this model we would expect that the thermopower would decrease very slowly down from the Heikes limit towards the limit given by the equation above as we reach temperatures higher than the interaction strength.

For the other transport parameters however we have no good way of estimating the exact intermediate and high temperature behavior within this model.

## 3.8 Application to $La_{1-x}Sr_xTiO_3$

Let us now turn to quantitative calculations of the thermopower in the intermediate temperature range, which is the range most pertinent to experiment and possible applications. In the class of materials that we want to consider, i.e. a system that is doped away from the Mott insulating state, the one that is best characterized is the perovskite-like $La_{1-x}Sr_xTiO_3$ [34]. The end compound $LaTiO_3$ is a Mott insulator with the valence on the titanium being +3.0 and is antiferromagnetically ordered below around 150K. By doping with strontium the insulating magnetic state is destroyed and the system becomes a Pauli paramagnetic metal. The doping percentage is found to give an accurate measure of the carrier density in the titanium 3d-bands and experiments indicate that system is a Fermi-liquid at low temperatures almost all the way up to zero doping.

We model this system with a Hubbard model on a cubic lattice, with half-bandwidth, $D = 0.5eV$ [35] and interaction strength $U = 2.0eV$ in the Mott insulating end at $x = 0$. The crystalline lattice of $LaTiO_3$ displays orthorhombic distortions that reduce the Ti-O-Ti bond angle from the ideal 180° to 154° [36]. As the system is doped with strontium the bond angle straightens out and reaches 180° around $x = 0.77$. The variation of the bond angle with doping is close to being linear as we can see from figure 3.13. The

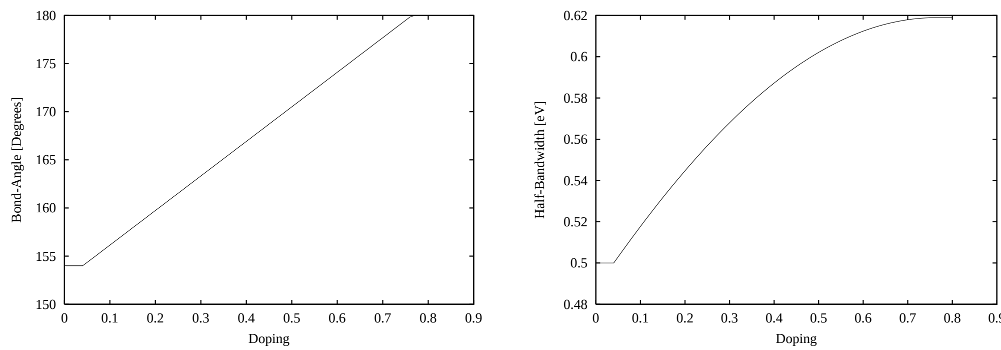


Figure 3.13: The ab plane Ti-O-Ti bond angle vs. doping for the system $La_{1-x}Sr_xTiO_3$ based on data from [37]. The figure on the right shows the corresponding change in the titanium half bandwidth of the titanium 3d-band.

hopping interaction between the titanium atoms is governed by supertransfer interaction over the oxygen sites and thus the band width of the system depends on the Ti-O-Ti bond angle with the exact dependence given by [38, page 1141]:

$$D(\theta) = D(180^\circ)\cos^2\theta \tag{3.116}$$

We should note here that the on-site interaction is assumed not to change with doping and therefore must be scaled appropriately with the bandwidth. Since we take the bandwidth in our programs to be equal to one the interaction in the Mott insulating end corresponds to $U = 4.0$ and then decreases down to around 3.2 in the other end of the doping scale.

The results of the computation of the thermopower for this system using IPT is displayed in figure 3.14. We see that for all computed values of doping the thermopower displays electron-like Fermi-liquid behavior at low temperature although at the smallest

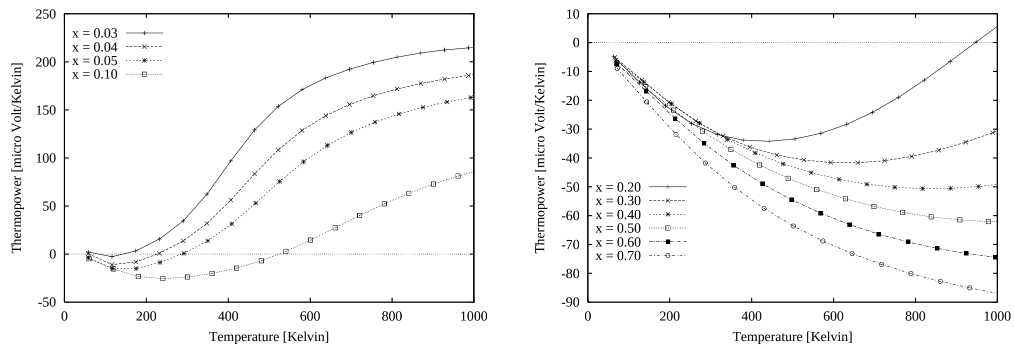


Figure 3.14: The thermopower in $La_{1-x}Sr_xTiO_3$ for various different values of doping.

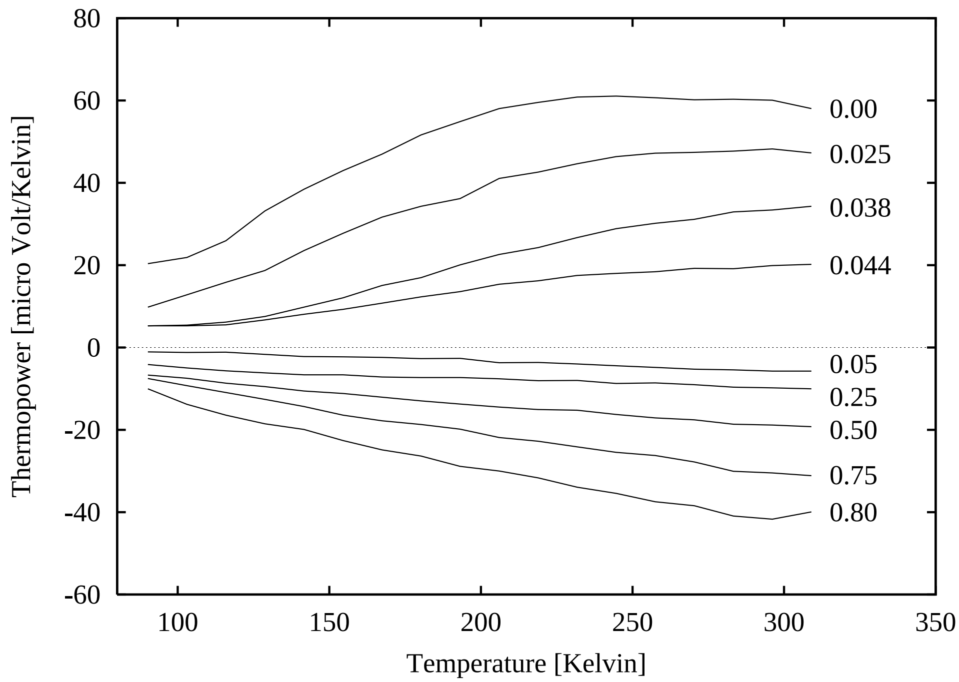


Figure 3.15: Experimental values of thermopower in $La_{1-x}Sr_xTiO_3$ for various different values of doping. The figure is reproduced from [39].

doping values the thermopower actually becomes positive again but that can be attributed to breakdown of the numerics in the IPT code. The transition temperature at which the Fermi liquid picture breaks down is clearly dependent on the proximity to the Mott transition and we see that for the lowest doping values the Fermi liquid range is quite small. Similar results have been observed in experiments by Onoda et.al. [40] and Hays et.al. (see figure 3.15) but in our case the transition to a hole-like thermopower occurs at lower temperature than indicated by experiments. In the higher doping range however the Fermi liquid behavior extends at least up to 300K and both this range and the value of the thermopower agrees quite well with experiments by Moos et.al. [41] on $La_{1-x}Sr_xTiO_3$ ceramics. Between 400 and 1000K the experimental data shows logarithmic, semiconducting behavior with the thermopower changing by around $-300\mu V/K$ per decade. In our data we see similar logarithmic behavior in this temperature range for the largest doping values but the change per decade depends on the doping and is only in the range of $-70$ to $-90\mu V/K$. This discrepancy could be due the fact that we assume here that we are dealing with a single crystal system but we should also note that IPT has its range of validity and is most dependable at lower temperatures.

## 3.9 Optimization of the figure of merit

Before we leave the Hubbard model let us try to assess how efficient these strongly correlated materials would be for thermoelectric purposes. We continue with the $La_{1-x}Sr_xTiO_3$ as in the previous section using the same parameters as before for the IPT. For the NCA with use the same doping dependent bandwidth and take the degeneracy equal to 2. To get a reasonable estimate for the figure of merit we have to assume that the lattice contribution to the thermal conductivity is finite. We are not aware any experiments on the thermal conductivity in these titanate compounds, so for the purpose of getting an order of magnitude estimate we use a value of 2.0 W/mK for $\kappa_L$ based on measurements made on manganite oxides [42]. We will moreover assume that this value does not depend on either temperature or doping. In figures 3.16 and 3.17 we have plotted the figures of

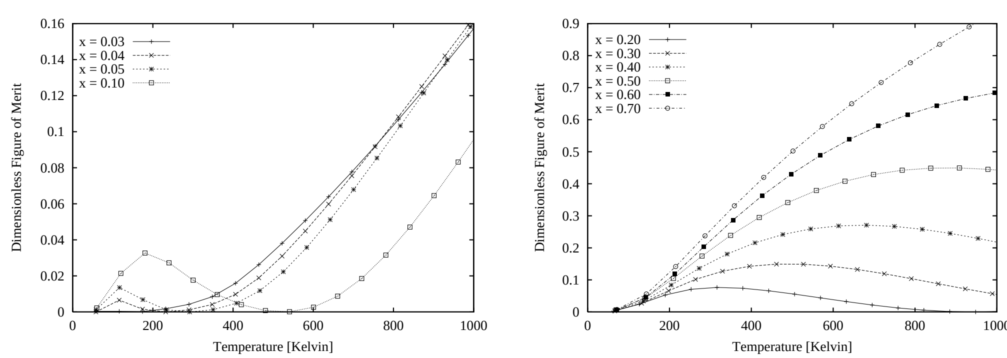


Figure 3.16: The dimensionless figure of merit for the $La_{1-x}Sr_xTiO_3$ system, computed using the IPT.

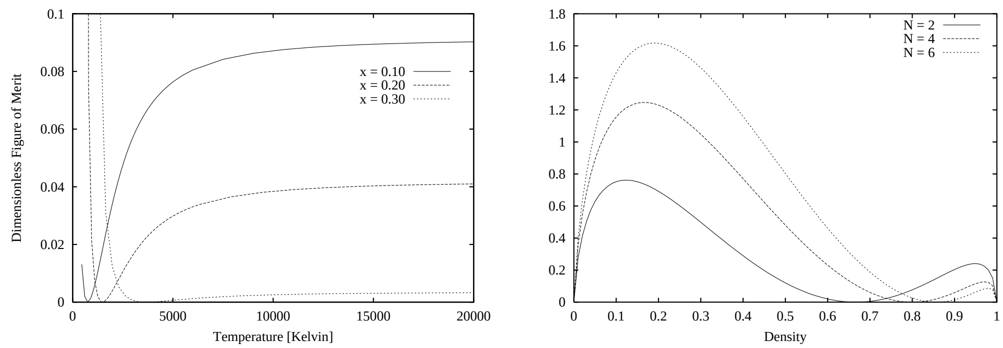


Figure 3.17: The dimensionless figure of merit for the $La_{1-x}Sr_xTiO_3$ system, computed using the NCA. The figure on the left shows the expected density dependence of the dimensionless figure of merit within the NCA (see equation (3.97).

merit computed with both the IPT and the NCA. Admittedly the temperature scale for the NCA figure is rather large, but as we have seen the NCA does brake down at low temperature preventing us from reaching lower temperatures. We can clearly see this breakdown in the divergence of the figure of merit for the two higher doping values. We have also displayed the expected doping dependence of the high temperature figure of merit within the NCA assuming a finite thermal lattice conduction. As we can see here the figure of merit does not diverge at all as we approach the Mott transition, instead it reaches a low maximum just below half filling and then tends to zero in a non-analytic fashion. It is clear that in this context the analysis of the NCA is not expected to be at all valid except in system with smaller bandwidth where it is easier to access the high temperature regime. We could also try to access the high temperature region by increasing the doping and in fact judging by the figure on the right in 3.17 we would do a much better job of maximizing the figure of merit that way.

This conclusion is borne out in the IPT data, which is much more pertinent to real systems. There we see that the figure of merit dramatically increases as we increase the doping. In the low temperature region we see typical metallic Fermi liquid behavior, characterized by small figure of merit but at higher temperatures the system shows more of a semiconducting behavior as discussed earlier in section 3.8 with quite a sizeable figure of merit.

In light of our results we have to conclude that it seems quite unlikely that a significant figure merit can be attained in this class of systems. In fact for the case of $La_{1-x}Sr_xTiO_3$ our results indicate that the semiconducting regime close to the strontium filled end of this system is more likely to give rise to large figures or merit. This of course is consistent with the general rule that large figure of merit are mainly to be obtained in semiconductors.

# Chapter 4

# Transport in Real Multiband Systems: Orthogonal Case

## 4.1 Introduction

In this chapter we will continue to focus on the computation of transport properties of correlated materials but instead of restricting ourselves to simple models like we did in previous chapters we will extend our discussion to realistic models. Thus we will be working with Hamiltonians obtained from first principle bandstructure calculations (LMTO) and we will derive the equations for the lowest order contributions to the transport parameters. As such the Hamiltonian will be given at each point in the Brillouin zone by a matrix in the space of valence orbitals that describes both the energies and the mixing of the orbitals in question.

As an example of such a Hamiltonian we can take for instance the Hamiltonian for LaTiO. In this material the bands that are closest to the Fermi surface and participate in the transport are transition metal d-orbitals which hybridize with oxygen p-orbitals that are slightly below the Fermi-surface. The rest of the orbitals are inert and can be either folded or to first approximation, ignored. We thus obtain an effective Hamiltonian of the form:

$$H_0 = \sum_{k\alpha\beta} \epsilon^p_{k\alpha\beta} p^+_{k\alpha} p_{k\beta} + \sum_{k\alpha\beta} \epsilon^d_{k\alpha\beta} d^+_{k\alpha} d_{k\beta} + \sum_{k\alpha\beta} \left( V_{k\alpha\beta} p^+_{k\alpha} d_{k\beta} + V^*_{k\alpha\beta} d^+_{k\beta} p_{k\alpha} \right). \tag{4.1}$$

Here we have suppressed the spin index. To this Hamiltonian we want to add an on-site Hubbard type interaction for the d-electron. Since this on-site interaction has been taken into account in some average fashion in the LMTO calculation some changes should be made also to the original Hamiltonian, $H_0$. We will however not worry about that for the moment. Thus our final Hamiltonian is:

$$H = H_0 + \frac{U}{2} \sum_i \sum_{(\alpha,\sigma)\neq(\alpha',\sigma')} d^+_{i\alpha\sigma} d_{i\alpha\sigma} d^+_{i\alpha'\sigma'} d_{i\alpha'\sigma'}. \tag{4.2}$$

To simplify the notation we will in the following write the LMTO Hamiltonian as follows:

$$H_0 = \sum_{kmn} \varepsilon_{kmn} c^+_{km} c_{kn} \tag{4.3}$$

where here $\varepsilon_{kmn}$ would equal $\epsilon^p_{kmn}$ and $\epsilon^d_{kmn}$ in the diagonal p-orbital sector and d-orbital sector respectively and $V_{kmn}$ in the off diagonal.

Now in order to compute the transport properties we also need the self energy and that is where the DMFT comes in. In recent years some efforts have been put into extending the DMFT to deal with real materials and the general DMFT approach to real materials and clusters has recently been formalized and been shown to be causally consistent [43].

In what follows here we will simply assume that the self energy is available as an output of a realistic DMFT calculation.

## 4.2 The currents and the transport equations

The classical approach to the computation of the transport properties in real materials is based on the Boltzmann equation [44, 45]. Here we however use the same approach as in the previous chapters, i.e. we use the Kubo formalism and relate the transport parameters to retarded current-current correlation functions. Hence the first thing we must do is to obtain expressions for the currents. In the multiorbital case the best framework for deriving the expressions for the currents is by using gauge invariance principles as explained by Moreno and Coleman [46]. Since the Hubbard type interaction is a density-density interaction it will not contribute to the expression for currents which can be derived from a gauge-principle as the particle current and the thermal current. Thus in the following we don't really have to worry about the interaction term except for the fact that all correlation functions that we encounter have to be calculated with the full Hamiltonian. Hence the currents are given by:

$$\vec{Q} = \frac{1}{2} \sum_{kmn} \vec{v}_{kmn} \left( \dot{c}^{+}_{km} c_{kn} - c^{+}_{km} \dot{c}_{kn} \right). \tag{4.4}$$

where $\vec{v}_{kmn} = \vec{\nabla}_k \varepsilon_{kmn}$. The particle current has a similar expression and is given by:

$$\vec{j} = \sum_{kmn} \vec{v}_{kmn} c^{+}_{km} c_{kn}. \tag{4.5}$$

To find the transport coefficients we must calculate the following correlation functions:

$$Z^{\nu\lambda}_{jj}(\tau) = \langle j^{\nu}(\tau) j^{\lambda}(0) \rangle = \sum_{k} \sum_{mn} \sum_{pq} v^{\nu}_{kmn} v^{\lambda}_{kpq} \Xi^{(1)}_{mnpq}(\tau, k) \tag{4.6}$$

$$Z^{\nu\lambda}_{jQ}(\tau) = \langle j^{\nu}(\tau) Q^{\lambda}(0) \rangle = \sum_{k} \sum_{mn} \sum_{pq} v^{\nu}_{kmn} v^{\lambda}_{kpq} \Xi^{(2)}_{mnpq}(\tau, k) \tag{4.7}$$

$$Z^{\nu\lambda}_{QQ}(\tau) = \langle Q^{\nu}(\tau) Q^{\lambda}(0) \rangle = \sum_{k} \sum_{mn} \sum_{pq} v^{\nu}_{kmn} v^{\lambda}_{kpq} \Xi^{(3)}_{mnpq}(\tau, k) \tag{4.8}$$

where we have defined the following expectation values:

$$\Xi^{(1)}_{mnpq}(\tau, k) = \langle c^{+}_{km}(\tau) c_{kn}(\tau) c^{+}_{k'p} c_{k'q} \rangle \tag{4.9}$$

$$\Xi^{(2)}_{mnpq}(\tau, k) = \frac{1}{2} \langle c^{+}_{km}(\tau) c_{kn}(\tau) \left( \dot{c}^{+}_{k'p} c_{k'q} - c^{+}_{k'p} \dot{c}_{k'q} \right) \rangle \tag{4.10}$$

$$\Xi^{(3)}_{mnpq}(\tau, k) = \frac{1}{4} \langle \left( \dot{c}^{+}_{km}(\tau) c_{kn}(\tau) - c^{+}_{km}(\tau) \dot{c}_{kn}(\tau) \right) \left( \dot{c}^{+}_{k'p} c_{k'q} - c^{+}_{k'p} \dot{c}_{k'q} \right) \rangle \tag{4.11}$$

These expectation values will be evaluated shortly but first we need to establish some notation. We define our Green's functions as follows ($\tau > 0$):

$$G_{mn}(\tau, k) = -\langle c_{km}(\tau) c^{+}_{kn} \rangle = \frac{-1}{Z} Tr \left\{ e^{-\beta H} e^{\tau H} c_{km} e^{-\tau H} c^{+}_{kn} \right\} \tag{4.12}$$

The Fourier transform of this can be calculated and is given by:

$$G_{mn}(i\omega, k) = \left[ \frac{1}{i\omega + \mu - \hat{\varepsilon}_k - \hat{\Sigma}(i\omega, k)} \right]_{mn} \tag{4.13}$$

Note that here both $\hat{\varepsilon}_k$ and $\hat{\Sigma}(i\omega, k)$ are matrices. It is useful to have a spectral representation of the Green's functions (see appendix C),

$$G_{mn}(i\omega, k) = \int_{-\infty}^{\infty} \frac{\rho_{kmn}(\epsilon)}{i\omega - \epsilon} d\epsilon \tag{4.14}$$

where the spectral density $\hat{\rho}_k(\epsilon)$ is the discontinuity of the Green's function at the branch cut on the real axis, i.e.

$$\hat{\rho}_k(\epsilon) = \frac{-1}{2\pi i} \left( \hat{G}^{ret}(\epsilon, k) - \hat{G}^{adv}(\epsilon, k) \right) = \frac{-1}{2\pi i} \left( \hat{G}^{ret}(\epsilon, k) - \left( \hat{G}^{ret}(\epsilon, k) \right)^{+} \right). \tag{4.15}$$

In terms of the spectral density we can write down an explicit formula for the time dependent Green's function:

$$G_{mn}(\tau,k) = -\int_{-\infty}^{\infty} d\epsilon \rho_{kmn}(\epsilon) e^{-\epsilon\tau} \left(\theta(\tau) f(-\epsilon) - \theta(-\tau) f(\epsilon)\right). \tag{4.16}$$

We now look at the expectation values above and evaluate them using a diagram expansion keeping only connected diagrams with no vertex corrections. The expectation value of time derivatives of the creation and annihilation operators can be related to the time derivative of the Green's function as discussed in Appendix C and using those relations we get:

$$\begin{aligned}
\Xi^{(1)}_{mnpq}(\tau,k) &= -G_{np}(\tau,k) G_{qm}(-\tau,k) \\
&= \int_{-\infty}^{\infty} d\epsilon d\epsilon' \rho_{knp}(\epsilon) \rho_{kqm}(\epsilon') e^{(\epsilon'-\epsilon)\tau} f(-\epsilon) f(\epsilon') \qquad (4.17) \\
\Xi^{(2)}_{mnpq}(\tau,k) &= \dot{G}_{np}(\tau,k) G_{qm}(-\tau,k) - G_{np}(\tau,k) \dot{G}_{qm}(-\tau,k) \\
&= \int_{-\infty}^{\infty} d\epsilon d\epsilon' \rho_{knp}(\epsilon) \rho_{kqm}(\epsilon') e^{(\epsilon'-\epsilon)\tau} f(-\epsilon) f(\epsilon') \left(\frac{\epsilon+\epsilon'}{2}\right) \qquad (4.18) \\
\Xi^{(3)}_{mnpq}(\tau,k) &= \dot{G}_{np}(\tau,k) \dot{G}_{qm}(-\tau,k) - G_{np}(\tau,k) \ddot{G}_{qm}(-\tau,k) \\
&- \ddot{G}_{np}(\tau,k) G_{qm}(-\tau,k) + \dot{G}_{np}(\tau,k) \dot{G}_{qm}(-\tau,k) \\
&= \int_{-\infty}^{\infty} d\epsilon d\epsilon' \rho_{knp}(\epsilon) \rho_{kqm}(\epsilon') e^{(\epsilon'-\epsilon)\tau} f(-\epsilon) f(\epsilon') \left(\frac{\epsilon+\epsilon'}{2}\right)^2 \qquad (4.19)
\end{aligned}$$

The current-current correlation functions are then:

$$\begin{aligned}
Z^{\nu\lambda}_{jj}(\tau) &= \sum_k \int_{-\infty}^{\infty} d\epsilon d\epsilon' \phi^{\nu\lambda}(\epsilon,\epsilon') e^{(\epsilon'-\epsilon)\tau} f(-\epsilon) f(\epsilon') \qquad (4.20) \\
Z^{\nu\lambda}_{jQ}(\tau) &= \sum_k \int_{-\infty}^{\infty} d\epsilon d\epsilon' \phi^{\nu\lambda}(\epsilon,\epsilon') e^{(\epsilon'-\epsilon)\tau} f(-\epsilon) f(\epsilon') \left(\frac{\epsilon+\epsilon'}{2}\right) \qquad (4.21) \\
Z^{\nu\lambda}_{QQ}(\tau) &= \sum_k \int_{-\infty}^{\infty} d\epsilon d\epsilon' \phi^{\nu\lambda}(\epsilon,\epsilon') e^{(\epsilon'-\epsilon)\tau} f(-\epsilon) f(\epsilon') \left(\frac{\epsilon+\epsilon'}{2}\right)^2. \qquad (4.22)
\end{aligned}$$

Where we have defined the transport function $\phi^{\nu\lambda}(\epsilon,\epsilon')$ as

$$\phi^{\nu\lambda}(\epsilon,\epsilon') \equiv \sum_k \mathrm{Tr}\left\{\hat{v}^{\nu}_k \hat{\rho}_k(\epsilon) \hat{v}^{\lambda}_k \hat{\rho}_k(\epsilon')\right\}. \tag{4.23}$$

Here Tr denotes trace in the space of orbitals at a given point in the Brillouin zone. We note that all the operators on the trace are hermitian so that the trace is a real number.

It is now easy to take the Fourier transform of the $Z$ functions and we obtain:

$$Z_{jj}^{\nu\lambda}(i\nu_n) = \int_{-\infty}^{\infty} d\epsilon d\epsilon' \phi^{\nu\lambda}(\epsilon,\epsilon') \frac{f(\epsilon)-f(\epsilon')}{i\nu_n+\epsilon'-\epsilon} \tag{4.24}$$

$$Z_{jQ}^{\nu\lambda}(i\nu_n) = \int_{-\infty}^{\infty} d\epsilon d\epsilon' \phi^{\nu\lambda}(\epsilon,\epsilon') \frac{f(\epsilon)-f(\epsilon')}{i\nu_n+\epsilon'-\epsilon}\left(\frac{\epsilon+\epsilon'}{2}\right) \tag{4.25}$$

$$Z_{QQ}^{\nu\lambda}(i\nu_n) = \int_{-\infty}^{\infty} d\epsilon d\epsilon' \phi^{\nu\lambda}(\epsilon,\epsilon') \frac{f(\epsilon)-f(\epsilon')}{i\nu_n+\epsilon'-\epsilon}\left(\frac{\epsilon+\epsilon'}{2}\right)^2 \tag{4.26}$$

Finally we obtain the kinetic coefficients by looking at the imaginary part of the retarded version of the $Z$ functions, dividing by $\beta\omega$ and taking the limit $\omega \to 0$. Thus we get:

$$\begin{aligned}
\zeta_{jj}^{\nu\lambda} \equiv \frac{1}{\beta}\lim_{\omega\to 0}\frac{1}{\omega}\,\mathrm{Im}\, Z_{jj}^{\nu\lambda}(\omega+i0) &= \pi\int_{-\infty}^{\infty} d\epsilon \phi^{\nu\lambda}(\epsilon)\left(-k_b T\frac{df(\epsilon)}{d\epsilon}\right) \\
\zeta_{jQ}^{\nu\lambda} \equiv \frac{1}{\beta}\lim_{\omega\to 0}\frac{1}{\omega}\,\mathrm{Im}\, Z_{jQ}^{\nu\lambda}(\omega+i0) &= \pi\int_{-\infty}^{\infty} d\epsilon \phi^{\nu\lambda}(\epsilon)\left(-k_B T\frac{df(\epsilon)}{d\epsilon}\right)\epsilon \\
\zeta_{QQ}^{\nu\lambda} \equiv \frac{1}{\beta}\lim_{\omega\to 0}\frac{1}{\omega}\,\mathrm{Im}\, Z_{QQ}^{\nu\lambda}(\omega+i0) &= \pi\int_{-\infty}^{\infty} d\epsilon \phi^{\nu\lambda}(\epsilon)\left(-k_B T\frac{df(\epsilon)}{d\epsilon}\right)\epsilon^2
\end{aligned} \tag{4.27}$$

where for simplicity we denote $\phi^{\nu\lambda}(\epsilon,\epsilon)$ by $\phi^{\nu\lambda}(\epsilon)$, i.e.

$$\phi^{\nu\lambda}(\epsilon) \equiv \sum_k \mathrm{Tr}\left\{\hat{v}_k^{\nu}\hat{\rho}_k(\epsilon)\hat{v}_k^{\lambda}\hat{\rho}_k(\epsilon)\right\}. \tag{4.28}$$

We should note here that if we make a momentum independent unitary transformation in the space of orbitals, the transport function is left invariant. Hence if the self energy is momentum independent which is the case in dynamical mean field theory we can always make a unitary transformation to a basis where at least the antihermitian damping part of the self energy is diagonal.

## 4.3 Transport function

It is useful for further numerical calculations to investigate the transport function a little bit closer. For this purpose let us look at the energy and write

$$\hat{\varepsilon}_k + \hat{\Sigma}(z,k) = \hat{U}(z,k)\hat{E}(z,k)\hat{U}^{-1}(z,k) \tag{4.29}$$

where the matrix $\hat{E}_{mn} = \delta_{mn}E_m$ is a diagonal matrix of eigenvalues and the columns of $\hat{U}$ contain the corresponding eigenvectors. Note that the eigenvalues are complex and thus the eigenvectors are not necessarily orthogonal. Then we can write:

$$\hat{G}(z,k) = \hat{U}(z,k)\hat{D}(z,k)\hat{U}^{-1}(z,k) \qquad \text{where} \qquad \hat{D}_{mn} = \frac{\delta_{mn}}{z+\mu-\hat{E}_m}. \tag{4.30}$$

Suppressing the frequency and momentum dependence, assuming that $\hat{G}$ is the retarded Green's function, using the cyclic property of the trace and the fact that the velocity is hermitian we get:

$$\begin{aligned}
\mathrm{Tr}\left\{\hat{v}^\nu\hat{\rho}\hat{v}^\lambda\hat{\rho}\right\} &= \frac{1}{(2\pi i)^2}\,\mathrm{Tr}\left\{\hat{v}^\nu(\hat{G}-\hat{G}^+)\hat{v}^\lambda(\hat{G}-\hat{G}^+)\right\} \\
&= \frac{-1}{(2\pi)^2}\left(\mathrm{Tr}\left\{\hat{v}^\nu\hat{G}\hat{v}^\lambda\hat{G}\right\} - \mathrm{Tr}\left\{\hat{v}^\nu\hat{G}^+\hat{v}^\lambda\hat{G}\right\}\right. \\
&- \left.\mathrm{Tr}\left\{\hat{v}^\nu\hat{G}\hat{v}^\lambda\hat{G}^+\right\} + \mathrm{Tr}\left\{\hat{v}^\nu\hat{G}^+\hat{v}^\lambda\hat{G}^+\right\}\right) \\
&= \frac{-1}{(2\pi)^2}\left(\mathrm{Tr}\left\{\hat{v}^\nu\hat{G}\hat{v}^\lambda\hat{G}\right\} - \mathrm{Tr}\left\{\hat{v}^\nu\hat{G}^+\hat{v}^\lambda\hat{G}\right\}\right. \\
&- \left.\mathrm{Tr}\left\{\hat{G}\hat{v}^\lambda\hat{G}^+\hat{v}^\nu\right\} + \mathrm{Tr}\left\{\hat{G}^+\hat{v}^\lambda\hat{G}^+\hat{v}^\nu\right\}\right) \\
&= \frac{-1}{(2\pi)^2}\left(\mathrm{Tr}\left\{\hat{v}^\nu\hat{G}\hat{v}^\lambda\hat{G} + \left[\hat{v}^\nu\hat{G}\hat{v}^\lambda\hat{G}\right]^+\right\}\right. \\
&- \left.\mathrm{Tr}\left\{\hat{v}^\nu\hat{G}^+\hat{v}^\lambda\hat{G} + \hat{v}^\lambda\hat{G}^+\hat{v}^\nu\hat{G}\right\}\right) \\
&= \frac{-2}{(2\pi)^2}\,\mathrm{Re}\left(\mathrm{Tr}\left\{L^{\nu\lambda}\right\} - \mathrm{Tr}\left\{M^{\nu\lambda}\right\}\right)
\end{aligned} \tag{4.31}$$

Where we have defined:

$$\begin{aligned}
L^{\nu\lambda} &= \hat{v}^\nu\hat{G}\hat{v}^\lambda\hat{G} = \hat{v}^\nu\hat{U}\hat{D}\hat{U}^{-1}\hat{v}^\lambda\hat{U}\hat{D}\hat{U}^{-1} \\
M^{\nu\lambda} &= \frac{1}{2}\left[\hat{v}^\nu\hat{G}^+\hat{v}^\lambda\hat{G} + \hat{v}^\lambda\hat{G}^+\hat{v}^\nu\hat{G}\right] \\
&= \frac{1}{2}\left[\hat{v}^\nu(\hat{U}^{-1})^+\hat{D}^+\hat{U}^+\hat{v}^\lambda\hat{U}\hat{D}\hat{U}^{-1} + \hat{v}^\lambda(\hat{U}^{-1})^+\hat{D}^+\hat{U}^+\hat{v}^\nu\hat{U}\hat{D}\hat{U}^{-1}\right]
\end{aligned} \tag{4.32}$$

Note that taking the real part of the $M$ matrix is really redundant since it is already real. Let us now define the following three operators:

$$\hat{r}^\nu = \hat{U}^{-1}\hat{v}^\nu\hat{U}, \qquad \hat{s}^\nu = \hat{U}^{-1}\hat{v}^\nu\left(\hat{U}^{-1}\right)^+ \qquad \text{and} \qquad \hat{t}_3^\nu = \hat{U}^+\hat{v}^\nu\hat{U}. \tag{4.33}$$

Then our trace can be written as

$$\mathrm{Tr}\left\{\hat{v}^\nu\hat{\rho}\hat{v}^\lambda\hat{\rho}\right\} = \frac{-1}{2\pi^2}\,\mathrm{Re}\,\mathrm{Tr}\left\{\hat{r}^\nu\hat{D}\hat{r}^\lambda\hat{D} - \frac{1}{2}\left(\hat{s}^\nu\left(\hat{D}\right)^+\hat{t}^\lambda\hat{D} + \hat{s}^\lambda\left(\hat{D}\right)^+\hat{t}^\nu\hat{D}\right)\right\} \tag{4.34}$$

We can thus write the transport function on the form

$$
\begin{aligned}
\phi^{\nu\lambda}(\epsilon) &= \frac{-1}{2\pi^2}\sum_k \mathrm{Re}\left(\mathrm{Tr}\left\{\hat{r}_k^\nu(\epsilon)\hat{D}_k(\epsilon)\hat{r}_k^\lambda(\epsilon)\hat{D}_k(\epsilon)\right\}\right) \\
&- \frac{1}{4\pi^2}\sum_k \left(\mathrm{Tr}\left\{\hat{s}_k^\nu(\epsilon)\left(\hat{D}_k(\epsilon)\right)^+\hat{t}_k^\lambda(\epsilon)\hat{D}_k(\epsilon) + \hat{s}_k^\lambda(\epsilon)\left(\hat{D}_k(\epsilon)\right)^+\hat{t}_k^\nu(\epsilon)\hat{D}_k(\epsilon)\right\}\right) \\
&= \frac{-1}{2\pi^2}\sum_k \mathrm{Re}\sum_{pq}\left(\hat{r}_{kpq}^\nu(\epsilon)D_{kq}(\epsilon)\hat{r}_{kqp}^\lambda(\epsilon)D_{kp}(\epsilon)\right) \\
&- \frac{1}{4\pi^2}\sum_k\sum_{pq}\left(\hat{s}_{kpq}^\nu(\epsilon)D_{kq}^*(\epsilon)\hat{t}_{kqp}^\lambda(\epsilon)D_{kp}(\epsilon) + \hat{s}_{kpq}^\lambda(\epsilon)D_{kq}^*(\epsilon)\hat{t}_{kqp}^\nu(\epsilon)D_{kp}(\epsilon)\right) \\
&= \frac{-1}{2\pi^2}\sum_k \mathrm{Re}\sum_{pq}\left(\frac{\alpha_{kpq}^{\nu\lambda}(\epsilon)}{(\epsilon+\mu-E_{kp}(\epsilon))(\epsilon+\mu-E_{kq}(\epsilon))}\right) \\
&+ \frac{1}{2\pi^2}\sum_k\sum_{pq}\left(\frac{\beta_{kpq}^{\nu\lambda}(\epsilon)}{(\epsilon+\mu-E_{kp}(\epsilon))(\epsilon+\mu-E_{kq}^*(\epsilon))}\right)
\end{aligned} \tag{4.35}
$$

where we have defined:

$$
\alpha_{kpq}^{\nu\lambda}(\epsilon) = \hat{r}_{kpq}^\nu(\epsilon)\hat{r}_{kqp}^\lambda(\epsilon) \qquad \text{and} \qquad \beta_{kpq}^{\nu\lambda}(\epsilon) = \frac{1}{2}\left(\hat{s}_{kpq}^\nu(\epsilon)\hat{t}_{kqp}^\lambda(\epsilon) + \hat{s}_{kpq}^\lambda(\epsilon)\hat{t}_{kqp}^\nu(\epsilon)\right) \tag{4.36}
$$

## 4.4 Small scattering limit

It is interesting to consider here the limit of the transport function when the scattering tends to zero. It is of course quite clear that the transport function diverges in this limit but it is nevertheless worthwhile to pursue this limit and see where the strongest contribution comes from. So we will assume that the self energy is given by

$$
\Sigma(\omega) = \gamma\Sigma_0(\omega) \tag{4.37}
$$

where $\gamma$ is a small parameter which approaches zero and $\Sigma_0$ is diagonal[1]. In the limit that $\gamma$ goes to zero the eigenvalues of the full Hamiltonian, $H_k + \Sigma$ will approach the eigenvalues of the bare Hamiltonian, $H_k$, and in particular the imaginary part of the eigenvalues will tend to zero linearly to first order in $\gamma$. The eigenvectors will also approach the eigenvectors of the bare Hamiltonian. Looking at the diagonalized expression for the transport function (4.35) we see that the expected divergence will come from

[1]Note that there is no loss of generality in assuming that the self energy is diagonal, see page 58.

the energy denominators and therefore is is enough to evaluate the numerators to zeroth order in $\gamma$. To zeroth order the eigenvector matrix $U$ is simply equal to the bare eigenvector matrix $U_B$ which is unitary and thus we find that in this approximation the matrices $r^x$, $s^x$ and $t^x$ are all equal and are simply:

$$r^x = s^x = t^x = U_B^+ v^x U_B. \tag{4.38}$$

Before we take this any further let us look again at the expression for the velocity. Using the diagonal representation of the bare Hamiltonian, $H_k = U_B E_B U_B^+$ where $E_B$ is the diagonal matrix of eigenvalues of the bare Hamiltonian we can write the velocity as

$$\vec{v} = \vec{\nabla}_k H_k = U_B \left\{ \vec{v}_B - [E_B, \vec{K}] \right\} U_B^+ \tag{4.39}$$

where we define the bare velocity and the matrix $\vec{K}$ as

$$\vec{v}_B = \vec{\nabla}_k E_b \qquad \text{and} \qquad \vec{K} = U_B^+ \vec{\nabla}_k U_B. \tag{4.40}$$

Hence we see that

$$r^x = v_B^x - [E_B, K^x]. \tag{4.41}$$

We note that the matric $E_B$ is diagonal so we can write the matrix elements of $r^x$ as

$$r_{pq}^x = \delta_{pq} v_p^x - K_{pq}^x (E_p - E_q). \tag{4.42}$$

The matrix elements $\alpha$ and $\beta$ from equation (4.35) are now given by:

$$\begin{aligned} \alpha_{pq}^{xx} &= \beta_{pq}^{xx} = r_{pq}^x r_{qp}^x = \delta_{pq} (v_p)^2 + K_{pq}^x (E_p - E_q) K_{qp}^x (E_q - E_p) \\ &= \delta_{pq} (v_p)^2 + |K_{pq}^x|^2 (E_p - E_q)^2. \end{aligned} \tag{4.43}$$

where we have used the fact that $K^x$ is antihermitian. The equation for the transport function simplifies now tremendously and becomes:

$$\phi^{xx} = \frac{1}{\pi^2} \sum_{kpq} \left[ \delta_{pq} (v_p)^2 + |K_{pq}^x|^2 (E_p - E_q)^2 \right] \mathrm{Im} \left( \frac{1}{\epsilon + \mu - E_{kp}} \right) \mathrm{Im} \left( \frac{1}{\epsilon + \mu - E_{kq}} \right). \tag{4.44}$$

Here we have still kept the complex energies in the denominator of the spectral function, but as the parameter $\gamma$ tends to zero these spectral functions become delta functions.

The off diagonal terms, $p \neq q$, in this expression will vanish on account of the delta function if the energies in the denominators are not the same, and if they are degenerate then the energy difference term in the matrix element will see to that they vanish. Hence we are left with only the diagonal term term involving the bare velocity and this term of course is formally divergent. This result is however quite often used in practice and then one takes one of the spectral functions as a delta function and the other gives the lifetime in the particular orbital. We can think of the lifetime of an orbital as given by:

$$\tau_{kp} = \frac{1}{2\pi |\operatorname{Im} E_{kp}|} \tag{4.45}$$

and even though we have assumed that this quantity is infinite in our derivation the final result is quite often written as:

$$\phi^{xx} = \sum_{kp} (v_{kp})^2 \tau_{kp} \delta(\epsilon + \mu - E_{B,kp}). \tag{4.46}$$

This expression is nothing but the Boltzmann equation expression for the transport function [44, 45] with the exception that our definition of the lifetime does not include vertex corrections [27]. This was of course clear from the start since the calculation here only includes the lowest order diagram contributing to the transport coefficients. This is consistent with the dynamical mean field theory [1] where vertex corrections drop out in the infinite dimensional limit. Undoubtedly vertex correction will play a role for real three dimensional materials but the numerical calculations would quickly become quite unwieldy.

Since the computation of the small scattering limit is much simpler than computing the full transport function it is useful to have this computation as a reference for the full transport function computation. By scaling it by the parameter $\gamma$ we obtain a finite result which can be compared to a similarly scaled full computation. Thus we define

$$\phi^{xx}_{Bare} = \sum_{kp} (v_{kp})^2 \tau_{kp} \delta(\epsilon + \mu - E_{B,kp}). \tag{4.47}$$

where the lifetime is computed by adding a very small scattering to the Hamiltonian and diagonalizing it and then we used the equation

$$\tau_{kp} = \frac{\gamma}{2\pi |\operatorname{Im} E_{kp}|}. \tag{4.48}$$

.

## 4.5 A detailed look at the integral

After this brief aside on the small scattering limit we now focus our attention on the task at hand, i.e. computing the integral:

$$\phi^{xx} = \sum_{k \in BZ} \mathrm{Tr}\left\{v_k^x \rho_k v_k^x \rho_k\right\} \tag{4.49}$$

where BZ denotes the Brillouin zone. In the numerical computation the Brillouin zone is the volume inside the cube spanned by the three basis vectors, $\vec{k}_1$, $\vec{k}_2$ and $\vec{k}_3$ of the reciprocal lattice. We construct from these vectors the so called minicell vectors, $\vec{p}_i$ by:

$$\vec{p}_i = \frac{1}{N_i}\vec{k}_i \tag{4.50}$$

where $N_1$ is an integer. A grid is then constructed in the Brillouin zone from the minicell vectors as follows:

$$\vec{k}_{i_1,i_2,i_3} = i_1\vec{p}_1 + i_2\vec{p}_2 + i_3\vec{p}_3 \qquad i_m = 0, \dots, N_m - 1. \tag{4.51}$$

In this manner the Brillouin zone is split up into a collection of minicells that can also be indexed by $i_1$, $i_2$ and $i_3$ and whose corners are at the points $\vec{k}_{i_1 \pm 1, i_2 \pm 1, i_3 \pm 1}$. Note that here we use the periodicity of the crystal to identify $\vec{k}_{N_1,i_2,i_3}$ with $\vec{k}_{0,i_2,i_3}$ and similarly for the other directions. Each of these minicells can now be split up into six tetrahedra (see figure 6.2) and those we will use for the computation of the transport function. There are four different ways to do this tetrahedral splitting and usually it is done such that the common diagonal is the shortest diagonal in the minicell. Once the splitting is decided the $m-th$ corner of a given tetrahedron, $t$, $t = 1, \dots, 6$ in the minicell indexed by $i_1$, $i_2$ and $i_3$ is given by

$$(j_1, j_2, j_3) = (i_1, i_2, i_3) + (kcut(m,t,1), kcut(m,t,2), kcut(m,t,3)) \tag{4.52}$$

where $kcut(m,t,n)$ takes the values zero or one. If we denote this tetrahedron by $\Delta(i_1, i_2, i_3, t)$ the transport function integral can now be written as follow:

$$\phi^{xx} = \sum_{i_1=0}^{N_1} \sum_{i_2=0}^{N_2} \sum_{i_3=0}^{N_3} \sum_{t=1}^{6} \sum_{k \in \Delta(i_1,i_2,i_3,t)} \mathrm{Tr}\left\{v_k^x \rho_k v_k^x \rho_k\right\} \tag{4.53}$$

In the LMTO computations of the band structure only the irreducible Brillouin zone (IBZ) is used and we get data for the Hamiltonian only at the so called irreducible mesh points.

The points in the irreducible zone are found in the following way. We enumerate all the mesh points in some fashion and then take the first mesh point to be irreducible. The rest of the irreducible mesh points are then found recursively by applying all the group operations of the system to each of the mesh points, if a given operation takes it into an irreducible mesh point (up to a translation by a reciprocal lattice vector) then it is reducible, otherwise we label it as irreducible.

In this fashion we end up with a total of $N_{kp}$ irreducible k-points and for each mesh point in the whole Brillouin zone we get a pointer $kirrptr(i_1, i2, i3)$ whose value is the index of the corresponding irreducible k-point and another pointer $gropptr(i_1, i_2, i_3)$ whose value is the number of the group operation, $\gamma$, that takes the irreducible point to the mesh point, possibly modulo a reciprocal lattice vector.

Let us now consider a given tetrahedron whose corners are $\vec{k}_i$, $i = 1, \dots, 4$. To these four points correspond four or less irreducible mesh points $\vec{k}_i^{irr}$ and we have $\vec{k} = R^{\gamma_i}\vec{k}_i^{irr}$ where $R^{\gamma_i}$ is a rotation matrix corresponding to the group operation $\gamma_i$. The four irreducible k points are said to be an irreducible tetrahedron.

The problem is now how to relate the spectral densities and velocities at the corners in the irreducible tetrahedron to the corresponding quantities at the corners of the real tetrahedron. The Hamiltonian transforms in the following manner [47]:

$$\begin{aligned} H_{l'm'\tau',lm\tau}(R^{\gamma}\vec{k}) &= e^{i\vec{k}\cdot(\vec{R}^g_{\tau'} - \vec{R}^g_{\tau})} \sum_{m_1 m_2} U^{l'}_{m'm_1}(\gamma) H_{l'm_1\hat{g}^{-1}(\tau),lm_2\hat{g}^{-1}(\tau')}(\vec{k}) U^{l*}_{mm_2}(\gamma) \\ &= e^{i\vec{k}\cdot(\vec{R}^g_{\tau'} - \vec{R}^g_{\tau})} \Big( U(\gamma) H_{\hat{g}^{-1}(\tau),\hat{g}^{-1}(\tau')}(\vec{k}) U^{+}(\gamma) \Big)_{l'm',lm} \end{aligned} \tag{4.54}$$

Here $\hat{g}^{-1}$ denotes the operation reciprocal (i.e. in real space) to $\gamma$ plus a possible shift (by a direct lattice vector) for non-symmorphic group. Hence $\hat{g}^{-1}(\tau)$ is the atom corresponding to $\tau$ after the rotation and if the operation does not directly rotate the atom to $\tau$ into $\hat{g}^{-1}(\tau)$ then it must be shifted back to the original cluster by a direct lattice vector given by $R^g_{\tau}$. This shift is responsible for the extra exponential factor in the transformation formula.

We note that the spectral density, $\rho_k$, being essentially the inverse of the Hamiltonian, transforms in the same way as the Hamiltonian but the velocity does not due to the extra exponential factor in the transformation. The velocity is given by the gradient of the Hamiltonian and therefore the velocity matrix in the $\tau', \tau$ sector is given by

$$\begin{aligned} v^x_{\tau',\tau}(R^\gamma\vec{k}) &= \frac{\partial}{\partial(R^\gamma\vec{k})_x}H_{\tau',\tau}(R^\gamma\vec{k}) = \frac{\partial}{\partial k_j}H_{\tau',\tau}(R^\gamma\vec{k})\frac{\partial k_j}{\partial(R^\gamma\vec{k})_x} \\ &= e^{i\vec{k}\cdot(\vec{R}^g_{\tau'}-\vec{R}^g_\tau)}U(\gamma)\left(i[(\vec{R}^g_{\tau'})^j-(\vec{R}^g_\tau)^j]H_{\hat{g}^{-1}(\tau),\hat{g}^{-1}(\tau')}(\vec{k})\right)U^+(\gamma)(R^\gamma)^{-1}_{jx} \\ &+ e^{i\vec{k}\cdot(\vec{R}^g_{\tau'}-\vec{R}^g_\tau)}U(\gamma)\left(v^j_{\hat{g}^{-1}(\tau),\hat{g}^{-1}(\tau')}(\vec{k})\right)U^+(\gamma)(R^\gamma)^{-1}_{jx}. \end{aligned} \tag{4.55}$$

Let us now define the semirotated velocity as:

$$v^{\gamma,x}_{\hat{g}^{-1}(\tau),\hat{g}^{-1}(\tau')}(\vec{k}) = \left(i[(\vec{R}^g_{\tau'})^j-(\vec{R}^g_\tau)^j]H_{\hat{g}^{-1}(\tau),\hat{g}^{-1}(\tau')}(\vec{k}) + v^j_{\hat{g}^{-1}(\tau),\hat{g}^{-1}(\tau')}(\vec{k})\right)(R^\gamma)^{-1}_{jx}. \tag{4.56}$$

Then we can write the rotated velocity in terms of the semirotated velocity as:

$$v^x_{\tau',\tau}(R^\gamma\vec{k}) = e^{i\vec{k}\cdot(\vec{R}^g_{\tau'}-\vec{R}^g_\tau)}U(\gamma)v^{\gamma,x}_{\hat{g}^{-1}(\tau),\hat{g}^{-1}(\tau')}(\vec{k})U^+(\gamma) \tag{4.57}$$

We can now proceed to evaluate the transport function trace at each of the corners in the tetrahedron and to make clear the atomic dependence we write explicitly the atomic labels (repeated indices are summed over):

$$\begin{aligned} \mathrm{Tr}\left\{v^x(\vec{k}_i)\rho(\vec{k}_i)v^x(\vec{k}_i)\rho(\vec{k}_i)\right\} &= \mathrm{Tr}\left\{v^x_{\tau_1\tau_2}(\vec{k}_i)\rho_{\tau_2\tau_3}(\vec{k}_i)v^x_{\tau_3\tau_4}(\vec{k}_i)\rho_{\tau_4\tau_1}(\vec{k}_i)\right\} \\ &= \mathrm{Tr}\Big\{v^{\gamma,x}_{\hat{g}^{-1}(\tau_1)\hat{g}^{-1}(\tau_2)}(\vec{k}^{irr}_i)\rho_{\hat{g}^{-1}(\tau_2)\hat{g}^{-1}(\tau_3)}(\vec{k}^{irr}_i) \\ &\quad \times v^{\gamma,x}_{\hat{g}^{-1}(\tau_3)\hat{g}^{-1}(\tau_4)}(\vec{k}^{irr}_i)\rho_{\hat{g}^{-1}(\tau_4)\hat{g}^{-1}(\tau_1)}(\vec{k}^{irr}_i)\Big\} \\ &= \mathrm{Tr}\left\{v^{\gamma,x}(\vec{k}^{irr}_i)\rho(\vec{k}^{irr}_i)v^{\gamma,x}(\vec{k}^{irr}_i)\rho(\vec{k}^{irr}_i)\right\}. \end{aligned} \tag{4.58}$$

Here we used the cyclicity of the trace to get rid of the Wigner matrices, the exponential factors cancel automatically and in the end we remove the group operation dependence on the dummy atomic labels. Thus we have managed to express the trace at each corner in terms of quantities at the corresponding irreducible k point but the velocity, as we see from equation (4.56), acquires an extra term from the Hamiltonian. We should remark here that since the Wigner matrices and the exponential factors have been canceled independently at each corner of the tetrahedron the individual factors of the trace at each corner do not match with the corresponding factors from the other corners. Thus it would make no sense for instance to linearize each of these factors inside the tetrahedron and try to do the resulting integral analytically. It is the whole expression that is continuous from one corner to the next, not the individual factors. The eigenvalues of the Hamiltonian on the other hand are the same at the real tetrahedron corner and the irreducible corners. Hence if we express the trace in terms of the eigenvalues of the Hamiltonian as we did in the last section the $\alpha$ and $\beta$ terms, evaluated at the irreducible corners but with the semirotated velocities, are continuous from one corner to the next and we are justified in using any approximation we want for those terms individually from the terms involving the eigenvalues. This is quite useful numerically since this means that we do not have to find the Hamiltonian all throughout the Brillouin zone and diagonalize it separately at each mesh point - diagonalization on the irreducible mesh is enough. We also do not need to compute the velocity at each mesh point, we just have to find it on the irreducible mesh and then the semirotated velocity can be generated as needed from the velocity and the Hamiltonian.

Hence we must compute $6 \times N_1 \times N_2 \times N_3$ tetrahedral contributions to the transport function. The computation of the velocity and the diagonalization of the Hamiltonian is just done at the irreducible mesh points which are much fewer. Since each mesh point occurs in a total of six tetrahedra the $\alpha$ and $\beta$ terms are best precomputed before we start summing up all the individual contributions.

## 4.6 Numerical evaluation of $\phi^{\nu\lambda}$

In this section we discuss the numerical computation of the tetrahedral contributions to the transport function. The calculation of the contribution from each tetrahedron involves the numerical evaluation of a triple integral of the form

$$T_{SS} = \sum_{k \in \Delta} \frac{F(k)}{(z - E_{k\alpha})(z - E_{k\gamma})} \qquad \text{or} \qquad T_{OS} = \sum_{k \in \Delta} \frac{F(k)}{(z - E_{k\alpha})(z - E^*_{k\gamma})} \tag{4.59}$$

where $\Delta$ denotes the tetrahedron. The subscripts $SS$ and $OS$ refer to the sign of the imaginary part of the energies in the denominator. In $T_{SS}$ they both have the same sign and in $T_{OS}$ they have the opposite sign. It is useful when doing integrals like these to symmetrize the function $F$ using the same symmetry operations as we use to collapse the whole Brillouin zone down to the irreducible part. Even though we are doing the integral over the whole Brillouin zone and therefore this symmetrization is not really necessary the results will probably be better and less dependent on the choice of tetrahedron splitting of the Brillouin zone minicells. This symmetrization is easily done and is formally given by the equation,

$$F_S(k) = \frac{1}{N_S} \sum_{\sigma} \mathcal{O}_{\sigma} F(k) \tag{4.60}$$

where $N_S$ is the number of symmetry operations and $\sigma$ denotes a symmetry operation with the corresponding operator being $\mathcal{O}_{\sigma}$. In our case here this symmetrization is done right from the start by symmetrizing the combination of the velocity factors in the transport function. So even though we are really computing $\sigma^{xx}$ we would in a cubic system compute $(\sigma^{xx} + \sigma^{yy} + \sigma^{zz})/3$.

The functions $E_{k\alpha}$, $E_{k\gamma}$ and $F(k)$ are of course only known at the corners of the tetrahedron. Let us denote their values at those corners by $\alpha_i$, $\gamma_i$ and $f_i$, $i = 1, 2, 3, 4$ and let $k_i$ denote the coordinate of corner $i$. Then a vector, $k$ inside the tetrahedron can be written on the form,

$$k = k_1 + a(k_2 - k_1) + b(k_3 - k_1) + c(k_4 - k_1) \qquad a, b, c \geq 0, \quad \text{and} \quad a + b + c \leq 1. \tag{4.61}$$

Using linear interpolation on the functions $F$ and $E$ inside the tetrahedron we can write them in terms of $a, b, c$ as follows,

$$F(a, b, c) = f_1 + a(f_2 - f_1) + b(f_3 - f_1) + c(f_4 - f_1) \tag{4.62}$$

$$E_{\alpha}(a, b, c) = \alpha_1 + a(\alpha_2 - \alpha_1) + b(\alpha_3 - \alpha_1) + c(\alpha_4 - \alpha_1) \tag{4.63}$$

It is useful to redefine the energies so as to get rid of the external frequency in the integral.

$$\alpha_i - z \rightarrow \alpha_i, \tag{4.64}$$

and we note that since $z$ is assumed real this does not change the imaginary part of the energies. Now since we use a linear interpolant for the function $F$ the integral will be linear in the values $f_i$ so the answer will be on the form:

$$w_1 f_1 + w_2 f_2 + w_3 f_3 + w_4 f_4 \tag{4.65}$$

where the symbol $w_i$ is called a weight factor for corner $i$.

There are four term that contribute to the transport function:

1. SSDD: The diagonal part ($\alpha = \gamma$) in the SS sector
2. SSOD: The off-diagonal part ($\alpha \neq \gamma$) in the SS sector
3. OSDD: The diagonal part ($\alpha = \gamma$) in the OS sector
4. OSOD: The off-diagonal part ($\alpha \neq \gamma$) in the OS sector

and we will use different methods depending on which contribution we are evaluating. The SSDD integral can be done analytically and that calculation is carried out in appendix E. The other contributions can to some extent be carried out analytically, depending on the degeneracy of the corners on the tetrahedron, but the lion's share of the tetrahedra are in the interior of the irreducible Brillouin zone and have four different irreducible corners and that case has not yielded an analytical solution.We will therefore explore alternative approximations.

1. OSDD: This case can be written in the following form

$$T = \sum_{k \in \Delta} \frac{F(k)}{|z - E_{k\alpha}|^2} = \sum_{k \in \Delta} \frac{F(k)}{\varepsilon_k^2 + \gamma_k^2} = \sum_{k \in \Delta} \frac{F(k)}{\gamma_k} \operatorname{Im} \left( \frac{1}{\varepsilon_k - i\gamma_k} \right) \tag{4.66}$$

   Here we have split the denominator $z - E_{k\alpha}$ into its real and imaginary parts. The imaginary part, $\gamma$ is due to the self energy and since the self energy in the DMFT is momentum independent it is reasonable to expect that $\gamma$ will not depend very strongly on momentum. Hence we propose to approximate the factor $F(k)/\gamma$ by a linear function and then we can simply calculate the integral using the analytical tetrahedron method of Lambin and Vigneron [48]. This way of splitting up the integrand also makes the dependence on the scattering rate evident by factoring it out and in the limit of small scattering rates it is clear that the resulting transport function will scale as the inverse of the scattering rate.

2. SSOD and OSOD: The method used for these two cases are the same. We want to try to reduce this case down to the analytical tetrahedron method and we will do that by identifying the part of the denominator that has greater modulus and then write

$$T = \sum_{k\in\Delta} \frac{F(k)}{(z-E_{k\alpha_1})(z-E_{k\alpha_2})} = \sum_{k\in\Delta} \left(\frac{F(k)}{(z-E_{k\alpha})_{large}}\right) \frac{1}{(z-E_{k\alpha})_{small}}. \quad (4.67)$$

The denominator in the parenthesis has a large modulus and thus the expression in the parentheses will change relatively little in the tetrahedron. We will therefore approximate the expression in the parentheses by a linear function and in that way we have managed to reduce the integral down to a form suitable for the analytical tetrahedron method as we had hoped for.

These methods seem to give quite good results as we can see in §4.9 here below, except for the fact that the OSDD integral sometimes needs to be treated a little differently depending on the behavior of the scattering. The reason for this is that in uncorrelated orbitals the scattering is only due to the hybridization with the correlated orbitals and at high symmetry points in the Brillouin zone some of the uncorrelated orbitals will not aquire any scattering in this manner.. This leads to a pole on the real axis in the spectral density and the transport function will diverge at that point. When this occurs far away from the Fermi-surface the philosophy is that we can simply ignore it knowing that when calculating the transport parameters the transport function will be weighted by a function which is exponentially decreasing away from the Fermi-surface. If, on the other hand this occurs close to the Fermi-surface we must go back and rethink our calculations because the transport function will diverge and there is nothing we can do better numerically to prevent that.

Going back to the calculation of the OSDD case we see by inspecting the formula and our strategy for evaluating it that we are liable to run into problems with divergence even though we are far from any real poles. The reason is that when we write:

$$\frac{1}{\epsilon_k^2+\gamma_k^2} = \frac{1}{\gamma_k}\,\mathrm{Im}\left(\frac{1}{\epsilon_k - i\gamma_k}\right) \quad (4.68)$$

we see that there is a delicate cancellation between the two factors in the limit that $\gamma$ goes to zero. If we however treat these two factors differently in the numerical calculation as we have proposed to do, this cancellation will not occur and we end up with diverging results where there was no divergence in the first place.

This problem was studied in detail with several different strategies for overcoming it such as writing the integral on the following form:

$$T = \sum_{k\in\Delta} \frac{F(k)}{|z-E_{k\alpha}|^2} = \sum_{k\in\Delta} \left(\frac{F(k)}{(z-E_{k\alpha})^*}\right) \frac{1}{(z-E_{k\alpha})} \tag{4.69}$$

and linearize completely the factor in parenthesis and then use the analytical tetrahedron method. Using this method proved problematic, since the switching between methods tended to introduce discontinuities in the results. It seems that the most consistent way to deal with this problem is to add a small artificial broadening to the uncorrelated orbitals but one should still keep in mind that any orbital that is close to the Fermi level will affect the transport properties and must be regarded as correlated in this context and should be assigned some reasonable self energy.

## 4.7 Numerical calculation of the velocity: Method I

The velocity matrix for the k-points in the irreducible Brillouin zone has to be calculated in order to be able to calculate the transport function. Thus we need to calculate the derivatives,

$$v^i_{kpq} = \frac{\partial}{\partial k^i}\epsilon_{kpq}. \tag{4.70}$$

This is done numerically by using the formula,

$$f'(0) \simeq \frac{1}{12}(f(-2) - 8f(-1) + 8f(1) - f(2)). \tag{4.71}$$

Using this formula means of course that we need to know what the neighbors of a given k-point in the irreducible zone are. These neighbors are possibly not inside the irreducible zone so we need to know to what points in the irreducible zone they correspond. This information can be obtained from the German LMTO program although a little modification is necessary in order to do so. The lattice points in the Brillouin zone are given by the equation:

$$\vec{k} = \sum_{j=1}^{3} p_j \frac{\vec{b}_j}{N_j}, \qquad p_j = 0, \ldots, N_j - 1 \tag{4.72}$$

where the vectors $\vec{b}_j$ are the generators of the reciprocal lattice. In terms of these we get,

$$v^i_{kpq} = \frac{\partial}{\partial k^i}\epsilon_{kpq} = \sum_{j=1}^{3} \frac{\partial p^j}{\partial k^i}\frac{\partial}{\partial p^j}\epsilon_{kpq}. \tag{4.73}$$

Using the generators $\vec{a}_i$ of the Bravais lattice and the fact that $\vec{a}_i \cdot \vec{b}_j = 2\pi\delta_{ij}$ we have,

$$p_j = \frac{N_j}{2\pi}\vec{a}_j \cdot \vec{k} \tag{4.74}$$

and thus we get

$$v^i_{kpq} = \sum_{j=1}^{3} \frac{N_j}{2\pi} a^i_j \frac{\partial}{\partial p^j}\epsilon_{kpq}. \tag{4.75}$$

We now define the matrix

$$A_{ij} = N_j a^i_j \tag{4.76}$$

and thus we can write

$$v^i_{kpq} = \frac{1}{2\pi}\sum_{j=1}^{3} A_{ij}\frac{\partial}{\partial p^j}\epsilon_{kpq}. \tag{4.77}$$

The energy is now defined on a grid of integers in terms of the $p$-variables and the derivative is found by using the formula quoted above.

## 4.8 Numerical calculation of the velocity: Method II

There is an alternative way to calculate the velocity which we should mention also. As discussed previously the Hamiltonian is approximated linearly within each tetrahedron and thus if we wanted to be faithful to that strategy the velocity should be taken as constant within each tetrahedron. Thus let us consider a tetrahedron with corners whose coordinates are given by $k_1$, $k_2$, $k_3$ and $k_4$ with $H_1$, $H_2$, $H_3$ and $H_4$ being the corresponding values of the Hamiltonian. Thus inside the tetrahedron the we can represent the momentum and approximate the Hamiltonian as follows:

$$\begin{gathered} k = k_1 + a\Delta k_{21} + b\Delta k_{31} + c\Delta k_{41} \\ H = H_1 + a\Delta H_{21} + b\Delta H_{31} + c\Delta H_{41} \\ a, b, c \geq 0 \quad \text{and} \quad a + b + c \leq 1 \end{gathered} \tag{4.78}$$

where $\Delta k_{ji} = k_j - k_i$ and $\Delta H_{ji} = H_j - H_i$. Let us now define the following vectors:

$$\Delta p_{21} = \frac{\Delta k_{31} \times \Delta k_{41})}{\Delta k_{21} \cdot (\Delta k_{31} \times \Delta k_{41})}, \tag{4.79}$$

$$\Delta p_{31} = \frac{\Delta k_{41} \times \Delta k_{21})}{\Delta k_{21} \cdot (\Delta k_{31} \times \Delta k_{41})} \tag{4.80}$$

$$\Delta p_{41} = \frac{\Delta k_{21} \times \Delta k_{31})}{\Delta k_{21} \cdot (\Delta k_{31} \times \Delta k_{41})}. \tag{4.81}$$

Now we see that we can write

$$a = (k - k_1) \cdot \Delta p_{21} \qquad \text{and} \qquad \vec{\nabla}_k a = \Delta p_{21} \qquad \text{etc.} \tag{4.82}$$

The gradient of the Hamiltonian inside the tetrahedron is therefore given by:

$$\begin{aligned} \vec{\nabla}_k H &= \left(\frac{\partial}{\partial a} H\right) \vec{\nabla}_k a + \left(\frac{\partial}{\partial b} H\right) \vec{\nabla}_k b + \left(\frac{\partial}{\partial c} H\right) \vec{\nabla}_k c \\ &= \Delta H_{21} \Delta p_{21} + \Delta H_{31} \Delta p_{31} + \Delta H_{41} \Delta p_{41} \end{aligned} \tag{4.83}$$

We should note here that this method, although closer in spirit to the approximations that we are making is not used in our calculations for the simple reason that one would then have to compute the velocity for every single tetrahedron in the Brillouin zone. With the other method we only need to compute the full velocity in the irreducible part of the Brillouin zone and then the semirotated velocity in the rest of the Brillouin zone. This would also mean that the cancellation that is described in connection with equation (4.58) would not be possible and we would thus have to carry out a rotation of the spectral density for each different value of the self energy whereas with the other method this is unnecessary.

## 4.9 Testing the methods

Most of the formulas that we have derived in the previous pages have been tested with some simple data using Mathematica. It is however also useful to be able to test the whole formalism on a case that can be calculated using some other means. For that purpose we have created a simple Hamiltonian based on the tight-binding Hamiltonian in a three dimensional cubic lattice. It is given by the following formula:

$$\begin{aligned} H &= \sum_{l=1,2}\sum_{k} c^{+}_{kl}c_{kl}(D_{low}\epsilon_k + E_{low}) + \sum_{k} d^{+}_{k}d_k(D_{high}\epsilon_k + E_{high}) \\ &+ \sum_{l=1,2}\sum_{k}(Vc^{+}_{kl}d_k + V^{*}d^{+}_{k}c_{kl}) \end{aligned} \tag{4.84}$$

with the dispersion relation given by:

$$\epsilon_k = \frac{1}{3}\sum_{i=1}^{3}\cos(ak_i). \tag{4.85}$$

This Hamiltonian describes a doubly degenerate low lying itinerant band of half-width $D_{low}$ coupled to a localized band of half-width $D_{high} < D_{low}$ which we assume lies close to the Fermi-surface. To this we add a frequency and momentum independent scattering, $\Gamma$, in the localized level. This model is a simplified version of what we expect to be dealing with for real Hamiltonians, i.e. a low lying itinerant band hybridizing with a localized correlated orbital close to the Fermi-surface. In figure (4.1) we have displayed

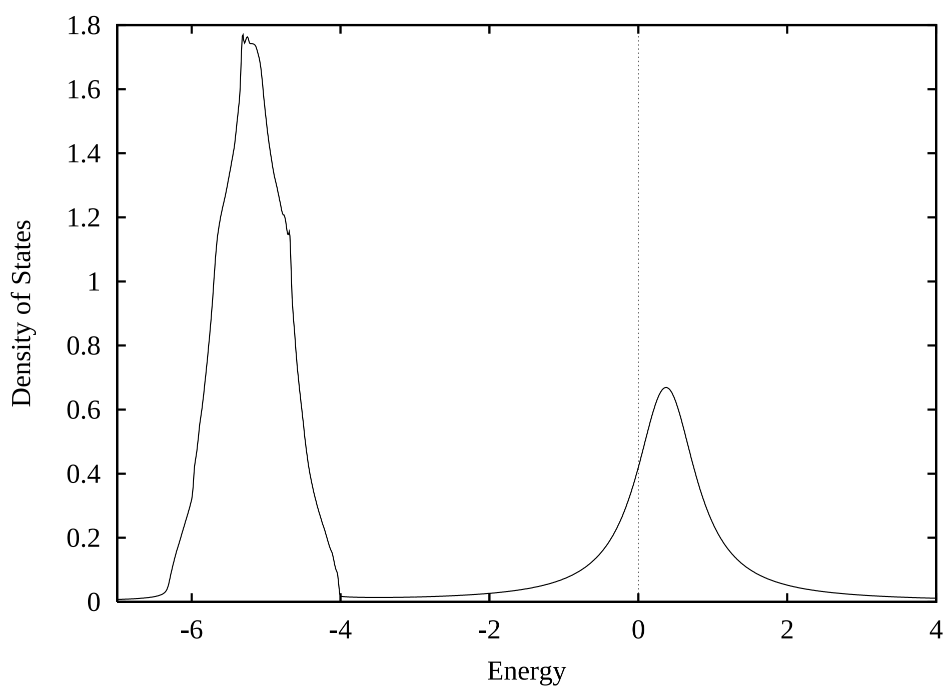


Figure 4.1: The total density of states of the model Hamiltonian. The parameters of the Hamiltonian used are: $E_{low} = -7.0$, $E_{high} = 0$, $\Gamma = 0.5$ and $V = 1.0$.

the DOS for this model corresponding to the parameters, $E_{low} = -7.0$, $E_{high} = 0$, $\Gamma = 0.5$, $V = 1.0$, $D_{low} = 1.0$ and $D_{high} = 0.1$. We can see the low lying band with fairly well defined band edges and then the higher correlated band with longer tails Due to the hybridization the bands are pushed slightly apart and the correlated level transfers a little bit of it's weight to the lower level and vice versa. Note however that for this value of scattering the width of the correlated peak is entirely governed by the magnitude of the scattering and is not due to the inherent width of the band or the hybridization with the itinerant band.

### 4.9.1 Analytical calculation of the transport function

We see that the velocity corresponding to the test Hamiltonian is diagonal and is given by,

$$\hat{v}_k^x = \hat{V}\frac{\partial \epsilon_k}{\partial k^x} \tag{4.86}$$

where $\hat{V}$ is diagonal and equal to the $D_{low}$ in the uncorrelated sector and $D_{high}$ in the correlated sector. The transport function is therefore given by,

$$\begin{aligned} \phi^{xx}(\omega) &= \sum_k \mathrm{Tr}\{\hat{v}_k^x \hat{\rho}_k(\omega)\hat{v}_k^x\hat{\rho}_k(\omega)\} \\ &= \int d\epsilon\, \mathrm{Tr}\{\hat{V}\hat{\rho}(\epsilon,\omega)\hat{V}\hat{\rho}(\epsilon,\omega)\}\left[\sum_k\left(\frac{\partial \epsilon_k}{\partial k^x}\right)^2 \delta(\epsilon-\epsilon_k)\right] \end{aligned} \tag{4.87}$$

On the three dimensional cubic lattice the function in brackets can be calculated accurately using Fourier transforms, and then the transport function can be calculated from there using numerical integration over $\epsilon$. In order to be able to test each part of the integration code is proves useful to expand the trace in terms of the Green's functions as we did earlier in the chapter and then the contribution from each term can be compared to the numerical code. We note that in order to make exact the correspondence between the analytic calculation and the numerical calculation we need to do same kind of diagonalization as we did in the numerical case. In figure (4.2) we have displayed the transport function for the test Hamiltonian in the region around the position of the correlated level. We do not compute the transport function around the position of the uncorrelated level since we did not assign any scattering to that orbital. As we can see the Brillouin zone integration method agrees very nicely with the exact calculation

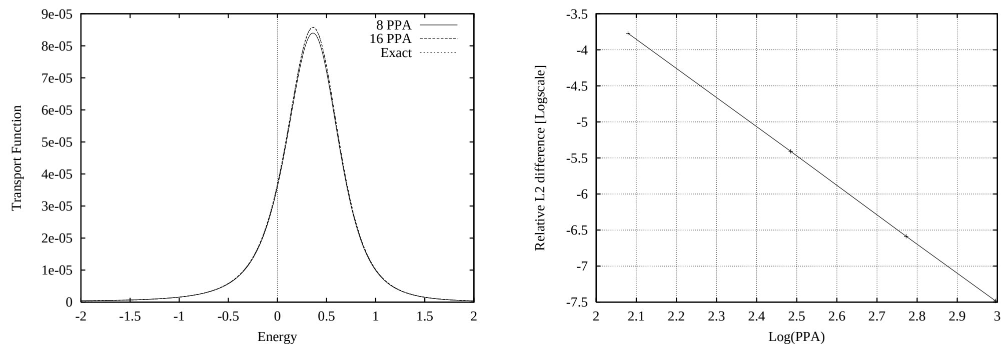


Figure 4.2: The transport function, $\phi$, calculated using the exact solution and the Brillouin zone integration with 8 and 16 points per axis. The parameters of the Hamiltonian used are: $E_{low} = -7.0$, $E_{high} = 0$, $\Gamma = 0.5$, $V = 1.0$, $D_{low} = 1.0$ and $D_{high} = 0.1$. Also shown is the relative $L_2$ deviation, $||\phi - \phi_{exact}||_2/||\phi_{exact}||_2$ computed over this interval.

and hardly any difference can be seen when using integration mesh corresponding to 16 points per axis. We have also displayed the relative $L_2$ error as a function of the number of points per axis and as we can see the error decreases here as the inverse fourth power of the number of points per axis.

In figure (4.3) where each of the four contributions to the transport function are displayed we can see that the convergence is equally good for each contribution. We also not that the contributions from the SS sector are almost mirror images of the contributions from the OS sector and therefore the final result depends on delicate cancellation between contributions from theses sectors.

The transport function diverges of course in the limit of zero scattering and we expect that it will go as $1/\Gamma$ for small values of $\Gamma$. Thus if we scale the transport function with the scattering then the scaled transport function should be approximately independent of the scattering, in fact one would expect that the result should not be very much different from the bare transport function computed with a constant lifetime equal to $1/2\pi$. In figures 4.4 we have displayed the scaled transport function using several values of $\Gamma$ and two different bandwidths for the correlated orbital. As we can see the scaling in the center of the broad band is quite good whereas the scaling for the narrow band is much worse. The reason why we see deviations from the scaling behavior is of course due to the broadening effect of the scattering. In the center of a broad featureless band the scattering does not alter the density of states significantly and in that case one can

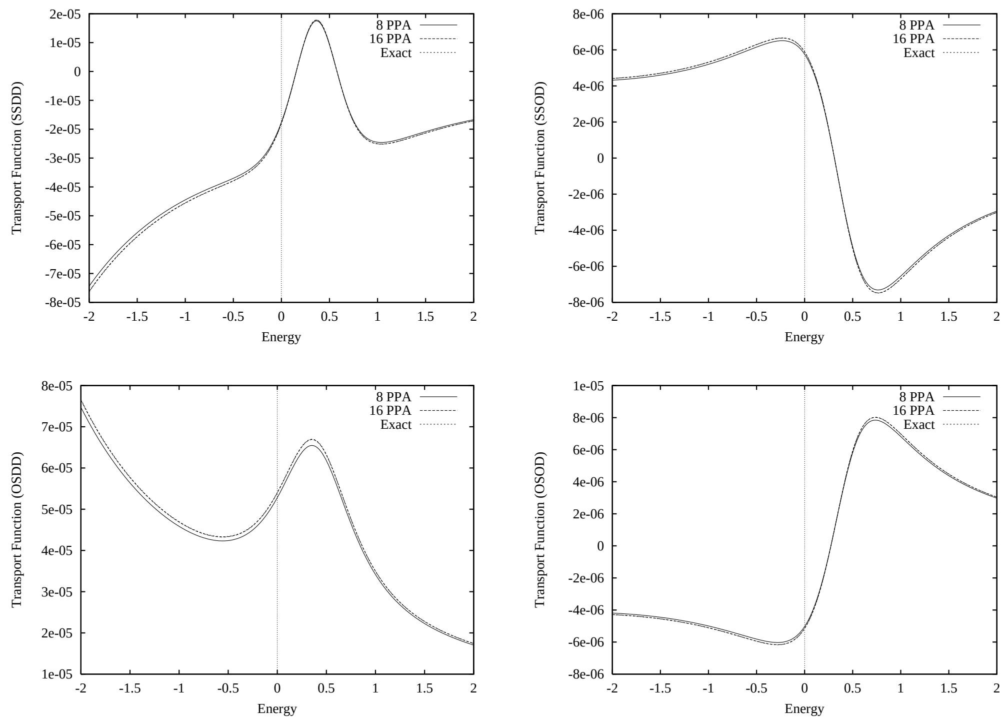


Figure 4.3: The four contributions to the transport function, $\phi$, calculated using the exact solution and the Brillouin zone integration with 8 and 16 points per axis. The parameters of the Hamiltonian used are the same as in figure (4.2).

expect that the scaling behavior would be manifest. However in narrow bands and close to band edges the scattering dramatically alters the density of states, creating long tails that extend outside the band and there the transport function will not exhibit scaling behavior. In fact outside the bands we should expect exactly the opposite scaling – the transport function will decrease with the value of the scattering.

Finally in figure 4.5 we have displayed the scaled transport function along with the bare transport function. As expected in light of the previous arguments we see that for the broad band the scaled transport function agrees fairly well with the bare one but for the narrow band the quantitative agreement is much worse.

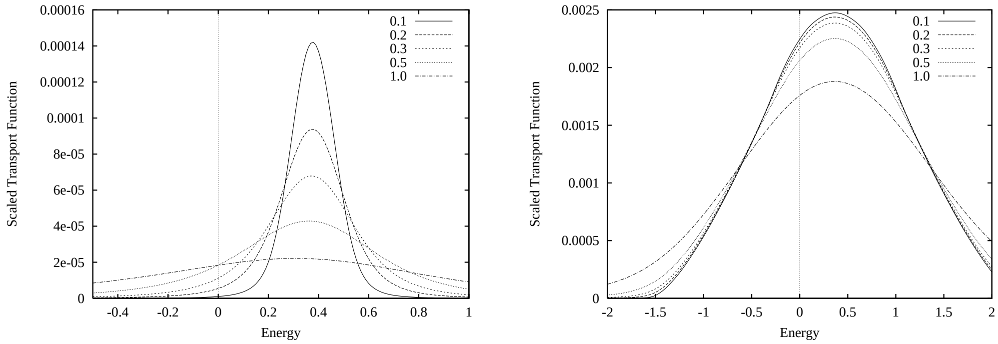


Figure 4.4: The scaled transport functions, $\Gamma\phi$, calculated with 16 PPA. In the left figure the parameters of the Hamiltonian are the same as in figure (4.2) but in the left figure we have $D_{high} = 2.0$.

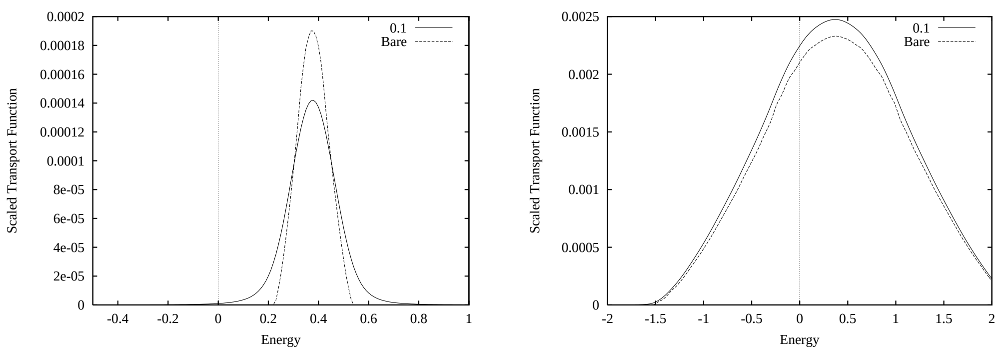


Figure 4.5: The scaled transport functions, $\Gamma\phi$, calculated with 16 PPA. compared with the bare transport function using a lifetime of $1/2\pi$. The parameters of the Hamiltonian are the same as used in figure 4.4.

# Chapter 5

# Transport in Real Multiband Systems: Non-Orthogonal Case

## 5.1 Introduction

In this chapter we will extend the discussion of chapter 4 to Hamiltonians defined in nonorthogonal bases. The reason why this is important is due to the fact that quite frequently the basis of wavefunctions used in the solution of the electronic structure problems is composed of localized atomic-like wavefunctions. These wavefunctions are by choice not orthogonal and although one could in principle construct an orthogonal basis by using the Gram-Schmidt method one would quite likely end up with a basis that is delocalized and the strong correlations that were local in the orthogonal basis become non-local and much harder to deal with.

The best way to start familiarizing oneself with the formalism of band structure calculations is to consider the problem in real space, where we construct localized wavefunctions $\chi_l(r)$ for each atom (here l is a multi-index representing angular momentum, spin and individual atoms within the unit cell) and consider the matrix elements of the Hamiltonian in the basis of these wavefunctions and their translations throughout the crystal lattice. Thus the wavefunctions basis consists of the $\{\chi_{lR}\}$ where $\chi_{lR}(r) = \chi_l(r-R)$ where $R$ is a lattice translation vector. If we denote the states of these wavefunctions by $|\chi_{lR}\rangle$ then we look at the matrix elements of the Hamiltonian and self energy:

$$H_{ll'}(R-R') = \langle\chi_{lR}|H|\chi_{l'R'}\rangle \qquad \text{and} \qquad \Sigma_{ll'}(R-R') = \langle\chi_{lR}|\Sigma|\chi_{l'R'}\rangle. \tag{5.1}$$

In addition we have a matrix of overlaps due to the nonorthogonality of the basis:

$$O_{ll'}(R-R') = \langle\chi_{lR}|\chi_{l'R'}\rangle. \tag{5.2}$$

As we have indicated the matrix elements depend only on the relative distance $t = R - R'$ and thus we can write our matrix elements in terms of $t$. These matrices elements are given to us in the Fourier transformed form,

$$H_{ll'}(k) = \sum_t e^{ikt} H_{ll'}(t) \tag{5.3}$$

etc. Similarly we can go back:

$$H_{ll'}(t) = \sum_k e^{-ikt} H_{ll'}(k). \tag{5.4}$$

In our calculations we assume that the correlations are local and lead to a local self energy within the dynamical mean field theory and thus $\Sigma_{ll'}(t) = \Sigma_{ll'}\delta_{t,0}$. So let us assume that the self energy is given by a local operator which is diagonal in the space of orbitals, and simply consist of multiplying the state by a given complex number, $\Gamma_l$. Then we have

$$\Sigma_{ll'}(t) = \Gamma_l \delta_{ll'} \delta_{t,0} \langle \chi_{l0} | \chi_{l0} \rangle. = \Gamma_l \delta_{ll'} \delta_{t,0} O_{ll}(0). \tag{5.5}$$

When we Fourier transform we end up with a momentum independent self energy

$$\Sigma_{ll'}(k) = \Gamma_l \delta_{ll'} O_{ll}(0) = \Gamma_l \delta_{ll'} \sum_k O_{ll}(k). \tag{5.6}$$

This equation is important because it tells us how to scale the self energy when it is added to the Hamiltonian. We can in fact also scale both the overlap matrix and the Hamiltonian in such a way that the diagonal on-site matrix elements of the overlap matrix are equal to 1.0. This we can obtain by defining:

$$O_l = \sum_k O_{ll}(k) \tag{5.7}$$

and then scaling the matrix elements such that

$$H_{ll'}(k) \longrightarrow \frac{H_{ll'}(k)}{\sqrt{O_l O_{l'}}} \qquad \text{and} \qquad O_{ll'}(k) \longrightarrow \frac{O_{ll'}(k)}{\sqrt{O_l O_{l'}}}. \tag{5.8}$$

This scaling has of course no effect on the actual calculations but makes the connection between the matrix elements of the Hamiltonian and the actual energy eigenvalues clearer.

## 5.2 Many Body Theory in Nonorthogonal Bases

Our starting point here is a representation of the kinetic term of the Hamiltonian in an orthogonal basis, $\{|i\rangle\}$ and we assume that this basis is related to the non-orthogonal basis, $\{|\alpha\rangle\}$ by the transformation matrix:

$$|i\rangle = \sum_\alpha |\alpha\rangle S_{\alpha i} \qquad \text{and} \qquad \langle i| = \sum_\alpha \langle\alpha| S^*_{\alpha i} = \sum_\alpha S^+_{i\alpha}\langle\alpha| \tag{5.9}$$

The Hamiltonian is now given by:

$$H = \sum_{ij} \langle i|H|j\rangle c_i^+ c_j = \sum_{ij\alpha\beta} S^+_{i\alpha}\langle\alpha|H|\beta\rangle S_{\beta j} c_i^+ c_j = \sum_{\alpha\beta} H_{\alpha\beta} c_\alpha^+ c_\beta. \tag{5.10}$$

The last term in the equation above is a requirement that we place on the creation and destruction operators in the non-orthogonal basis and thus we find that:

$$c_\alpha^+ = \sum_i c_i^+ S^+_{i\alpha} \qquad \text{and} \qquad c_\alpha = \sum_j S_{\alpha j} c_j. \tag{5.11}$$

The non-orthogonality of the basis is encoded in the overlap matrix, $O_{\alpha\beta} = \langle\alpha|\beta\rangle$ and this matrix can be related to the transformation matrix, $S$ in the following manner

$$\delta_{ij} = \langle i|j\rangle = \sum_{\alpha\beta} S^+_{i\alpha}\langle\alpha|\beta\rangle S_{\beta j} = \sum_{\alpha\beta} S^+_{i\alpha} O_{\alpha\beta} S_{\beta j} \tag{5.12}$$

Therefore we see that the overlap matrix is given by:

$$O = (SS^+)^{-1}. \tag{5.13}$$

We should note here that the creation operator $c_\alpha^+$ does not create a particle in the state $|\alpha\rangle$ when acting on the vacuum, since as we see

$$c_\alpha^+|0\rangle = \sum_i c_i^+ S^+_{i\alpha}|0\rangle = \sum_i |i\rangle S^+_{i\alpha} = \sum_{i\beta} |\beta\rangle S_{\beta i} S^+_{i\alpha} = \sum_\beta |\beta\rangle O^{-1}_{\beta\alpha}. \tag{5.14}$$

It is however worth noting that this state has unit overlap with the state $|\alpha\rangle$ and zero overlap with all of the other basis-states! The commutation relationship of these operators are the same as for regular Fermi operators except that we get:

$$\{c_\alpha^+, c_\beta\} = \sum_{ij} S_{\beta j}\{c_i^+, c_j\} S^+_{i\alpha} = S_{\beta i} S^+_{i\alpha} = O^{-1}_{\beta\alpha} \tag{5.15}$$

Let us finally obtain the expression for the Green's function in the non orthogonal basis:

$$G_{\alpha\beta}(\tau) = -\langle c_\alpha(\tau) c_\beta^+(0)\rangle. \tag{5.16}$$

The easiest way to calculate this Green's function is by looking at the Lagrangian for the system in the orthogonal basis and then simply transform it into the non-orthogonal one. We have (summation over repeated indices implied):

$$\begin{aligned} \mathcal{L} &= c_i^+ \frac{\partial}{\partial\tau} c_i - c_i^+ H_{ij} c_j \\ &= S_{i\beta}^{-1} c_\alpha^+ \frac{\partial}{\partial\tau} c_\beta (S^+)_{\alpha i}^{-1} - c_\alpha^+ H_{\alpha\beta} c_\beta \\ &= c_\alpha^+ O_{\alpha\beta} \frac{\partial}{\partial\tau} c_\beta - c_\alpha^+ H_{\alpha\beta} c_\beta. \end{aligned} \tag{5.17}$$

The free Matsubara Green's function can now be obtained by simply Fourier transforming the operators in the Lagrangian and then the inverse of the Green's function, $G_{\alpha\beta}^0(i\omega)$ is simply the term multiplying $c_\alpha^+ c_\beta$. Thus we obtain

$$G_{\alpha\beta}^0(\omega) = [i\omega O - H]_{\alpha\beta}^{-1}. \tag{5.18}$$

The renormalized Green's function is now obtained just as in the orthogonal case by adding a self energy to the Hamiltonian and thus

$$G(i\omega) = [i\omega O - H - \Sigma]. \tag{5.19}$$

We should remark here that these Green's function do not share the same properties as their cousins in the orthogonal bases do and in particular the total density is not given by trace of $G(\tau = 0^-)$. To see that we go back to the orthogonal basis where we know how things work and write the density operator as:

$$\rho = \sum_i c_i^+ c_i = \sum_{i\alpha\beta} S_{i\beta}^{-1} c_\alpha^+ c_\beta (S^+)_{\alpha i}^{-1} = \sum_{\alpha\beta} O_{\alpha\beta} c_\alpha^+ c_\beta. \tag{5.20}$$

Thus the total density of electrons in the system is:

$$n_{tot} = \langle\rho\rangle = \sum_{\alpha\beta} O_{\alpha\beta} \langle c_\alpha^+ c_\beta\rangle = \sum_{\alpha\beta} G_{\beta\alpha}(\tau = 0^-) O_{\alpha\beta} \tag{5.21}$$

We should note in particular that this means that there seems to be no good way of assigning a density to a particular orbital in the non orthogonal case.

## 5.3 Transport Calculation

Now that we know a little bit about many body theory in non orthogonal bases we can turn to the calculation of the transport function. At first one might be tempted to simply use the old expression:

$$\phi^{\mu\nu}(\epsilon) = \mathrm{Tr}\{v^{\mu}\rho(\epsilon)v^{\nu}\rho(\epsilon)\} \tag{5.22}$$

where the velocity is as before given by the relation:

$$\vec{v}_{\alpha\beta} = \vec{\nabla} H_{\alpha\beta}. \tag{5.23}$$

The following exercise will however convince us that this is not quite the correct expression for the velocity and will also point the way to the correct formula. Let us therefore consider the effect of changing the zero of energy in the Hamiltonian and moving it up by $\epsilon_0$. The way this should affect the transport function is simply by shifting it rigidly up the energy axis. More concretely let us denote the original Hamiltonian by $H$ and the shifted Hamiltonian by $H'$. Due to the overlap we have $H' = H + \epsilon_0 O$. Now omitting the axis labels and defining $u = \vec{\nabla}_k O_k$ we have

$$\begin{aligned} \phi'(\epsilon) &= \mathrm{Tr}\{v'\rho'(\epsilon)v'\rho'(\epsilon)\} \\ &= \mathrm{Tr}\{(v+\epsilon_0 u)\rho(\epsilon-\epsilon_0)(v+\epsilon_0 u)\rho(\epsilon-\epsilon_0)\} \\ &= \phi(\epsilon-\epsilon_0) + \mathrm{Tr}\{\epsilon_0 u \rho(\epsilon-\epsilon_0)(2v+\epsilon_0 u)\rho(\epsilon-\epsilon_0)\}. \end{aligned} \tag{5.24}$$

Thus we see that the effect of this change was not just a simple translation of the transport function but in addition we have now an extra term. We see from this however that if we define the velocity in the non orthogonal basis as:

$$\vec{v}^{no}_k(\epsilon) = \vec{\nabla}_k (H - \epsilon O) = \vec{v} - \epsilon \vec{u} \tag{5.25}$$

then the transport function will behave as expected. Let us now derive this expression more rigorously. We follow the exposition of [46] which gives gauge-theoretic derivation of the heat current for strongly correlated systems. The starting point for this derivation is the action for the system which in the non orthogonal basis is given by:

$$S = \int d\tau \mathcal{L}(\tau) = \int d\tau \sum_k c^+_{k\alpha}\left(O_{k\alpha\beta}\overleftrightarrow{\partial_\tau} + H_{k\alpha\beta}\right)c_{k\beta}. \tag{5.26}$$

Here $\overleftrightarrow{\partial_\tau} = \frac{1}{2}(\overrightarrow{\partial_\tau} - \overleftarrow{\partial_\tau})$ denotes the anti-symmetrized time derivative. The particle and heat currents can now be obtained by considering the invariance of the action under local phase transformation and local translations in time respectively. In the orthogonal case one is lead to the following expression for the currents:

$$\vec{j} = -\frac{\partial H[\vec{A}_p]}{\partial \vec{A}_p}|_{\vec{A}_p=0} \qquad \text{and} \qquad \vec{Q} = -\frac{\partial H[\vec{A}_h]}{\partial \vec{A}_p}|_{\vec{A}_h=0} \tag{5.27}$$

where $\vec{A}_p$ and $\vec{A}_h$ are gauge fields conjugate to the currents and $H[\vec{A}_p]$ and $H[\vec{A}_h]$ denote the gauged Hamiltonian, i.e. the Hamiltonian with the replacements $\vec{k} \to \vec{k} - \vec{A}_p$ and $\vec{k} \to \vec{k} + \vec{A}_h \overleftrightarrow{\partial_\tau}$ respectively[1] This replacement is performed in both the kinetic and the interaction terms but not in the field operators. In our case however the overlap matrix appearing in the action depends also on momentum and therefore the proper generalization of the currents to non orthogonal basis will also take the overlap matrix into account. Thus we obtain:

$$\vec{j} = -\frac{\partial (O[\vec{A}_p]\overleftrightarrow{\partial_\tau} + H[\vec{A}_p])}{\partial \vec{A}_p}|_{\vec{A}_p=0} \qquad \text{and} \qquad \vec{Q} = -\frac{\partial (O[\vec{A}_h]\overleftrightarrow{\partial_\tau} + H[\vec{A}_h])}{\partial \vec{A}_h}|_{\vec{A}_h=0} \tag{5.28}$$

Performing these operations lead to the following expressions:

$$\begin{aligned} \vec{j} &= \sum_{k\alpha\beta} c^+_{k\alpha} \left( \vec{\nabla}_k O_{\alpha\beta} \overleftrightarrow{\partial_\tau} + \vec{\nabla}_k H_{\alpha\beta} \right) c_{k\beta} \\ &= \sum_{k\alpha\beta} c^+_{k\alpha} \left( \vec{u}_{\alpha\beta} \overleftrightarrow{\partial_\tau} + \vec{v}_{\alpha\beta} \right) c_{k\beta} \end{aligned} \tag{5.29}$$

$$\begin{aligned} \vec{Q} &= \sum_{k\alpha\beta} c^+_{k\alpha} \left( -\vec{\nabla}_k O_{\alpha\beta} \left( \overleftrightarrow{\partial_\tau} \right)^2 - \vec{\nabla}_k H_{\alpha\beta} \overleftrightarrow{\partial_\tau} \right) c_{k\beta} \\ &= \sum_{k\alpha\beta} c^+_{k\alpha} \left( -\vec{u}_{\alpha\beta} \left( \overleftrightarrow{\partial_\tau} \right)^2 - \vec{v}_{\alpha\beta} \overleftrightarrow{\partial_\tau} \right) c_{k\beta} \end{aligned} \tag{5.30}$$

Let us now define the following operators:

$$B^{(n)}_{\alpha\beta} = (-1)^n c^+_\alpha \left( \overleftrightarrow{\partial_\tau} \right)^n c_\beta = \frac{1}{2^n} \sum_{p=0}^{n} \binom{n}{p} (-1)^p \left( c^+_\alpha \right)^{(n-p)} c^{(p)}_\beta \tag{5.31}$$

[1] Note that there is a plus for the second replacement instead of a minus as in [46]. This is due to the fact that here we are using complex time $\tau = it$.

The currents can then be written as:

$$\vec{j} = \sum_{k\alpha\beta} \left( \vec{v}_{\alpha\beta} B^{(0)}_{\alpha\beta} - \vec{u}_{\alpha\beta} B^{(1)}_{\alpha\beta} \right) \tag{5.32}$$

$$\vec{Q} = \sum_{k\alpha\beta} \left( \vec{v}_{\alpha\beta} B^{(1)}_{\alpha\beta} - \vec{u}_{\alpha\beta} B^{(2)}_{\alpha\beta} \right) \tag{5.33}$$

To obtain the transport coefficients we must now calculate the following current-current correlation functions, sum over momentum and repeated orbital indices implied:

$$\begin{aligned}
\langle j^\mu(\tau) j^\nu(0) \rangle &= v^\mu_{\alpha\beta} v^\nu_{\gamma\delta} \langle B^{(0)}_{k\alpha\beta}(\tau) B^{(0)}_{k\gamma\delta}(0) \rangle - v^\mu_{\alpha\beta} u^\nu_{\gamma\delta} \langle B^{(0)}_{k\alpha\beta}(\tau) B^{(1)}_{k\gamma\delta}(0) \rangle \\
&\quad - u^\mu_{\alpha\beta} v^\nu_{\gamma\delta} \langle B^{(1)}_{k\alpha\beta}(\tau) B^{(0)}_{k\gamma\delta}(0) \rangle + u^\mu_{\alpha\beta} u^\nu_{\gamma\delta} \langle B^{(1)}_{k\alpha\beta}(\tau) B^{(1)}_{k\gamma\delta}(0) \rangle \qquad (5.34) \\
\langle j^\mu(\tau) Q^\nu(0) \rangle &= v^\mu_{\alpha\beta} v^\nu_{\gamma\delta} \langle B^{(0)}_{k\alpha\beta}(\tau) B^{(1)}_{k\gamma\delta}(0) \rangle - v^\mu_{\alpha\beta} u^\nu_{\gamma\delta} \langle B^{(0)}_{k\alpha\beta}(\tau) B^{(2)}_{k\gamma\delta}(0) \rangle \\
&\quad - u^\mu_{\alpha\beta} v^\nu_{\gamma\delta} \langle B^{(1)}_{k\alpha\beta}(\tau) B^{(1)}_{k\gamma\delta}(0) \rangle + u^\mu_{\alpha\beta} u^\nu_{\gamma\delta} \langle B^{(1)}_{k\alpha\beta}(\tau) B^{(2)}_{k\gamma\delta}(0) \rangle \qquad (5.35) \\
\langle Q^\mu(\tau) Q^\nu(0) \rangle &= v^\mu_{\alpha\beta} v^\nu_{\gamma\delta} \langle B^{(1)}_{k\alpha\beta}(\tau) B^{(1)}_{k\gamma\delta}(0) \rangle - v^\mu_{\alpha\beta} u^\nu_{\gamma\delta} \langle B^{(1)}_{k\alpha\beta}(\tau) B^{(2)}_{k\gamma\delta}(0) \rangle \\
&\quad - u^\mu_{\alpha\beta} v^\nu_{\gamma\delta} \langle B^{(2)}_{k\alpha\beta}(\tau) B^{(1)}_{k\gamma\delta}(0) \rangle + u^\mu_{\alpha\beta} u^\nu_{\gamma\delta} \langle B^{(2)}_{k\alpha\beta}(\tau) B^{(2)}_{k\gamma\delta}(0) \rangle \qquad (5.36)
\end{aligned}$$

Note here that we have already taken into account that the correlation functions are diagonal in momentum and thus one of the dummy momentum indices is gone. We must now evaluate the correlation functions:

$$\Gamma^{mn}_{k\alpha\beta\gamma\delta}(\tau) = \langle B^{(m)}_{k\alpha\beta}(\tau) B^{(n)}_{k\gamma\delta} \rangle \tag{5.37}$$

and that we do to lowest order by evaluating a single Feynman diagram:[2]

$$
\begin{aligned}
\Gamma^{mn}_{k\alpha\beta\gamma\delta}(\tau) &= \frac{1}{2^{m+n}}\sum_{p=0}^{m}\sum_{q=0}^{n}\binom{m}{p}\binom{n}{q}(-1)^{p+q} \\
&\quad\times\left\langle \left(c^{+}_{\alpha}\right)^{(m-p)}(\tau)c^{(p)}_{\beta}(\tau)\left(c^{+}_{\gamma}\right)^{(n-q)}c^{(q)}_{\delta}\right\rangle \\
&= \frac{1}{2^{m+n}}\sum_{p=0}^{m}\sum_{q=0}^{n}\binom{m}{p}\binom{n}{q}(-1)^{p+q} \\
&\quad\times\left\langle \left(c^{+}_{\alpha}\right)^{(m-p)}(\tau)c^{(q)}_{\delta}\right\rangle\left\langle c^{(p)}_{\beta}(\tau)\left(c^{+}_{\gamma}\right)^{(n-q)}\right\rangle \\
&= \frac{1}{2^{m+n}}\sum_{p=0}^{m}\sum_{q=0}^{n}\binom{m}{p}\binom{n}{q}(-1)^{p+q} \\
&\quad\times(-1)^{q}G^{(m-p+q)}_{\delta\alpha}(-\tau)(-1)^{n-q+1}G^{(n-q+p)}_{\beta\gamma}(\tau) \\
&= \int d\epsilon d\epsilon' \rho_{k\beta\gamma}(\epsilon)\rho_{k\delta\alpha}(\epsilon')\frac{1}{2^{m+n}}\sum_{p=0}^{m}\sum_{q=0}^{n}\binom{m}{p}\binom{n}{q}\epsilon^{n-q+p}(\epsilon')^{m-p+q} \\
&= \int d\epsilon d\epsilon' \rho_{k\beta\gamma}(\epsilon)\rho_{k\delta\alpha}(\epsilon')e^{(\epsilon'-\epsilon)\tau}f(-\epsilon)f(\epsilon')\left(\frac{\epsilon+\epsilon'}{2}\right)^{m+n} \qquad (5.38)
\end{aligned}
$$

Let us now define the transport function as:

$$\phi^{\mu\nu}(\epsilon,\epsilon') = \sum_{k}\mathrm{Tr}\left\{\left[v^{\mu}_{k} - \left(\frac{\epsilon+\epsilon'}{2}\right)u^{\mu}_{k}\right]\rho_{k}(\epsilon)\left[v^{\nu}_{k} - \left(\frac{\epsilon+\epsilon'}{2}\right)u^{\nu}_{k}\right]\rho_{k}(\epsilon')\right\} \qquad (5.39)$$

Then we can write the current-current correlation functions as

$$
\begin{aligned}
\langle j^{\mu}(\tau)j^{\nu}(0)\rangle &= \int d\epsilon d\epsilon' \phi^{\mu\nu}(\epsilon,\epsilon')e^{(\epsilon'-\epsilon)\tau}f(-\epsilon)f(\epsilon') \qquad (5.40)\\
\langle j^{\mu}(\tau)j^{\nu}(0)\rangle &= \int d\epsilon d\epsilon' \phi^{\mu\nu}(\epsilon,\epsilon')e^{(\epsilon'-\epsilon)\tau}f(-\epsilon)f(\epsilon')\left(\frac{\epsilon+\epsilon'}{2}\right) \qquad (5.41)\\
\langle j^{\mu}(\tau)j^{\nu}(0)\rangle &= \int d\epsilon d\epsilon' \phi^{\mu\nu}(\epsilon,\epsilon')e^{(\epsilon'-\epsilon)\tau}f(-\epsilon)f(\epsilon')\left(\frac{\epsilon+\epsilon'}{2}\right)^{2} \qquad (5.42)
\end{aligned}
$$

For simplicity let us now symmetrize these functions with respect to the indices $\mu$ and $\nu$. The symmetrized transport function will then be real, due to the cyclicity of the trace and the hermiticity of the matrices appearing in the trace. It is now a simple matter to obtain the retarded version of the symmetrized correlation functions and that calculation proceeds exactly as before in §4.2. We should note here that the what we usually refer to as the transport function is the value of $\phi$ on the diagonal, i.e.

$$\phi^{\mu\nu}(\epsilon) = \phi^{\mu\nu}(\epsilon,\epsilon) \qquad (5.43)$$

---

[2]See Appendix C for a discussion on the Green's function and its derivatives.

and this function is of course real and we don't need any symmetrization. It is only when the two arguments are not equal that we need to symmetrize to be able to simplify the retarded version of the correlation function.

## 5.4 Transport function calculation

We see from the previous section that the main task is the evaluation of the transport function, i.e. the computation of the Brillouin zone integral. This calculation is almost exactly the same as discussed in §4.3 and §4.6 but since we are dealing with a non orthogonal basis it is worth commenting on the numerical diagonalization of the Hamiltonian. The eigenvalue problems that we have to solve are the following:

$$H_{\alpha\beta}\Psi_{\beta}^{R,p} = E^p O_{\alpha\beta}\Psi_{\beta}^{R,p} \qquad \text{and} \qquad \Psi_{\alpha}^{L,p} H_{\alpha\beta} = E^p \Psi_{\alpha}^{L,p} O_{\alpha\beta}. \tag{5.44}$$

We should note here that we are now solving the Hamiltonian which includes the self energy so the Hamiltonian is no longer Hermitian but the overlap matrix is of course Hermitian. The strategy is to reduce this problem to a regular eigenvalue problem and in principle one could simply find the inverse of the overlap matrix and calculate the matrix representation of the Hamiltonian, $\hat{H}$ and then solve the regular eigenvalue problem. A better solution is to use the fact that the overlap matrix is both Hermitian and positive definite and thus we can use Cholesky decomposition and write:

$$O = U^{+}U \tag{5.45}$$

where $U$ is an upper triangular matrix. Now $U$ can be inverted quite efficiently, so let

$$B = U^{-1}. \tag{5.46}$$

We now define the transformed Hamiltonian as

$$H' = B^{+}HB \tag{5.47}$$

and then solve the regular left and right eigenvalue problems for this matrix. If we denote those eigenvectors by $\bar{v}^L$ and $\bar{v}^R$ then our back-transformed eigenvectors are given by

$$\bar{v}^L B^{+} \qquad \text{and} \qquad B\bar{v}^R \tag{5.48}$$

We should note that the left and the right eigenvectors corresponding to different eigenvalues are orthogonal in the following sense:

$$\Psi_\alpha^{L,p} O_{\alpha\beta} \Psi_\beta^{R,p'} = 0 \tag{5.49}$$

when $p \neq p'$. We can choose to normalize them in such a way that the equation above becomes:

$$\Psi_\alpha^{L,p} O_{\alpha\beta} \Psi_\beta^{R,p'} = \delta_{pp'}. \tag{5.50}$$

This is easily seen considering the following:

$$\Psi_\alpha^{L,p} H_{\alpha\beta} \Psi_\beta^{R,p'} = E^p \Psi_\alpha^{L,p} O_{\alpha\beta} \Psi_\beta^{R,p'} = E^{p'} \Psi_\alpha^{L,p} O_{\alpha\beta} \Psi_\beta^{R,p'} \tag{5.51}$$

and thus if $p \neq p'$ we arrive at the conclusion above. Let us now define the eigenvector matrices $A^L$ and $A^R$ such that:

$$A_{p,\alpha}^L = \Psi_\alpha^{L,p} \qquad \text{and} \qquad A_{\alpha,p}^L = \Psi_\alpha^{P,p} \tag{5.52}$$

i.e. the rows of $A^L$ are the left eigenvectors and the columns of $A^R$ are the right eigenvectors. Then we see that $A^L O A^R$ equals the identity matrix. It is now easy to see by inspection that the Hamiltonian can be written on the form:

$$H = OA^R E A^L O \tag{5.53}$$

where $E$ is a diagonal matrix of eigenvalues. The Green's function can therefore be written as:

$$\begin{aligned} G(z) &= [zO - H]^{-1} = [zO - OA^R E A^L O]^{-1} \\ &= [OA^R (zI - E) A^L O]^{-1} = [A^L O]^{-1} [zI - E]^{-1} [OA^R]^{-1} \\ &= A^R [zI - E]^{-1} A^L. \end{aligned} \tag{5.54}$$

Here $z$ can be any complex value outside the real axis. We note of course that the self energy and therefore the Hamiltonian depends on $z$ and thus both the eigenvectors and eigenvalues depend on $z$. In particular we can consider $z = \omega + i0$ in which case we obtain the retarded Green's function and from there we get the spectral density:

$$\begin{aligned} \rho(\omega) &= \frac{-1}{2\pi i} \left\{ G^R(\omega) - \left(G^R\right)^+ \right\} \\ &= \frac{-1}{2\pi i} \left\{ A^R [\omega I - E]^{-1} A^L - \left(A^L\right)^+ [\omega I - E^+]^{-1} \left(A^R\right)^+ \right\}. \end{aligned} \tag{5.55}$$

Putting this into the expression for the transport function we find again that it can be expressed as:

$$\phi^{\mu\nu}(\omega) = \frac{-1}{2\pi^2}\,\mathrm{Re}\,\mathrm{Tr}\left\{r^{\mu}_{qp}r^{\mu}_{pq}D_pD_q - \frac{1}{2}\left(s^{\mu}_{qp}t^{\nu}_{pq} + s^{\nu}_{pq}t^{\mu}_{qp}\right)D_pD^{+}_{q}\right\} \tag{5.56}$$

where the matrices $r$, $s$ and $t$ are given by

$$r^{\mu} = A^{L}v^{\mu}A^{R}, \qquad s^{\mu} = A^{L}v^{\mu}(A^{R})^{+}, \qquad \text{and} \qquad t^{\mu} = (A^{L})^{+}v^{\mu}A^{L} \tag{5.57}$$

and the diagonal elements $D$ are given in terms of the eigenvalues of the Hamiltonian as:

$$D_p = \frac{1}{\omega + i0 - E_p}. \tag{5.58}$$

## 5.5 An alternative look at the velocity

In this section we will take another look at the definition of the current operator and instead of arriving at it from a gauge invariance argument let us simply look at the standard quantum mechanical representation of the particle current:

$$\vec{j}(r) = \frac{1}{2mi}\left\{\psi^{+}(r)\vec{\nabla}_r\psi(r) - [\vec{\nabla}_r\psi^{+}(r)]\psi(r)\right\}. \tag{5.59}$$

In our case we are interested in the zero momentum component of the current which is simply the integral over $r$ of this quantity and then we see that the current can simply be regarded as the real part of the expectation value of the operator:

$$\mathcal{V} = \frac{1}{im}\vec{\nabla}_r. \tag{5.60}$$

Let us now see how the matrix elements of this quantity looks like in the crystal within the LMTO single electron formalism. The basis functions we take are of the form [49]:

$$\begin{aligned}
\chi^{\alpha}_{k}(r) &= \sum_{lm} a^{\alpha k}_{lm} \sum_{R} e^{ikR}\chi_{lm}(E, r-R) \\
&= e^{ikr}\sum_{lm} a^{\alpha k}_{lm} \sum_{R} e^{-ik(r-R)}\chi_{lm}(E, r-R) \\
&= e^{ikr}u^{\alpha}_{k}(r).
\end{aligned} \tag{5.61}$$

Here we have, in keeping with Bloch's theorem, written the basis function in terms of a traveling wave multiplied by a function that has the periodicity of the lattice. The Hamiltonian we are trying to solve is nothing but a single particle Hamiltonian:

$$H = -\frac{\nabla_r^2}{2m} + V(r) \tag{5.62}$$

and here $V(r)$ is the periodic potential due to the atoms in the lattice and the rest of the electrons. Acting with this Hamiltonian on the basis functions gives:

$$\begin{aligned} H\chi_k^\alpha(r) &= \left(-\frac{\nabla_r^2}{2m} + V(r)\right) e^{ikr} u_k^\alpha(r) \\ &= e^{ikr}\left(-\frac{(\vec{\nabla}_r + ik)^2}{2m} + V(r)\right) u_k^\alpha(r) \equiv e^{ikr} H_k u_k^\alpha(r). \end{aligned} \tag{5.63}$$

The matrix elements can now be written as:

$$H_{k\alpha\beta} = \langle \chi_k^\alpha | H | \chi_k^\beta \rangle = \langle u_k^\alpha | H_k | u_k^\beta \rangle. \tag{5.64}$$

Let us now take the gradient of this operator with respect to momentum:

$$\vec{\nabla}_k H_{k\alpha\beta} = \langle \vec{\nabla}_k u_k^\alpha | H_k | u_k^\beta \rangle + \langle u_k^\alpha | H_k | \vec{\nabla}_k u_k^\beta \rangle + \langle u_k^\alpha | \frac{\vec{\nabla}_r + ik}{im} | u_k^\beta \rangle. \tag{5.65}$$

We see now that:

$$\langle u_k^\alpha | \frac{\vec{\nabla}_r + ik}{im} | u_k^\beta \rangle = \langle \chi_k^\alpha | \frac{\vec{\nabla}_r}{im} | \chi_k^\beta \rangle = \mathcal{V}_{k\alpha\beta} = \vec{j}_{k\alpha\beta} \tag{5.66}$$

and thus

$$\vec{j}_{k\alpha\beta} = \vec{\nabla}_k H_{k\alpha\beta} - \langle \vec{\nabla}_k u_k^\alpha | H_k | u_k^\beta \rangle - \langle u_k^\alpha | H_k | \vec{\nabla}_k u_k^\beta \rangle. \tag{5.67}$$

Now we do not necessarily assume that the basis is orthogonal and the overlaps of the basis functions are given by the overlap matrix:

$$O_{k\alpha\beta} = \langle \chi_k^\alpha | \chi_k^\beta \rangle = \langle u_k^\alpha | u_k^\beta \rangle \tag{5.68}$$

and the resolution of the identity in terms of the $u_k^\alpha$ basis is given by

$$|u_k^\alpha\rangle (O^{-1})_{k\alpha\beta} \langle u_k^\beta| \tag{5.69}$$

as can easily be seen by simply acting with this operator on one of the $u$ functions. We now insert this into the expression for the current operator and get:

$$\vec{j}_{k\alpha\beta} = \vec{\nabla}_k H_{k\alpha\beta} - \langle \vec{\nabla}_k u_k^\alpha | u_k^\gamma \rangle (O^{-1})_{k\gamma\delta} H_{k\delta\beta} - H_{k\alpha\gamma}(O^{-1})_{k\gamma\delta} \langle u_k^\delta | \vec{\nabla}_k u_k^\beta \rangle. \tag{5.70}$$

Now we note that:

$$\vec{\nabla}_k O_{k\alpha\beta} = \langle \vec{\nabla}_k u_k^\alpha | u_k^\beta \rangle + \langle u_k^\alpha | \vec{\nabla}_k u_k^\beta \rangle \tag{5.71}$$

and thus we get

$$\begin{aligned} \vec{j}_{k\alpha\beta} &= \vec{\nabla}_k H_{k\alpha\beta} - (\vec{\nabla}_k O_{k\alpha\gamma})(O^{-1})_{k\gamma\delta} H_{k\delta\beta} \\ &\quad + \langle u_k^\alpha | \vec{\nabla}_k u_k^\gamma \rangle (O^{-1})_{k\gamma\delta} H_{k\delta\beta} - H_{k\alpha\gamma}(O^{-1})_{k\gamma\delta} \langle u_k^\delta | \vec{\nabla}_k u_k^\beta \rangle. \end{aligned} \tag{5.72}$$

We have now finally succeeded in writing the current in terms of the gradient of the Hamiltonian along with some other terms. We note that the third and fourth terms in this expression are invariant with respect to a shift in the energy level and the second term ensures the same invariance for the first two terms.

The second term is quite similar to the extra term we obtained in the current in §5.3 and plays the same role. The other additional terms are similar to what is obtained if one carries out a momentum dependent rotation in the space of orbitals.

Let us for simplicity define the following quantities:

$$\tilde{H}_{k\alpha\beta} = O^{-1}_{k\alpha\gamma} H_{k\gamma\beta} \qquad \text{and} \qquad \vec{A}_{k\alpha\beta} = \langle u_k^\alpha | \vec{\nabla}_k u_k^\beta \rangle. \tag{5.73}$$

Then the current matrix element can be written as:

$$\vec{j}_{k\alpha\beta} = \vec{\nabla}_k H_{k\alpha\beta} - (\vec{\nabla}_k O_{k\alpha\gamma}) \tilde{H}_{k\gamma\beta} + \vec{A}_{k\alpha\gamma} \tilde{H}_{k\gamma\beta} - \tilde{H}^+_{k\alpha\gamma} \vec{A}_{k\gamma\beta} \tag{5.74}$$

Since this expression for the current matrix elements looks surprisingly similar to the one that we derived previously using the local gauge invariance method it is worthwhile to try to see if we can show their equivalence. So let us consider the complex time, noninteracting, Schrödinger equation:

$$H|\Psi\rangle = \overrightarrow{\partial_\tau}|\Psi\rangle \qquad \text{and} \qquad \langle\Psi|H = -\langle\Psi|\overleftarrow{\partial_\tau}. \tag{5.75}$$

Now expanding the wave function in terms of the basis functions that we are using and looking at the matrix elements we get (sum over repeated indices implied)

$$H_{\alpha\beta} c^{+}_{\beta} = O_{\alpha\beta} \dot{c}^{+}_{\beta} \qquad \text{and} \qquad c_{\alpha} H_{\alpha\beta} = -\dot{c}_{\alpha} O_{\alpha\beta}. \tag{5.76}$$

Hence we see that

$$O^{-1}_{\gamma\alpha} H_{\alpha\beta} c^{+}_{\beta} = \tilde{H}_{k\gamma\beta} c^{+}_{\beta} = \dot{c}^{+}_{\gamma} \qquad \text{and} \qquad c_{\alpha} H_{\alpha\beta} O^{-1}_{\beta\gamma} = c_{\alpha} \tilde{H}^{+}_{\alpha\gamma} = -\dot{c}_{\gamma}. \tag{5.77}$$

Now plugging these expression into equation (5.74) we get:

$$\vec{j}_{k\alpha\beta} = \vec{\nabla}_k H_{k\alpha\beta} - (\vec{\nabla}_k O_{k\alpha\beta}) \overrightarrow{\partial_\tau} + \vec{A}_{k\alpha\beta} \overrightarrow{\partial_\tau} + \overleftarrow{\partial_\tau} \vec{A}_{k\alpha\beta}. \tag{5.78}$$

If we now decide to anti-symmetrize the time derivative, we see that the last two terms do indeed vanish and we end up with exactly the same expression as we had from the previous derivation of the current.

# Chapter 6

# Computing the transport function

The computation of the transport parameters of real materials as described in the previous chapters has been implemented in a computer program which will be described in this chapter. The program is quite large, over 7000 lines, and is written in Fortran 90 which allows for greater flexibility and modularity than the standard Fortran 77. This means that almost all arrays used in the program are *dynamically allocated* and related variables are grouped together in *MODULES* which serve a purpose similar to the common blocks in Fortran 77 but are easier to use and less likely to cause errors.

The program relies heavily on the *LAPACK* program library of linear algebra subroutines which on Dec Alpha computers is included in the pre-installed *DXML* library. We have however written an interface to all the routines that are called from the LAPACK library. This is useful since many of the LAPACK routines need work-arrays and job parameters and these are now be allocated in the interface routines thereby minimizing the hassle and errors associated with using the library routines. Also if the program needs to be compiled with a different linear algebra library only the interface needs to be changed but actual calls to the interface routines will remain the same.

## 6.1 What is computed and unit conventions

The main output of the program is the transport function,

$$\phi^{xx}(\epsilon) = \frac{1}{V_{cell}} \sum_k \mathrm{Tr}\left\{ v_k^x \rho_k(\epsilon) v_k^x \rho_k(\epsilon) \right\}, \tag{6.1}$$

or more specifically a symmetrized version of this expression. Here $V_{cell}$ is the volume of the unit cell. The units used in the program are electron volt $[eV]$, Bohr radius $[a_0]$ and $[\hbar]$ so the units of the spectral density $\rho$ are $[1/eV]$ and the units of the velocity are $[eVa_0/\hbar]$, since $k$ is measured in units of $[1/a_0]$ and the velocity is the momentum derivative of the Hamiltonian. Hence the units of the transport function are $[1/a_0\hbar^2]$. The kinetic coefficients, $A_n$, are now given by:

$$A_n = N_{spin}\pi\hbar \int_{-\infty}^{\infty} d\epsilon \phi^{xx}(\epsilon) f(\epsilon) f(-\epsilon)(\beta\epsilon)^n \tag{6.2}$$

and thus the units of $A_n$ are $[eV/a_0\hbar]$. Note that if there is some interaction between spins in the Hamiltonian then all spin sectors must be included in the Hamiltonian and the factor of $N_{spin}$ is omitted. The factor of $\hbar$ comes from the final division by $\omega$ in the expression for the kinetic coefficients (see equation (4.27)). The reason why we get a factor of $\hbar$ here is due to the fact that this $\omega$ comes from the relation between the electric field and the vector potential and there of course $\omega$ is not measured in units of energy. The transport parameters and their units are now given by:

$$\begin{array}{ccc} \rho = \dfrac{k_B T}{e^2}\dfrac{1}{A_0} & S = \dfrac{-k_B}{e}\dfrac{A_1}{A_0} & \kappa = k_B\left(A_2 - \dfrac{A_1^2}{A_0}\right) \\ \left[\dfrac{a_0\hbar}{e^2}\right] & \left[\dfrac{k_B}{e}\right] & \left[\dfrac{k_B eV}{a_0\hbar}\right]. \end{array} \tag{6.3}$$

The numerical values of these units are shown in table 6.1.

| Quantity | Natural unit |
|---|---|
| electrical resistivity | 0.2173985 $\mu\Omega m$ |
| thermopower | 86.173857 $\mu V/K$ |
| thermal conductivity | 396.38665 $W/(mK)$ |

Table 6.1: The natural units for the transport parameters.

In addition to the transport function, the program computes a few other auxiliary quantities which will be described in the following sections.

## 6.2 Input and overview

We will now give a detailed prescription of what the input for the calculation is and an overview of the different components of the computational program used to implement the calculation. In figure 6.1 we have displayed a schematic overview of the program that computes the transport function. As we can see there are quite a lot of data files needed for the computation. We will now describe each of the data files and the variables they contain.

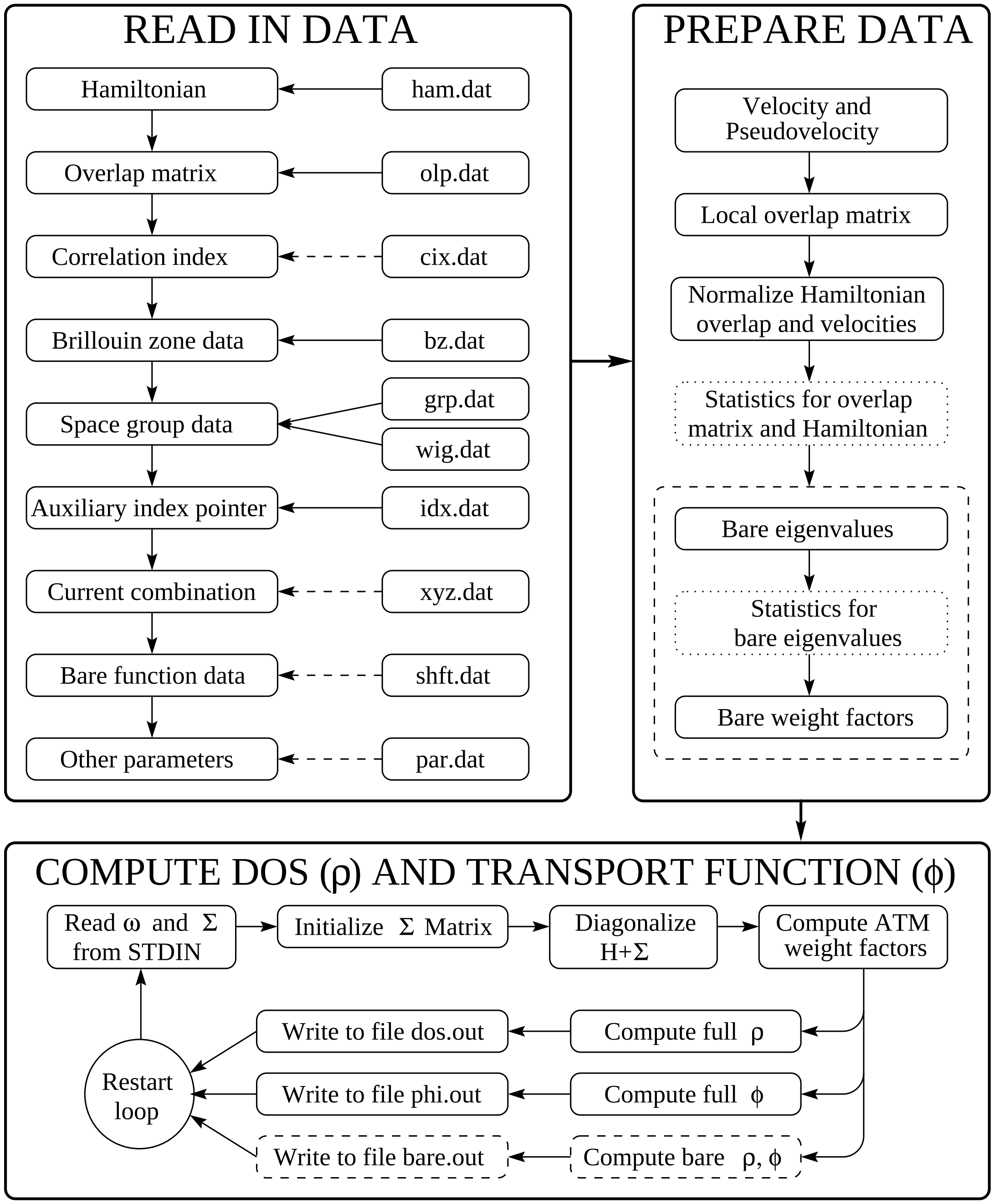


Figure 6.1: A schematic overview of the computation of the transport function. The statements within the dashed line boxes are only executed in mode *bare*. The statements within the dotted line boxes are only used for control purposes. If the *dat* files connected to program statements with a dashed line do not exist default settings are used.

### 6.2.1 Hamiltonian data (ham.dat), subroutine: ini_ham

This file contains the Hamiltonian matrix at each irreducible mesh point in the Brillouin zone. To facilitate and standardize the rotations of the Hamiltonian within the Brillouin zone the Hamiltonian is always assumed to be written in a spherical harmonics basis. This means that if one wants to consider a model Hamiltonian for only the $t_{2g}$ levels of a crystal field split d-level one must read in the whole Hamiltonian for the d-level. All the computations within the code are done in electron volts, but the default units

| Quantity | Variable |
|---|---|
| Number of irreducible k-points | nkp |
| Dimension of Hamiltonian | ndim |
| Hamiltonian | hamf (1:ndim,1:ndim,1:nkp) |

Table 6.2: Variables read in from file ham.dat

on the Hamiltonian are Rydbergs and the unit conversion is done within the program. If the Hamiltonian is already in electron volts the conversion can be suppressed by the command line switch **elv**. The program checks if the Hamiltonian is Hermitian and will exit if that check fails.

### 6.2.2 Overlap matrix data (olp.dat), subroutine: ini_ham

This file contains the overlap matrix at each irreducible mesh point in the Brillouin zone. The dimension of this matrix should be equal to the dimension of the Hamiltonian and the number of irreducible k-points should also match with the Hamiltonian data. This is checked by the code and the program exits if the check fails. If one is working in an orthogonal basis the overlap matrix is redundant and in that case the program can be run in mode **orth** in which case the file olp.dat is not read. As with the Hamiltonian the program checks for hermiticity.

| Quantity | Variable |
|---|---|
| Number of irreducible k-points | nkp |
| Dimension of overlap matrix | ndim |
| Overlap matrix | olap (1:ndim,1:ndim,1:nkp) |

Table 6.3: Variables read in from file olp.dat

### 6.2.3 Correlation index data (cix.dat), subroutine: ini_cix

The file cix.dat contains the so called correlation index for each of the orbitals in the Hamiltonian. This index can be used when the self energy in diagonal in the spherical harmonics basis. Then we can simply read in the different diagonal values of the self energy at each frequency point and apply them to the appropriate orbital. Thus the orbitals will be assigned an index from zero to **ncorr** where zero denotes an uncorrelated orbital and a nonzero index corresponds to data in the self energy file. If the file cix.dat does not exist it is assumed that all orbitals are correlated with the same correlation index, equal to 1. If the self energy is not diagonal in the spherical harmonics basis then we must of course read in the whole self energy matrix (see §6.2.10).

| Quantity | Variable |
|---|---|
| Correlation index | idnsu (1:ndim) |

Table 6.4: Variables read in from file cix.dat

### 6.2.4 Group operations (grp.dat and wig.dat), subroutine: ini_grp

The file grp.dat contains information about the space group operations of the crystal. Here we read in both the number of atoms and the number of group operations that exist. In principle the maximum number of symmetry operations is 48 but in low symmetry crystals they could be less and if one is using a reducible (i.e. not minimal) unit cell they could be more. To each of the symmetry operation corresponds a group operation element but since the maximum number of group elements is 48, two or more symmetry operations could correspond to a given group element. In addition to knowing the correspondence between the symmetry operations and the group elements we must know how the atoms move under the action of the symmetry operation if there are more than one atom of a given type in the unit cell. There is also the possibility that the symmetry operation takes the atom out of the unit cell and then it must be translated back by a lattice vector back to the original unit cell. Since we are using the Hamiltonian in the Brillouin zone these translations must be known because they introduce phase factors into the equation for the transformation of the Hamiltonian.

| Quantity | Variable |
|---|---|
| Number of symmetry operations | ngroup |
| Number of atoms in unit cell | natom |
| Symmetry operation to group element pointer | ikov (1:ngroup) |
| Atom to atom mapping for each symmetry operation | igatom (1:natom,1:ngroup) |
| Back to cell translation vectors for each atom and symmetry operation | rdc (1:3,1:natom,1:ngroup) |

Table 6.5: Variables read in from file grp.dat

The file wig.dat contains Wigner matrices for spherical harmonics angular momenta up $l = 3$. This is needed to both rotate the Hamiltonian and the overlap matrix and to create the vector rotation matrices for each group operation. Here we read in the number of group operations (should always be 48) and the maximum angular momentum (should be 3). The Wigner matrix is stored as a vector in the computer and the mapping from the angular momentum labels, $(l, m_1, m_2)$, to the vector component, $i$, is given by: $i = l(2l-1)(2l+1)/3 + (2l+1)(l+m_2) + (l+m_1+1)$

| Quantity | Variable |
|---|---|
| Number of group operations | ng $\equiv$ 48 |
| Maximum angular momentum | lmax $\equiv$ 3 |
| Wigner matrices | wigmat (1:imax,1:48) |

Table 6.6: Variables read in from file wig.dat

In addition to reading in the variables discussed above we also initialize rotation matrices for vectors in cubic representation as well as a pointer from a symmetry operation to its inverse. This is needed to compute the semirotated velocity (4.56) which is used in the computation of the transport function. Here we also compute the displacement term, $[(\vec{R}^g_{\tau'})^j - (\vec{R}^g_{\tau})^j](R^\gamma)^{-1}_{jx}$, in the semirotated velocity.

| Quantity | Variable |
|---|---|
| Cubic rotation matrices | rotmat (1:3,1:3,1:ngroup) |
| Operation to inverse operation pointer | groupinv (1:ngroup) |
| Velocity displacement term | drmat (1:3,1:natom,1:natom,1:ngroup) |

Table 6.7: Additional variables initialized in symmetry group phase.

### 6.2.5 Brillouin zone data (bz.dat), subroutine: ini_bz

The file bz.dat contains the data on the Brillouin zone mesh. Here we read in various information about the lattice and the Brillouin zone such as the lattice constant, the mesh divisions, the irreducible k-points and tetrahedra as well as information about the group transformations that connect each k-point to its irreducible representative. In

| Quantity | Variable |
|---|---|
| Lattice constant $[a_0]$ | latcon |
| Number of irreducible k-points | nkp |
| Number of irreducible tetrahedra | ntet |
| Total number of k-points | nktot |
| Number of k-points along each direction | ndiv (1:3) |
| Coordinate array for irreducible k-points | bk (1:3,1:nkp) |
| Integration weight array for irreducible k-points | wk (1:nkp) |
| Pointer from each irreducible tetrahedron to its multiplicity, irreducible k-point corners and type | itt (1:6,1:ntet) |
| kcut matrices for all tetrahedron types (see figure 6.2) | kcut (1:3,1:4,1:6) |
| Pointer from irreducible k-point to the four nearest irreducible neighbors in each direction | nbr (1:3,1:4,1:nkp) |
| Pointer from irreducible k-point to the group operation that rotates the irreducible neighbor to the real neighbor | grop (1:3,1:4,1:nkp) |
| Bravais lattice vectors, multiplied by the division along the reciprocal direction in Brillouin zone (see eq. (4.76)) | rvec (1:3,1:3) |
| Brillouin zone minicell vectors (i.e. $\vec{b}_j/N_j$ from eq. (4.72)) | mvec (1:3,1:3) |
| Pointer from each mesh points to its irreducible representative | kirrptr (0:ndiv(1)-1,0:ndiv(2)-1,0:ndiv(3)-1) |
| Pointer from each mesh point to the group operation that takes the irreducible representative to that point | gropptr (0:ndiv(1)-1,0:ndiv(2)-1,0:ndiv(3)-1) |

Table 6.8: Variables read in from file bz.dat.

addition to the variables in table 6.2.5 that are read in from the file bz.dat there are two more variables that are initialized in this phase of the program. One of them is the total number of tetrahedra which is computed from the variable *itt* but should of course be equal to $6 \times ndiv(1) \times ndiv(2) \times ndiv(3)$. The other one is a pointer from each corner

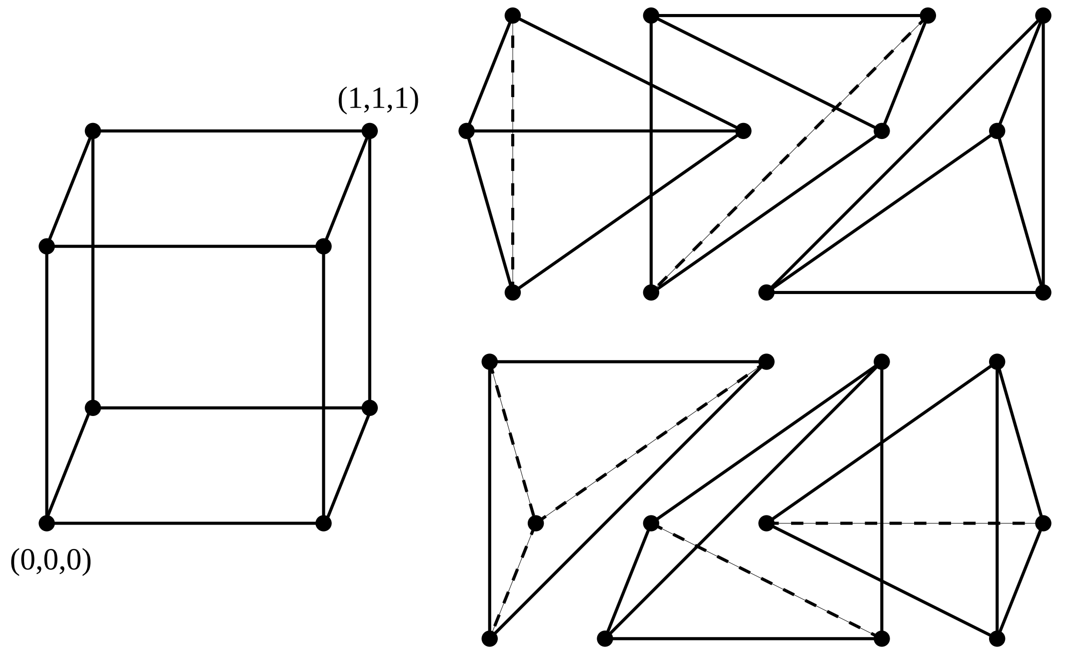


Figure 6.2: One of four different ways of splitting the unit cube into six tetrahedra, here the common diagonal is chosen from $(0,1,0)$ to $(1,0,1)$. The coordinates of a given corner $i = 1, \ldots, 4$ of each tetrahedron $j = 1, \ldots, 6$ are given by the pointer kcut($\mu$,$i$,$j$)$\in \{0,1\}$ where $\mu = 1,2,3$.

of every tetrahedron to its irreducible representative.

| Quantity | Variable |
|---|---|
| Total number of tetrahedra | mtet |
| Pointer from each tetrahedron corner to its irreducible representative | coridx (1:4,1:6,1:ndiv(1),1:ndiv(2),1:ndiv(3)) |

Table 6.9: Additional variables initialized in Brillouin zone phase.

### 6.2.6 Auxiliary index data (idx.dat), subroutine: ini_idx

The file idx.dat contains pointers from the computer representation of the physical quantities (Hamiltonian etc.) as array to the corresponding atoms and angular momenta. Here we also get information about how many sorts of atoms there are, a pointer from each atom to its sort and what is the maximum angular momentum for a given atomic sort. We also have a logical array that indicates if some angular momenta are omitted from the Hamiltonian. This is useful if we want to consider simplified models where certain angular momenta have been ignored, usually because they are of much to low

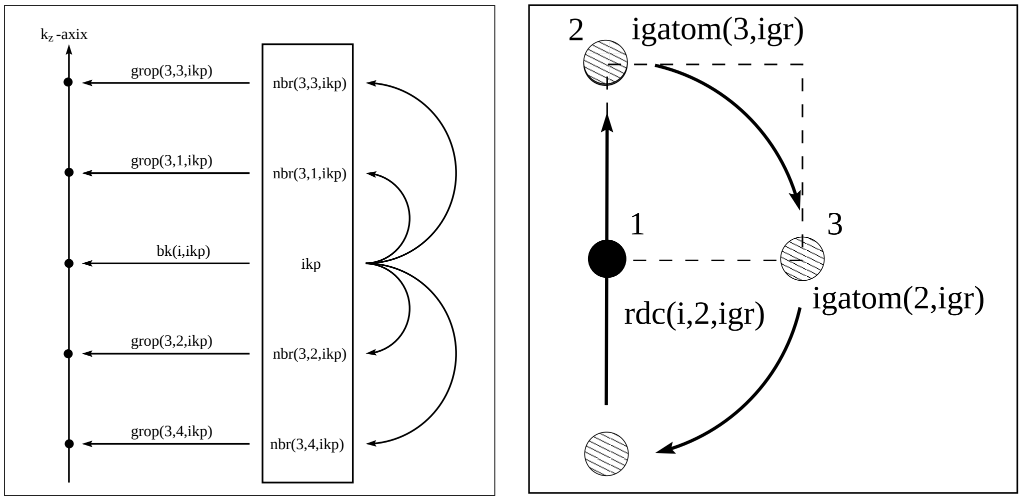


Figure 6.3: Left figure: An illustration of the information encoded in the arrays **nbr** and **grop** along the 3rd ($k_z$) direction. Right figure: An illustration of the back-to-cell vectors **rdc** that take an atom that is rotated by the transformation igr out of the unit cell back to its equivalent position in the unit cell.

energy to be of interest.

| Quantity | Variable |
|---|---|
| Number of atoms in unit cell | natom |
| Number of atomic sorts | nsort |
| Pointer from each atom to its sort | is (1:natom) |
| Pointer from each sort to its maximum angular momentum | ilsb (1:nsort) |
| Logical array indicating whether a given angular momentum is present for a given sort of atoms | ltpan (1:lmax,1:natom) |
| A pointer from each orbital state of every to its position in the Hamiltonian matrix | lmtind (1:(lmax+1)$^2$,1:natom) |

Table 6.10: Variables read in from file idx.dat.

### 6.2.7 Current combination data (xyz.dat), subroutine: ini_xyz

This data is actually now computed inside the subroutine ini_xyz but it was originally read from the file xyz.dat. This data is used to properly symmetrize the quantity that is being calculated. In our case we want to compute the transport function $\phi^{xx}$ but for instance in a cubic crystal we would instead want compute $(\phi^{xx} + \phi^{yy} + \phi^{zz})/3$ and what this routine does is to properly generate the symmetrization factors, $S_{ij}$, for the case $\phi^{xx}$, i.e.

$$\phi^{xx} \longrightarrow \sum_{ij} S_{ij}\phi^{ij}. \tag{6.4}$$

If another case is needed, say $\phi^{xy}$ then the routine would have to be changed appropriately. In addition to the symmetrization parameter we also create the "rotation" matrices for all the symmetry operations, expressed in a cubic coordinate system. These rotation matrices are used to create the symmetrization parameters and for control purposes they are also printed to the file **rot.out**.

| Quantity | Variable |
|---|---|
| Cubic rotation matrices | rot_car (1:3,1:3) |
| Transport function symmetrization parameters | curxyz (1:3,1:3) |

Table 6.11: Variables generated in subroutine ini_xyz.

### 6.2.8 Bare function data (shft.dat), subroutine: ini_shift

The file shft.dat contains data that is used in the computation of the bare transport function and the bare density of states (see §4.4). When we compute the bare quantities from the LMTO Hamiltonian we might want to apply a shift to some of the orbitals to account for, say, a Hartree shift in certain orbitals. In addition we can can envision using a different value of the scattering when we compute the lifetimes that go into the computation of the bare transport function. This corresponds to taking $\Sigma_0$ from equation (4.37) to be different from the identity, which is the default setting.

| Quantity | Variable |
|---|---|
| The real part of the diagonal values of the self energy $\Sigma$ from equation (4.37) | levelshift (0:ncorr) |
| The imaginary part of the diagonal values of the $\Sigma_0$ matrix from equation (4.37) | gammaratio (0:ncorr) |

Table 6.12: Variables read in from file shft.dat.

### 6.2.9 External parameter data (par.dat), subroutine: ini_par

The file par.dat contains several parameter, the only one of which is used here is the chemical potential. The rest of the parameters that are read in are not needed for the calculation as it is done now, they are remains of the original DMFT code from the Russian group of V. Anisimov.

| Quantity | Variable |
|---|---|
| Chemical potential [eV] | efmu |
| Inverse temperature [1/eV] | beta |
| Hubbard U parameter [eV] | upar |
| Density of LDA electrons | nlda |
| Degeneracy of the correlated band | degen |

Table 6.13: Variables read in from file par.dat.

### 6.2.10 Self energy (STDIN):

The retarded self energy is needed in a region around the Fermi surface. A rough estimate is that one needs to have data of about $20k_BT$ around the Fermi surface in order to get a good estimate of the transport parameters. Depending on the structure of the self energy we have two choices as to how it is read in from the standard input. If the self energy is diagonal in the spherical harmonics basis we can simply read in all the different diagonal values and assign them to the proper orbitals (see §6.2.3). In that case we keep the self energy in tabular form in the datafile that is read from standard input. If the self energy is not diagonal in the spherical harmonic basis then we need to read in the whole matrix at each frequency and this is done by using the mode **mat** and then we read in the frequency first and then each matrix element separately.

It is necessary to make sure that the self energy is actually retarded and for that we must make sure that the eigenvalues of the matrix have negative imaginary part and this is checked in the program and the program will exit if the check fails. In addition we add some artificial broadening to the self energy. This is done in order to regularize the integral and decrease noise from weakly correlated bands. It should of course be emphasized that if the bands around the Fermi-surface are very weakly correlated then this artificial broadening is going to dominate the behavior of the transport function and the bare transport function is probably a better choice for the computation of the transport parameters.

## 6.3 Computational modes

The program can be run in several different computational modes depending on what information is desired. The self energy is needed for all these modes even though only the external frequency is used like in the bare mode.

1. **bare:** Program computes the bare dos and transport functions.
2. **dos:** Program computes the full[1] spectral density.
3. **phi:** Program computes the full transport function.
4. **eig:** Program computes eigenvalue characteristics (not useful).
5. **orth:** Program assumes orthonormal basis.
6. **elv:** Program assumes Hamiltonian is given in electron Volts.
7. **mat:** Program reads in the whole self energy matrix.

## 6.4 Data written by the program

The program writes out several files that contain information about the progress of the program and the results of computations.

1. **phi.info** This file contains information about the progress of the program. Most of the information is written out during the preparation process, i.e. before we start looping over the frequency data. It contains such things as the dimensions of the Brillouin zone data, information about the Hamiltonian and the overlap matrix and information about the CPU time taken for various tasks.
2. **bare.out** This file contains the bare quantities

[1]Here *full* refers to quantities computed using a realistic self energy, as opposed to the simpler *bare* quantities (see equation (4.47)).

- Column #1: Frequency
- Column #2: Bare density of states
- Column #3: Bare transport function for lifetime = $1/2\pi$
- Column #4: Bare transport function for averaged lifetime
- Column #5: Bare transport function for k-dependent lifetime

3. **phi.out** This file contains the actual transport function data.

   - Column #1: Frequency
   - Column #2: Transport function
   - Column #3: Transport function, SSDD part
   - Column #4: Transport function, SSOD part
   - Column #5: Transport function, OSDD part
   - Column #6: Transport function, OSOD part

4. **dos.out** This file contains the density of states data.

   - Column #1: Frequency
   - Column #2: Density of states
   - Column #n+2: Density of states for Hamiltonian orbital #n (not necessarily positive)

5. **rot.out** This file contains the vector rotation matrices for each group operation.

6. **wig.out** This file contains the Wigner matrices written out in nice form.

7. **drmat.out** This file contains the possible values of the direct lattice vector difference $R^g_{\tau'} - R^g_{\tau}$ used in the rotation of the Hamiltonian.

# Chapter 7

# Transport Computations: Simple Metals

## 7.1 Introduction

We are now in the position to start testing and applying the tools that have been developed in the previous chapters to real materials and to start out we will consider the so called simple metals, the monovalent alkali and noble metals. Our main goal in this chapter is not so much to obtain any realistic numbers for the transport parameters of the simple metal, we do not have any realistic scattering data to do that, but rather to test the code on a real Hamiltonian with some simple assumptions about the scattering. This is important from the standpoint of obtaining an understanding of the behavior of the transport function as we modify the scattering.

In spite of their apparent simplicity a good theoretical description of the thermoelectric power in the simple metals is still lacking. In this respect the alkali metals are somewhat better understood, except for Lithium which along with the noble metals exhibits a positive thermoelectric power contrary to all expectations.

The behavior of the thermopower is further complicated by the presence of a phonon contribution to the low temperature thermopower. In general there are two contributions to the so called absolute thermopower of a given material, one coming from the diffusion of electrons, (this is the one that we compute) and the other one coming from phonons that scatter with the moving electrons. The latter one is referred to as the phonon-drag thermopower and is mainly present at low temperatures, often below 150K or so. So far we have completely ignored this contribution in our discussion and we do not intend to take this into account in our computations except to note that its presence limits the applicability of our calculations at lower temperatures

The phonon drag is however not to blame for the positivity of the thermopower in the noble metals and Lithium, at higher temperature the thermopower is completely of a diffusive nature and still it is positive. Various proposals have been put forth in order to obtain the correct sign [26], many focusing on the direct influence of the distortion of the Fermi surface in these materials and others using the distortion as a means of obtaining anharmonic relaxation lifetimes at the Fermi-level.

## 7.2 Bandstructure calculations

In table 7.1 we have gathered some data on the monovalent metals that is used in the band structure calculation. The computation of the band structure is done using

| Material | Crystal Structure | Electron Structure | Lattice Constant [au] |
|---|---|---|---|
| Li | BCC | $1s^2 2s^2$ | 6.635 |
| Na | BCC | $[Ne]3s^1$ | 8.111 |
| K | BCC | $[Ar]4s^1$ | 10.072 |
| Rb | BCC | $[Kr]5s^1$ | 10.557 |
| Cs | BCC | $[Xe]6s^1$ | 11.609 |
| Cu | FCC | $[Ar]3d^{10}4s^1$ | 6.833 |
| Ag | FCC | $[Kr]4d^{10}5s^1$ | 7.223 |
| Au | FCC | $[Xe]4f^{14}3d^{10}4s^1$ | 7.709 |

Table 7.1: The electronic and crystal structure of the monovalent metals. Here au denotes atomic units, i.e. Bohr radius.

the *lmtart* code of Sergei Savrasov in the atomic spheres approximation using screened wavefunctions in the basis. The program furnishes both the Hamiltonian and the overlap matrix for the valence orbitals of these materials along with all the necessary space group information and Brillouin zone data. The computations are all done using twenty points per axis in the Brillouin zone so we will have enough points to get a good computation of the transport function. In figures 7.1 and 7.2 we have displayed the bare density of states as computed from the LMTO Hamiltonian with the zero temperature Fermi level being at zero energy. For all the materials except Lithium the Hamiltonian is a nine by nine matrix corresponding to s, p and d orbitals. In Lithium we only have s and p orbitals so the Hamiltonian is only four by four. In all cases the density of states

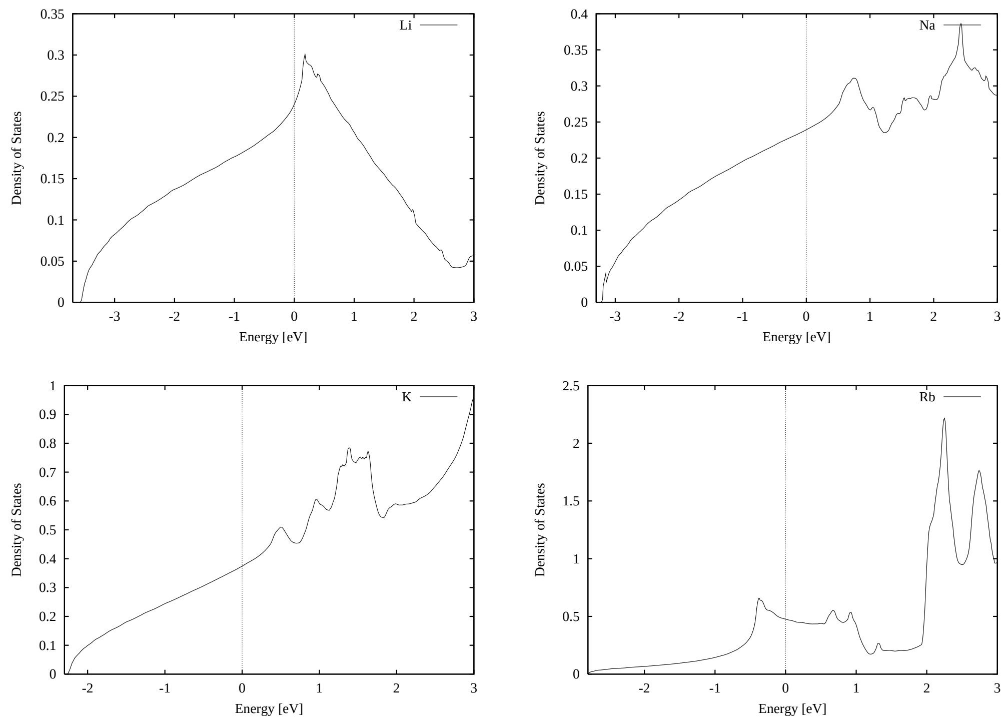


Figure 7.1: The bare densities of states for the simple monovalent metals.

exhibits a typical free electron square root behavior at the band edge but as we move further away more bands start showing up and we get more structure in the DOS. We note that the density of states of the last two elements in the alkali metal column is quite different from the other alkali metals and in fact it looks strangely like a tight binding simple cubic DOS in the vicinity of the Fermi level. For the noble metals we see a filled d-band 2-3 eV below the Fermi level and we note that the width of the band decreases as we move down the noble metal column.

## 7.3 Transport function

As mentioned before we do not have any realistic scattering data for this computation, the only data we have is the bandstructure, i.e. the Hamiltonian. We therefore propose at first to compute the transport properties by simply taking the imaginary part of the self energy to be a small frequency independent constant. Since the simple metals are weakly correlated one might be tempted to believe that such a simple form for the scattering would be sufficient for the computation of the transport parameters. We

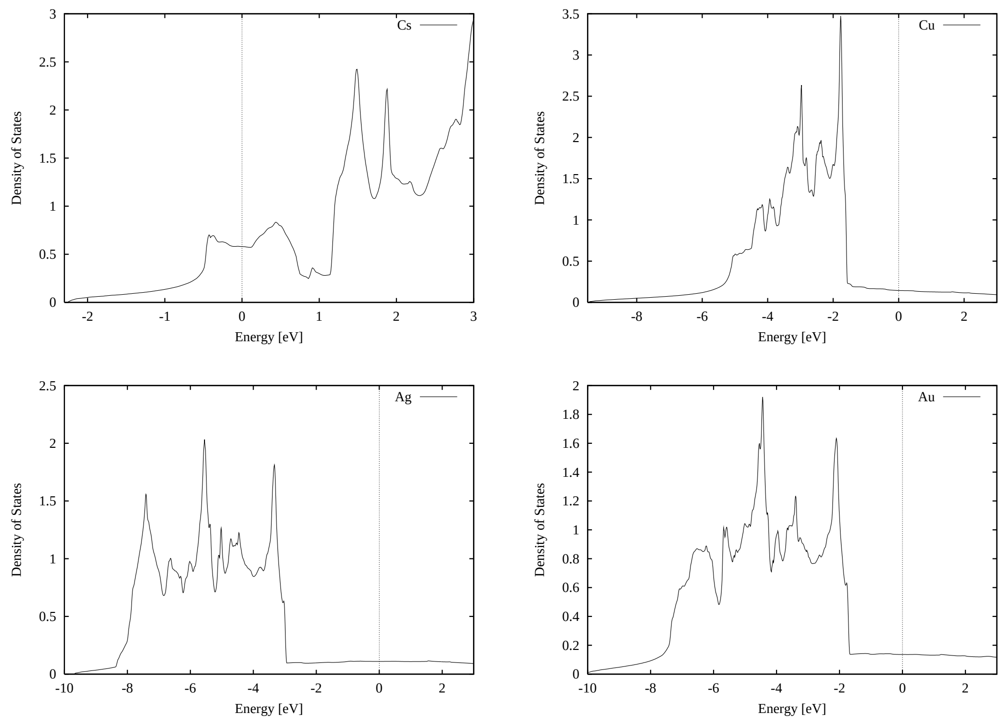


Figure 7.2: The bare densities of states for the simple monovalent metals.

should note however that this will not allow us to obtain any real numbers for the conductivities but the thermopower should in the small scattering limit be more or less independent of the value of the scattering. In this limit the transport function should also scale as the inverse of the scattering and when normalized should tend towards the bare transport function considered in §4.4. We will thus be able to see if this scaling holds and compare our computed thermopower to the experimental data. This test will also give us a clue as to whether our initial assumption of a frequency independent scattering is reasonable. There is also another issue that confronts us here and that is that even though we use a simple constant scattering we have in principle no reason to assign the same scattering to the s, p and d orbitals and the result will of course depend quite sensitively on how they are assigned.

In figures 7.3 and 7.4 we have displayed the density of states computed with a frequency independent scattering equal to $-0.1eV$ in all orbitals. In addition to the total DOS we have also displayed the DOS for the individual orbitals. We note that for Rb and Cs the spectral density of the p-orbitals becomes negative. This can be attributed to

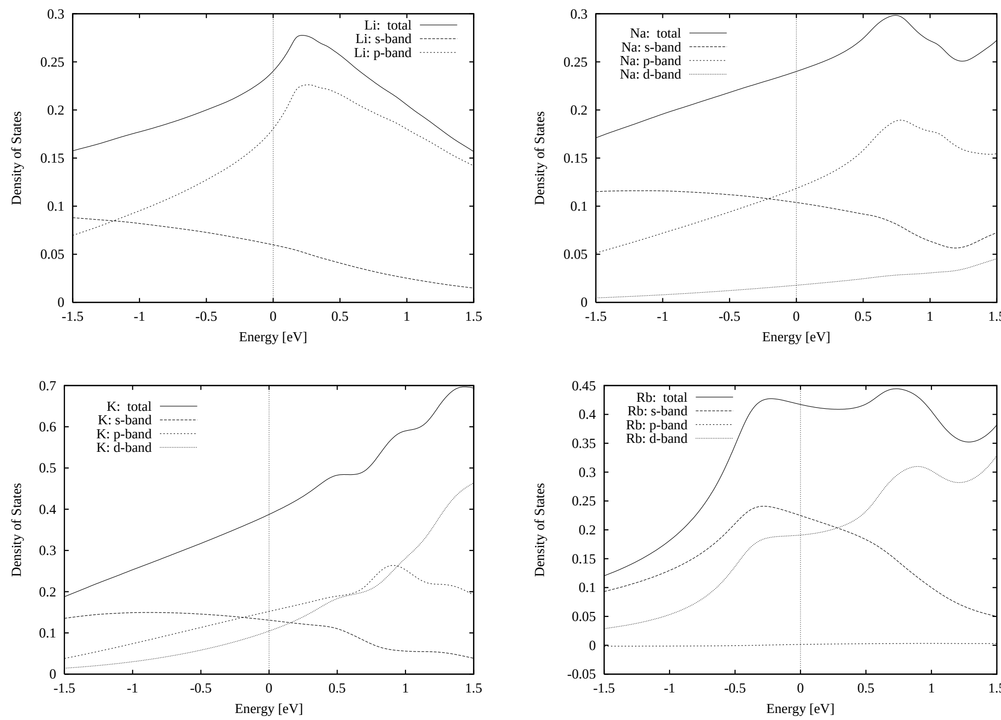


Figure 7.3: The orbital spectral densities computed with a constant scattering of 0.1eV in each orbital.

the non-orthogonality of the basis and the ambiguous definition of the individual orbital spectral densities as discussed in §5.2. Nevertheless the individual spectral densities can be quite useful in practice and they can give us an indication of how the transport function reacts to changes in the scattering assigned to individual orbitals. For all the materials we see that the spectral density of the s orbital is decreasing around the Fermi surface and the p orbital is increasing except in the case of Rb and Cs. For the noble metals we see the tail of d orbitals that lie below the Fermi surface.

In figures 7.5 and 7.6 we have displayed the scaled transport function computed with the same choice of self energy as used in figures 7.3 and 7.4 along with the corresponding calculation of the bare transport function from §4.4 (see equation (4.47)). We have here used three different choices for the lifetime; the simplest one is taking the lifetime to be a constant $1/2\pi$, but we can also compute it using equation (4.48) and use the full momentum dependent version, finally the third case uses the Brillouin zone average of the momentum dependent lifetime. We see that the full computation compares quite favorably with bare computation using the momentum dependent lifetime and this gives

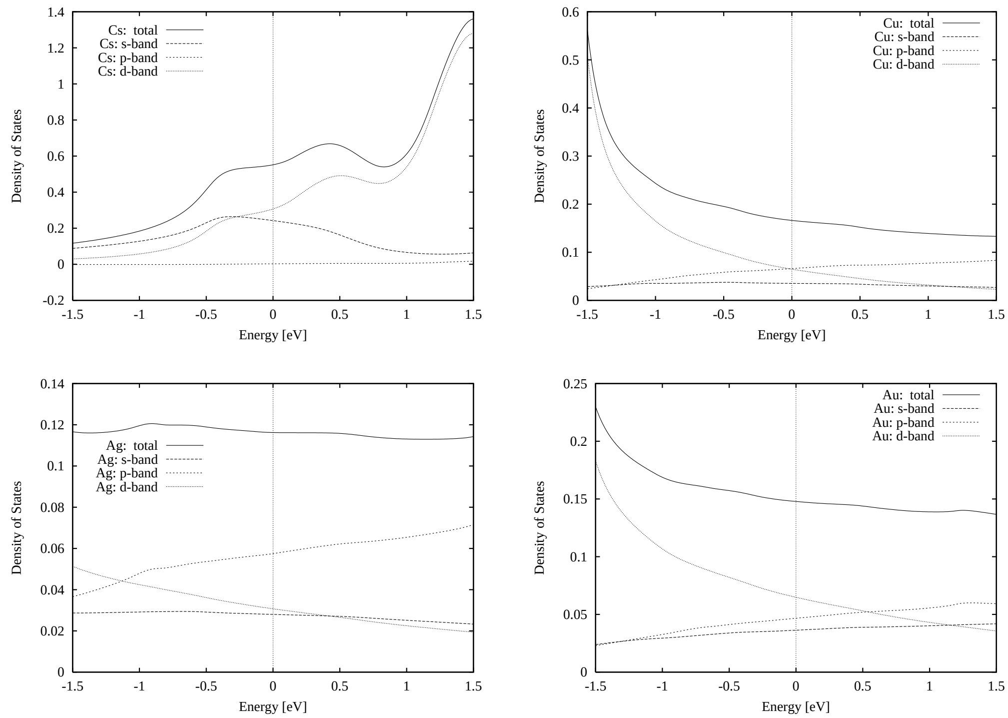


Figure 7.4: The orbital spectral densities computed with a constant scattering of 0.1eV in each orbital.

us further evidence for the accuracy of the full computation. The average lifetime computation is not too far off from the full result, which indicates that our previous assumption of slow variation in the imaginary part of the eigenvalues is quite good.

It is worth noting that for the all the alkali metals except Rubidium the spectral density and transport function have a positive slope at the Fermi-level – the positive slope of the transport function indicating that the low-temperature thermopower is negative or electron-like. For the noble metals the slope of the density of states is negative, the Fermi-level being in the upper tail of the d-bands, whereas the slope of the transport function is positive. Quite often the slope of the density of states is used as an indicator of the sign of the thermopower, and in this case the prediction for the noble metals would give the correct sign, i.e. positive or hole-like. The transport function that we obtain here however indicates a negative thermopower contradicting experiment. The reason for this difference in the slopes of the density of states and the transport function is due to the fact that the transport function is essentially equal to the density of states weighted by the squared velocity. If we now look back at figure 7.4 we see

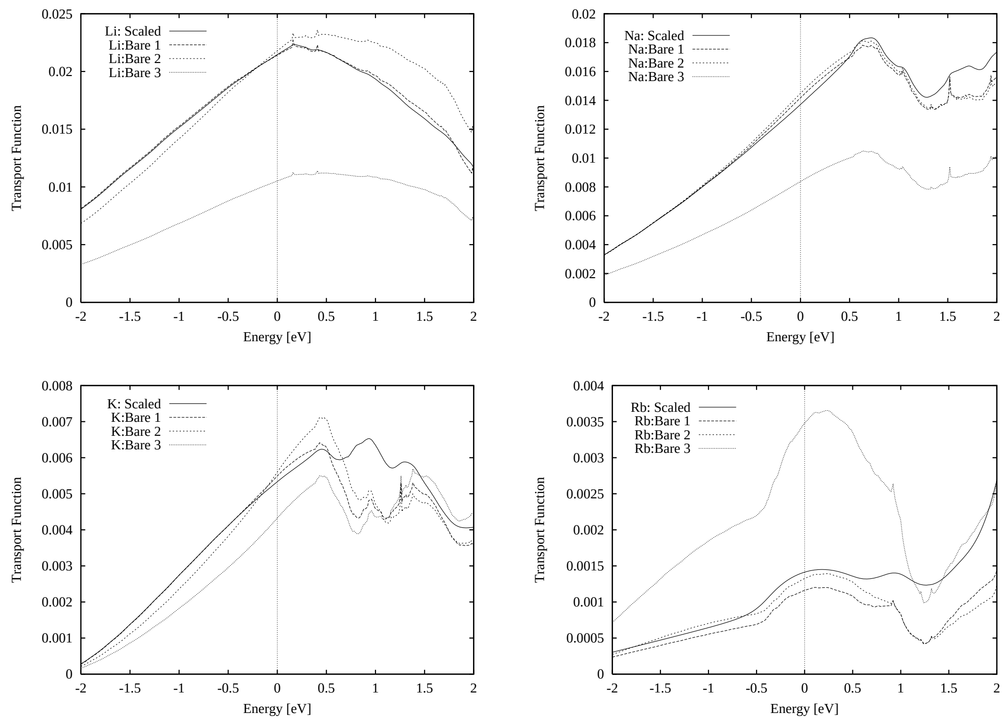


Figure 7.5: The scaled transport function computed with a scattering of 0.1 in each orbital. Also shown is the bare transport function. Bare 1 is computed with a momentum dependent lifetime, Bare 2 is computed with the average lifetime of each orbital and Bare 3 is computed with a constant lifetime of $1/2\pi$.

that for all the noble metals the density of states for the p-bands is increasing with frequency at the Fermi-level. Thus even though the density of states for the d-bands is much greater than the p-band density of states the p-band contributes much more to the transport function. This is due to the fact that the electrons in the p-band are extended and have much greater velocity than the more localized electrons in the d-band. Thus it would seem that in order to effect a change in the sign of the thermopower for the noble metals we would have to cut off the contribution from the p-band and probably the s-band also by assigning a much greater scattering to those bands.

## 7.4 Thermopower

In figures 7.7 and 7.8 we have displayed the transport functions computed with three different scattering scenarios using always frequency independent scattering but assigning different scattering to different orbitals. The values used for the scattering rates are

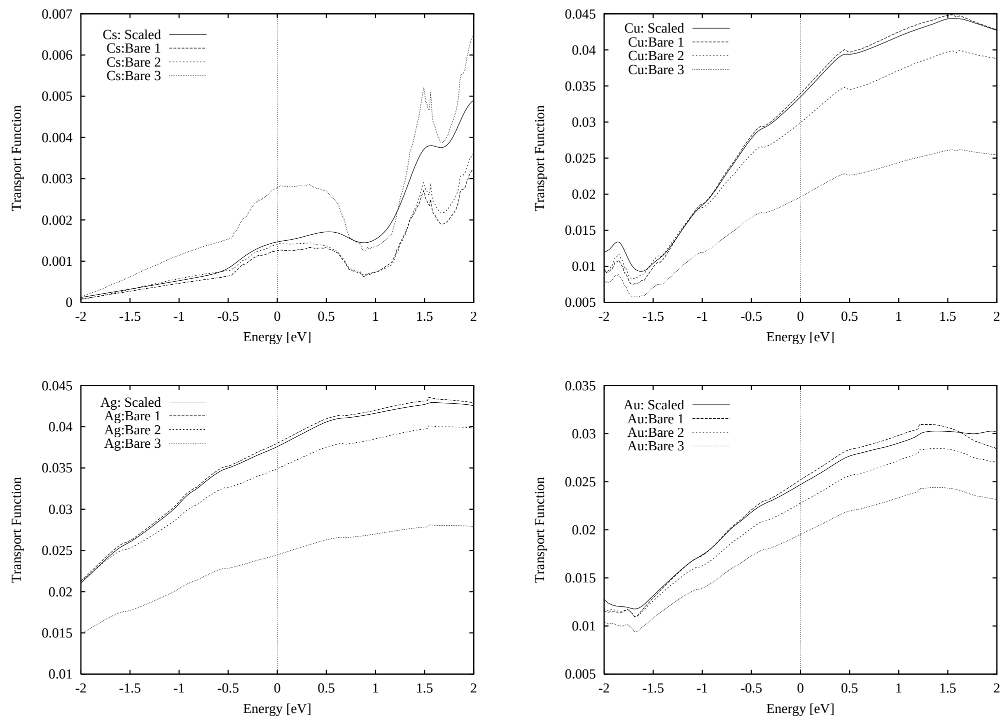


Figure 7.6: The scaled transport function computed with a scattering of 0.1 in each orbital. Also shown is the bare transport function. Bare 1 is computed with a momentum dependent lifetime, Bare 2 is computed with the average lifetime of each orbital and Bare 3 is computed with a constant lifetime of $1/2\pi$.

displayed in table 7.2.

| Scenario | s-band scattering | p-band scattering | d-band scattering |
|---|---|---|---|
| 1 | -0.1 | -0.1 | -0.1 |
| 2 | -0.5 | -0.1 | -0.1 |
| 3 | -0.1 | -0.5 | -0.1 |

Table 7.2: The three different scattering scenarios used in the computation of the transport parameters.

We note that the scattering is smallest in scenario number 1 and thus the magnitude of the transport function is generally greatest there. We see however that at certain frequencies an increase in the scattering actually increases the magnitude of the transport function. This is due to the broadening of the underlying band as the scattering is increased (see §4.9.1).

In table 7.3 we see a comparison of the experimental and the computed thermopower at zero degrees Celsius using the three different scattering scenarios mentioned above.

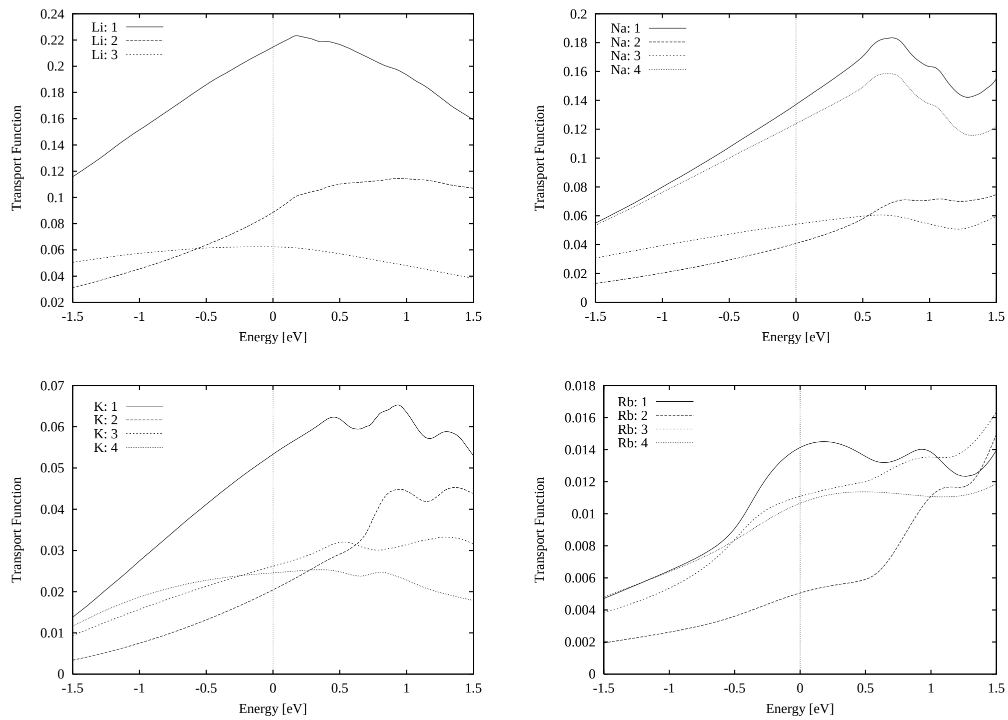


Figure 7.7: The transport functions computed with the three different scattering scenarios outlined in table 7.2.

In all cases the thermopower is linear in temperature at low temperatures as is to be expected when there is no change in the scattering with temperature and the data is consistent with the Fermi-liquid computation for the thermopower given in appendix B. We see that the different scattering scenarios produce different values of the thermopower and although we do obtain the correct sign for the simpler alkali metals the actual values are quite off. It is however clear that one might in principle be able to tune the values of the scattering in each orbital to reach the correct values. For the other materials, except Lithium, we are not able to reproduce the correct sign of the thermopower and it is likely that one would need to introduce a more complex, frequency dependent, self energy in order to do so. Since the

In order to assess the quality of the underlying local-density-approximation of the bandstructure we have also displayed in the table 7.3 the linear coefficient of specific heat, $\gamma$, both experimental values and as computed from the data. This coefficient can

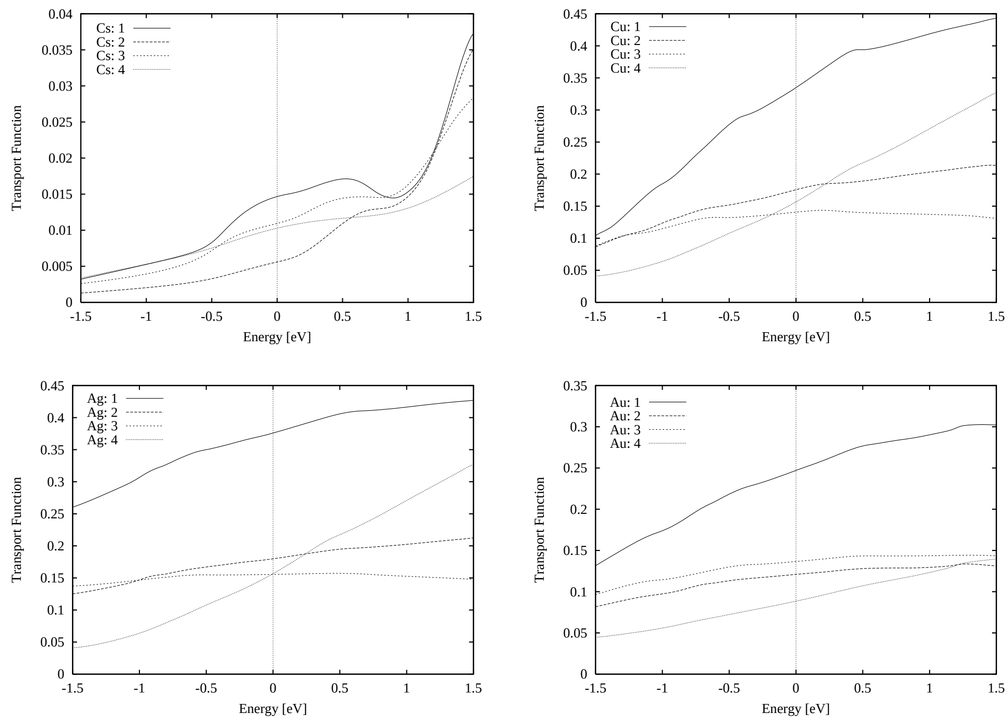


Figure 7.8: The transport functions computed with the three different scattering scenarios outlined in table 7.2.

easily be extracted from the original bandstructure using the equation [51]

$$\gamma = \frac{\pi^2}{3} k_B^2 \rho_{tot}(E_f), \tag{7.1}$$

where $\rho_{tot}(E_f)$ is the total density of states at the Fermi-level, including spin. The ratio of the experimental and the computed $\gamma$'s defines the effective mass of the charge carriers at the Fermi-level and as we can see the effective mass is not very far from unity, indicating that the bandstructure computation is quite accurate. The small discrepancy can be attributed to mass enhancement due to electron-phonon interactions [52]. It is interesting to note that some of the lowest values of the mass enhancement are found for the noble metals where our computation of the thermopower is the worst.

## 7.5 Conclusion

As we have seen from the computations outlined in this chapter the evaluation of the thermopower of even the simplest metals requires a detailed knowledge of the scattering mechanism at the Fermi-level. The simplified calculations done here, using essentially

| Material | S (exp) | S (#1) | S (#2) | S (#3) | $\gamma_{exp}$ | $\gamma_{calc}$ | $m^*/m_0$ |
|---|---|---|---|---|---|---|---|
| Lithium | 10.6 | -1.67 | -4.81 | 0.20 | 4.2 | 2.70 | 1.56 |
| Sodium | -5.8 | -3.03 | -4.31 | -1.56 | 3.5 | 2.69 | 1.30 |
| Potassium | -12.9 | -2.77 | -5.32 | -2.38 | 4.7 | 4.22 | 1.11 |
| Rubidium | -9.5 | -1.94 | -3.14 | -1.45 | 5.8 | 5.36 | 1.08 |
| Cesium | -0.9 | -2.37 | -5.35 | -2.97 | 7.7 | 6.51 | 1.18 |
| Copper | 1.70 | -2.73 | -2.02 | -0.96 | 1.6 | 1.62 | 0.99 |
| Silver | 1.38 | -1.02 | -1.07 | -0.15 | 1.6 | 1.24 | 1.29 |
| Gold | 1.79 | -1.60 | -0.80 | -0.71 | 1.6 | 1.53 | 1.05 |

Table 7.3: Computed and experimental values for thermopower of the monovalent metals measured in $\mu V/K$. The three different computed values correspond to the scattering scenarios outlined in table 7.2. The experimental values are taken from [50, page 225]. The values of the linear coefficient of specific heat, $\gamma$, are measured in $10^{-4}$cal/(mole K$^2$) and the experimental data is taken from [51, chapter 2]. The effective mass is computed as $\gamma_{exp}/\gamma_{calc}$.

constant lifetimes, tend to draw out the role of the bandstructure in the behavior of the thermopower as the lifetime dependency cancels out. It is seen that there is significant discrepancy between our simple theory and experiment, especially for the noble metals and it is clear that one must have a more realistic model for the self energies of these metals. On the other hand, as we see from the evaluation of the linear coefficient of specific heat, the numerical value of the density of states is fairly accurate and thus any changes in the scattering should not change appreciably the density of states at the Fermi-level.

# Chapter 8

# Transport computation: Doped $LaTiO_3$

In this chapter we will revisit the doped $LaTiO_3$ system that we considered in the first chapters of this thesis. We will not be able to treat the full realistic bandstructure model but will rather consider a slightly simpler model where only the correlated d-band of the titanium is retained. This is a better realization of the real bandstructure than the model we considered earlier insofar as it treats properly the symmetry and the degeneracy of the band and we are also able to treat degenerate models that have a finite value for the interaction. The interaction term that we treat in this model is $SU(N)$ symmetric Hubbard type interaction, i.e. there is penalty of $U$ associated with each pair of electrons present at each site. This is probably a different interaction than exist for these orbitals in the real material insofar as we do expect there to be the same interaction energy between two electrons in the same band as there is between two electrons in different bands. So far methods to deal with this, more general, case have not been developed so we will here consider only the $SU(N)$ case.

The solution method is based on recent progress made in solving DMFT equations and and impurity models for multiband systems and these calculations are essentially the first fruits of that work.

## 8.1 The $LaTiO_3$ system

As we have mentioned before (see §3.8) $LaTiO_3$ is a Mott insulator. What that means of course is that the insulating nature is due to correlations and not due to the band structure. Indeed with the valence of titanium being equal to one the system should be a metal according to band theory and that is what we see in the LDA computation of the density of states for this system in figure 8.1. In the figure on the left we see the total

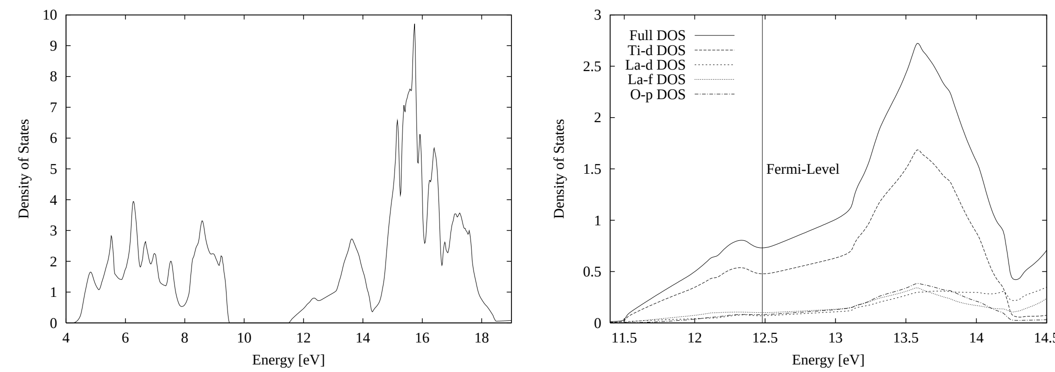


Figure 8.1: The LDA density of states for the $LaTiO_3$ system computed in the atomic spheres approximation. The left figure shows the total DOS over a wide energy range. The right figure shows the total DOS around the Fermi-level and the different components that make up the complete DOS.

density of states per spin over a large energy range, where the filled oxygen p-bands are clearly visible below the Fermi-surface. In the figure on the right we have shown the density of states per spin in the region around the Fermi-level and also displayed the various components that make up the total density of states. As we can see the main contribution to the total density of states is from the titanium d-bands, and the rest is due to contributions from lanthanum and oxygen. We see that some of the spectral density is due to the oxygen p-bands and thus the deep level beneath the Fermi-level can't be wholly due to oxygen and indeed there is some contribution from titanium d-levels down there.

In the discussion that follows we will make the assumption that the structure in the spectral density from 11.5eV up to 14.2eV is wholly due to titanium d-bands or more specifically due to titanium $t_{2g}$-bands. A simple calculation reveals that the total LDA spectral weight in this energy range is equal to 3.0 which is consistent with the triply degenerate titanium $t_{2g}$-band. With this we aim to model the correlations and the low temperature behavior of the doped $LaTiO_3$ system with a simple tight binding $t_{2g}$ model with a bandwidth of 2.7eV.

## 8.2 The model

In $LaTiO_3$ the crystal structure around the titanium ions has cubic symmetry so if we only want to retain the d-band of the titanium in the Hamiltonian we must first change the d-band basis of spherical harmonics,

$$\begin{aligned}
\Psi^s_{2,0}(\theta,\phi) &= \sqrt{\frac{5}{16\pi}}(3\cos^2\theta - 1) \\
\Psi^s_{2,\pm1}(\theta,\phi) &= \mp\sqrt{\frac{15}{8\pi}}\sin\theta\cos\theta e^{\pm i\phi} \\
\Psi^s_{2,\pm2}(\theta,\phi) &= \sqrt{\frac{15}{32\pi}}\sin^2\theta e^{\pm 2i\phi} \qquad (8.1)
\end{aligned}$$

to a basis that respects this symmetry, the so called cubic harmonic basis:

$$\Psi^c_{2,1}(x,y,z) = \frac{1}{4}\sqrt{\frac{15}{\pi}}\frac{2xy}{r^2} \qquad \Psi^c_{2,2}(x,y,z) = \frac{1}{4}\sqrt{\frac{15}{\pi}}\frac{2xz}{r^2} \qquad \Psi^c_{2,3}(x,y,z) = \frac{1}{4}\sqrt{\frac{15}{\pi}}\frac{2yz}{r^2}$$
$$\Psi^c_{2,4}(x,y,z) = \frac{1}{4}\sqrt{\frac{15}{\pi}}\frac{x^2-y^2}{r^2} \qquad \Psi^c_{2,5}(x,y,z) = \frac{1}{4}\sqrt{\frac{15}{\pi}}\frac{3z^2-r^2}{\sqrt{3}r^2}. \qquad (8.2)$$

The Coulomb interaction from the eight oxygen ions surrounding the titanium ion splits the 5-fold degenerate d-band into a lower lying 3-fold band comprised of $\Psi^c_{2,1}$, $\Psi^c_{2,2}$ and $\Psi^c_{2,3}$, and a upper 2-fold degenerate band of $\Psi^c_{2,4}$ and $\Psi^c_{2,5}$. The lower band is referred to as the $t_{2g}$ band and the upper one as the $e_g$ band. The splitting is referred to as crystal field splitting. Since the band has only one electron in it, or less upon doping with strontium, the fermi-level will be far below the $e_g$-band edge. Hence in our model we will simply assign some large energy to the $e_g$-band and no dynamics, i.e. no hopping of $e_g$ electrons between sites. The hopping between the $t_{2g}$ orbitals can be found by considering the overlap between the $t_{2g}$ orbitals on neighboring sites and using symmetry consideration we find the following Hamiltonian:

$$\begin{aligned}
H &= \sum_i E_{t_{2g}}\left(d^+_{xy,i}d_{xy,i} + d^+_{xz,i}d_{xz,i} + d^+_{yz,i}d_{yz,i}\right) \\
&+ \sum_i E_{e_g}\left(d^+_{x^2+y^2,i}d_{x^2+y^2,i} + d^+_{3z^2-1,i}d_{3z^2-1,i}\right) \\
&- \sum_{i,j=\pm x}\left(t_1 d^+_{xy,i}d_{xy,i+j} + t_1 d^+_{xz,i}d_{xz,i+j} + t_2 d^+_{yz,i}d_{yz,i+j}\right) \\
&- \sum_{i,j=\pm y}\left(t_1 d^+_{xy,i}d_{xy,i+j} + t_2 d^+_{xz,i}d_{xz,i+j} + t_1 d^+_{yz,i}d_{yz,i+j}\right) \\
&- \sum_{i,j=\pm z}\left(t_2 d^+_{xy,i}d_{xy,i+j} + t_1 d^+_{xz,i}d_{xz,i+j} + t_1 d^+_{yz,i}d_{yz,i+j}\right). \qquad (8.3)
\end{aligned}$$

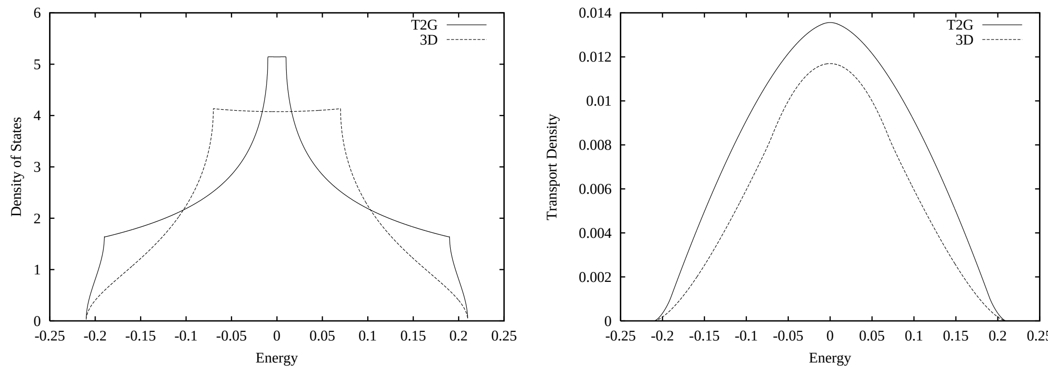


Figure 8.2: The bare density of states and the bare transport density for the $t_{2g}$ band corresponding to $t_1 = 0.05$ and $t_2 = 0.005$. For comparison we show a generic cubic s-band of the same bandwidth.

Fourier transforming the variables in the Hamiltonian we get:

$$\begin{aligned} H &= \sum_k E_{e_g}\left(d^+_{x^2+y^2,k} d_{x^2+y^2,k} + d^+_{3z^2-1,k} d_{3z^2-1,k}\right) \\ &+ \sum_k d^+_{xy,k} d_{xy,k}\left(E_{t_{2g}} - 2t_1\cos(k_x) - 2t_1\cos(k_y) - 2t_2\cos(k_z)\right) \\ &+ \sum_k d^+_{xz,k} d_{xz,k}\left(E_{t_{2g}} - 2t_1\cos(k_x) - 2t_2\cos(k_y) - 2t_1\cos(k_z)\right) \\ &+ \sum_k d^+_{yz,k} d_{yz,k}\left(E_{t_{2g}} - 2t_2\cos(k_x) - 2t_1\cos(k_y) - 2t_1\cos(k_z)\right). \end{aligned} \tag{8.4}$$

The reason why we get two hopping integrals, $t_1$ and $t_2$ is because of orientation of the different orbitals – there is more overlap between $xy$ orbitals and $xz$ orbitals at $i$ and $i + x$ than there is between $yz$ at the same sites. Thus we have $t_2 < t_1$. The half width of the $t_{2g}$ band is easily found from the Hamiltonian above and is given by:

$$D_{t_{2g}} = 2(2|t_1| + |t_2|). \tag{8.5}$$

It is easy to compute the density of states for this Hamiltonian since we have already diagonalized it – the total density of states is simply the sum of the density of states for the individual degrees of freedom. For the $e_g$ band the density of states is simply a delta function centered at $E_{e_g}$ and we will ignore that. For the $t_{2g}$ band the density of states is best computed using Fourier transforms, namely:

$$D(\epsilon) = 3\sum_k \delta\left(\epsilon - [-2t_1\cos(k_x) - 2t_1\cos(k_y) - 2t_2\cos(k_z)]\right) = \int_{-\infty}^{\infty} ds e^{is\epsilon}\tilde{D}(s) \tag{8.6}$$

where (see equation (3.74))

$$\begin{aligned}\tilde{D}(s) &= \int_{-\infty}^{\infty}\frac{d\epsilon}{2\pi}e^{-is\epsilon}D(\epsilon) = 3\frac{1}{2\pi}\sum_k e^{2ist_1\cos(k_x)+2ist_1\cos(k_y)+2ist_2\cos(k_z)} \\ &= 3\frac{1}{2\pi}\left(\int_{-\pi}^{\pi}\frac{dk}{2\pi}e^{2ist_1\cos(k)}\right)^2\left(\int_{-\pi}^{\pi}\frac{dk}{2\pi}e^{2ist_2\cos(k)}\right) \\ &= 3\frac{1}{2\pi}\left(J_0(2t_1 s)\right)^2 J_0(2t_2 s). \end{aligned} \tag{8.7}$$

Here we have taken $E_{t_{2g}} = 0$. In figure 8.2 we have displayed the density of states for the $t_{2g}$-band with the parameters $t_1 = 0.05$ and $t_2 = 0.005$ which gives a bandwidth of 0.42.[1] For comparison we plot the generic cubic s-band with the same bandwidth. It is seen that by tuning the $t_2$ parameters we can go continuously from a realization of the generic s-band, tight binding, density of states in 2 dimensions ($t_2 = 0$) to the 3 dimensional one ($t_2 = t_1$). In addition we have also displayed in figure 8.2 the transport density:

$$\Phi(\epsilon) = 3\sum_k(\vec{v}_k)^2\delta\left(\epsilon - [-2t_1\cos(k_x) - 2t_1\cos(k_y) - 2t_2\cos(k_z)]\right) \tag{8.8}$$

where $\vec{v} = \vec{\nabla}_k[-2t_1\cos(k_x) - 2t_1\cos(k_y) - 2t_2\cos(k_z)]$. This quantity can also be easily computed through Fourier transforms and allows us to compute the transport function without having to do the full Brillouin zone integral.

## 8.3 DMFT solution

The method [53] that is used here to solve the impurity model associated with the DMFT equations is based on interpolated perturbation theory. By construction the method is exact in the following limits:

- $i\omega \to 0$ for all values of $U$
- $i\omega \to \infty$ for all values of $U$
- $U \to 0$ for all values of $i\omega$
- $U \to \infty$ for all values of $i\omega$

[1] This bandwidth is of course arbitrary and will be scaled to 2.7eV in the rest of our discussion.

and interpolates smoothly between these limits for intermediate values of $U$ and $i\omega$.

By properly treating these limits the method ensures that both high energy properties, such as total energy as well as low energy properties such as quasiparticle renormalization and the Mott transition are captured correctly.

## 8.4 Results: Spectral densities and basic parameters

In this section we will look at solutions for the $t_{2g}$ model and consider the variation in the physical quantities as a function of interaction strength. In our computation here we use the following choices for the parameters of the band:

$$t_1 = 0.05 \qquad \text{and} \qquad t_2 = 0.005. \tag{8.9}$$

These parameters can be regarded as the internal parameters within the numerical code and the results will be scaled after the computation to produce the correct bandwidth. In what follows we will always assume that the bandwidth is 2.7eV but we should note that the units could also be determined a-posteriori by comparing the results of the computation to available experimental data. Hopefully this way of determining the units on the hopping parameters would also lead to a bandwidth of 2.7eV. The reason why we chose to fix the bandwidth a-priori is because that is more in line with the DMFT methodology, i.e. we compute the effects of the correlations on top of previously determined LDA or single particle results.

So, since the internal bandwidth of the model is equal to 0.42 which should be equal to 2.7eV the unit in which our parameters are measured is equal to 6.429eV. From now on however we will quote all energy values in eV, they can be translated back to the original values when needed.

In the data-series that we consider in this section we have taken the density, $n$, to be 0.95, 0.9 and 0.80 which corresponds to 5, 10 and 20% doping from the Mott insulating state at $n = 1.0$. The temperature is taken as $T = 74K$. The calculation is started at a small value of interaction $U = 1.93eV$ and then it is slowly increased to $U = 11.57eV$. The computation is done is two steps:

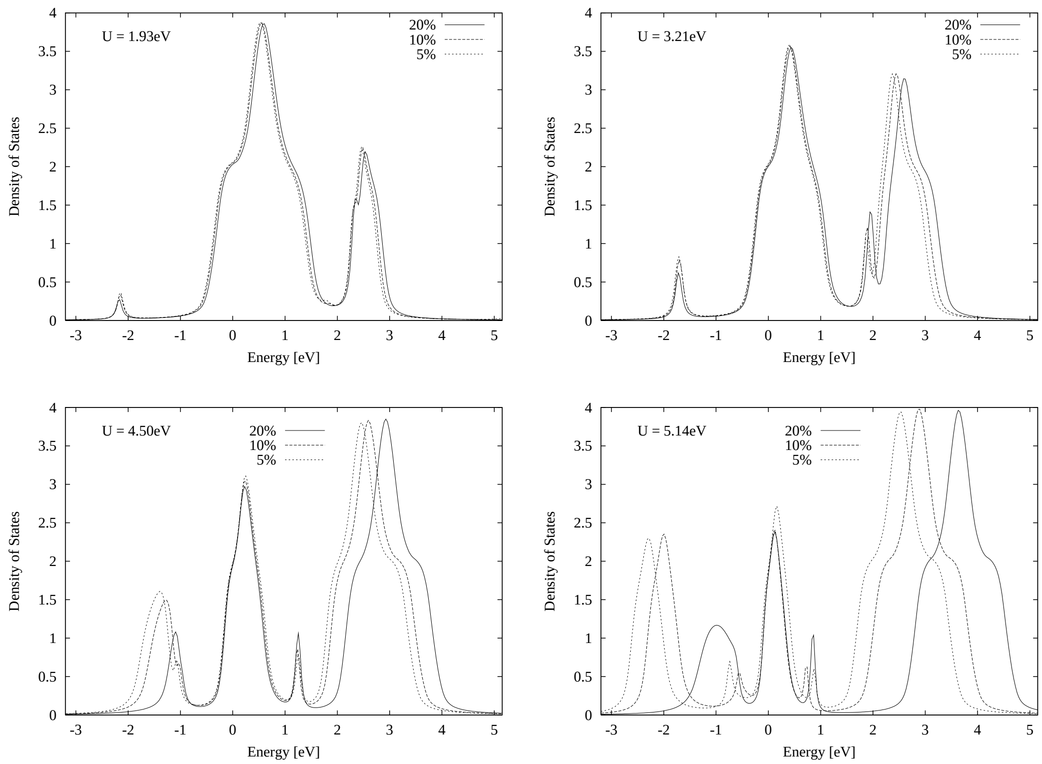


Figure 8.3: The renormalized density of states for the $t_{2g}$ band computed for various values of interaction. $U$.

1. The self energy is computed on the Matsubara axis, where computations are usually more stable.

2. The solution from the Matsubara axis is used to compute the retarded self energy on the real axis.

The second step of this procedure is usually more likely to incur numerical instabilities. For this reason we have not been able to obtain retarded self energies for values of the interaction larger than about $U = 5.2eV$ and hence we cannot compute the full density of states or the transport parameters for $U$ larger than that. On the Matsubara axis the model can be solved for larger values of $U$ and here we have gone all the way up to $U = 11.57eV$.

If we start by looking at the real axis data we see from figure 8.3 that the density of states around the Fermi-surface for the smallest value of the interaction is quite similar to the bare density of states in figure 8.2, but in addition we have an upper Hubbard peak centered around 2.5eV. We also see a small satellite peak below the Fermi-surface and since this peak is close to 5eV below the upper Hubbard peak it does not seem to correspond to lower Hubbard band and looks like it might be spurious. However, as the interaction is increased this satellite peak moves closer to the Fermi-level and increases in weight and for $U = 5.14$eV this peak should clearly be identified as the lower Hubbard band. At the same time we see that the peak that is originally at the Fermi-level narrows, most of the spectral weight is transferred up to the upper Hubbard band and for $U = 0.5.14$eV this peak should be identified as the quasiparticle peak. The width of the quasiparticle peak as compared to the width of the original band is given by the quasiparticle residue, defined by:

$$Z = \left(1 - \frac{\partial \,\mathrm{Re}\,\Sigma(\omega)}{\partial \omega}\bigg|_{\omega=0}\right)^{-1} = \left(1 - \frac{\partial \,\mathrm{Im}\,\Sigma(i\omega_n)}{\partial (i\omega_n)}\bigg|_{i\omega_n \to 0}\right)^{-1}. \tag{8.10}$$

We see from this equation that the quasiparticle residue can be computed from the Matsubara axis data and in figure 8.4 we have displayed $Z$ along with the chemical potential, the real part of the self energy at the Fermi-surface and the density of states at the Fermi-surface which we compute simply by finding the zero frequency limit of the imaginary part of the Matsubara Green's function. We see clearly from the figure that there is a qualitative change in the solution occurring around $U = 6eV$eV. The quasiparticle residue becomes less a function of the interaction strength, and depends essentially only on doping. The large $U$ values of the quasiparticle residue are in close agreement with previous estimates for the Mott insulator [54]. It seems likely that at half filling the quasiparticle residue would go to zero for interaction strengths above 5.5-6eV and thus the model would be insulating in that regime and metallic for lower values. Upon doping away from half filling the metallic state does not change very drastically as we can see from the doping independence of the quasiparticle residue whereas the insulating state is always rendered metallic for any value of $U$.

The behavior of the chemical potential is indicative of the transfer of spectral weight as we increase the interaction strength. For small values of the interaction the chemical potential increases which tells us that the spectral weight from the noninteracting band is being transferred to the upper Hubbard band. For higher values of the interaction

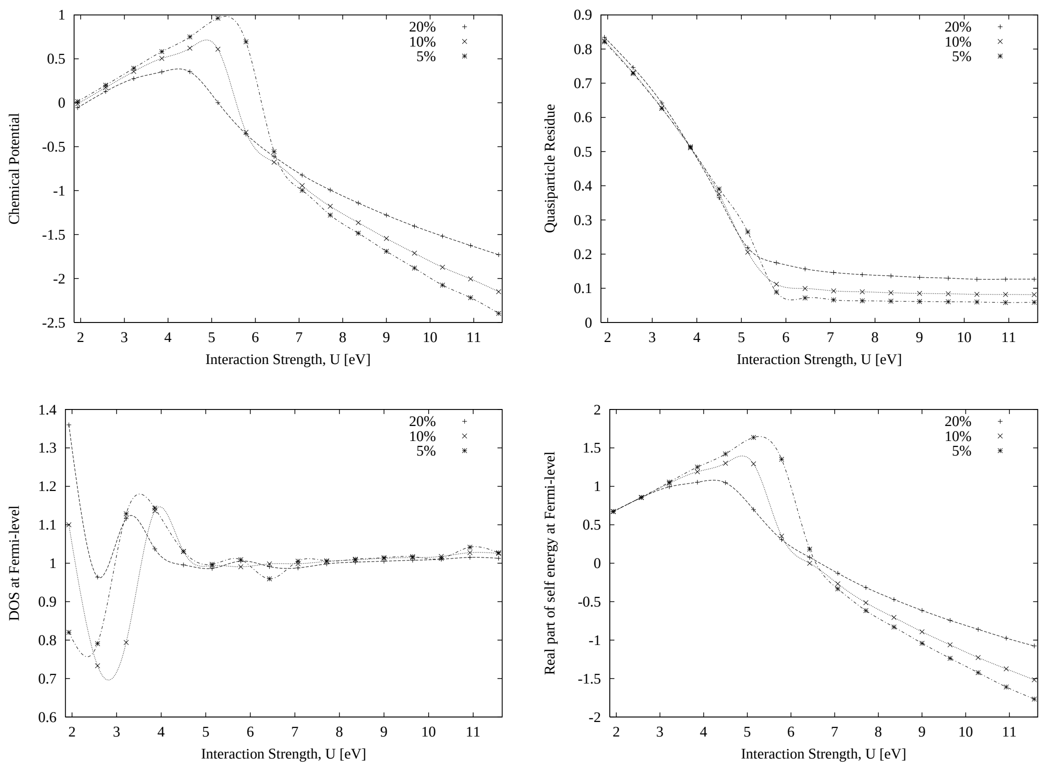


Figure 8.4: The chemical potential, quasiparticle residue, density of states at the Fermi-level and the real part of the self energy at the Fermi-level for the $t_{2g}$ model as a function of interaction strength, U.

strength this trend is reversed and now the spectral weight is being transferred to energies below the Fermi-level. Hence the scenario as the interaction strength is increased unfolds as follows: At zero $U$ we start out with a noninteracting band and when $U$ is increased the spectral weight is transferred to an upper Hubbard band and the original noninteracting peak can be regarded as the lower Hubbard band. As we increase $U$ even further the peak that we identified as the lower Hubbard band loses weight to a structure that forms below the Fermi-level – the lower Hubbard band, and the original noninteracting band can now be identified with the quasiparticle peak.

We should note that the value of interaction at which the metal insulator crossover takes place here is about two times the bandwidth or four times the half bandwidth. This is a somewhat larger number than is obtained in single band models where the critical $U$ is found to be around 2.5-3.0 times the half bandwidth [1]. Using estimates for multiband models from [55] we find that the critical $U$ for the Mott transition takes place at $U_c \simeq 6.1eV$ which agrees very well with our data.

### 8.4.1 Comparison with experiment: photoemission

It is instructive to compare the spectral densities that we have obtained for our model to experimental measurements of photoemission in this system. The photoemission data can be thought of as essentially the local spectral density below the Fermi-level, convolved with some response function that characterizes the apparatus being used, say a Gaussian [1]. The resulting spectra is simply a smoothed out version of the spectral density below the Fermi-level and here we can simply compare the photoemission data directly to the spectral densities in figure 8.1 and 8.3.

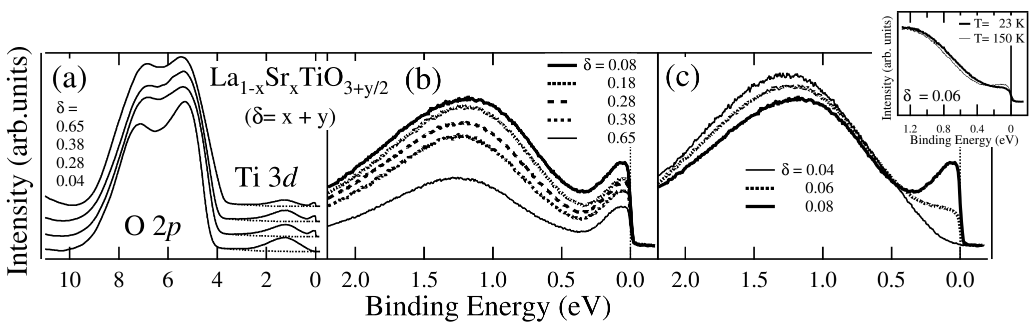


Figure 8.5: (a) Valence band photoemission spectra of $La_{1-x}Sr_xTiO_{3+y/2}$ taken from [56]. Figure (b) shows the photoemisson spectrum in the titanium 3d band region.

From photoemission measurements [56] conducted on the system $La_{1-x}Sr_xTiO_{3+y/2}$ (see figure 8.5) we see clearly the presence of an oxygen 2p-band deep beneath the Fermi-surface just as in the LDA spectral density from figure 8.1. Both the position of the band compared to the Fermi-level and its width are quite consistent with the LDA data. Closer to the Fermi-level we see a small hump, about half an electron volt beneath the Fermi-surface with a width of about 2eV. This hump clearly corresponds well to the lower Hubbard band in density of states that we obtain with our model at, say 4.5eV (see figure 8.3). We note here that both the position of the peak as well as the width is quite consistent with our data for that interaction value.

## 8.5 Results: transport Functions

We now turn to the computation of the transport functions. In figure 8.6 we have displayed the transport function for the $t_{2g}$ model for various values of the interaction strength, $U$, using the same doping and temperature values as in the previous section. For clarity we have also displayed the transport function for the largest values of the interaction in a smaller window around the Fermi-level.

It should be noted here that the method that is used to compute the self energy at low Matsubara energies assumes that the self energy is zero at the Fermi-level. Then in the subsequent computation of the self energy on the real axis a small broadening is added by hand to the self energy in order to stabilize the computation. This is of course is bad news when it comes to computing the transport properties since it is clear that the transport function will depend very strongly on the broadening. We will nevertheless push forward with this calculation and we can probably expect to obtain fairly good results for the thermopower, but the absolute values of the conductivities should be taken with a grain of salt.

In addition to presenting the values computed by the method developed in the previous chapters (denoted BZI in the figures) we have also displayed the exact value computed from the dispersion relation using Fourier transforms (denoted FFT in the figures). We see that there is excellent agreement between the two methods although the direct integration method is quite noisy due to the smallness of the imaginary part of the self energy. We see clearly how the increase in interaction strength decreases the value of the transport function at the Fermi-surface, indicating a decrease in the value of the conductivities.

### 8.5.1 Transport parameters

In figures 8.7 we have displayed the transport coefficients for the $t_{2g}$ model taking the lattice constant as 7.4 Bohr radii which corresponds to the $LaTiO_3$ system.

As we can see the conductance of the model decreases as we increase the interaction; the electrical resistivity increases tenfold from the smallest to the largest $U$ and

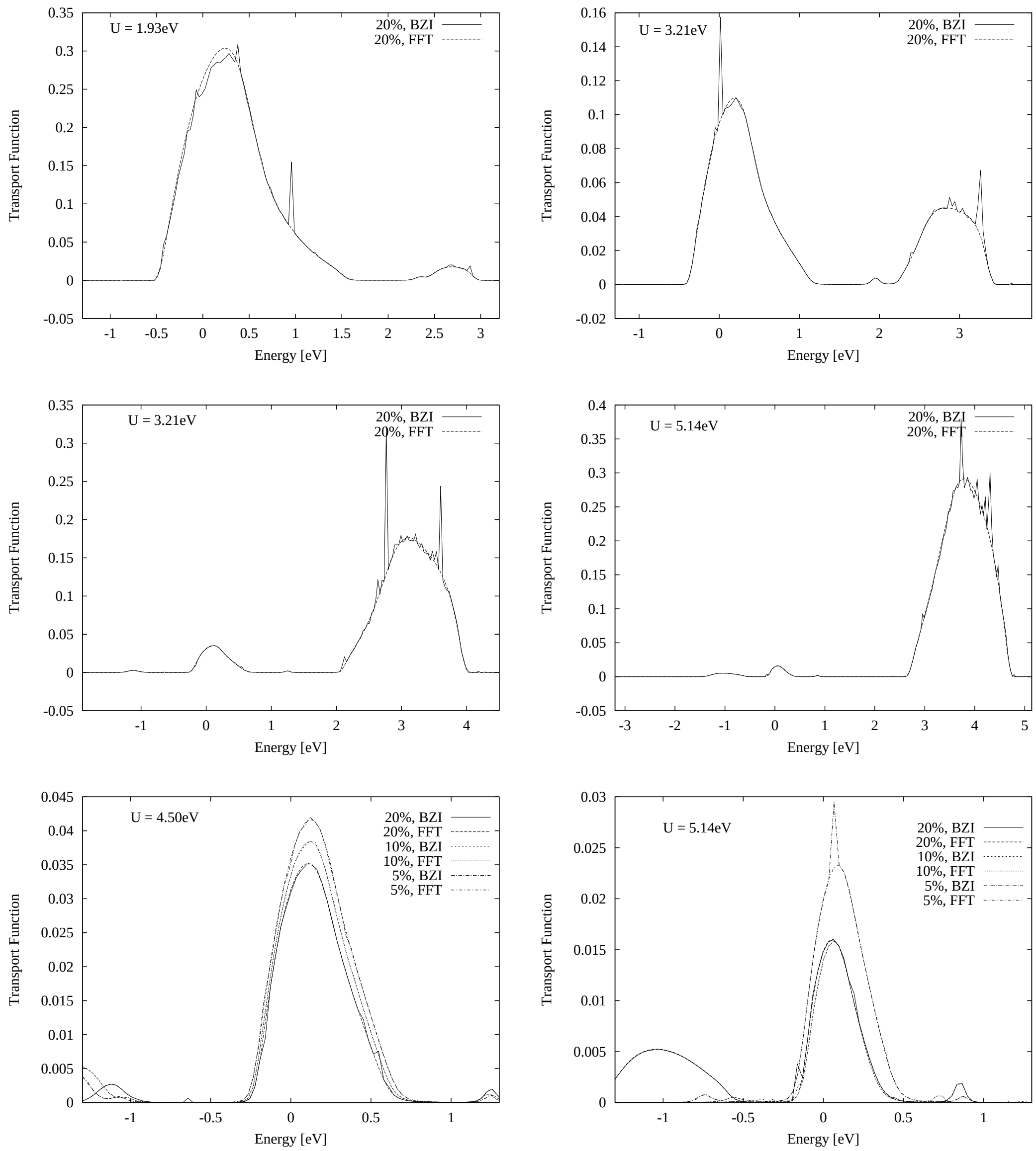


Figure 8.6: The transport function for the $t_{2g}$ model computed for various values of the interaction, $U$. BZI denotes Brillouin zone integration, FFT denotes exact calculation.

a concomitant decrease is seen in the thermal conductivity. We note that the Lorentz ratio is very close to the classical value of $24.4 \mathrm{nW\Omega/K^2}$ for impurity scattering and the values of the resistivity and thermal conductivity for the lower values of $U$ are in the range of typical metals [51, chapter 1]. We note also that as the interaction increases the Lorentz ratio decreases indicating a crossover to Fermi-liquid type behavior in the self energy around the Fermi-level, in accordance with our discussion in Appendix B.

The thermopower is negative, indicating that the carriers are electron-like and both

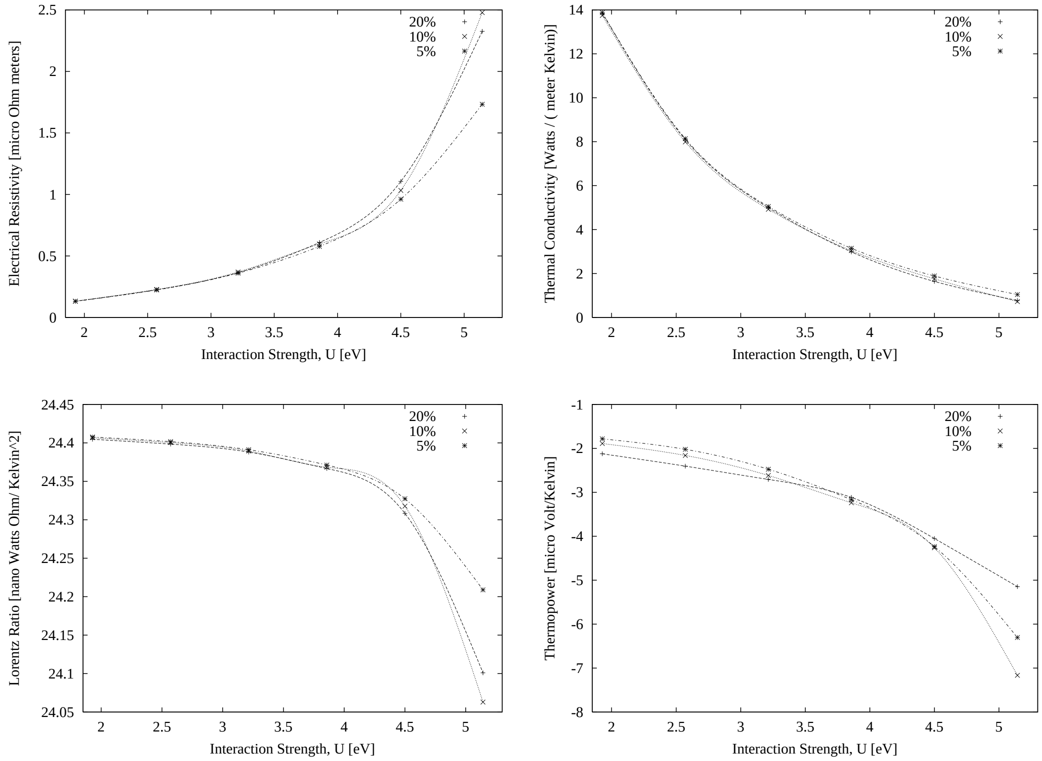


Figure 8.7: The electrical resistivity, thermal conductivity, thermopower and Lorentz ratio for the $t_{2g}$ model as a function of interaction strength, U.

the magnitude and the sign of the thermopower are consistent with the $La_{1-x}Sr_xTiO_3$ data from Goodenough [57] shown in figure 3.15. The increase in the magnitude of the thermopower with increasing value of $U$ agrees with the intuitive notion of localization of carriers with increasing interaction leading to larger entropy per carrier and therefore larger values of thermopower.

## 8.6 Results: specific heat and thermopower

The linear coefficient of specific heat is another quantity that we can easily compare to experiment and has a simple connection to the quasiparticle residue and the transition from the metallic to the insulating state. The linear coefficient of specific heat, $\gamma$ is given by the following equation:

$$\begin{aligned}\gamma &= \frac{\pi^2}{3Z}k_B^2\rho_{tot}(E_f) = 2.357\left[\frac{mJ}{molK^2}\right]\frac{\rho_{tot}(E_f)[1/eV]}{Z}\\ &= 5.631\left[\frac{10^{-4}cal}{molK^2}\right]\frac{\rho_{tot}(E_f)[1/eV]}{Z}\end{aligned} \tag{8.11}$$

where $Z$ is the quasiparticle residue and $\rho_{tot}$ is the total density of states per unitcell at the Fermi-surface. Table 8.1 contains the computed values of $Z$ and $\gamma$ for the $t_{2g}$ model over the whole interaction range. In figure 8.8 we have also displayed a graph

| Quantity | $Z$ | | | $\gamma$ $[mJ/molK^2]$ | | | $S$ $[\mu V/K]$ | | |
|---|---|---|---|---|---|---|---|---|---|
| $U$ $[eV]$ | 5% | 10% | 20% | 5% | 10% | 20% | 5% | 10% | 20% |
| 1.93 | 0.821 | 0.824 | 0.834 | 5.8 | 5.7 | 5.5 | -2.9 | -3.0 | -3.3 |
| 2.57 | 0.728 | 0.731 | 0.746 | 6.5 | 6.4 | 6.1 | -3.2 | -3.4 | -3.7 |
| 3.21 | 0.627 | 0.627 | 0.642 | 7.6 | 7.5 | 7.1 | -3.8 | -4.0 | -4.2 |
| 3.86 | 0.514 | 0.511 | 0.512 | 9.2 | 9.2 | 9.0 | -4.7 | -4.9 | -5.1 |
| 4.50 | 0.390 | 0.376 | 0.365 | 12.1 | 12.5 | 12.7 | -6.2 | -6.5 | -7.0 |
| 5.14 | 0.265 | 0.206 | 0.219 | 17.8 | 22.8 | 21.3 | -9.2 | -12.1 | -11.7 |
| 5.79 | 0.089 | 0.112 | 0.175 | 53.4 | 41.7 | 27.1 | -26.3 | -22.4 | -13.6 |
| 6.43 | 0.072 | 0.099 | 0.157 | 63.0 | 47.3 | 29.8 | -39.0 | -24.5 | -16.0 |
| 7.07 | 0.066 | 0.092 | 0.146 | 71.8 | 50.9 | 31.9 | -35.7 | -26.3 | -17.4 |
| 7.71 | 0.063 | 0.090 | 0.140 | 74.9 | 52.8 | 33.6 | -37.0 | -26.5 | -17.5 |
| 8.36 | 0.062 | 0.087 | 0.136 | 76.4 | 54.6 | 34.7 | -37.0 | -27.0 | -17.7 |
| 9.00 | 0.061 | 0.085 | 0.132 | 77.9 | 56.1 | 35.9 | -37.0 | -27.2 | -18.1 |
| 9.64 | 0.061 | 0.084 | 0.130 | 79.2 | 56.9 | 36.6 | -37.1 | -27.4 | -18.2 |
| 10.29 | 0.060 | 0.082 | 0.126 | 79.6 | 58.3 | 37.7 | -38.1 | -27.7 | -18.6 |
| 10.93 | 0.058 | 0.082 | 0.127 | 84.1 | 59.1 | 37.7 | -35.6 | -26.9 | -18.2 |
| 11.57 | 0.059 | 0.081 | 0.127 | 81.9 | 59.3 | 37.7 | -36.8 | -27.2 | -18.3 |

Table 8.1: The quasiparticle residue and the linear coefficient of specific heat as a function of the interaction strength.

of $\gamma$ as a function of $U$ for the three values of doping. Since the density of states at the Fermi-surface is almost independent of interaction strength the $U$ dependence of $\gamma$ mirrors that of the quasiparticle residue.

Experimental values of this coefficient for the $La_{1-x}Sr_xTiO_3$ system can be obtained from [34] and are shown in table 8.2 along with values computed using the DMFT at $U = 5.4$eV. For comparison we have also displayed the values obtained from bare LDA tight binding density of states with $Z = 1.0$. We see that the LDA values are quite different from the experimental values indicating the failure of the LDA for this system. For the DMFT values there is some ambiguity as to what value of the interaction

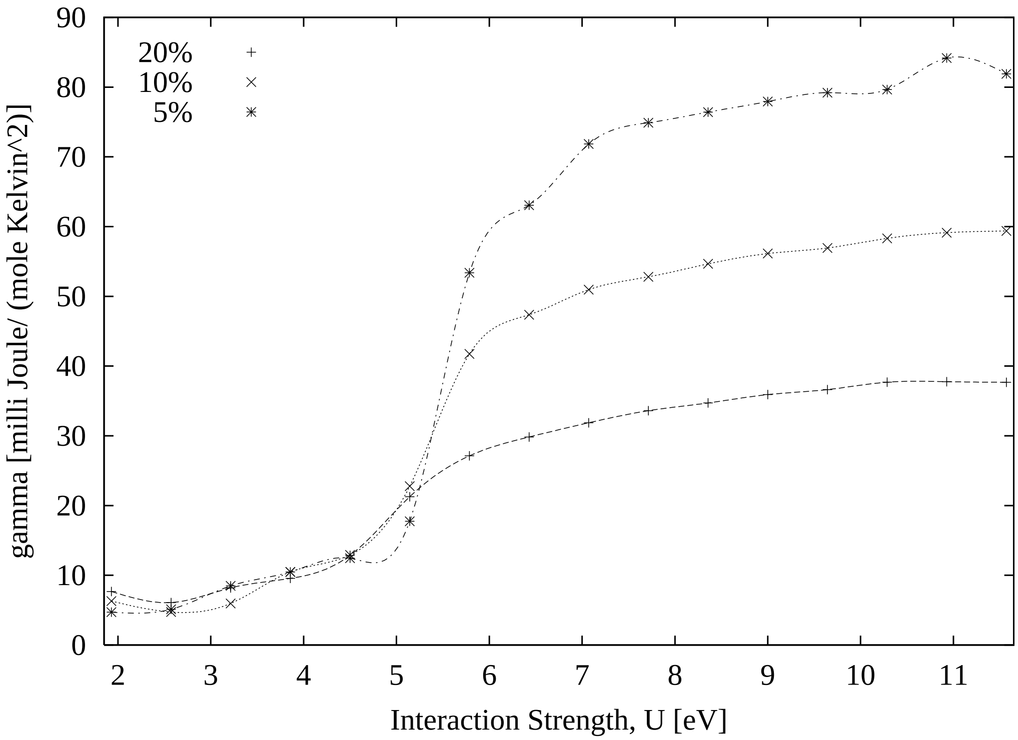


Figure 8.8: The linear coefficient of specific heat for the $t_{2g}$ model as a function of the interaction strength, $U$.

| Doping (%) | $\gamma_{EXP}$ | $\gamma_{LDA}$ | $\gamma_{DMFT}$ | $Z$ | $U_{eff}$ | $Z_{eff}$ |
|---|---|---|---|---|---|---|
| 5 | 17.0 | 4.58 | 31.26 | 0.188 | 5.122 | 0.270 |
| 10 | 11.5 | 4.51 | 30.64 | 0.156 | 4.143 | 0.456 |
| 20 | 9.0 | 4.40 | 24.13 | 0.191 | 3.555 | 0.576 |

Table 8.2: Experimental values for the linear coefficient of specific heat obtained from [34]. The units of $\gamma$ are $\left[mJ/molK^2)\right]$. The values of $\gamma_{DMFT}$ and the quasiparticle residue, $Z$, correspond to $U = 5.4$eV or twice the bandwidth. $U_{eff}$ is the interaction value at which the computed $\gamma$ is the same as the experimental $\gamma$ and $Z_{eff}$ is the corresponding quasiparticle residue.

corresponds to the real material. It is reasonable to assume that this value is close to the boundary of the metal-insulator transition given the fact that very small doping renders this material metallic. Hence we pick $U = 5.4$eV which according to our previous discussion seems to correspond to the metal-insulator transition.

We see that this value gives $\gamma$ that is somewhat higher than the experimental value. It is therefore instructive to use the experimental values for guidance to extract the effective value of $U$ that corresponds to each doping. That data is given in the last two columns of table 8.2 and shows that the effective interaction decreases as the interaction increases. This is quite reasonable since we can expect the interaction to be more screened as the doping increases. We note also that the effective interaction does indeed seem to be tending toward the value at which we have estimated the metal insulator transition to be.

### 8.6.1 Evaluation of thermopower from Matsubara data

Since the transport parameters depend essentially only on the value of the transport function at and around the Fermi-surface (see appendix B) it is tempting to try to evaluate these parameters from the Matsubara data. Here we will try to do this for the thermopower since for small scattering we expect the thermopower to be essentially independent of the scattering. Thus we approximate the self energy around the Fermi-level in the following way:

$$\Sigma(\omega) = \Sigma' + \omega\left(1 - \frac{1}{Z}\right) - i\Sigma'' \tag{8.12}$$

where $\Sigma'$ is the zero frequency limit of the real part of the Matsubara self energy, and $\Sigma''$ is a similar limit for the imaginary part. The second parameter, $\Sigma''$, we actually put in by hand and simply pick a small value (of the order of $T$) for it.

Once we have a functional form for the self energy we can compute the transport function around the Fermi-surface and proceed to evaluate the thermopower. The results from this are shown in figure 8.9 and the data itself can be seen in table 8.2. In the small $U$ regime this evaluation agrees well with our previous calculation but as we can see there is a significant change in the thermpower around the metal-insulator crossover. This change reflects essentially the change in the quasiparticle residue, in a similar fashion as the linear coefficient of specific heat. The qualitative behavior of the thermopower above the crossover does not however agree with the experimental data from figure 3.15.

The reason for this discrepancy is most likely due to the distribution of spectral weight around the Fermi-surface. To recall how the doping affects the thermopower we need to look back at the Hubbard model discussed earlier in this thesis. In the figure we obtained for the thermopower in the Hubbard model using the IPT (see figure 3.14) the

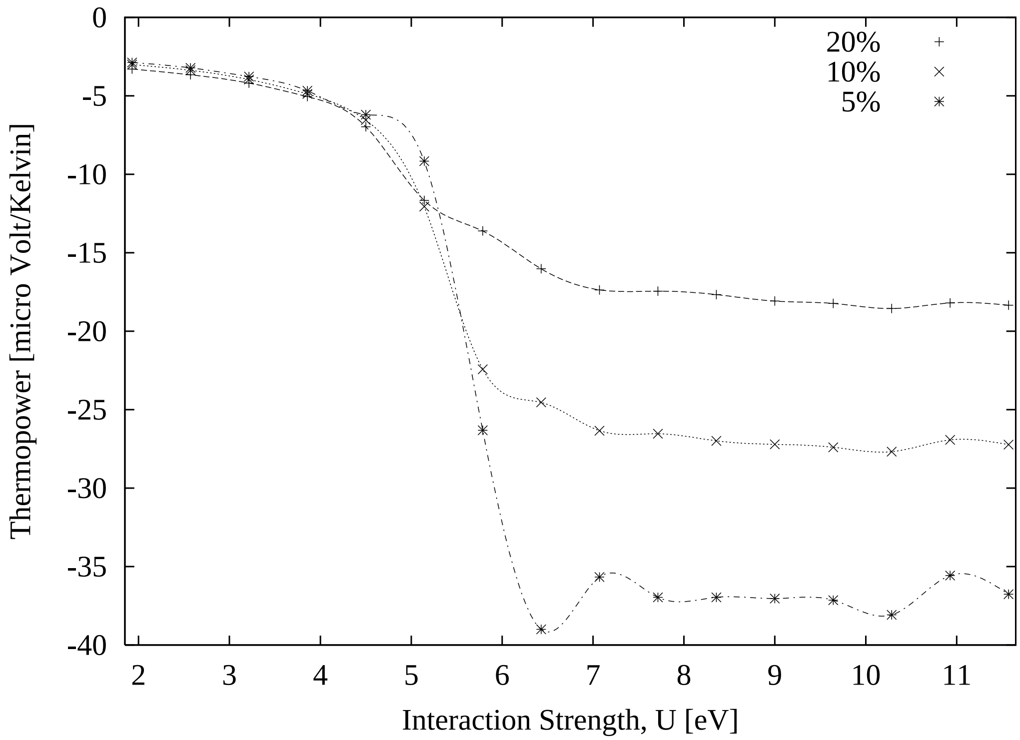


Figure 8.9: The results of the analytic evaluation of the thermopower from the Matsubara data.

behavior of the thermopower is qualitatively very similar to the experimental data. In this case the reason why there is a positive change in the thermopower as we decrease the doping is due to the disappearance of the quasiparticle peak. The quasiparticle peak is an electron-like phenomenon and contributes to negative thermopower but as the temperature is increased this peak vanishes and the intrinsic contribution from the Hubbard bands takes over – which in the case of small doping leads to positive thermopowers. The temperature at which the quasiparticle peak melts away increases as we increase the doping and thus the smaller doping values have larger, i.e. less negative or more positive, thermopower. It seems that in our case here there is hardly any contribution from the lower Hubbard band, it is too far below the Fermi-level to exert any influence on any of the transport parameters. In this sense this model, or at least the solution of it, is somewhat flawed.

## 8.7 Comparison with other models

In this, penultimate section of this chapter we will again take a look at the quasiparticle residue and the linear coefficient of specific heat and compare the results that we obtain in this model with models that have fewer number of bands and different underlying dispersion relation.

## 8.8 Conclusion

In this chapter we have looked at simple model for doped $LaTiO_3$ using the dynamical mean field theory and a newly developed method for solving the associated DMFT impurity model. This calculation is one of the first steps in the extension of the DMFT to realistic models. We investigated the solution of the model as a function of interaction strength and found strong indications of a metal insulator crossover at interaction strength corresponding to about twice the bandwidth, which agrees with previous estimates in the literature. Breakdown of the solution on the real axis prevented us from computing the density of states and the transport function in the insulating regime but in the metallic regime we obtained parameters in the range of typical metals with electron majority carriers. However, since undoped $LaTiO_3$ is an insulator it is of prime importance to be able to compute the parameters of the model in the insulating regime and further investigations are needed.

# Chapter 9

# Summary and Conclusion

In this thesis we have studied transport properties of strongly correlated electron systems with a special focus on the thermoelectric transport.

In chapter 1 we introduced the tools of the trade, namely the dynamical mean field theory and its use in solving problems in strongly correlated electron systems. We then motived the transport calculations done in the first half of the thesis by considering the theoretical importance and practical application of thermoelectric transport. We then discussed the ongoing extension of the dynamical mean field theory for dealing with real materials. This motivates the second half of the thesis where the computation of transport properties of real material within the dynamical mean field theory is considered and the details of such a computation are expounded.

In chapter 2 we introduced the Hubbard model and gave a short overview of the dynamical mean field theory. We then discussed a particular method for solving the dynamical mean field equations, the so called non crossing approximation and implemented a numerical procedure for solving those equations. The numerical solutions were investigated and their region of validity established. Analytic results were obtained for the behavior of the solution in the asymptotic high temperature regime.

In chapter 3 we started with a short introduction to the irreversible thermodynamics of electrical and thermal transport and considered some simple thermoelectric devices in order to introduce the thermoelectric figure of merit, its importance and its relation to material properties. We then proceeded to use the results of chapter 2 to compute the transport parameters for the Hubbard model as well as some other thermodynamic parameters for completeness. In order to extend our investigation to parameter regimes not accessible by the non-crossing approximation, mainly at low temperature, we made use of the so called iterated perturbation theory to obtain solutions of the dynamical mean field equation and compute transport parameters in those regimes. Analytic modeling of the transport parameters was carried out in the high and low temperature regimes and the low temperature results were shown to agree well with experimental data. We then considered the optimization of the figure of merit in strongly correlated system and reached the conclusion that significant figure of merit is not likely to occur in these systems.

In chapter 4 we extended the discussion of transport parameters to real materials and derived the lowest order expressions for the transport parameters in terms of real tight-binding Hamiltonians and self energies. We considered the small scattering limit of our expressions and showed that it agrees with the classical Boltzmann equation expression for the transport parameters. The numerical evaluation of the transport parameters was then discussed in great detail and we considered the role of symmetry and the computation of velocities. Finally we conducted some simple tests on the methods that have been developed.

Chapter 5 is an extension of the work in chapter 4 to systems described in terms of a non-orthogonal basis. We commented on the reason why non-orthogonal bases are necessary and discussed briefly the many body theory of electrons described in non-orthogonal bases. We then gave a derivation of the proper extension of the many body current operator to non-orthogonal bases. The expressions for the transport parameters were re-derived and finally we discussed the alternative computation of the current operator from basic quantum theory.

In chapter 6 we gave an overview of the program that was written to compute the transport parameters according to the algorithms developed in chapters 4 and 5.

Finally in chapters 7 and 8 we conducted some simple test of the computational methods.

In chapter 7 we considered simple metals under very simple assumptions for the functional form of the self energy. The computation revealed the inherent ambiguity with such an approach when there are multiple bands that are crossing the Fermi-surface. The thermopower computed for the alkali metals is in fairly good agreement with experimental data but for the noble metals and for Lithium we predict the wrong sign for the thermopower. This is a well known problem and was not expected to be resolved with such a simplistic approach.

In chapter 8 we looked at a simple model for $La_{1-x}Sr_xTiO_3$ for which the self energy can be computed. We discussed the behavior of the solution as a function of the interaction energy and found indications of the Mott metal-insulator transition at a critical $U$ which agrees well with theoretical estimates [55]. The nail down the energy scales in the model the data was compared to experimental results for both photoemission and specific heat measurements. The bandwidth of the model was determined from photoemission to be around 5.4eV which is consistent with the specific heat data.

The transport functions were then computed both using the methods developed in chapters 4 and 5 as well as with exact Fourier transform techniques which are available for this simple model. The two methods were found to be in good agreement with each other. The transport parameters were then computed from the transport functions and found to be in reasonable agreement with experiment.

In the appendices we have gathered additional details relevant for the computations performed in the previous chapters.

Appendix A contains a few analytic results for integrals associated with the computation of energy and transport parameters on the Bethe lattice.

Appendix B contains Fermi-liquid derivations of the transport parameters at low temperatures.

Appendix C contains details on the spectral representation of multi-orbital Green's functions, a topic which is not well known. We also discussed here the time derivatives of the Green's function and their connections to response functions of creation and destruction operators.

In appendix D we have collected together the basic equations for the regular tetrahedron method and rewritten the equations on a simpler and hopefully more stable form.

In appendix E we extended the regular tetrahedron method to integrands with a double pole.

In appendix F we extended the regular tetrahedron method to integrands with two non-degenerate single poles and derived the formulas for the weight factors that can easily be computed analytically. The case for the most general type of tetrahedron still resists an analytical solution but an approximate method was proposed.

Appendix G contains notes on an integral that comes up in the analytic solution obtained in appendix E.

# Appendix A

# A few integrals on the Bethe lattice

In this appendix I want to calculate a few integrals that appear frequently when one is dealing with mean field theory on the infinite dimensional Bethe lattice. In what follows I use the notation

$$a = \omega + \mu - Re\Sigma(\omega), \qquad b = Im\Sigma(\omega), \qquad \sigma = a - ib. \tag{A.1}$$

Remember that the bare spectral density for the infinite dimensional Bethe lattice is given by

$$D(\epsilon) = \frac{2}{\pi}\sqrt{1-\epsilon^2} \tag{A.2}$$

The first integral is the calculation of the local Green's function.

$$\begin{aligned} G_{loc}(\omega) &= \int d\epsilon \frac{D(\epsilon)}{\sigma - x} \quad = \quad \frac{2}{\pi}\int_{-1}^{1} dx \frac{\sqrt{1-x^2}}{\sigma - x} \\ &= \frac{2}{\pi}\int_0^{\pi} d\theta \sin^2\theta \frac{1}{\sigma - \cos\theta} \quad = \quad \frac{1}{\pi}\int_0^{2\pi} d\theta \sin^2\theta \frac{1}{\sigma - \cos\theta} \\ &= K_1(\sigma) \end{aligned} \tag{A.3}$$

Here I have defined

$$K_n(\sigma) = \frac{1}{\pi}\int_0^{2\pi} d\theta \sin^2\theta \frac{1}{(\sigma - \cos\theta)^n} \quad = \quad \frac{(-1)^{n-1}}{(n-1)!}\frac{d^{n-1}}{d\sigma^{n-1}}K_1(\sigma). \tag{A.4}$$

The second integral pops up in calculation of transport parameters.

$$\begin{aligned} H(\omega) &= \int d\epsilon \frac{1}{2} D(\epsilon)\rho^2(\epsilon,\omega) \quad = \quad \frac{1}{\pi^3}\int_{-1}^{1} dx \sqrt{1-x^2}\left(\frac{b}{(a-x)^2 + b^2}\right)^2 \\ &= \frac{1}{2\pi^3}\int_0^{2\pi} d\theta \sin^2\theta \left(\frac{b}{(\sigma - \cos\theta)(\sigma^* - \cos\theta)}\right)^2 \\ &= \frac{-1}{(2\pi)^3}\int_0^{2\pi} d\theta \sin^2\theta \left(\frac{1}{(\sigma - \cos\theta)} - \frac{1}{(\sigma^* - \cos\theta)}\right)^2 \\ &= \frac{-1}{(2\pi)^2} ReK_2(\sigma) + \frac{1}{(2\pi)^2 b} ImK_1(\sigma). \end{aligned} \tag{A.5}$$

Now let me turn to calculating the function $K_1(\sigma)$.

$$K_1(\sigma) = \frac{1}{\pi}\int_0^{2\pi} d\theta \sin^2\theta \frac{1}{\sigma-\cos\theta} = \frac{1}{\pi}\oint \frac{dz}{iz}\frac{\frac{-1}{4}(z-\frac{1}{z})^2}{\sigma-\frac{1}{2}(z+\frac{1}{z})}$$
$$= \frac{1}{2\pi i}\oint \frac{dz}{z^2}\frac{(z^2-1)^2}{z^2-2\sigma z+1} \tag{A.6}$$

The integrand has poles at

$$z_0 = 0, \quad z_1 = \sigma + \sqrt{\sigma^2-1} \quad \text{and} \quad z_2 = \sigma - \sqrt{\sigma^2-1} = \frac{1}{z_2}$$

Only one of two latter poles is within the unit circle, let's say it is $z_1$. The integral is now easily done by the residue method.

$$K_1(\sigma) = \frac{d}{dz}\left(\frac{(z^2-1)^2}{z^2-2\sigma z+1}\right)_{z=0} + \left(\frac{(z-\frac{1}{z})^2}{2(z-\sigma)}\right)_{z=z_1} = 2(\sigma+\sqrt{\sigma^2-1}) = 2z_1. \tag{A.7}$$

From this I now get

$$K_2 = -2\frac{\sigma+\sqrt{\sigma^2-1}}{\sqrt{\sigma^2-1}} \tag{A.8}$$

The original integrals are now

$$G_{loc}(\omega) = 2(\sigma+\sqrt{\sigma^2-1}) \tag{A.9}$$

and

$$H(\omega) = \frac{1}{2\pi^2}\left(Re\frac{\sigma+\sqrt{\sigma^2-1}}{\sqrt{\sigma^2-1}} + \frac{1}{b}Im(\sigma+\sqrt{\sigma^2-1}))\right)$$
$$= \frac{1}{4\pi^2}\left(Re\frac{G_{loc}}{\frac{1}{2}G_{loc}+\Sigma-\omega-\mu} + \frac{ImG_{loc}}{Im\Sigma}\right) \tag{A.10}$$

The third integral comes up in calculation of energy on the Bethe lattice.

$$\Gamma(\omega) = \int \rho(\epsilon,\omega)D(\epsilon)\epsilon d\epsilon = \frac{1}{\pi}Im\int G(\epsilon,\omega)D(\epsilon)\epsilon d\epsilon$$
$$= \frac{-2}{\pi^2}Im\int_{-1}^{1}\frac{x\sqrt{1-x^2}dx}{x-\sigma} \tag{A.11}$$

$$2\int_{-1}^{1}\frac{x\sqrt{1-x^2}dx}{x-\sigma} = \int_0^{2\pi}\frac{\cos\theta\sin^2\theta d\theta}{\cos\theta-\sigma}$$
$$= \oint \frac{dz}{iz}\frac{\frac{1}{2}(z+\frac{1}{z})\frac{-1}{4}(z-\frac{1}{z})^2}{\frac{1}{2}(z+\frac{1}{z})-\sigma}$$
$$= \frac{-1}{4i}\oint\frac{dz}{z^3}\frac{(z^2+1)(z^2-1)^2}{z^2-2\sigma z+1} \tag{A.12}$$

The last integrand has a triple pole at 0 and a single pole at $z_1$. Thus I get

$$\begin{aligned} 2\int_{-1}^{1}\frac{x\sqrt{1-x^2}dx}{x-\sigma} &= \frac{-\pi}{2}\left(\frac{1}{2}\frac{d^2}{dz^2}\left[\frac{(z^2+1)(z^2-1)^2}{z^2-2\sigma z+1}\right]_{z=0}+\left[\frac{(z+\frac{1}{z})(z-\frac{1}{z})^2}{2(z-\sigma)}\right]_{z=z_1}\right) \\ &= \frac{-\pi}{2}(4\sigma^2-2+4\sigma\sqrt{\sigma^2-1}) = -\pi(\sigma G_{loc}-1) \end{aligned} \tag{A.13}$$

Hence

$$\Gamma(\omega) = \frac{1}{\pi}Im(\sigma G_{loc}) = 2t^2\rho_{loc}(\omega)ReG_{loc}(\omega). \tag{A.14}$$

Here I used the fact that

$$\Sigma(\omega) = \omega+\mu-t^2G_{loc}(\omega)-\frac{1}{G_{loc}(\omega)}. \tag{A.15}$$

# Appendix B

# Fermi-liquid calculation of transport parameters

For small temperatures it is admissible in the calculation of transport parameters to make the following expansion of the self-energy:

$$\begin{aligned}
\Sigma(\omega) &= \Sigma'\omega + i\Sigma''\omega \\
&= \Sigma'(0) + \omega\frac{\partial\Sigma'(0)}{\partial\omega} + \Sigma'(0) + \frac{1}{2}\omega^2\frac{\partial^2\Sigma'(0)}{\partial\omega^2} \\
&= \Sigma'(0) + (1-\frac{1}{Z})\omega - \gamma_0((k_BT)^2 + (\frac{\omega}{\pi})^2) \\
&= \Sigma'(0) + (1-\frac{1}{Z})\omega - \gamma(1 + (\frac{\beta\omega}{\pi})^2)
\end{aligned} \tag{B.1}$$

Then we get (using $x = \beta\omega$),

$$\begin{aligned}
G(\omega,\epsilon) &= \frac{1}{\omega + \mu - \epsilon - \Sigma(\omega)} \\
&= \frac{1}{\frac{xk_BT}{Z} + \tilde{\mu} - \epsilon + \gamma(1 + (\frac{x}{\pi})^2)}
\end{aligned} \tag{B.2}$$

The parameter $Z$ is the quasiparticle residue, $\gamma$ is the scattering rate at the Fermi surface and $\tilde{\mu}$ is the renormalized Fermi energy. The correlation functions $A_n$'s used in the calculation of the transport parameters (see section 3.4) are given by

$$\begin{aligned}
A_n &= \frac{\pi N}{z}\int d\epsilon\Phi(\epsilon)\int d\omega\frac{\rho^2(\omega,\epsilon)(\beta\omega)^n}{4\cosh^2(\frac{\beta\omega}{2})} \\
&= \frac{\pi N k_BT}{z}\int d\epsilon\Phi(\epsilon)\int dx\frac{x^n}{4\cosh^2(\frac{x}{2})}\left\{\frac{\frac{\gamma}{\pi}[1+(\frac{x}{\pi})^2]}{[\frac{xT}{Z}+\tilde{\mu}-\epsilon]^2+\gamma^2[1+(\frac{x}{\pi})^2]^2}\right\}^2
\end{aligned} \tag{B.3}$$

Now $\gamma$ is proportional to $T^2$ so at very low temperatures the $\epsilon$ integral is concentrated around $\epsilon = \tilde{\mu} + xk_BT/Z$ but first note that

$$\int dx\frac{\gamma/\pi}{x^2+\gamma^2} = 1 \quad \text{and} \quad \int dx\left(\frac{\gamma/\pi}{x^2+\gamma^2}\right)^2 = \frac{1}{2\pi\gamma} \tag{B.4}$$

and thus for small $\gamma$ we replace $\left(\frac{\gamma/\pi}{x^2+\gamma^2}\right)^2$ with $\frac{\delta(x)}{2\pi\gamma}$. Then we get

$$\begin{aligned}
A_n &= \frac{\pi N k_B T}{2\pi z}\int dx \frac{x^n}{4\cosh^2(\frac{x}{2})}\frac{\Phi(\tilde{\mu}+\frac{xk_BT}{Z})}{\gamma[1+(\frac{x}{\pi})^2]} \\
&= \frac{Nk_BT}{2z\gamma}\int dx \frac{x^n}{4\cosh^2(\frac{x}{2})}\frac{\left\{\Phi(\tilde{\mu})+\frac{xk_BT}{Z}\frac{d\Phi(\tilde{\mu})}{d\tilde{\mu}}+\frac{1}{2}\left(\frac{xk_BT}{Z}\right)^2\frac{d^2\Phi(\tilde{\mu})}{d\tilde{\mu}^2}\right\}}{[1+(\frac{x}{\pi})^2]} \\
&= \frac{Nk_BT}{2z\gamma}\left\{\Phi(\tilde{\mu})E_n+\frac{k_BT}{Z}\frac{d\Phi(\tilde{\mu})}{d\tilde{\mu}}E_{n+1}+\frac{1}{2}\frac{(k_BT)^2}{Z^2}\frac{d^2\Phi(\tilde{\mu})}{d\tilde{\mu}^2}E_{n+2}\right\} \qquad \text{(B.5)}
\end{aligned}$$

where

$$E_m = \int dx \frac{x^m}{4\cosh^2(\frac{x}{2})[1+(\frac{x}{\pi})^2]}. \qquad \text{(B.6)}$$

I believe that these numbers have to be calculated numerically, which is easily done. We note that $E_m = 0$ for $m$ odd and we get

$$E_0 = 0.822467 \qquad \text{and} \qquad E_2 = 1.752180 \qquad \text{(B.7)}$$

The low temperature transport parameters are then:

$$\begin{aligned}
\sigma &= E_0\frac{Ne^2}{2z\gamma}\Phi(\tilde{\mu}) \qquad \text{(B.8)} \\
S &= -\frac{k_B}{e}\frac{E_2}{E_0}\frac{k_BT}{Z}\frac{d\ln(\Phi(\tilde{\mu}))}{d\tilde{\mu}} = -\frac{k_B}{e}\frac{E_2}{E_0}\frac{k_BT}{Z}\frac{d\ln(\sigma)}{d\tilde{\mu}} \qquad \text{(B.9)} \\
\kappa &= E_2\frac{k_BN(k_BT)}{2z\gamma}\Phi(\tilde{\mu}) \qquad \text{(B.10)}
\end{aligned}$$

The figure of merit is then given by

$$ZT = \frac{S^2\sigma T}{\kappa} = \frac{E_2}{E_0}\left(\frac{k_BT}{Z}\frac{d\ln\Phi(\tilde{\mu})}{d\tilde{\mu}}\right)^2. \qquad \text{(B.11)}$$

We note here that since the scattering rate goes as $T^2$ the conductivities diverge at zero temperature, $\sigma \sim T^{-2}$ and $\kappa \sim T^{-1}$. In this case we can of course neglect any contribution from the lattice thermal conductivity when computing the figure of merit.

We can go through the same exercise assuming that the scattering can be attributed to impurities in which case it would be finite at zero temperature and essentially independent of frequency – we end up with the same formulas as before except that now the constants $E_m$ would be different. Thus we get

$$\sigma = \frac{Ne^2}{2z\gamma}\Phi(\tilde{\mu}) \tag{B.12}$$

$$S = -\frac{k_B}{e}\frac{E_2}{E_0}\frac{k_BT}{Z}\frac{d\ln(\Phi(\tilde{\mu}))}{d\tilde{\mu}} = -\frac{k_B}{e}\frac{E_2}{E_0}\frac{k_BT}{Z}\frac{d\ln(\sigma)}{d\tilde{\mu}} \tag{B.13}$$

$$\kappa = \frac{\pi^2 k_B N(k_BT)}{6z\gamma}\Phi(\tilde{\mu}). \tag{B.14}$$

Now of course the electrical conductivity is finite at zero temperature and the thermal conductivity tends linearly to zero, which means that one would have to take the lattice thermal conductivity into account when the figure of merit is computed.

We should note here also that Wiedeman-Franz law holds for both cases but the Lorenz ratio, $\kappa/\sigma T$, is different, namely

$$L_{Fermi-Liquid} = \frac{E_2}{E_0}\left(\frac{k_B}{e}\right)^2 = 15.8 nW\Omega/K^2 \tag{B.15}$$

$$L_{Impurity} = \frac{\pi^2}{3}\left(\frac{k_B}{e}\right)^2 = 24.4 nW\Omega/K^2. \tag{B.16}$$

Hence one could use the Lorentz ratio as an indicator of the character of the low temperature scattering.

# Appendix C

## Spectral Representation of Green's functions

In this appendix we will derive the spectral representation of the multiorbital Green's function. Our starting point is the definition of the Green's function for complex time, $\tau$:

$$\begin{aligned}
G_{pq}(\tau) &= -\langle T_\tau c_p(\tau) c_q^+(0)\rangle \\
&\stackrel{\tau\geq 0}{=} \frac{-1}{Z}\,\mathrm{Tr}\left\{e^{\beta H} e^{\tau H} c_p e^{-\tau H} c_q^+\right\} \\
&= \frac{-1}{Z}\sum_n \langle n|e^{\beta H} e^{\tau H} c_p e^{-\tau H} c_q^+|n\rangle \\
&= \frac{-1}{Z}\sum_{nm} e^{(\tau-\beta)E_n - \tau E_m}\langle n|c_p|m\rangle\langle m|c_q^+|n\rangle
\end{aligned} \tag{C.1}$$

This expression is now Fourier transformed to Matsubara frequency axis and noting that $i\omega$ is Fermionic we get:

$$\begin{aligned}
G_{pq}(i\omega) &= \int_0^\beta G_{pq}(\tau) e^{i\omega\tau} \\
&= \frac{1}{Z}\sum_{nm}\langle n|c_p|m\rangle\langle m|c_q^+|n\rangle \frac{e^{-\beta E_n} + e^{-\beta E_m}}{i\omega - E_m + E_n}.
\end{aligned} \tag{C.2}$$

The retarded and the advanced Green's functions are now obtained by replacing the Matsubara frequency, $i\omega$ by $\omega + i0$ and $\omega - i0$ respectively. Using the fact that we can write:

$$\frac{1}{\omega \pm i0 + \omega_0} = \mathcal{P}\frac{1}{\omega + \omega_0} \mp i\pi\delta(\omega + \omega_0) \tag{C.3}$$

we get,

$$\begin{aligned}
G^R_{pq}(\omega) &= \frac{1}{Z}\sum_{nm}\langle n|c_p|m\rangle\langle m|c_q^+|n\rangle \left(e^{-\beta E_n} + e^{-\beta E_m}\right) \\
&\quad\times\left(\mathcal{P}\frac{1}{\omega - E_m + E_n} - i\pi\delta(\omega - E_m + E_n)\right)
\end{aligned} \tag{C.4}$$

and similarly,

$$\begin{aligned} G^A_{pq}(\omega) &= \frac{1}{Z}\sum_{nm}\langle n|c_p|m\rangle\langle m|c^+_q|n\rangle\left(e^{-\beta E_n}+e^{-\beta E_m}\right) \\ &\quad\times\left(\mathcal{P}\frac{1}{\omega-E_m+E_n}+i\pi\delta(\omega-E_m+E_n)\right). \end{aligned} \tag{C.5}$$

Let us now look at the complex conjugate of the matrix elements of the retarded Green's function.

$$\begin{aligned} (G^R_{pq}(\omega))^* &= \frac{1}{Z}\sum_{nm}\langle m|c^+_p|n\rangle\langle n|c_q|m\rangle\left(e^{-\beta E_n}+e^{-\beta E_m}\right) \\ &\quad\times\left(\mathcal{P}\frac{1}{\omega-E_m+E_n}+i\pi\delta(\omega-E_m+E_n)\right) \\ &= G^A_{qp}(\omega). \end{aligned} \tag{C.6}$$

Thus we see that the advanced Green's function is the Hermitian conjugate of the retarded one. From the representation above we see that the Green's function can be written as

$$G_{pq}(z) = \int \frac{\rho_{pq}(\epsilon)}{z-\epsilon} \tag{C.7}$$

where the so called spectral density matrix, $\rho_{pq}$ is given by:

$$\rho_{pq}(\epsilon) = \frac{1}{Z}\sum_{nm}\langle n|c_p|m\rangle\langle m|c^+_q|n\rangle\left(e^{-\beta E_n}+e^{-\beta E_m}\right)\delta(\epsilon-E_m+E_n). \tag{C.8}$$

and by looking at the expressions for the real and the advanced Green's function we see that the spectral density can be written as:

$$\rho_{pq}(\epsilon) = \frac{-1}{2\pi i}\left[G^R_{pq}(\epsilon)-G^A_{pq}(\epsilon)\right] = \frac{-1}{2\pi i}\left[G^R_{pq}(\epsilon)-\left(G^R\right)^+_{pq}(\epsilon)\right]. \tag{C.9}$$

We should note here that in contrast to the single orbital spectral densities that we are used to from regular many body theory, the spectral density matrix is not necessarily real and positive, but as we can see it is Hermitian and its diagonal values are all real and positive.

Using the spectral representation it is now easy to compute the complex time Green's function:

$$G_{pq}(\tau) = -\int_{-\infty}^{\infty} d\epsilon\rho_{pq}(\epsilon)e^{-\epsilon\tau}\left(\theta(\tau)f(-\epsilon)-\theta(-\tau)f(\epsilon)\right). \tag{C.10}$$

Finally let us see how we can relate the complex time derivative of the Green's function to expectation values like $\langle(\partial_\tau c_p)(\tau)c_q^+(0)\rangle$. To do this we note first that:

$$\begin{aligned}
&\frac{1}{Z}\operatorname{Tr}\left\{e^{\beta H}(\partial_\tau A)(\tau)B(0)\right\} = \frac{1}{Z}\operatorname{Tr}\left\{e^{\beta H}e^{\tau H}[H,A]e^{-\tau H}B(0)\right\} \\
=&\frac{-1}{Z}\operatorname{Tr}\left\{e^{\beta H}e^{\tau H}Ae^{-\tau H}[H,B]\right\} = \frac{-1}{Z}\operatorname{Tr}\left\{e^{\beta H}A(\tau)(\partial_\tau B)(0)\right\}.
\end{aligned} \tag{C.11}$$

Now since there is no time dependence in the $B$ operator we see that:

$$\begin{aligned}
&\frac{\partial^n}{\partial\tau^n}\left(\frac{1}{Z}\operatorname{Tr}\left\{e^{\beta H}A(\tau)B(0)\right\}\right) = \frac{1}{Z}\operatorname{Tr}\left\{e^{\beta H}(\partial_\tau^n A)(\tau)B(0)\right\} \\
=&\frac{(-1)^q}{Z}\operatorname{Tr}\left\{e^{\beta H}(\partial_\tau^{(n-q)}A)(\tau)(\partial_\tau^q B)(0)\right\} = \frac{(-1)^n}{Z}\operatorname{Tr}\left\{e^{\beta H}A(\tau)(\partial_\tau^n B)(0)\right\}.
\end{aligned} \tag{C.12}$$

We see now that for $\tau \in ]0,\beta[$ we have

$$\begin{aligned}
\left\langle(\partial_\tau^m c_p)(\tau)(\partial_\tau^n c_q^+)\right\rangle &= (-1)^{n+1}\frac{\partial^{(m+n)}}{\partial\tau^{(m+n)}}G_{pq}(\tau) \\
\left\langle(\partial_\tau^m c_q^+)(\tau)(\partial_\tau^n c_p)\right\rangle &= (-1)^{n}\frac{\partial^{(m+n)}}{\partial\tau^{(m+n)}}G_{pq}(-\tau)
\end{aligned} \tag{C.13}$$

Strictly speaking these equations do not hold at $\tau = 0$ where the Green's function has a discontinuity and the time derivative would therefore be a delta-function at zero. The expectation values however do not have any such pathologies. As we know the value of the Green's function at zero is arbitrary and depends on definition and is usually defined as the limit as one approaches zero from either the positive or the negative direction. The same should of course hold for its derivative, i.e. the derivative is computed in an open interval that does not include zero and the value at zero depends on definition, and has not delta-function. If we understand the derivatives in that sense the equations above hold for all $\tau$.

# Appendix D

# The analytic tetrahedron method

In this appendix we will write up the equations of Lambin and Vigneron for the weight factors used in the analytical tetrahedron method. The purpose of this is to rewrite their formulas in a simpler, more readable and hopefully more stable form.

Before we start writing out the equations let us define a few symbols. The external frequency is denoted by $z$ and the energy at corner number $i$ is denoted by $E_i$. We define $z_i = z - E_i$ and also $E_{ij} = E_i - E_j$.

In the general case when all the tetrahedron corners have different energies the equation for the weight factor at corner $i$ is according to LV

$$\begin{aligned} r_i &\equiv 6\int_0^1 dc \int_0^{1-c} db \int_0^{1-b-c} da \frac{(1-a-b-c)\delta_{i1} + a\delta_{i2} + b\delta_{i3} + c\delta_{i4}}{z_1 - aE_{21} - bE_{31} - cE_{41}} \\ &= \frac{z_i^2}{\prod_{k\neq i} E_{ki}} + \sum_{j\neq i} \frac{z_j^3}{\prod_{k\neq j} E_{kj}} \frac{\log\left(\frac{z_j}{z_i}\right)}{E_{ij}}. \end{aligned} \tag{D.1}$$

If we now use the identity:

$$0 = \sum_{i=1}^{4} \frac{z_i^2}{\prod_{j\neq i}(z_i - z_j)} = \sum_{i=1}^{4} \frac{z_i^2}{\prod_{j\neq i} E_{ji}} \tag{D.2}$$

the equation for the weight factor can be written as

$$\begin{aligned} r_i &= \sum_{j\neq i} \frac{z_j^2}{\prod_{k\neq j} E_{kj}} \left\{ \frac{z_j}{E_{ij}} \log\left(\frac{z_j}{z_i}\right) - 1 \right\} \\ &= \sum_{j\neq i} \frac{z_j}{\prod_{k\neq i,j} E_{kj}} \left\{ \frac{z_j}{E_{ji}} - \frac{z_j^2}{E_{ij}^2} \log\left(1 + \frac{E_{ji}}{z_j}\right) \right\} \\ &= \sum_{j\neq i} \frac{z_j}{\prod_{k\neq i,j} E_{kj}} \mathrm{lv}\left(\frac{z_j}{E_{ji}}\right). \end{aligned} \tag{D.3}$$

Here we have defined the so called Lambin-Vigneron function as:

$$\mathrm{lv}(x) = x\left(1 - x\log\left[1 + \frac{1}{x}\right]\right). \tag{D.4}$$

This is a simple function which is easy to compute and also has the added benefit of having nice asymptotic limits, i.e.

$$\lim_{x\to 0} \mathrm{lv}(x) = 0 \qquad \text{and} \qquad \lim_{x\to\infty} \mathrm{lv}(x) = \frac{1}{2}. \tag{D.5}$$

For considering the cases where the some of the corner energies are identical it is useful to write out the equations above explicitly for each corner:

$$\begin{aligned}
r_1 &= \frac{z_2}{E_{32}E_{42}}\mathrm{lv}\left(\frac{z_2}{E_{21}}\right) + \frac{z_3}{E_{23}E_{43}}\mathrm{lv}\left(\frac{z_3}{E_{31}}\right) + \frac{z_4}{E_{24}E_{34}}\mathrm{lv}\left(\frac{z_4}{E_{41}}\right) \\
r_2 &= \frac{z_1}{E_{31}E_{41}}\mathrm{lv}\left(\frac{z_1}{E_{12}}\right) + \frac{z_3}{E_{13}E_{43}}\mathrm{lv}\left(\frac{z_3}{E_{32}}\right) + \frac{z_4}{E_{14}E_{34}}\mathrm{lv}\left(\frac{z_4}{E_{42}}\right) \\
r_3 &= \frac{z_1}{E_{21}E_{41}}\mathrm{lv}\left(\frac{z_1}{E_{13}}\right) + \frac{z_2}{E_{12}E_{42}}\mathrm{lv}\left(\frac{z_2}{E_{23}}\right) + \frac{z_4}{E_{14}E_{24}}\mathrm{lv}\left(\frac{z_4}{E_{43}}\right) \\
r_4 &= \frac{z_1}{E_{21}E_{31}}\mathrm{lv}\left(\frac{z_1}{E_{14}}\right) + \frac{z_2}{E_{12}E_{32}}\mathrm{lv}\left(\frac{z_2}{E_{24}}\right) + \frac{z_3}{E_{13}E_{23}}\mathrm{lv}\left(\frac{z_3}{E_{34}}\right)
\end{aligned} \tag{D.6}$$

The next case we consider is when two corners have equal energies and we assume here that the corners have been ordered in such as way that $E_1 = E_2$. Looking at the formulas in (D.6) we see that the limit $E_1 \to E_2$ is trivial take for the weight factors for corners 1 and 2 but for corners 3 and 4 two terms must be taken together and using Mathematica we get:

$$\begin{aligned}
r_2 &= \frac{1}{2}\frac{z_2}{E_{32}E_{42}} + \frac{z_3}{E_{23}E_{43}}\mathrm{lv}\left(\frac{z_3}{E_{32}}\right) + \frac{z_4}{E_{24}E_{34}}\mathrm{lv}\left(\frac{z_4}{E_{42}}\right) \\
r_3 &= \frac{z_2}{E_{23}E_{24}} - \left[\frac{2z_3}{E_{23}E_{24}} + \frac{z_4}{E_{24}^2}\right]\mathrm{lv}\left(\frac{z_2}{E_{23}}\right) + \frac{z_4}{E_{24}^2}\mathrm{lv}\left(\frac{z_4}{E_{43}}\right) \\
r_4 &= \frac{z_2}{E_{23}E_{24}} - \left[\frac{2z_4}{E_{23}E_{24}} + \frac{z_3}{E_{23}^2}\right]\mathrm{lv}\left(\frac{z_2}{E_{24}}\right) + \frac{z_3}{E_{23}^2}\mathrm{lv}\left(\frac{z_3}{E_{34}}\right)
\end{aligned} \tag{D.7}$$

The next case we consider is $E_1 = E_2$ and $E_4 = E_3$ and we see from the formulas in equation (D.7) that the limit $E_4 \to E_3$ is trivial for corners 3 and 4 and the weight factor for corner 2 follows from symmetry. Hence we get:

$$\begin{aligned}
r_2 &= \frac{z_3}{E_{32}^2} + \frac{1}{2}\frac{z_2}{E_{32}^2} - 3\frac{z_2}{E_{32}^2}\mathrm{lv}\left(\frac{z_3}{E_{32}}\right) \\
r_3 &= \frac{z_2}{E_{23}^2} + \frac{1}{2}\frac{z_3}{E_{23}^2} - 3\frac{z_3}{E_{23}^2}\mathrm{lv}\left(\frac{z_2}{E_{23}}\right)
\end{aligned} \tag{D.8}$$

Next case is $E_1 = E_2 = E_3$ and this case we can either obtain from the formulas in equation (D.7) or simply do the corresponding integral which is simple in this case since we have:

$$\begin{aligned} r_3 &= \int_0^1 dc \int_0^{1-c} db \int_0^{1-b-c} da \frac{b}{z_3 - cE_{43}} \\ r_4 &= \int_0^1 dc \int_0^{1-c} db \int_0^{1-b-c} da \frac{c}{z_3 - cE_{43}}. \end{aligned} \tag{D.9}$$

Performing these integrals we obtain:

$$\begin{aligned} r_3 &= \frac{2z_3 - 5z_4}{6E_{34}^2} + \frac{z_4}{E_{34}^2} \mathrm{lv}\left(\frac{z_4}{E_{43}}\right) \\ r_4 &= \frac{z_4}{E_{43}^2} + \frac{1}{2}\frac{z_3}{E_{43}^2} - 3\frac{z_3}{E_{43}^2} \mathrm{lv}\left(\frac{z_4}{E_{43}}\right) \end{aligned} \tag{D.10}$$

The final case is of course the simplest one where all the corners have the same energy and in that case we obtain:

$$r_4 = \frac{1}{4}\frac{1}{z_4} \tag{D.11}$$

# Appendix E

# The integration weights for the SSDD case

In this appendix we will write up the equations for the tetrahedral integration weights of the SSDD case. These equations can be obtained very simply from the equations of Lambin and Vigneron in appendix D. Namely we have:

$$\begin{aligned} w_i(z) &\equiv 6\int_0^1 dc \int_0^{1-c} db \int_0^{1-b-c} da \frac{(1-a-b-c)\delta_{i1} + a\delta_{i2} + b\delta_{i3} + c\delta_{i4}}{(z_1 - aE_{21} - bE_{31} - cE_{41})^2} \\ &= -\frac{d}{dz}\int_0^1 dc \int_0^{1-c} db \int_0^{1-b-c} da \frac{(1-a-b-c)\delta_{i1} + a\delta_{i2} + b\delta_{i3} + c\delta_{i4}}{z_1 - aE_{21} - bE_{31} - cE_{41}} \\ &= -\frac{d}{dz} r_i(z). \end{aligned} \tag{E.1}$$

Thus the only thing we need to do is to differentiate the equation from appendix D to obtain our integration weights. We will write the results in terms of the Lambin-Vigneron function from appendix D, its derivative $\mathrm{lv}'$ and the associated function $\mathrm{lv}_2$ which we define as:

$$\mathrm{lv}_2(x) = -\mathrm{lv}(x) - x\,\mathrm{lv}'(x). \tag{E.2}$$

All of these functions are quite simple and have nice asymptotic limits.

The weight factors are now as follows:

### Case 1: All corners different

$$\begin{aligned} w_1 &= \frac{1}{E_{32}E_{42}}\mathrm{lv}_2\left(\frac{z_2}{E_{21}}\right) + \frac{1}{E_{23}E_{43}}\mathrm{lv}_2\left(\frac{z_3}{E_{31}}\right) + \frac{1}{E_{24}E_{34}}\mathrm{lv}_2\left(\frac{z_4}{E_{41}}\right) \\ w_2 &= \frac{1}{E_{31}E_{41}}\mathrm{lv}_2\left(\frac{z_1}{E_{12}}\right) + \frac{1}{E_{13}E_{43}}\mathrm{lv}_2\left(\frac{z_3}{E_{32}}\right) + \frac{1}{E_{14}E_{34}}\mathrm{lv}_2\left(\frac{z_4}{E_{42}}\right) \\ w_3 &= \frac{1}{E_{21}E_{41}}\mathrm{lv}_2\left(\frac{z_1}{E_{13}}\right) + \frac{1}{E_{12}E_{42}}\mathrm{lv}_2\left(\frac{z_2}{E_{23}}\right) + \frac{1}{E_{14}E_{24}}\mathrm{lv}_2\left(\frac{z_4}{E_{43}}\right) \\ w_4 &= \frac{1}{E_{21}E_{31}}\mathrm{lv}_2\left(\frac{z_1}{E_{14}}\right) + \frac{1}{E_{12}E_{32}}\mathrm{lv}_2\left(\frac{z_2}{E_{24}}\right) + \frac{1}{E_{13}E_{23}}\mathrm{lv}_2\left(\frac{z_3}{E_{34}}\right) \end{aligned} \tag{E.3}$$

**Case 2: Two corners equal**

$$\begin{aligned}
w_2 &= \frac{-1}{2E_{32}E_{42}} + \frac{1}{E_{23}E_{43}}\mathrm{lv}_2\left(\frac{z_3}{E_{32}}\right) + \frac{1}{E_{24}E_{34}}\mathrm{lv}_2\left(\frac{z_4}{E_{42}}\right) \\
w_3 &= \frac{-1}{E_{23}E_{24}} + \frac{1}{E_{24}^2}\mathrm{lv}_2\left(\frac{z_4}{E_{43}}\right) \\
&+ \left[\frac{2}{E_{23}E_{24}} + \frac{1}{E_{24}^2}\right]\mathrm{lv}\left(\frac{z_2}{E_{23}}\right) + \left[\frac{2z_3}{E_{23}^2E_{24}} + \frac{z_4}{E_{23}E_{24}^2}\right]\mathrm{lv}'\left(\frac{z_2}{E_{23}}\right) \\
w_4 &= \frac{-1}{E_{23}E_{24}} + \frac{1}{E_{23}^2}\mathrm{lv}_2\left(\frac{z_3}{E_{34}}\right) \\
&+ \left[\frac{2}{E_{23}E_{24}} + \frac{1}{E_{23}^2}\right]\mathrm{lv}\left(\frac{z_2}{E_{24}}\right) + \left[\frac{2z_4}{E_{23}E_{24}^2} + \frac{z_3}{E_{23}^2E_{24}}\right]\mathrm{lv}'\left(\frac{z_2}{E_{24}}\right)
\end{aligned} \tag{E.4}$$

**Case 3: Two pairs of equal corners**

$$\begin{aligned}
w_2 &= \frac{z_3}{E_{32}^2} + \frac{1}{2}\frac{z_2}{E_{32}^2} - 3\frac{z_2}{E_{32}^2}\mathrm{lv}\left(\frac{z_3}{E_{32}}\right) \\
w_3 &= \frac{-3}{2E_{23}^2} + \frac{3}{E_{23}^2}\mathrm{lv}\left(\frac{z_2}{E_{23}}\right) + 3\frac{z_3}{E_{23}^3}\mathrm{lv}'\left(\frac{z_2}{E_{23}}\right)
\end{aligned} \tag{E.5}$$

**Case 4: Three equal corners**

$$\begin{aligned}
w_3 &= \frac{1}{2E_{34}^2} + \frac{1}{E_{34}^2}\mathrm{lv}_2\left(\frac{z_4}{E_{43}}\right) \\
w_4 &= \frac{-3}{2E_{43}^2} + \frac{3}{E_{43}^2}\mathrm{lv}\left(\frac{z_4}{E_{43}}\right) + 3\frac{z_3}{E_{43}^3}\mathrm{lv}'\left(\frac{z_4}{E_{43}}\right)
\end{aligned} \tag{E.6}$$

**Case 5: All corners equal**

$$w_4 = \frac{-1}{4}\frac{1}{z_4^2} \tag{E.7}$$

# Appendix F

# Integration weights for nondegenerate denominators

In this appendix we will derive the equations for the integration weight factors associated with computing the SSOD, OSDD and OSOD contributions to the transport function. The integral that we want to do is

$$w_i(z) = 6\int_\Delta \frac{[(1-a-b-c)\delta_{i1} + a\delta_{i2} + b\delta_{i3} + c\delta_{i4}]\, dadbdc}{[z - E_1^p - aE_{21}^p - bE_{31}^p - cE_{41}^p]\,[z - E_1^q - aE_{21}^q - bE_{31}^q - cE_{41}^q]} \tag{F.1}$$

where $\Delta = \{(a,b,c)|a,b,c \geq 0, a+b+c \leq 1\}$. Note that here $E^q$ might actually be the complex conjugate of the eigenvalues of the Hamiltonian. The only thing we assume is that the two denominators are different. To simplify notation here we define:

$$\alpha_i = E_i^p \qquad \text{and} \qquad \gamma_i = E_i^q \tag{F.2}$$

and then the integral that we need to do here is the following:

$$w_i(z) = 6\int_\Delta \frac{[(1-a-b-c)\delta_{i1} + a\delta_{i2} + b\delta_{i3} + c\delta_{i4}]\, dadbdc}{[\alpha_1 + a\alpha_{21} + b\alpha_{31} + c\alpha_{41}]\,[\gamma_1 + a\gamma_{21} + b\gamma_{31} + c\gamma_{41}]}. \tag{F.3}$$

Note that since we assume that the energies $\alpha_i$ and $\gamma_i$ are different we do not have to distinguish between the SS and the OS cases.

## F.1 Preliminaries

Before we start tackling these integrals let us define for later convenience the following functions and symbols:

$$\mathrm{Ld}(x, p_i, p_j; p_k) = \log[p_i + x(p_k - p_i)] - \log[p_j + x(p_k - p_j)] \tag{F.4}$$

$$\mathrm{Lx}_n(p_i, p_j; p_k) = \int_0^1 dx x^n \mathrm{Ld}(x, p_i, p_j; p_k) \tag{F.5}$$

$$\mathrm{Gx}_1(p_i, p_j; p_k, r) = \int_0^1 dx \frac{\mathrm{Ld}(x, p_i, p_j; p_k)}{x - r} \tag{F.6}$$

$$\alpha^i_{jk} = \frac{\alpha_i}{\alpha_{jk}}, \qquad \gamma^i_{jk} = \frac{\gamma_i}{\gamma_{jk}}, \qquad D^{jk}_{\alpha\gamma} = \alpha_j\gamma_k - \alpha_k\gamma_j \tag{F.7}$$

$$\Delta^{ijk}_{\alpha\gamma} = \begin{vmatrix} 1 & 1 & 1 \\ \alpha_i & \alpha_j & \alpha_k \\ \gamma_i & \gamma_j & \gamma_k \end{vmatrix} = \alpha_{ji}\gamma_{ki} - \alpha_{ki}\gamma_{ji} = D^{ij}_{\alpha\gamma} + D^{jk}_{\alpha\gamma} + D^{ki}_{\alpha\gamma}, \qquad \Gamma^{ijk}_{\alpha\gamma} = \frac{D^{jk}_{\alpha\gamma}}{\Delta^{ijk}_{\alpha\gamma}}. \tag{F.8}$$

We see that both $D^{jk}_{\alpha\gamma}$ and $\Delta^{ijk}_{\alpha\gamma}$ are antisymmetric in both $j, k$ and $\alpha, \gamma$ and thus $\Gamma^{ijk}_{\alpha\gamma}$ is symmetric in these indices. We note also for future reference the following identities:

$$1 + \alpha^n_{mn} = \alpha^m_{mn}, \qquad \alpha_{ab}\left(\alpha^b_{ab} + \Gamma^{abc}_{\alpha\gamma}\right) = \alpha_{bc}\Gamma^{cab}_{\alpha\gamma} \tag{F.9}$$

Similar identities for $\gamma$ are obtained by using the symmetry properties of the symbols. The functions $\mathrm{Lx}_n$ are elementary and easily evaluated but $\mathrm{Gx}_1$ is a rather tricky function to evaluate and we refer the reader to appendix G for further details.

The task at hand is now to evaluate a triple integral. We will denote the first one of these by $I_1$ the second one by $I_2$ and the third one, which is equal to the desired weight factor, by $I_3$.

## F.2 All the corner energies are the same

In this case the integral is trivial, all the weight factors are equal and we get,

$$w_1 = \frac{1}{4\alpha_1\gamma_1} \tag{F.10}$$

## F.3 Three corner energies are equal

We assume here that the energies at the first three corners are equal. The weight factors for those corners will therefore be equal to $w_1$ and the one for the last corner is $w_4$.

### F.3.1 Weight factor for corners 1,2 and 3

$$I_1(b,c) = 6\int_0^{1-b-c} \frac{a\,da}{[\alpha_1 + c\alpha_{41}][\gamma_1 + c\gamma_{41}]} = 3\frac{(1-b-c)^2}{[\alpha_1 + c\alpha_{41}][\gamma_1 + c\gamma_{41}]} \tag{F.11}$$

$$I_2(c) = \int_0^{1-c} I_1(b,c)\,db = \frac{(1-c)^3}{[\alpha_1 + c\alpha_{41}][\gamma_1 + c\gamma_{41}]} = \frac{1}{D^{14}_{\alpha\gamma}}\left[\frac{(c-1)^3}{c + \alpha^1_{41}} - \frac{(c-1)^3}{c + \gamma^1_{41}}\right] \tag{F.12}$$

We now use the following factorization:

$$(x-1)^3 = (x+a)[x^2 - 3x + 3 + a^2 + a(3-x)] - (1+a)^3 \tag{F.13}$$

and thus we have

$$I_2(c) = \frac{1}{D^{14}_{\alpha\gamma}} \left\{ \alpha^1_{41}(\alpha^1_{41} + 3 - c) - \gamma^1_{41}(\gamma^1_{41} + 3 - c) - \frac{(\alpha^4_{41})^3}{c + \alpha^1_{41}} + \frac{(\gamma^4_{41})^3}{c + \gamma^1_{41}} \right\}. \tag{F.14}$$

This is now easy to integrate over c and we obtain:

$$\begin{aligned} I_3 &= \frac{1}{D^{14}_{\alpha\gamma}} \left\{ \alpha^1_{41}(\alpha^1_{41} + 5/2) - (\alpha^4_{41})^3 \log\left(\frac{\alpha_4}{\alpha_1}\right) \right\} \\ &- \frac{1}{D^{14}_{\alpha\gamma}} \left\{ \gamma^1_{41}(\gamma^1_{41} + 5/2) - (\gamma^4_{41})^3 \log\left(\frac{\gamma_4}{\gamma_1}\right) \right\}. \end{aligned} \tag{F.15}$$

### F.3.2 Weight factor for corner 4

$$I_1(b,c) = 6 \int_0^{1-b-c} \frac{c\,da}{[\alpha_1 + c\alpha_{41}][\gamma_1 + c\gamma_{41}]} = \frac{6c(1-b-c)}{[\alpha_1 + c\alpha_{41}][\gamma_1 + c\gamma_{41}]} \tag{F.16}$$

$$\begin{aligned} I_2(c) &= \int_0^{1-c} I_1(b,c)\,db = \frac{3c(1-c)^2}{[\alpha_1 + c\alpha_{41}][\gamma_1 + c\gamma_{41}]} \\ &= \frac{3}{D^{14}_{\alpha\gamma}} \left[ \frac{c(c-1)^2}{c + \gamma^1_{41}} - \frac{c(c-1)^2}{c + \alpha^1_{41}} \right] \end{aligned} \tag{F.17}$$

We now use the following factorization:

$$x(x-1)^2 = (x+a)[x^2 - 2x + 1 + a(a + 2 - x)] - a(1+a)^2 \tag{F.18}$$

and thus we have

$$I_2(c) = \frac{3}{D^{14}_{\alpha\gamma}} \left\{ \gamma^1_{41}(\gamma^1_{41} + 2 - c) - \alpha^1_{41}(\alpha^1_{41} + 2 - c) - \frac{\gamma^1_{41}(\gamma^4_{41})}{c + \gamma^1_{41}} + \frac{\alpha^1_{41}(\alpha^4_{41})^2}{c + \alpha^1_{41}} \right\}. \tag{F.19}$$

We integrate over $c$ as before and get:

$$\begin{aligned} I_3 &= \frac{3}{D^{14}_{\alpha\gamma}} \left\{ \gamma^1_{41}(\gamma^1_{41} + 3/2) - \gamma^1_{41}(\gamma^4_{41})^2 \log\left(\frac{\gamma_4}{\gamma_1}\right) \right\} \\ &- \frac{3}{D^{14}_{\alpha\gamma}} \left\{ \alpha^1_{41}(\alpha^1_{41} + 3/2) - \alpha^1_{41}(\alpha^1_{41})^2 \log\left(\frac{\alpha_4}{\alpha_1}\right) \right\} \end{aligned} \tag{F.20}$$

## F.4 Two pairs of corner energies are equal

We assume here that corner 1 and 2 have equal energies and weight factor, $w_1$ and that corner 3 and 4 have equal energies and weight factor $w_4$.

### F.4.1 Weight factor for corners 1 and 2

$$
\begin{aligned}
I_1(b,c) &= 6\int_0^{1-b-c} \frac{a\,da}{[\alpha_1+(b+c)\alpha_{41}][\gamma_1+(b+c)\gamma_{41}]} \\
&= 3\frac{(b+c-1)^2}{[\alpha_1+(b+c)\alpha_{41}][\gamma_1+(b+c)\gamma_{41}]}
\end{aligned} \tag{F.21}
$$

We now make the following change of variables:

$$
u = b+c, \qquad v = b-c, \qquad \int_0^1 dc \int_0^{1-c} db \longrightarrow \frac{1}{2}\int_0^1 du \int_{-u}^{u} dv \tag{F.22}
$$

The integral is then:

$$
I_1(u,v) = 3\frac{(u-1)^2}{[\alpha_1+u\alpha_{41}][\gamma_1+u\gamma_{41}]} \tag{F.23}
$$

Now the integral over $v$ just multiplies $I_1$ by $u$ with the factor of 2 being canceled by the Jacobian. Then we get

$$
\begin{aligned}
I_3 &= \int_0^1 \frac{3u(u-1)^2du}{[\alpha_1+u\alpha_{41}][\gamma_1+u\gamma_{41}]} \\
&= \frac{3}{D^{14}_{\alpha\gamma}}\left\{\gamma^1_{41}(\gamma^1_{41}+3/2)-\gamma^1_{41}(\gamma^4_{41})^2\log\left(\frac{\gamma_4}{\gamma_1}\right)\right\} \\
&- \frac{3}{D^{14}_{\alpha\gamma}}\left\{\alpha^1_{41}(\alpha^1_{41}+3/2)-\alpha^1_{41}(\alpha^4_{41})^2\log\left(\frac{\alpha_4}{\alpha_1}\right)\right\}.
\end{aligned} \tag{F.24}
$$

Here we got the answer right away since we noticed that the integral was the same as the one being done in §F.3.2.

### F.4.2 Weight factor for corners 3 and 4

To obtain the weight factors for corners 3 and 4 we just have to take the answer from §F.4.1 and switch the indices 1 and 4. Thus we get:

$$
\begin{aligned}
I_3 &= \frac{3}{D^{41}_{\alpha\gamma}}\left\{\gamma^4_{14}(\gamma^4_{14}+3/2)-\gamma^4_{14}(\gamma^1_{14})^2\log\left(\frac{\gamma_1}{\gamma_4}\right)\right\} \\
&- \frac{3}{D^{41}_{\alpha\gamma}}\left\{\alpha^4_{14}(\alpha^4_{14}+3/2)-\alpha^4_{14}(\alpha^1_{14})^2\log\left(\frac{\alpha_1}{\alpha_4}\right)\right\}.
\end{aligned} \tag{F.25}
$$

## F.5 One pair of corner energies are equal

We assume here that corner 1 and 2 have equal energies and weight factor, $w_1$.

### F.5.1 Weight factor for corners 1 and 2

$$
\begin{aligned}
I_1(b,c) &= 6\int_0^{1-b-c} \frac{a\,da}{[\alpha_1+b\alpha_{31}+c\alpha_{41}][\gamma_1+b\gamma_{31}+c\gamma_{41}]} \\
&= \frac{3(1-b-c)^2}{[\alpha_1+b\alpha_{31}+c\alpha_{41}][\gamma_1+b\gamma_{31}+c\gamma_{41}]}
\end{aligned} \tag{F.26}
$$

We now make the following change of variables:

$$
u = 1-b-c, \qquad v = c, \qquad \int_0^1 dc \int_0^{1-c} db \longrightarrow \int_0^1 du \int_0^{1-u} dv \tag{F.27}
$$

and then we can write $I_1$ on the form:

$$
\begin{aligned}
I_1(u,v) &= \frac{3u^2}{[\alpha_3+u\alpha_{13}+v\alpha_{43}][\gamma_1+u\gamma_{13}+v\gamma_{43}]} \\
&= \frac{3u^2}{[\alpha_3+u\alpha_{13}]\gamma_{43}-[\gamma_3+u\gamma_{13}]\alpha_{43}} \\
&\quad\times\left(\frac{\gamma_{43}}{[\gamma_3+u\gamma_{13}+v\gamma_{43}]}-\frac{\alpha_{43}}{[\alpha_3+u\alpha_{13}+v\alpha_{43}]}\right) \\
&= \frac{3}{\Delta^{134}_{\alpha\gamma}}\frac{u^2}{u-\Gamma^{134}_{\alpha\gamma}}\left(\frac{\alpha_{43}}{[\alpha_3+u\alpha_{13}+v\alpha_{43}]}-\frac{\gamma_{43}}{[\gamma_3+u\gamma_{13}+v\gamma_{43}]}\right)
\end{aligned} \tag{F.28}
$$

We can now easily get the second integral,

$$
\begin{aligned}
I_2(u) &= \int_0^{1-u} I_1(u,v)dv \\
&= \frac{3}{\Delta^{134}_{\alpha\gamma}}\frac{u^2}{u-\Gamma^{134}_{\alpha\gamma}}\left[\mathrm{Ld}(u,\gamma_3,\gamma_4;\gamma_1)-\mathrm{Ld}(u,\alpha_3,\alpha_4;\alpha_1)\right] \\
&= \frac{3}{\Delta^{134}_{\alpha\gamma}}\left(u+\Gamma^{134}_{\alpha\gamma}+\frac{(\Gamma^{134}_{\alpha\gamma})^2}{u-\Gamma^{134}_{\alpha\gamma}}\right)\mathrm{Ld}(u,\gamma_3,\gamma_4;\gamma_1) \\
&- \frac{3}{\Delta^{134}_{\alpha\gamma}}\left(u+\Gamma^{134}_{\alpha\gamma}+\frac{(\Gamma^{134}_{\alpha\gamma})^2}{u-\Gamma^{134}_{\alpha\gamma}}\right)\mathrm{Ld}(u,\alpha_3,\alpha_4;\alpha_1)
\end{aligned} \tag{F.29}
$$

Now we go back to our table of integrals in §F.1 and do the integral over $u$.

$$
\begin{aligned}
I_3 &= \frac{3}{\Delta^{134}_{\alpha\gamma}}\left[\mathrm{Lx}_1(\gamma_3,\gamma_4;\gamma_1)-\mathrm{Lx}_1(\alpha_3,\alpha_4;\alpha_1)\right] \\
&+ \frac{3}{\Delta^{134}_{\alpha\gamma}}\Gamma^{134}_{\alpha\gamma}\left[\mathrm{Lx}_1(\gamma_3,\gamma_4;\gamma_1)-\mathrm{Lx}_1(\alpha_3,\alpha_4;\alpha_1)\right] \\
&+ \frac{3}{\Delta^{134}_{\alpha\gamma}}(\Gamma^{134}_{\alpha\gamma})^2\left[\mathrm{Gx}_1(\gamma_3,\gamma_4;\gamma_1,\Gamma^{134}_{\alpha\gamma})-\mathrm{Gx}_1(\alpha_3,\alpha_4;\alpha_1,\Gamma^{134}_{\alpha\gamma})\right]
\end{aligned} \tag{F.30}
$$

### F.5.2 Weight factor for corner 4

$$
\begin{aligned}
I_1(b,c) &= 6\int_0^{1-b-c} \frac{c\,da}{[\alpha_1+b\alpha_{31}+c\alpha_{41}][\gamma_1+b\gamma_{31}+c\gamma_{41}]} \\
&= \frac{c(1-b-c)}{[\alpha_1+b\alpha_{31}+c\alpha_{41}][\gamma_1+b\gamma_{31}+c\gamma_{41}]} \\
&= \frac{6uv}{[\alpha_3+u\alpha_{13}+v\alpha_{43}][\gamma_1+u\gamma_{13}+v\gamma_{43}]} \\
&= \frac{6uv}{[\alpha_3+u\alpha_{13}]\gamma_{43}-[\gamma_3+u\gamma_{13}]\alpha_{43}} \\
&\quad\times\left(\frac{\gamma_{43}}{[\gamma_3+u\gamma_{13}+v\gamma_{43}]}-\frac{\alpha_{43}}{[\alpha_3+u\alpha_{13}+v\alpha_{43}]}\right) \\
&= \frac{6}{\Delta^{134}_{\alpha\gamma}}\frac{u}{u-\Gamma^{134}_{\alpha\gamma}}\left(\frac{v\alpha_{43}}{[\alpha_3+u\alpha_{13}+v\alpha_{43}]}-\frac{v\gamma_{43}}{[\gamma_3+u\gamma_{13}+v\gamma_{43}]}\right) \\
&= \frac{6}{\Delta^{134}_{\alpha\gamma}}\frac{u}{u-\Gamma^{134}_{\alpha\gamma}}\left(\frac{\gamma_1+u\gamma_{13}}{[\gamma_3+u\gamma_{13}+v\gamma_{43}]}-\frac{\alpha_3+u\alpha_{13}}{[\alpha_3+u\alpha_{13}+v\alpha_{43}]}\right) \\
&= \frac{6}{\Delta^{134}_{\alpha\gamma}}\left(1+\frac{\Gamma^{134}_{\alpha\gamma}}{u-\Gamma^{134}_{\alpha\gamma}}\right)\frac{\gamma_{13}}{\gamma_{43}}\frac{\gamma_{43}(u+\gamma^3_{13})}{[\gamma_3+u\gamma_{13}+v\gamma_{43}]} \\
&- \frac{6}{\Delta^{134}_{\alpha\gamma}}\left(1+\frac{\Gamma^{134}_{\alpha\gamma}}{u-\Gamma^{134}_{\alpha\gamma}}\right)\frac{\alpha_{13}}{\alpha_{43}}\frac{\alpha_{43}(u+\alpha^3_{13})}{[\alpha_3+u\alpha_{13}+v\alpha_{43}]} \qquad \text{(F.31)}
\end{aligned}
$$

We can now easily get the second integral,

$$
\begin{aligned}
I_2(u) &= \int_0^{1-u} I_1(u,v)dv \\
&= \frac{6}{\Delta^{134}_{\alpha\gamma}}\left(1+\frac{\Gamma^{134}_{\alpha\gamma}}{u-\Gamma^{134}_{\alpha\gamma}}\right)\frac{\alpha_{13}}{\alpha_{43}}(u+\alpha^3_{13})\mathrm{Ld}(u,\alpha_3,\alpha_4;\alpha_1) \\
&- \frac{6}{\Delta^{134}_{\alpha\gamma}}\left(1+\frac{\Gamma^{134}_{\alpha\gamma}}{u-\Gamma^{134}_{\alpha\gamma}}\right)\frac{\gamma_{13}}{\gamma_{43}}(u+\gamma^3_{13})\mathrm{Ld}(u,\gamma_3,\gamma_4;\gamma_1) \\
&= \frac{6}{\Delta^{134}_{\alpha\gamma}}\frac{\alpha_{13}}{\alpha_{43}}\left([\alpha^3_{13}+\Gamma^{134}_{\alpha\gamma}]+u+\frac{[\alpha^3_{13}+\Gamma^{134}_{\alpha\gamma}]\Gamma^{134}_{\alpha\gamma}}{u-\Gamma^{134}_{\alpha\gamma}}\right)\mathrm{Ld}(u,\alpha_3,\alpha_4;\alpha_1) \\
&- \frac{6}{\Delta^{134}_{\alpha\gamma}}\frac{\gamma_{13}}{\gamma_{43}}\left([\gamma^3_{13}+\Gamma^{134}_{\alpha\gamma}]+u+\frac{[\gamma^3_{13}+\Gamma^{134}_{\alpha\gamma}]\Gamma^{134}_{\alpha\gamma}}{u-\Gamma^{134}_{\alpha\gamma}}\right)\mathrm{Ld}(u,\gamma_3,\gamma_4;\gamma_1) \qquad \text{(F.32)}
\end{aligned}
$$

We now use the identities (F.9) and see that

$$
\frac{\alpha_{13}}{\alpha_{43}}\left(\alpha^3_{13}+\Gamma^{134}_{\alpha\gamma}\right)=-\Gamma^{413}_{\alpha\gamma} \qquad \text{and} \qquad \frac{\gamma_{13}}{\gamma_{43}}\left(\gamma^3_{13}+\Gamma^{134}_{\alpha\gamma}\right)=-\Gamma^{413}_{\alpha\gamma}. \qquad \text{(F.33)}
$$

Then we get,

$$
\begin{aligned}
I_2(u) &= \frac{6}{\Delta^{134}_{\alpha\gamma}}\left(\frac{\alpha_{13}}{\alpha_{43}}u-\Gamma^{413}_{\alpha\gamma}-\frac{\Gamma^{413}_{\alpha\gamma}\Gamma^{134}_{\alpha\gamma}}{u-\Gamma^{134}_{\alpha\gamma}}\right)[\log(\alpha_3+u\alpha_{13})-\log(\alpha_4+u\alpha_{14})] \\
&- \frac{6}{\Delta^{134}_{\alpha\gamma}}\left(\frac{\gamma_{13}}{\gamma_{43}}u-\Gamma^{413}_{\alpha\gamma}-\frac{\Gamma^{413}_{\alpha\gamma}\Gamma^{134}_{\alpha\gamma}}{u-\Gamma^{134}_{\alpha\gamma}}\right)[\log(\gamma_3+u\gamma_{13})-\log(\gamma_4+u\gamma_{14})] \qquad \text{(F.34)}
\end{aligned}
$$

Now it is a simple matter to write down the final integral over $u$ in terms of the functions we defined earlier, Hence we get,

$$\begin{aligned} I_3 &= \frac{6}{\Delta^{134}_{\alpha\gamma}} \left[ \frac{\alpha_{13}}{\alpha_{43}} \mathrm{Lx}_1(\alpha_3, \alpha_4; \alpha_1) - \frac{\gamma_{13}}{\gamma_{43}} \mathrm{Lx}_1(\gamma_3, \gamma_4; \gamma_1) \right] \\ &- \frac{6\Gamma^{413}_{\alpha\gamma}}{\Delta^{134}_{\alpha\gamma}} \left[ \mathrm{Lx}_0(\alpha_3, \alpha_4; \alpha_1) - \mathrm{Lx}_0(\gamma_3, \gamma_4; \gamma_1) \right] \\ &- \frac{6\Gamma^{413}_{\alpha\gamma}\Gamma^{134}_{\alpha\gamma}}{\Delta^{134}_{\alpha\gamma}} \left[ \mathrm{Gx}_1(\alpha_3, \alpha_4; \alpha_1, \Gamma^{134}) - \mathrm{Gx}_1(\gamma_3, \gamma_4; \gamma_1, \Gamma^{134}) \right] \end{aligned} \tag{F.35}$$

Finally to obtain the weight factor for corner 3 we just take the result for corner 4 and switch the indices 3 and 4.

$$\begin{aligned} I_3 &= \frac{6}{\Delta^{134}_{\alpha\gamma}} \left[ \frac{\alpha_{14}}{\alpha_{34}} \mathrm{Lx}_1(\alpha_3, \alpha_4; \alpha_1) - \frac{\gamma_{14}}{\gamma_{34}} \mathrm{Lx}_1(\gamma_3, \gamma_4; \gamma_1) \right] \\ &- \frac{6\Gamma^{314}_{\alpha\gamma}}{\Delta^{134}_{\alpha\gamma}} \left[ \mathrm{Lx}_0(\alpha_3, \alpha_4; \alpha_1) - \mathrm{Lx}_0(\gamma_3, \gamma_4; \gamma_1) \right] \\ &- \frac{6\Gamma^{314}_{\alpha\gamma}\Gamma^{134}_{\alpha\gamma}}{\Delta^{134}_{\alpha\gamma}} \left[ \mathrm{Gx}_1(\alpha_3, \alpha_4; \alpha_1, \Gamma^{134}) - \mathrm{Gx}_1(\gamma_3, \gamma_4; \gamma_1, \Gamma^{134}) \right] \end{aligned} \tag{F.36}$$

## F.6 All corners are different

In this case we have not been able to derive analytical formulas for the weight factors. The approximate solution that we have come up with is to express the integrals in the following fashion where $I(a,b,c,d)$ denotes the integral in question calculated with the energies at corners $a$, $b$, $c$ and $d$.

$$\begin{aligned} I(1,2,3,4) &= \frac{1}{12}[I(1,1,3,4) + I(2,2,3,4) + I(1,2,1,4) + I(3,2,3,4) \\ &+ I(1,2,3,1) + I(4,2,3,4) + I(1,2,2,4) + I(1,3,3,4) \\ &+ I(1,2,3,2) + I(1,4,3,4) + I(1,2,3,3) + I(1,2,4,4)]. \end{aligned} \tag{F.37}$$

The idea is to collapse two of the four corners and approximate the integral as the weighted contribution from all such collapses.

# Appendix G

# A note on a particular integral

In this note I want to take a look at the calculation of an integral that comes up in the evaluation of transport integrals over tetrahedral volumes. The integral in question is the following:

$$J(p,q,r) = \int_0^1 \frac{\log(p+qx)}{x-r} dx \tag{G.1}$$

Here $p$ and $q$ are such that both $p$ and $p+q$ are in the same half-plane and $r$ is a complex number and we note that the integral defines an analytic function of $r$ with a branch cut on the real axis between 0 and 1. The analytic solution to this integral can be written down explicitly in terms of the dilogarithm function, $\mathrm{Li}_2(x)$ and logarithms and is (ostensibly) given by:

$$\begin{aligned} J(p,q,r) &= \mathrm{Li}_2\left(\frac{p+q}{p+qr}\right) + \log(p+q)\log\left(1-\frac{p+q}{p+qr}\right) \\ &- \mathrm{Li}_2\left(\frac{p}{p+qr}\right)\log(p)\log\left(1-\frac{p}{p+qr}\right) \end{aligned} \tag{G.2}$$

The $\mathrm{Li}_2$ is defined in the following way:

$$\mathrm{Li}_2(z) = \sum_{k=1}^{\infty} \frac{z^k}{k^2} = -\int_0^z \frac{\log(1-w)dw}{w} = -\int_0^1 \frac{\log(1-zx)dx}{x}. \tag{G.3}$$

We note that the sum converges only for $|z| < 1$ but the integrals provide an analytic extension to the whole complex plane with a branch cut on the real axis from 1 to $\infty$. There are numerous identities and relations that exist between dilogarithms of different arguments [58, 59] but the one that we need to use here is:

$$\mathrm{Li}_2(z) = -\mathrm{Li}_2(1-z) - \log(z)\log(1-z) + \frac{\pi^2}{6}. \tag{G.4}$$

Let us now look more closely at the solution to the integral. Using the definition of the dilogarithm we see by direct differentiation that

$$J(z;p,q,r) = \int^z \frac{\log(p+qx)}{x-r}dx = \mathrm{Li}_2\left(\frac{p+qz}{p+qr}\right) + \log(p+qz)\log\left(1-\frac{p+qz}{p+qr}\right). \tag{G.5}$$

Now if line segment from $\frac{p}{p+qr}$ to $\frac{p+q}{p+qr}$ does not cut the real axis above 1 we see that we have indeed:

$$J(p,q,r) = J(1,p,q,r) - J(0,p,q,r). \tag{G.6}$$

However, if that happens, we have to take the branch cut into account and make sure that we stay on the right branch, i.e. the branch that we start out on. Thus let us write:

$$\begin{aligned}
\int_0^z \frac{\log(p+qx)}{x-r}dx &= \mathrm{Li}_2\left(\frac{p+qz}{p+qr}\right) + \log(p+qz)\log\left(1-\frac{p+qz}{p+qr}\right) - J(0,p,q,r) \\
&= \frac{\pi^2}{6} - \mathrm{Li}_2\left(1-\frac{p+qz}{p+qr}\right) - J(0,p,q,r) \\
&+ \left[\log(p+qz) - \log\left(\frac{p+qz}{p+qr}\right)\right]\log\left(1-\frac{p+qz}{p+qr}\right)
\end{aligned} \tag{G.7}$$

Here we have used the identity above and now we see that we don't have any problems with the dilogarithms and we need to consider the branch cut only for the term:

$$\log\left(1-\frac{p+qz}{p+qr}\right) \tag{G.8}$$

which is easy because we know exactly how it behaves at the branch cut. Thus we come to the conclusion that there are three cases that need to be considered depending on the position of the line segment:

$$l = \{z | z = z_0 + t(z_f - z_0), t \in [0,1]\} \tag{G.9}$$

where we have defined

$$z_0 = 1 - \frac{p}{p+qr} \qquad \text{and} \qquad z_f = 1 - \frac{p+q}{p+qr} \tag{G.10}$$

1. $l$ does not cut the negative real axis:

$$J(p,q,r) = \mathrm{Li}_2(1-z_f) + \log(p+q)\log(z_f) - \mathrm{Li}_2(1-z_0) - \log(p)\log(z_0) \tag{G.11}$$

2. $l$ does cut the negative real axis and $Im(z_0) > 0$

$$\begin{aligned} J(p,q,r) &= \frac{\pi^2}{6} - \mathrm{Li}_2(z_f) + [\log(p+q) - \log(1-z_f)]\,[\log(z_f) + 2\pi i] \\ &- \mathrm{Li}_2(1-z_0) - \log(p)\log(z_0) \end{aligned} \tag{G.12}$$

3. $l$ does cut the negative real axis and $Im(z_0) < 0$

$$\begin{aligned} J(p,q,r) &= \frac{\pi^2}{6} - \mathrm{Li}_2(z_f) + [\log(p+q) - \log(1-z_f)]\,[\log(z_f) - 2\pi i] \\ &- \mathrm{Li}_2(1-z_0) - \log(p)\log(z_0) \end{aligned} \tag{G.13}$$

We can now use the identity again on case 2 and 3 and we get:

$$\begin{aligned} J(p,q,r) &= \mathrm{Li}_2(1-z_f) + \log(p+q)\log(z_f) - \mathrm{Li}_2(1-z_0) - \log(p)\log(z_0) \\ &+ 2\pi i Sign[Im(z_0)](\log(p+q) - \log(1-z_f)) \end{aligned} \tag{G.14}$$

# References

[1] Antoine Georges, Gabriel Kotliar, Werner Krauth, and Marcelo J. Rozenberg. Dynamical mean-field theory of strongly correlated fermion system and the limit of infinite dimensions. *Rev. Mod. Phys.*, 68(1):13–125, 1996.

[2] J. Hubbard. Electron correlations in narrow energy bands. *Proc. Roy. Soc. London A*, 276:238–257, 1963.

[3] Martin C. Gutzwiller. Effects of correlation on the ferromagnetism of transition metals. *Phys. Rev. Lett.*, 10(5):159–162, 1963.

[4] P. Coleman. New approach to the mixed-valence problem. *Phys. Rev. B*, 29:3035–3044, 1984.

[5] N. E. Bickers. Review of techniques on the large-N expansion for dilute magnetic alloys. *Rev. Mod. Phys.*, 59(4):845–939, 1987.

[6] Daniel Lee Cox. *Dynamics of valence fluctuating rare earth compounds*. PhD thesis, Materials Science Center, Cornell University, Ithaca, New York, 1985.

[7] Th. Pruschke and N. Grewe. The Anderson Model with finite Coulomb repulsion. *Z. Phys. B*, 74:439–449, 1989.

[8] F.B. Anders. An enhanced perturbational study on spectral properties of the Anderson model. *J. Phys. C*, 7:2801–2818, 1995.

[9] W. H. Press, B. P. Flannery, S. A. Teukolsky, and W. T. Vetterling. *Numerical Recipes in C*. Cambridge University Press, New York NY, 2nd edition, 1994.

[10] P.M. Chaikin and G. Beni. Thermopower in the correlated hopping regime. *Phys. Rev. B*, 13(2):647–651, 1976.

[11] E. Müller-Hartmann. Self-Consistent Perturbation Theory of the Anderson Model: Ground State Properties. *Z. Phys. B*, 57:281–287, 1984.

[12] Olivier Parcollet, Antoine Georges, Gabriel Kotliar, and Anirvan Sengupta. Overscreened multichannel SU($N$) Kondo model: Large-$N$ solution and conformal field theory. *Phys. Rev. B*, 58:3794–3813, 1998.

[13] Gerald Mahan, Brian Sales, and Jeff Sharp. Thermoelectric materials: New approaches to an old problem. *Physics Today*, 50(3):42–47, 1997.

[14] Charles Kittel. *Introduction to Solid State Physics*. John Wiley & Sons, Inc., New York, 6th edition, 1986.

[15] D.M. Rowe, editor. *CRC Handbook of Thermoelectrics*. CRC Press, Boca Raton, Florida, 1995.

[16] B.C. Sales, D. Mandrus, B.C. Chakoumakos, V. Keppens, and J.R. Thompson. Filled skutterudite antimonides: Electron crystals and phonon glasses. *Phys. Rev. B*, 56:15081–15089, 1997.

[17] L.D. Hicks, T.C. Harman, X. Sun, and M.S. Dresselhaus. Experimental study of the effect of quantum-well structures on the thermoelectric figure of merit. *Phys. Rev. B*, 53(16):10493–10496, 1996.

[18] J.O. Sofo and G.D. Mahan. Thermoelectric figure of merit of superlattices. *Appl. Phys. Lett.*, 65(21):2690–2692, 1994.

[19] D.A. Broido and T.L. Reineicke. Effect of superlattice structure on the thermoelectric figure of merit. *Phys. Rev. B*, 51(19):13797–13800, 1995.

[20] D.A. Broido and T.L. Reineicke. Thermoelectric figure of merit of quantum wire superlattices. *Appl. Phys. Lett.*, 67(1):100–103, 1995.

[21] J.S. Blakemore. *Solid state physics.* Cambridge University Press, Cambridge, Great Britain, 2nd edition, 1985.

[22] Gerald Mahan. Figure of merit for thermoelectrics. *J. Appl. Phys.*, 65(4):1578–1583, 1989.

[23] G.D. Mahan and J.O. Sofo. The best thermoelectric. *Proc. Natl. Acad. Sci. USA*, 93:7436–7439, 1996.

[24] Herbert B. Callen. *Thermodynamics.* John Wiley & Sons, Inc., New York, N.Y., 1960.

[25] Robert R. Heikes and Roland W. Ure. *Thermoelectricity: Science and Engineering.* Interscience Publishers, Inc., New York, N.Y., 1961.

[26] R.D. Barnard. *Thermoelectricity in metals and alloys.* John Wiley & Sons, Inc., New York, N.Y., 1972.

[27] Gerald D. Mahan. *Many-Particle Physics.* Plenum, New York, N.Y., 2nd edition, 1993.

[28] I. S. Gradshteyn and I. M. Ryshik. *Table of Integrals, Series, and Products.* Academic Press, London, 5th edition, 1994.

[29] Akira Oguri and Sadamichi Maekawa. Electrical resistivity, thermal conductivity, and thermopower in the $U = \infty$ Hubbard model. *Phys. Rev. B*, 41:6977–6988, 1990.

[30] Henrik Kajueter and Gabriel Kotliar. New Iterative Perturbation Scheme for Lattice Models with Arbitrary Filling. *Phys. Rev. Lett.*, 77(1):131–134, 1996.

[31] Henrik Kajueter. *Interpolating perturbation scheme for correlated electron systems.* PhD thesis, Rutgers University, Graduate School New Brunswick, NJ, 1996.

[32] P. Nozièrez. *Le Problème à N Corps.* Dunod, Paris, France, 1963.

[33] A.A. Abrikosov, L.P. Gorkov, and I.E. Dzyaloshinski. *Methods of quantum field theory in statistical physics.* Dover, New York, N.Y., 1963.

[34] Y. Tokura, Y. Taguchi, Y. Okada, Y. Fujishima, T. Arima, K. Kumagai, and Y. Iye. Filling Dependence of Electronic Properties on the Verge of Metal-Mott-Insulator Transitions in $Sr_{1-x}La_xTiO_3$. *Phys. Rev. Lett.*, 70(14):2126–2129, 1993.

[35] D.A. Crandles, T. Timusk, J.D. Garrett, and J.E. Greedan. The midinfrared absorption in $\mathrm{RTiO_3}$ perovskites (R=La, Ce, Pr, Nd, Sm, Gd) The Hubbard Gap? *Physica C*, 201:407–412, 1992.

[36] Y. Tokura, Y. Taguchi, Y. Okada, T. Katsufuji, T. Arima, and K. Kumagai. Change of electronic structures with hole doping in strongly correlated electron systems: titanium oxides. *Physica B*, 186-188:992–994, 1993.

[37] Joseph E. Sunstrom, IV, Susan M. Kauzlarich, and Peter Klavins. Synthesis, Structure, and Properties of $\mathrm{La_{1-x}Sr_xTiO_3}$ $(0 \leq x \leq 1)$. *Chem. Mater.*, 4(2):346–353, 1992.

[38] Masatoshi Imada, Atsushi Fujimori, and Yoshinori Tokura. Metal-insulator transitions. *Rev. Mod. Phys.*, 70:1039–1264, 1998.

[39] C.C. Hays, J.S. Zhou, J.T. Markert, and J.B. Goodenough. Electronic transition in $\mathrm{La_{1-x}Sr_xTiO_3}$. *Phys. Rev. B*, 60(14):10367–10373, 1999.

[40] Masashige Onoda and Masaki Kohno. Antiferromagnetic correlation effects in the metal-insulator crossover of the perovskite-type $\mathrm{La_{1-x}Sr_xTiO_3}$ system. *J. Phys. Cond. Matter*, 10:1003–1011, 1998.

[41] Ralf Moos, Alain Gnudi, and Karl Heinz Härdtl. Thermopower of $\mathrm{Sr_{1-x}La_xTiO_3}$ ceramics. *J. Appl. Phys.*, 78(8):5042–5047, 1995.

[42] D.W. Visser, A.P. Ramirez, and M.A. Subramanian. Thermal Conductivity of Manganite Perovskites: Colossal Magnetoresistance as a Lattice-Dynamics Transition. *Phys. Rev. Lett.*, 78(20):3947–3950, 1997.

[43] Gabriel Kotliar, Sergej Y. Savrasov, and Gunnar Pálsson. Abstract Cluster Dynamical Mean Field Theory. Submitted to Physical Review Letters.

[44] J.M. Ziman. *Principles of the Theory of Solids.* Cambridge University Press, London, England, 1964.

[45] Seong-Gon Kim, I.I. Mazin, and D.J. Singh. First Principles Study of Zn-Sb Thermoelectrics. *Electronic Archive, xxx.lanl.gov, cond-mat/9709148*, 1997.

[46] J. Moreno and P. Coleman. Thermal currents in highly correlated systems. *Electronic Archive, xxx.lanl.gov, cond-mat/9603079*, 1996.

[47] Sergej Y. Savrasov. Unpublished notes.

[48] Ph. Lambin and J.P. Vigneron. Computation of crystal Green's functions in the complex-energy plane with the use of the analytical tetrahedron method. *Phys. Rev. B*, 29(6):3430–3437, 1984.

[49] H.L. Skriver. *The LMTO Method.* Springer-Verlag, Heidelberg, Germany, 1984.

[50] Frank J. Blatt, Peter A. Schroeder, Carl L. Foiles, and Denis Greig. *Thermoelectric power of metals.* Plenum Press, New York, N.Y., 1976.

[51] N.W. Ashcroft and N.D. Mermin. *Solid State Physics.* Saunders College, Philadelphia, 1976.

[52] S.Y. Savrasov and D.Y. Savrasov. Electron-phonon interactions and related physical properties of metals from linear-response theory. *Phys. Rev. B*, 54:16487–16501, 1996.

[53] Sergej Y. Savrasov, Gabriel Kotliar, and Dario Villani. Fast impurity solver in dynamical mean-field calculations. Unpublished.

[54] Henrik Kajueter, Gabriel Kotliar, and Goetz Moeller. Doped Mott insulator: Results from mean field theory. *Phys. Rev. B*, 53(24):16214–16226, 1996.

[55] Raymond Frésard and Gabriel Kotliar. Interplay of Mott transition and ferromagnetism in the orbitally degenerate Hubbard model. *Phys. Rev. B*, 56:12909–12915, 1997.

[56] T. Yoshida, A. Ino, T. Mizokawa, A. Fujimori, Y. Taguchi, T. Katsufuji, and Y. Tokura. Photoemission Spectral Weight Transfer and Mass Renormalization in the Fermi-Liquid System $La_{1-x}Sr_xTiO_{3+y/2}$. *Electronic Archive, xxx.lanl.gov, cond-mat/9911446*, 1999.

[57] J.B. Goodenough. Private communication.

[58] Leonard Lewin. *Polylogarithms and associated functions.* Elsevier, North Holland, Inc., New York, N.Y., 1981.

[59] Carlos Osácar, Jesús Palacián, and Manuel Palacios. Numerical evaluation of the dilogarithm of complex argument. *Celestial Mechanics and Dynamical Astronomy*, 62:93–98, 1995.

# Vita

## Gunnar Pálsson

| | |
|---|---|
| **1990** | Graduated from The Akureyri Junior College, Akureyri, Iceland. |
| **1990 - 1994** | **Attended University of Iceland, Reykjavík, Iceland.** Majors: Physics and Mathematics. |
| **1994** | **Bachelor of Science** in Physics and Mathematics. |
| **1994 - present** | **Graduate Studies in Condensed Matter Physics, Rutgers University, New Brunswick, New Jersey.** |
| **1994 - 1996** | Excellence Fellowship, Rutgers University. |
| **1996 - 1997** | Teaching Assistant. |
| **1997 - 2000** | Graduate Assistant. |
| **2001** | **Ph.D. in Physics.** |

### Publications

| | |
|---|---|
| **1994** | Screening of an impurity in a two-dimensional electron gas within the Hartree and Hartree-Fock approximation in the quantum Hall regime<br>Vidar Gudmundsson and Gunnar Pálsson, *Physical Review B.* **73**, 13712, (1994). |
| **1994** | Enhancement of the g-factor and spin-density wave state in a confined 2DEG in the quantum Hall regime<br>Vidar Gudmundsson and Gunnar Pálsson, *Physica Scripta* **T54**, 92, (1994). |
| **1998** | Thermoelectric response near the density driven Mott transition<br>Gunnar Pálsson and Gabriel Kotliar, *Physical Review Letters* **80**, 4775 (1998). |
| **2000** | Cellular Dynamical Mean Field Approach to Strongly Correlated Systems<br>Gabriel Kotliar, Sergej Y. Savrasov and Gunnar Pálsson, submitted to *Physical Review Letters.* |